Characterisation and spectroscopy of laser-cooled atoms with an optical nanofibre

Laura Russell
BSc
104375696

NATIONAL UNIVERSITY OF IRELAND, CORK

Faculty of Science

Department of Physics

Thesis submitted for the degree of Doctor of Philosophy

September 2013

Supervisor: Prof. Síle Nic Chormaic

Head of Department/School: Prof. John McInerney

Research supported by Science Foundation Ireland under Grant No. 08/ERA/l1761 through the NanoSci-E+ project NOIs, Grant No. 06/W.1/I866 and 07/RFP/PHYF518. The author acknowledges support from IRCSET under the Embark Initiative. This work was also supported by Okinawa Institute of Science and Technology Graduate University.

Contents

List of Figures

List of Tables

I, Laura Russell, certify that this thesis is my own work and I have not obtained a degree in this university or elsewhere on the basis of the work submitted in this thesis.

Laura Russell

To my parents, Max and Mary, who deserve honorary physics degrees

Acknowledgements

This thesis would not have been possible without the guidance and experience of many people. I wish to express my gratitude to my supervisor, Dr Síle Nic Chormaic for allowing me to join the Quantum Optics Group and not only gain an enormous wealth of experimental skills, but also giving me the opportunity to travel far and wide with my research, to meet hundreds of physicists and to present my research at numerous conferences. Additionally, throughout my time in the Quantum Optics Group, I came to know and work with many people who aided my research and development as a physicist. I would like to thank those who I worked closely with on the experiment – Dr Michael Morrissey, Dr Kieran Deasy, and Mark Daly. I wish to thank Dr V B Tiwari for his guidance as a post-doc. I also wish to thank Prof Vladimir Minogin for his unbounded expertise over the years. The other members of the group: Dr Jonathan Ward, Dr Yuqiang Wu, Dr Yong Yang, Dr Giang Truong, Mary Frawley, Amy Watkins, Ravi Kumar, Alex Petcu-Colan, Ramgopal Madugani, Aili Maimaiti, Vandna Gokhroo, Poppy Semonyo, Eugen Prel, Dr Ivan Gusachenko, Alan Curtis; thank you all for making each day in the lab exciting!

In 2010, I spent time in the Quantum Technologies research group in Universitat Bonn, Germany. I wish to thank Prof Dieter Meschede for this opportunity. These three months were inspirational not least because of the people I met – Dr Kotya Karapetyan, Dr Tobias Kampschulte, Fabian Bruse, Andreas Steffan, Dr Ulrich Wiedemann, Dr Artur Widera, Dr Wolfgang Alt, Dr Andrea Alberti, Ms Annelise von Rudloff-Miglo and the many other group members I came to know.

Towards the end of my studies, many people lent helping hands where programming, electronics and analysis were concerned. For this, I extend my gratitude to Eddie Cotter, Aidan Daly and Dr Giang Truong. Additionally, the staff in the mechanical workshop in the Physics Department were an extremely valuable resource – I wish to thank them for the time they spent fabricating some customised items for the experiment.

I also wish to thank Dr Thomas Busch for his support, motivation, and insistence on attendence at the Journal Club; and the Ultracold Quantum Gases group members who I came to know during my PhD.

Finally, to my flying friends around the globe, I think I'd go crazy without you all to show me the lighter side to life. Brian: your skill in diffusing my frustration after long, unproductive days in the lab, even from half way across the globe, is admirable. Joe and Cathy, thank you for your common sense. To my parents – your unquenchable support and interest in my research has propelled me along. I wonder where I would be without you both.

Thanks Nan.

Laura Russell

Abstract

In this thesis, a magneto-optical trap setup is used to laser cool and confine a cloud of ^{85}Rb. The cloud typically contains 10^8 atoms in a 1 mm^3 volume at a temperature in the region of the Doppler Limit (146 μK for ^{85}Rb). To study the cold cloud, a subwavelength optical fibre – a nanofibre, or ONF – is positioned inside the cloud. The ONF can be used in two ways. Firstly, it is an efficient fluorescence collection tool for the cold atoms. Loading times, lifetimes and temperatures can be measured by coupling the atomic fluorescence to the evanescent region of the ONF. Secondly, the ONF is used as a probe beam delivery tool using the evanescent field properties of the device, allowing one to perform spectroscopy on few numbers of near-surface atoms. With improvements in optical density of the cloud, this system is an ideal candidate in which to generate electromagnetically induced transparency and slow light. A theoretical study of the van der Waals and Casimir-Polder interactions between an atom and a dielectric surface is also presented in this work in order to understand their effects in the spectroscopy of near-surface atoms.

List of Publications

1. Russell, L., Gleeson, D. A., Minogin, V. G. and Nic Chormaic, S. Spectral distribution of atomic fluorescence coupled into an optical nanofibre. Journal of Physics B: Atomic, Molecular and Optical Physics 42, 185006 (2009).

2. Russell, L., Deasy, K., Daly, M. J., Morrissey, M. J. and Nic Chormaic, S. Sub-Doppler temperature measurements of laser-cooled atoms using optical nanofibres. Measurement Science and Technology 23, 015201 (2012).

3. Russell, L., Daly, M. and Nic Chormaic, S. 1- and 2-photon absorption by laser-cooled ^{85}Rb using an optical nanofiber. AIP Conference Proceedings 1469, 82–90 (2012).

4. Russell, L., Kumar, R., Tiwari, V. B. and Nic Chormaic, S. Measurements on release-recapture of cold ^{85}Rb atoms using an optical nanofibre in a magneto-optical trap. Optics Communications 309, 313-317 (2013).

5. Morrissey, M., Deasy, K., Frawley, M., Kumar, R., Prel, E., Russell, L., Truong, V. G. and Nic Chormaic, S. Spectroscopy, Manipulation and Trapping of Neutral Atoms and Other Particles using Optical Nanofibers: A Review, Sensors 2013, 13(8), 10449-10481 (2013).

6. Russell, L., Kumar, R., Tiwari, V. B. and Nic Chormaic, S. Investigation of a ^{85}Rb-dark magneto-optical trap using an optical nanofibre, *in preparation*.

List of Presentations

1. L. Russell, D. A. Gleeson, V. G. Minogin and S. Nic Chormaic, Atomic fluorescence coupled into an optical nanofibre: theory, poster YAO09, Vienna, Austria, February 2009.
2. L. Russell, V. Minogin and S. Nic Chormaic, Influence of surface interactions on the line shape of atomic resonance fluorescence coupled into an ultrathin optical fibre, poster at Photonics Ireland, Cork, Ireland, September 2009. Winner of Best Student Paper.
3. L. Russell, S. Nic Chormaic, J. M. Ward and M. J. Morrissey, Thermo-optical tuning of whispering gallery modes in microspheres around the 85Rb cooling transition, talk FThC2 at Frontiers in Optics, San Jose, USA, October 2009.
4. L. Russell, S.Nic Chormaic, K. Deasy, M. Morrissey, A. Watkins, M. Frawley and R. Schmidt, Ultrathin optical fibres as tools in atom optics, talk FMG3 at Frontiers in Optics, San Jose, USA, October 2009.
5. L. Russell, D. Gleeson, V. G. Minogin and S. Nic Chormaic, Atomic fluorescence coupled into an optical nanofibre: Theory, poster at the North-South Quantum Information School, NUI Maynooth, Ireland, January 2010.
6. L. Russell, D. Gleeson, V. G. Minogin and S. Nic Chormaic, Atomic fluorescence coupled into an optical nanofibre: Theory, poster at 450th WE-Heraeus Seminar "Mixed States of Light and Matter", Physikzentrum Bad Honnef, Germany, February 2010.
7. L. Russell, K. Deasy, M. Daly, A. Watkins, M. Morrissey and S. Nic Chormaic, Ultrathin optical fibres as spectroscopic tools in cold atoms, talk at Photon10, Southampton, UK, September 2010.
8. L. Russell, M. Daly, K. Deasy and S. Nic Chormaic, 1- and 2-photon absorption by laser cooled ^{85}Rb via an optical nanofibre, poster at IOP Ireland Spring Weekend, Carlingford, Ireland, April 2011.
9. L. Russell, M. Daly and S. Nic Chormaic, 1- and 2-photon absorption with a bright optical nanofibre probe in laser cooled rubidium, talk at Photonics Ireland 2011, Malahide, Dublin, September 2011.
10. L. Russell, R. Kumar, V.B. Tiwari and S. Nic Chormaic, Optical nanofibres as probes for bright and dark cold atoms (contributed talk): Quantum Africa 2, South Africa September 2012

List of Figures

List of Tables

List of Acronyms, Symbols and Notations[1]

a	ONF radius
AOM	Acousto-optical modulator
APD	Avalanche photodiode
B	Magnetic field
B_x, B_y, B_z	Magnetic field components
BS/PBS	Beam-splitter/Polarising beam-splitter
β	Propagation constant
C_3	Van der Waals constant
C_4	Casimir-Polder constant
CCD	Charge-coupled device
CF	ConFlat
CO	Crossover
D_f	$= 2a$, diameter of an ONF
D_{SMF}	Single mode cut-off diameter for an ONF
DAQ	Data acquisition
DSO	Digital storage oscilloscope
δ	Detuning
$\delta\omega_{CP}$	Frequency shift due to the Casimir-Polder interaction
$\delta\omega_{vdW}$	Frequency shift due to the van der Waals interaction
E	Electric field
E_x, E_y, E_z, E_r, E_ϕ	Electric field components
ECDL	Extended cavity diode laser
ϵ	Static relative permittivity
F, F', F''	Ground state, first excited state, second excited state hyperfine level
FO	Forced oscillation (temperature measurement)
FWHM	Full width half max
γ_0	Natural linewidth of a transition
γ	Total spontaneous emission rate
$\gamma^{(g)}$	Spontaneous emission rate into the guided mode(s) of an ONF
$\gamma^{(r)}$	Spontaneous emission rate into the radiative mode(s) of an ONF
HE	Hybrid electric
I_{cool}	Cooling beam intensity
IR	Infrared
k_0	Freespace wavenumber
K_l, J_l	Bessel functions of the first kind and modified Bessel functions of the second kind, respectively
KF	Klein flange
LP	Linearly polarised

[1]Mathematical constants and symbols are denoted by *emphasized* text, acronyms are given by CAPITALS, and notations are written in regular text with 'single quotations.'

Λ	Natural linewidth of an atom
λ	Wavelength
MOT	Magneto-optical trap
MS	Multiple scattering
N_A	Number of atoms (in the MOT)
ND	Neutral density (filter)
N_{eff}	Effective number of atoms in the evanescent field of an ONF carrying a probe beam
n_{eff}	Effective number of atoms emitting fluorescence into the evanescent region of an ONF
ONF	Optical nanofibre – the nanoscale region of a tapered fibre
Ω	Rabi frequency
P	Power
PC	Personal computer
PID	Proportional integral differential
PZT	Piezo-electric transducer
QOG	Quantum Optics Group
r	Radial distance
Rb	Rubidium
RF	Radio frequency
RR	Release-recapture
RVP	Rotary vane pump
SAS	Saturated absorption spectroscopy
SEM	Scanning electron microscope/microscopy
SMF	Single mode fibre
SPCM	Single photon counting module
Tapered fibre	General term describing the exponentially-tapered fibres used in this work
TE	Transverse electric
TL	Temperature limited
TM	Transverse magnetic
TMP	Turbomoleular pump
TOF	Time-of-flight
UHV	Ultra-high vacuum
UV	Ultraviolet
V	Voltage
V-number	$= 2\pi aNA/\lambda$
VCO	Voltage-controlled oscillator
ω	Frequency of laser
ω_0	Position-dependent atomic transition frequency

Chapter 1

Introduction

This body of work is motivated by the concept of trapping, guiding and probing single atoms, few atoms, or many atoms, around and along a subwavelength optical fibre using optical techniques. To achieve microscopic atom guidance, researchers used current carrying wires. The first of these was created by Schmiedmayer in 1995 [**?**] where atoms from an atom beam were guided along a 1 m long, 150 μm diameter, segment of wire. Reichel *et al.* [**?**] loaded cold rubidium atoms into a magnetic guide by gradually transforming the MOT trapping potential. Fortagh *et al.* [**?**] demonstrated that a fraction of 14% of the initially trapped atoms were transferred into the linear microtrap at a temperature of 39 μK. These initial techniques led to wires being nanofabricated on the surface of a chip whose associated magnetic fields could then be used to guide atoms near to the chip surface [**?**].

To achieve higher precision atomic manipulation, optical fields must be used. Generally, this implies that a field with high intensity gradient must be set up to generate strong confinement for laser cooled atoms. This was first proposed for neutral atoms by Ashkin in 1978 [**?**] and successfully implemented by Chu *et al.* in 1985 [**?**]. There are a number of ways to create such a high intensity gradient in an optical field. For example, Miller *et al.* [**?**] demonstrated the far-off-resonant optical dipole trap in 1993, transporting atoms a distance of the order of centimetres with submicron precision.

Evanescent fields can also be used to create a large intensity gradient and, thus, have the potential to trap atoms close to surfaces. This is of primary importance for the work presented in this thesis. In 1995, Renn *et al.* [**?**] used red detuned evanescent fields through a hollow-core optical fibre to attract atoms to high

intensities in the central region along the axis, and thus guide the atoms along the internal axis of the fibre. In a similar method, Müller *et al.* [?] used hollow-core optical fibres with blue-detuned laser light to guide atoms through a hollow fibre. Three methods have been proposed where atoms can be trapped very close to the surface of the fibre [?, ?, ?]. The two methods of most importance here are [?] and [?] – the first of these two has been demonstrated with cold caesium by two different groups [?, ?].

In relation to the work presented in this thesis, the attraction of the ONF is due to its ability to multitask. Atoms close to the ONF surface can spontaneously emit photons into the guided modes of the waveguide [?]. This offers a technique whereby small numbers of atoms can be efficiently probed, even if they are just held in a magnetic-optical trapping scheme. The ONF can also be used to trap laser-cooled atoms using the strong evanescent field surrounding its surface. After trapping, the evanescent field can be modified in real time to manipulate the trapping sites and, thus, guide the atoms. The confined atoms can then be probed using the absorption of an on-resonance beam propagating through the ONF. Eventually, laser cooling and nanofibre technologies will enable realisation of trapping in controlled sites specifically for atom entanglement via photon exchange [?, ?, ?, ?] and controlled atomic collisions [?, ?].

1.1 Laser-cooling

A Google Scholar search yields more than 10^6 results for the terms 'laser cooling'. As much of today's literature illustrates, the methodologies of laser cooling are varied and dependent on *what* is being cooled and to what *amount* it is being cooled. Temperatures achieved can be in the mK, μK, or even nK range depending on the method used.

The Nobel Prize in Physics was awarded to Steven Chu, Claude Cohen-Tannoudji and William D. Phillips in 1997 for "the development of methods to cool and trap atoms with laser light" [?, ?, ?]. In the last decade, advances in our understanding of metrology, quantum information, tests of fundamental theories, and degenerate gas studies have been facilitated by our ability to cool atoms, ions and a small number of molecules. Most experimental studies use alkali atoms such as sodium, rubidium and caesium.

One of the most popular and relatively simple cooling methods is Doppler cooling,

where dissipative optical forces are exerted via absorption and subsequent spontaneous emission of photons. The lowest temperature attainable with Doppler cooling is the Doppler Limit (146 μK for ^{85}Rb), but in combining Doppler cooling with an inhomogeneous magnetic field in a magneto-optical trap (MOT) arrangement, temperatures below this are reachable. The MOT used in this body of work is described in Chapter 2. In 1987, the first MOT was created by Raab *et al.* [**?**]: an atomic cloud of sodium was cooled to μK temperatures and trapped. Following this, Lett *et al.* [**?**] observed that, under certain conditions, the temperatures obtained in optical molasses are in fact much colder than the Doppler limit. There are several techniques in addition to the MOT that can be used to achieve sub-Doppler temperatures. Most of these techniques use the feature of non-adiabatic response of moving atoms to the light field. In the limit of low intensity, the orientation of moving atoms always lags behind that which would exist for stationary atoms. Thus, sub-Doppler cooling requires optical arrangements which incur spatially-dependent optical pumping processes in the atoms.

Doppler cooling is limited to a certain number of elements/atomic species for two reasons. Firstly, the more complicated the hyperfine structure of an atom is, the more routes it has to leave the cooling cycle which Doppler cooling operates on. Large sections of the periodic table are considered off-limits to magneto-optical trapping because of the perceived "optical leak" problem. Secondly, only certain optical transitions exist which have matching laser systems. For wavelengths below 300 nm, inexpensive and powerful lasers are hard to come by. Nevertheless, the catalogue of species which can be laser-cooled is continuously growing.

1.2 Subwavelength optical fibres

The development of subwavelength optical fibre has revolutionised a great number of experimental areas in physics. In the mid 1900's, a number of publications appeared which discussed the "open bound taper" waveguide in different configurations [**?**, **?**] and its relation to the retinal receptors in the human eye [**?**, **?**].

In 1887, a British physicist called Charles Vernon Boys reported drawing very thin glass fibres from molten minerals using flying arrows [**?**]. This may be the first written account of creating micro- and nano-scale tapered glass fibres. The technique of drawing these thin fibres was reported in 'On Laboratory Arts' by Richard Threlfall in 1898 [**?**]. These fibres were made for mechanical applications rather than the guidance of light. One of the first publications which reported

guiding light through a submicron fibre was in 1959 [?]. Here, the author dispels the belief that the waveguide must be 10-20 wavelengths in diameter to carry an electromagnetic signal. In the 60's, with the birth of the laser [?], Kao and Hockman proposed the possibility of achieving low optical loss in high-purity glasses which helped advance the future of fibre optics in the industry of optical communications [?].

In more recent decades, the fields and modes of tapered waveguides have become much better understood [?, ?, ?, ?] allowing experimentalists to fabricate such devices to higher levels of accuracy. In the early 70's, the tapered glass fibre began to take on roles as an optical coupler [?, ?, ?, ?], a filter [?, ?], a sensor [?], an amplifier for evanescent fields [?, ?, ?], and in supercontinuum generation [?, ?]. In 1999, Bures and Ghosh predicted the enhanced power density of the evanescent field in the vicinity of the tapered region which may be used in atomic mirrors [?]. The characteristic enhancement of the field density is one of the major advantages in using the ONF with external samples such as the cold cloud of ^{85}Rb atoms described in this work. The ONFs fabricated and used for the work presented in this thesis are described in Chapter 3.

1.3 Cold atoms and optical nanofibres

The aim of this work is to facilitate interplay between a subwavelength optical fibre and a sample of cold atoms. This introduces many topics in atom optics and a consideration for surface interactions. The atom cloud which is the subject of study here has a diameter in the range of a fraction of a millimetre to a few millimetres. Under typical experimental conditions, the cloud density is $\approx 10^{10}$ atoms/cm^3. These characteristics imply that, when the atom cloud is positioned around the nanofibre, there are a number of atoms near the glass surface. Typically, dipole interactions in the form of the van der Waals force are a significant consideration for atoms that exist somewhere in the first 100 nm from the fibre surface. In Chapter 4, a study of the van der Waals and the Casimir-Polder forces on the atom illustrate the broadening effects which are then seen in the resonance fluorescence of the atom. Further, the theoretical results show that the Casimir-Polder interaction can largely be neglected for our system.

The field of atom optics has evolved with our understanding of the wavelike properties of atoms. Atom mirrors [?, ?, ?] and atom guides [?, ?, ?], created with evanescent fields, are analogues of conventional "macroscale" devices. The

wider goal of this thesis is to create these atom optics elements via atom trapping and guiding with ONFs.

Atoms can be coupled to, and trapped near, a dielectric nanostructure such as an ONF without the need for additional external light fields. In 2004, theoretical work by Balykin *et al.* [**?**] described atom trapping and guiding using the evanescent field from a subwavelength-diameter optical fibre. Later that year, another proposal from Le Kien *et al.* [**?**] detailed a two-color evanescent light field around a subwavelength-diameter fibre to trap and guide atoms. Due to the small thickness of the ONF, far-off-resonance light fields can be used as they have substantially differing evanescent field decay lengths that produce a net potential with a deep minimum, a large coherence time, and a large trap lifetime [**?**]. Another proposal in 2008 [**?**] described the use of higher mode interference in ONFs to engineer trapping potentials for atoms.

One of the first steps of integrating atoms and ONFs is to use the ONF to collect the spontaneous emission from the surrounding laser-cooled atoms. This was investigated theoretically from 2005 onwards by Le Kien *et al.* [**?**, **?**, **?**, **?**]. For caesium, when the fiber radius is about 200 nm, up to 28% of the spontaneous emission from the atom can be channeled into the ONF guided modes. Furthermore, the confinement of the guided modes and the degeneracy of the excited and ground states can substantially affect the spontaneous emission process. Related theoretical work by Le Kien *et al.* in 2005 [**?**] described ONF-based energy transfer between two distant atoms near the ONF surface.

The efficient coupling of atomic fluorescence from laser cooled caesium to the guided mode of an ONF was demonstrated experimentally in [**?**]. Additionally, [**?**] highlighted the need for studies into the surface interactions between an ONF and surrounding laser cooled atoms in order to understand the asymmetric fluorescence excitation spectra obtained in the atom + ONF system. This asymmetry was observed again experimentally in 2007 by Sagué *et al.* [**?**] via the absorption of a resonant probe beam passing through the ONF while inside a laser-cooled sample of caesium atoms. Theoretical work in 2009 [**?**] studied the contributions to these lineshapes of the van der Waals and Casimir-Polder forces. The first demonstration of absorption through an ONF by ^{85}Rb is reported in [**?**].

Work by Morrissey *et al.* [**?**] and Deasy *et al.* [**?**] demonstrated that many of the characteristics of a MOT can easily be measured with an ONF. By placing the ONF in the central, most dense region of the atom cloud, new insight is gained into the dynamics of the MOT during loading and while recording the lifetime.

As reported in [?] and [?], the presence of the relatively hot ONF in the cold sample of atoms does not significantly effect the operating temperature of the MOT, allowing for the possibility to use an ONF with a BEC.

The first experimental demonstration of atom trapping was reported in 2010 using the two-colour method [?]. In [?], approximately 2000 caesium atoms were trapped and interfaced in a one-dimensional optical lattice created by a two-color evanescent field surrounding an ONF, approximately 230 nm from the ONF surface. The two-colour method was also used for caesium in [?] and an optical depth of 66 was achieved in the system.

1.4 Overview of this thesis

This thesis presents a variety of studies with cold atoms, tapered fibres and interactions between both. Chapter 2 describes the theoretical background for the magneto-optical trap and the experimental systems required for its operation. During the course of my PhD studies, I had the opportunity to work in the Laser Physics Group of Prof. Dr. Dieter Meschede at the University of Bonn. Throughout this three month period, a single-atom imaging objective which had been developed initially by W. Alt [?] was constructed and tested. Details of the resulting custom design is given at the end of Chapter 2.

Chapter 3 provides a summary of the waveguiding properties of optical fibres and optical nanofibres (ONFs). The end of the chapter focuses on the fibre-pulling-rig and the installation of the ONF in the vacuum chamber. An important point to note is that Chapters 3, 4 and 5 concentrate solely on the ONF as a collector of light rather than a device which delivers a probe beam. Thus, the evanescent field around the ONF will not be discussed until Chapter 7 where its characteristics are of critical importance.

Chapter 4 examines the surface interactions between a dielectric waveguide and a surrounding sample of atoms. This work can be found in [?]. The relevance of the Casimir-Polder force is assessed in the atom-surface system and lineshapes are modelled for the resonance fluorescence of rubidium and caesium near an ONF.

Chapter 5 summarises a number of experimental results obtained with the ONF. Two methods of temperature measurement are presented and compared: the method of forced oscillations [?] and the release-recapture method [?]. Important points regarding coupling efficiency are also discussed in the context of atomic

fluorescence and the guided mode of the ONF.

Chapter 6 presents recent work on the implementation of a dark magneto-optical trap for ^{85}Rb. Results from freespace spectroscopy are compared with results measured via the ONF.

Chapter 7 is a summary of ONF absorption spectroscopy. Theoretical considerations for the evanescent field surrounding an ONF are first presented and followed by experimental absorption results.

Finally, Chapter 8 illustrates some potential studies which the experiment can be used for provided a number of ONF-based limitations can be overcome. This chapter highlights the exciting possibilities open to the combination of high-density atomic samples with precisely-designed ONFs.

Chapter 2

Laser cooling with a magneto-optical trap for ^{85}Rb

The technique of laser cooling uses light to manipulate atoms. Through absorption and spontaneous re-emission of light, the translational kinetic energy of an atom – and therefore its temperature – can be reduced. Although many different cooling and trapping schemes exist to achieve cold gases in 1-, 2- and 3-dimensions, the most commonly-used scheme for neutral atoms is the magneto-optical trap (MOT). This hybrid trap uses a combination of laser and magnetic fields to optically pump slow-moving atoms in a linearly-inhomogeneous magnetic field. The scheme works for any atom with total angular momentum, J, of its ground and excited electronic state separated by 1: $J_g \rightarrow J_e = J_g + 1, J_g - 1, ...$ etc. The MOT has been described as the workhorse of the laser cooling world. It allows milli- and micro-Kelvin temperatures to be reached with neutral alkali atoms using modest laser powers and well-established laser frequency stabilisation techniques.

This chapter will outline the theoretical background to laser cooling in terms of atom-light interactions and the relevant atomic properties of rubidium-85 (^{85}Rb). In the second part of the chapter, the experimental setup used in this body of work will be outlined. This will include the laser locking scheme, optical setup and electronics. The final section of the chapter will discuss an inexpensive optical setup for a diffraction-limited, long working distance monochromotic objective to collect light from a MOT. This will be implemented in the setup for future work where high resolution imaging will be required to detect single atoms in optical traps.

2.1 Theory of laser-cooling

^{85}Rb (relative abundance = 72%) has 37 electrons, only one of which is in the outermost shell. The ground state ($5S_{1/2}$) has a total angular momentum, J_g, of 1/2. In the excited state, the total angular momentum (J_e) can be 1/2 ($5P_{1/2}$) or 3/2 ($5P_{3/2}$). The nuclear angular momentum, **I**, of ^{85}Rb is 5/2. The interaction between **I** and **J** leads to hyperfine structure, which means the total atomic angular momentum (**F**) is then given by $\mathbf{F} = \mathbf{J}+\mathbf{I}$, where the angular momentum can take the following values: $|J - I| \leq F \leq J + I$. When a magnetic field is applied to ^{85}Rb, the degeneracy is lifted from the $2F + 1$ Zeeman sublevels ($m_F = -F, ..., F$).

A brief explanation of how the MOT operates follows. For simplicity, take an atom with an atomic transition from $J_g = 0 \rightarrow J_e = 1$. In a magnetic field, this transition will have three Zeeman components ($m_e = -1, 0, +1$) which are excited by each of three polarisations (σ^-, π, σ^+) according to selection rules [**?**]. Figure **??** illustrates what happens when this atom experiences a linearly varying magnetic field and two counterpropagating, oppositely circularly-polarised laser beams (each with identical red-detuning, (δ<0) from the atomic resonance). When the external magnetic field is greater than 0, $m_e = +1$ is shifted upwards in energy and $m_e = -1$ is shifted downwards in energy due to the Zeeman effect. Thus, if the atom is in a position where $\mathbf{B} > 0$, then the $\Delta m = -1$ transition is in resonance: more light is scattered from the σ^- beam than the σ^+ beam. The atom is driven towards the centre of the trap. The reverse is true for $\mathbf{B} < 0$: $m_e = +1$ is shifted down and $m_e = -1$ is shifted up and the atom will scatter more light from the σ^+ beam and be driven towards the trap centre. The further the atom is from the centre of the MOT, the closer to resonance it is with the laser. This generates a restoring force towards the MOT centre. Since the laser light is detuned below the atomic resonance (δ<0), both compression and cooling of the atoms is achieved simultaneously in a MOT. The cooling itself is described by the 'optical molasses' effect of the optical part of the MOT. When the rubidium atom absorbs a photon from an oncoming laser beam, the atom makes a transition to the excited state (Figure **??**(a)-(b)). In addition to the transfer of photon energy, the atom experiences a momentum kick in the direction of propagation of the laser field due to the conservation of momentum (Figure **??**(b)). This recoil, whose strength is given by $\hbar k_0$, slows the atom by an amount $v_{rec} = hk_0/m_{Rb}$ for each photon absorption, i.e. 6 mm/s for Rb atoms (where m_{Rb} is the mass of the ^{85}Rb atom).

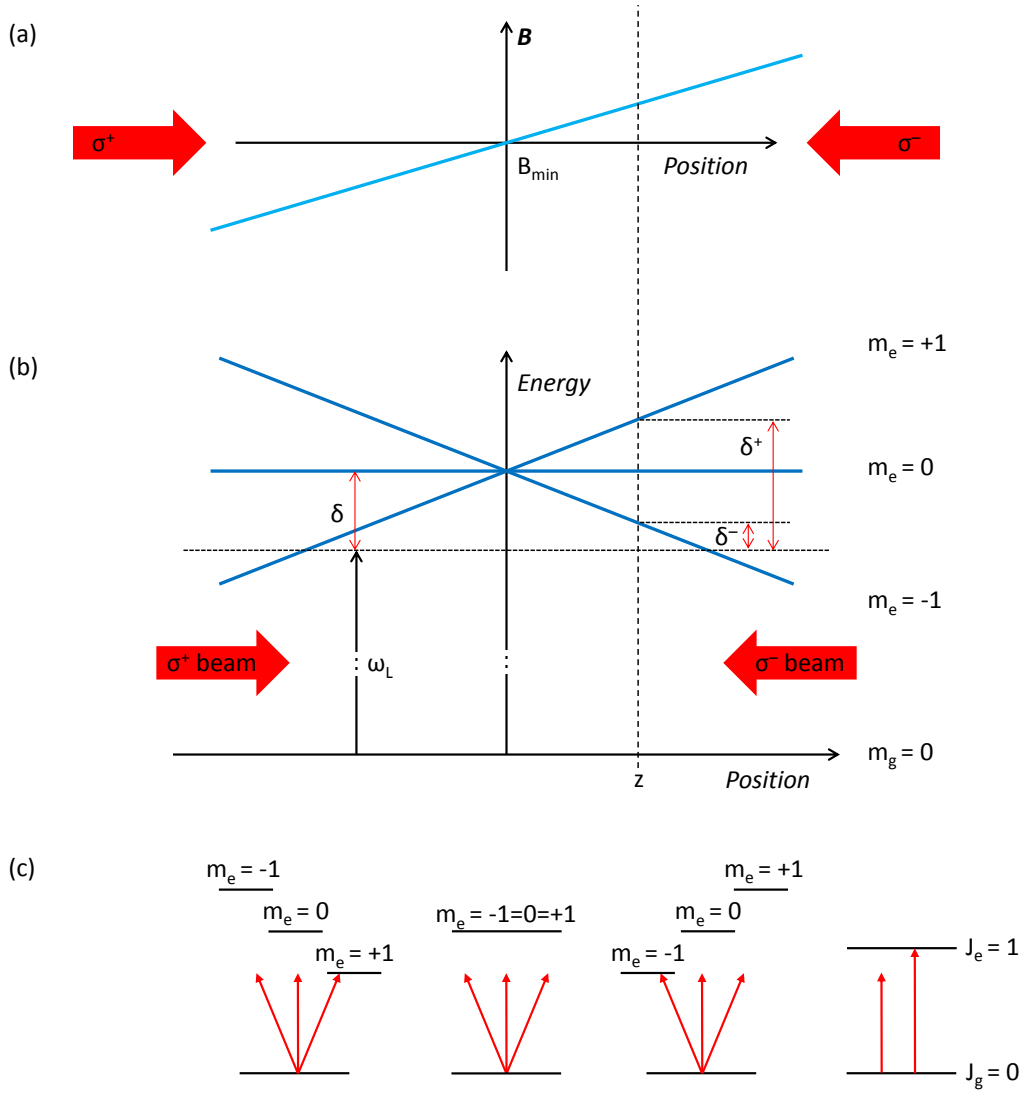

Figure 2.1: *1-dimensional model of a magneto-optical trap for a $J_g = 0 \rightarrow J_e = J_g + 1$ atom ($J_g = 0 \rightarrow J_e = 1$ is used for simplicity). (a) Oppositely circularly-polarised light beams of the same red-detuned frequency counterpropagate in a linearly inhomogeneous magnetic field. (b) The atom experiences splitting and shifting of its electronic transition levels according to its position in the magnetic field. The quantities δ^+ and δ^- indicate the position-dependent detuning of the cooling laser frequency from the shifted Zeeman levels $m_e = 1$ and $m_e = -1$, respectively. (c) Shifting of levels at three different positions in the MOT.*

The return to the ground state can be either by spontaneous or by stimulated emission. In the case of the work described here, the laser intensity is low and thus emission will be spontaneous in nature. The spatial symmetry of the emitted fluorescence results in an average of zero net momentum transfer from many such fluorescence events as indicated by Figure **??**(c). Thus, the net force on the atoms is in the direction of the laser beam (i.e. as a result of the initial absorption event),

and the maximum deceleration is limited by the spontaneous emission rate. By using intersecting, oppositely-directed laser beams, the movement of the atoms in the intersection region can be severly restricted. For $\delta<0$, the force experienced by the atoms due to the oncoming laser beams viscously damps the atomic motion. While the average momentum transfer of many spontaneous emissions is zero as mentioned, the rms scatter of these events is finite which leads to the Doppler cooling limit [**?**].

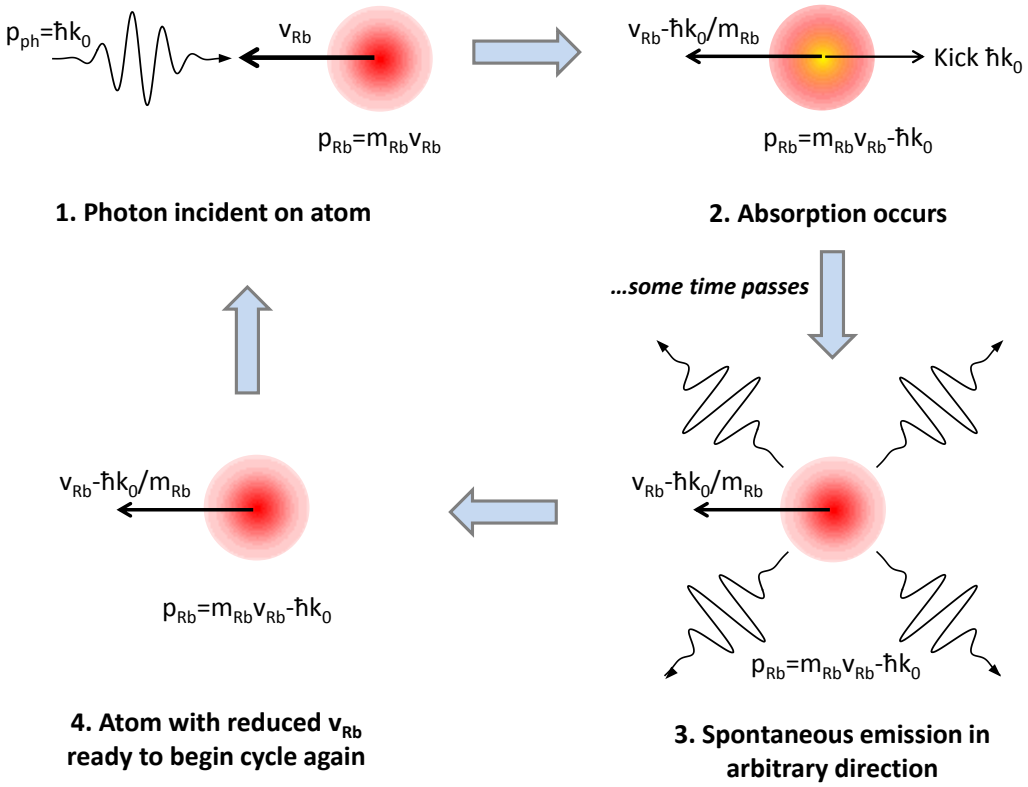

Figure 2.2: *An illustration of laser cooling in 1-dimension via spontaneous emission with momentum conservation considerations.*

Conceptually, the Doppler cooling limit can be understood from the finite natural linewidth of the cooling transition. This width automatically selects a frequency range within which the cooling laser can operate. With increased red-detuning, lower temperatures can be achieved but a corresponding drop in absorption efficiency must occur as the frequency of the laser is 'on-resonance' with some position on the side of the lineshape.

The Doppler limit temperature can also be understood to result from an equilibrium between laser cooling and the heating process arising from the random nature of both the absorption and emission of photons. The random addition to the average momentum transfer produces a random walk of the atomic mo-

mentum and an increase in the mean square atomic momentum. This heating is countered by the cooling force which opposes atomic motion. The force is proportional to the atomic velocity, as the Doppler shift is proportional to velocity. In this, the cooling force is similar to the friction force experienced by a body moving in a viscous fluid hence the term 'optical molasses'. The rate at which energy is removed by cooling is proportional to v^2, so the cooling rate is proportional to the kinetic energy. By contrast, the heating rate, proportional to the total photon scattering rate, is independent of atomic kinetic energy for low velocities. As a result, the heating and cooling come to equilibrium at a certain value of the average kinetic energy. This defines the temperature for Doppler cooling, which is

$$m\langle v_i^2\rangle = k_B T = \frac{\hbar\Gamma}{4}\left(\frac{\Gamma}{2\delta} + \frac{2\delta}{\Gamma}\right) \tag{2.1}$$

where v_i is the velocity along some axis. This expression is valid for 3D Doppler cooling in the limit of low intensity and when the recoil energy $\hbar^2k^2/2m \ll \Gamma$ [**?**]. The minimum value of this temperature is called the Doppler cooling limit, occurring when $T_D = h\gamma/2k_B$, where γ is the natural linewidth of the cooling transition.

In this work, the MOT is implemented in 3-dimensions by using three pairs of laser beams and a spherical quadrupole magnetic field. The technical specifications of this are contained in the following section. The transition $F = 3 \rightarrow F' = 4$ is used for cooling as, by selection rules, scattering from $F' = 4$ to $F = 2$ is not possible. In reality, atoms will accumulate in $F = 2$ after many cooling cycles. This necessitates the use of a repumping laser tuned to $F = 2 \rightarrow F' = 3$. The laser frequencies used are illustrated in Figure **??**. Typically, δ is set to two or three natural linewidths ($\sim$ 2–3 $\times$ 6 MHz) below resonance as this range gives the best compromise between steady-state atom number, scattering rate and temperature.

2.2 Experimental setup

To create a magneto-optical trap for ^{85}Rb, three main systems are required: (a) two frequency-stabilised lasers – one for laser cooling on the closed transition and one for repumping the atom back into this closed transition, (b) a spherical

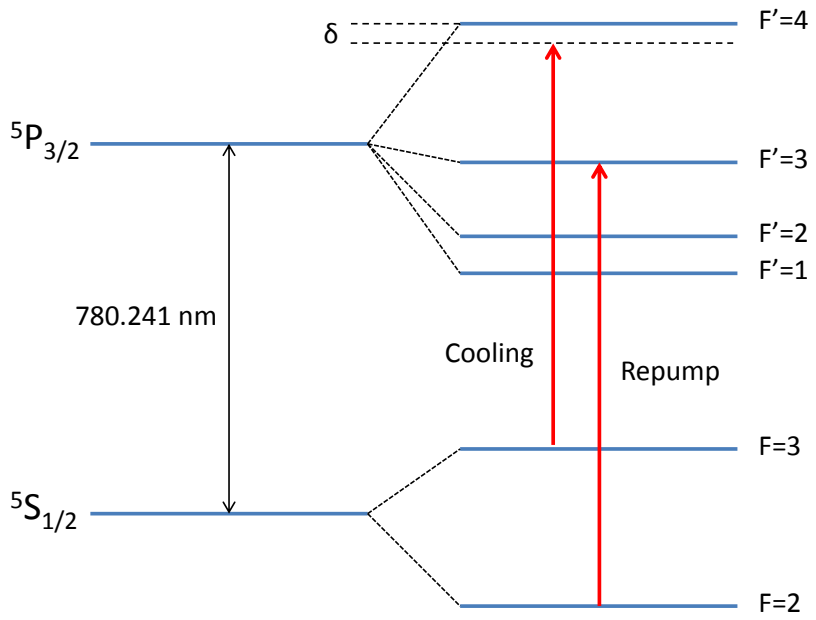

Figure 2.3: *Energy level scheme for the ground and first excited state electronic transition (D2) in ^{85}Rb and the laser frequencies used in the MOT. The cooling laser is detuned from the $F = 3 \rightarrow F' = 4$ transition by an amount δ.*

quadrupole magnetic field to create a linear magnetic field gradient in the region of the laser intersection, and (c) an ultra-high vacuum (UHV) chamber to minimise collisions between the cold atoms and thermal background. The following sections describe these technologies as well as the optical setup, the ^{85}Rb source and the operational procedures of each system.

2.2.1 Laser system and optical arrangement

Two tunable, narrow linewidth extended cavity diode lasers (ECDLs) are used to cool ^{85}Rb. The cooling laser consists of a Sacher-Lasertechnik TEC-300 diode (Tiger) inside a Sacher Lasertechnik housing. The repump laser is a 150 mW Sacher-Lasertechnik TEX-120 (Lynx) design. Both lasers are *Littrow* configuration – an illustration of a Littrow-configuration ECDL is shown in Figure **??**.

Often, in Littrow configuration, the main output beam will be along the direction of the 0$^{\text{th}}$-order indicated in Figure **??**. If the grating is moved to tune the wavelength, this will change the direction of the output beam, which is inconvenient for many applications. While there are other designs which circumvent this disadvantage [**?**], the design described in Figure **??** is used by Sacher-Lasertechnik and Toptica in the laser setups used here. The -1 order diffracted beam from a

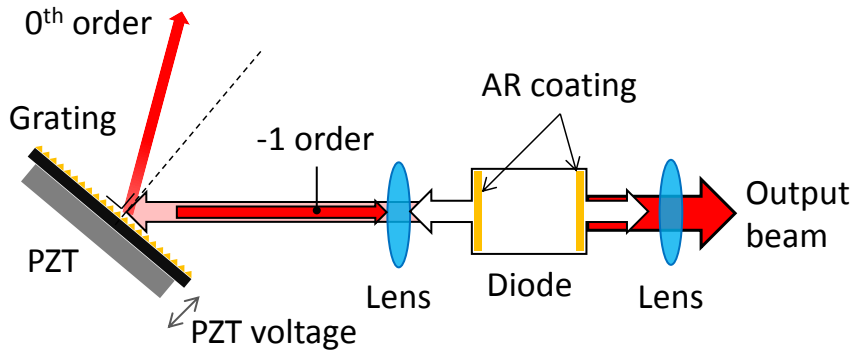

Figure 2.4: *An extended cavity diode laser in Littrow configuration. The anti-reflection coated diode emits a laser beam toward a diffraction grating. The grating is aligned such that the -1 order reflects back into the diode to amplify the output signal.*

grating is directed back into the laser cavity resulting in a single mode, whose frequency matches that of the -1 order. Only a fraction of the power which is incident on the diffraction grating is lost through the zero order beam, which itself can be used for alignment diagnostics.

The ECDL configuration narrows the linewidth of the diode [**?**, **?**]. Without the extended cavity, the diode can be tuned only with supply current and temperature. However, by introducing a PZT-mounted grating in the extended cavity, the cavity length can be finely adjusted to allow precise control of the wavelength over a small range. This increases the mode-hop-free tuning range to tens of GHz. With suitable electronics, a modulated signal can be sent to the PZT to scan the wavelength of the laser over a chosen range.

Both ECDLs are frequency-stabilised using saturated absorption specroscopy (SAS). The SAS setup generates an error signal which is used as a locking loop to control the laser output. Two variations of SAS are used – the SAS arrangement for the cooling laser is shown in Figure **??** (a). A small fraction (≈5–10%) of the main ECDL ouput is sent to a single-line spectroscopy setup: the intensity ratio of the forward-going (pump) and retro-reflected (probe) beam is controlled with two waveplate-PBS combinations. The probe beam is aligned such that it intersects with the pump beam. The photodiode (PD) is positioned to detect the probe beam and the signal is sent to an oscilloscope to derive an error signal for the feedback loop. Additionally, by scanning the laser wavelength with the piezoelectric transducer voltage, the Doppler broadened peaks for the D2 transition (i.e. $5^2S_{1/2} \rightarrow 5^2P_{3/2}$) can be identified, with the hyperfine structure visible within the peaks. The Doppler-broadened SAS spectrum for ^{85}Rb and ^{87}Rb is

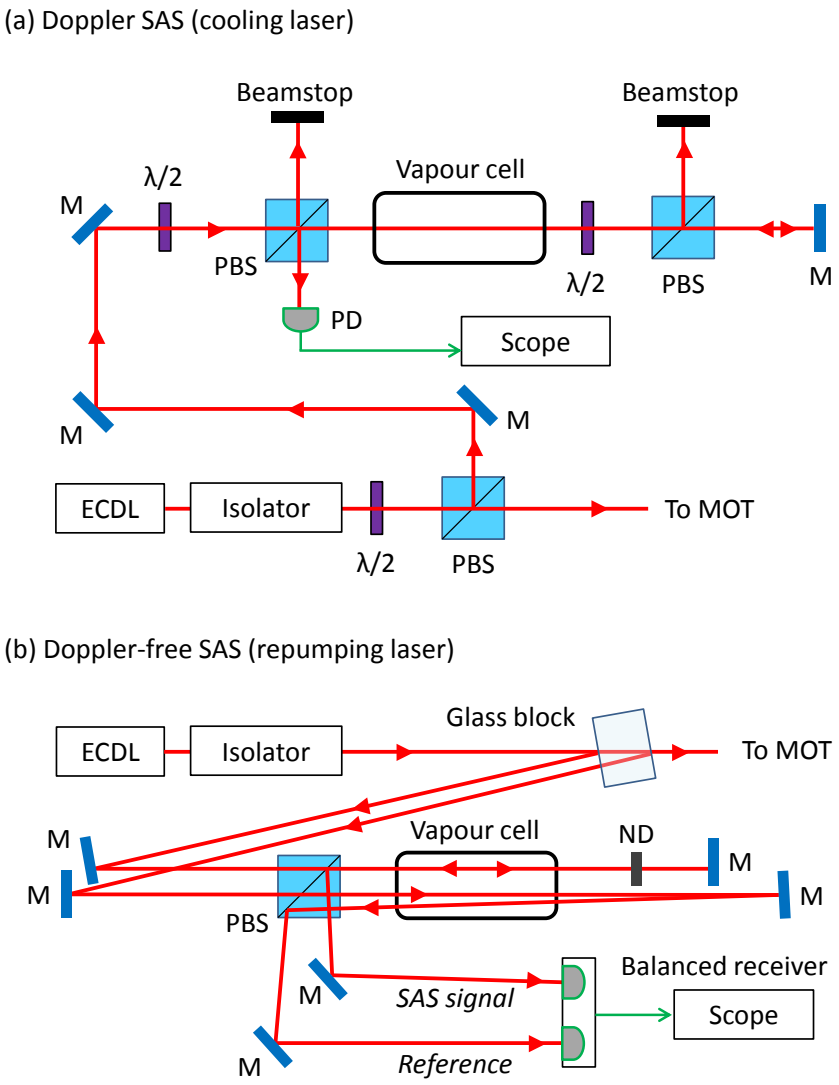

Figure 2.5: *(a) Experimental setup for Doppler-broadened saturated absorption spectroscopy used for the cooling laser. (b) Using a reference beam, the Doppler peaks can be eliminated from the Doppler-broadened SAS signal with a balanced receiver. M = mirror, λ/2 = half waveplate, PBS = polarising beamsplitter, ND = neutral density filter.*

shown in Figure **??** as a function of PZT voltage.

In Figure **??**(b), the Doppler-free SAS setup for the repumping laser is shown. A glass block is used to split two small fractions (4% at each glass-air interface) of the primary beam off and send it to the spectroscopy setup. One of these beams is sent through the vapour cell and retroreflected on itself to generate the SAS signal. A neutral density filter (ND) is used to reduce the intensity of the retroreflected beam. A secondary beam is sent through the vapour cell and back again, without overlap, to act as another pump beam. This generates the

Doppler-broadened spectrum which can be inverted to cancel out the Doppler-broadened component in the SAS signal. An example of this is shown in Figure **??**. For most of the experiments described in this work, such high-resolution spectroscopy of the repump hyperfine peaks is not essential. It can be assumed that, unless mentioned otherwise, the repump laser is locked to the cross-over peak ("CO") between $F' = 1$ and $F' = 3$: $(1' \rightarrow 3')_{\text{co}}$. This is sufficient for transferring the atoms from $F = 2$ back to $F = 3$.

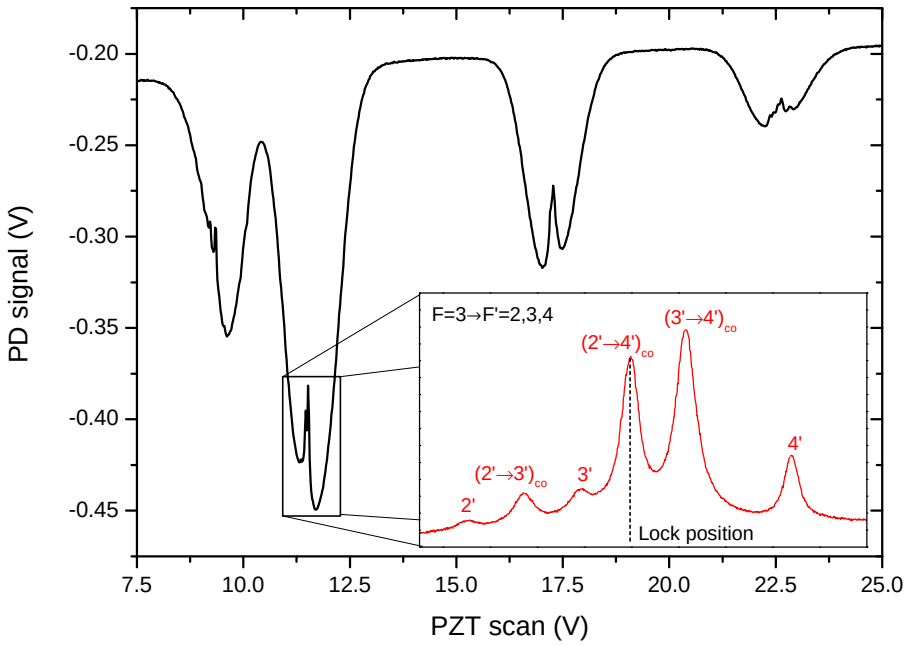

Figure 2.6: *A plot showing the Doppler-broadened SAS spectrum for ^{85}Rb and ^{87}Rb. The inset shows a close-up of the hyperfine peaks for the $F = 3 \rightarrow F' = 2, 3, 4$ transitions in ^{85}Rb. The cooling laser is locked to the crossover peak $(2' \rightarrow 4')_{co}$. Both x-axes are represented in terms of PZT voltage: a linear scan of voltage results in a linear scan of ECDL frequency (wavelength).*

Laser-locking is facilitated by a Toptica DigiLock system. This unit takes in the SAS signal from the laser, generates an error signal which is fed back to the ECDL (either via PZT voltage or bias-T, or both). User-controlled PID settings are chosen to improve lock quality.

A diagram showing the optical arrangement for preparing the MOT beams is shown in Figure **??**. For the cooling laser, to allow the beam to shape correctly, a distance of 1 m was left free of optics between the primary PBS and the next mirror to direct the beam through the AOM. This was necessary due to characteristics of the diode.

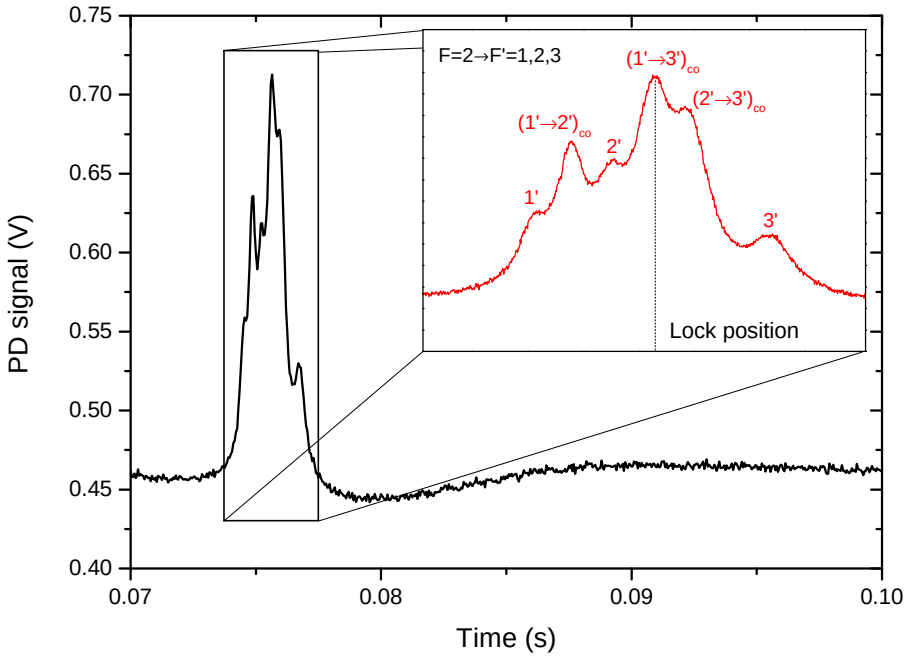

Figure 2.7: *The main plot shows the Doppler-free hyperfine peaks of the repump transitions in ^{85}Rb. The inset shows a zoom in of the densely-packed peaks. The x-axis is represented in units of time: a linear scan of voltage in time results in a linear scan of ECDL frequency (wavelength).*

2.2.2 Magnetic field

Experimentally, the magnetic field for the MOT is created using an anti-parallel configuration as shown in Figure **??**. This generates an inhomogeneous magnetic field which has a minimum at some position along the z-axis between the two coils. The field is zero at $z = 0$ when the currents in each coil are equal in value but opposite in direction. The field gradient is essentially linear throughout the capture region of the intersecting laser beams.

The magnetic field strength along the z-axis can be approximated by [**?**]

$$B_z = \frac{NI\mu_0}{2r_{coil}} \left(\frac{1}{\left(1 + \left(\frac{z}{r_{coil}} - \frac{d}{2r_{coil}}\right)^2\right)^{3/2}} - \frac{1}{\left(1 + \left(\frac{z}{r_{coil}} + \frac{d}{2r_{coil}}\right)^2\right)^{3/2}} \right), \qquad (2.2)$$

where r_{coil} is the radius of the coils, with N turns in each of the coils, a separation between the coils of d, current in the coils of I, a distance from the geometrical centre between the coils z and μ_0 is the permeability of the vacuum.

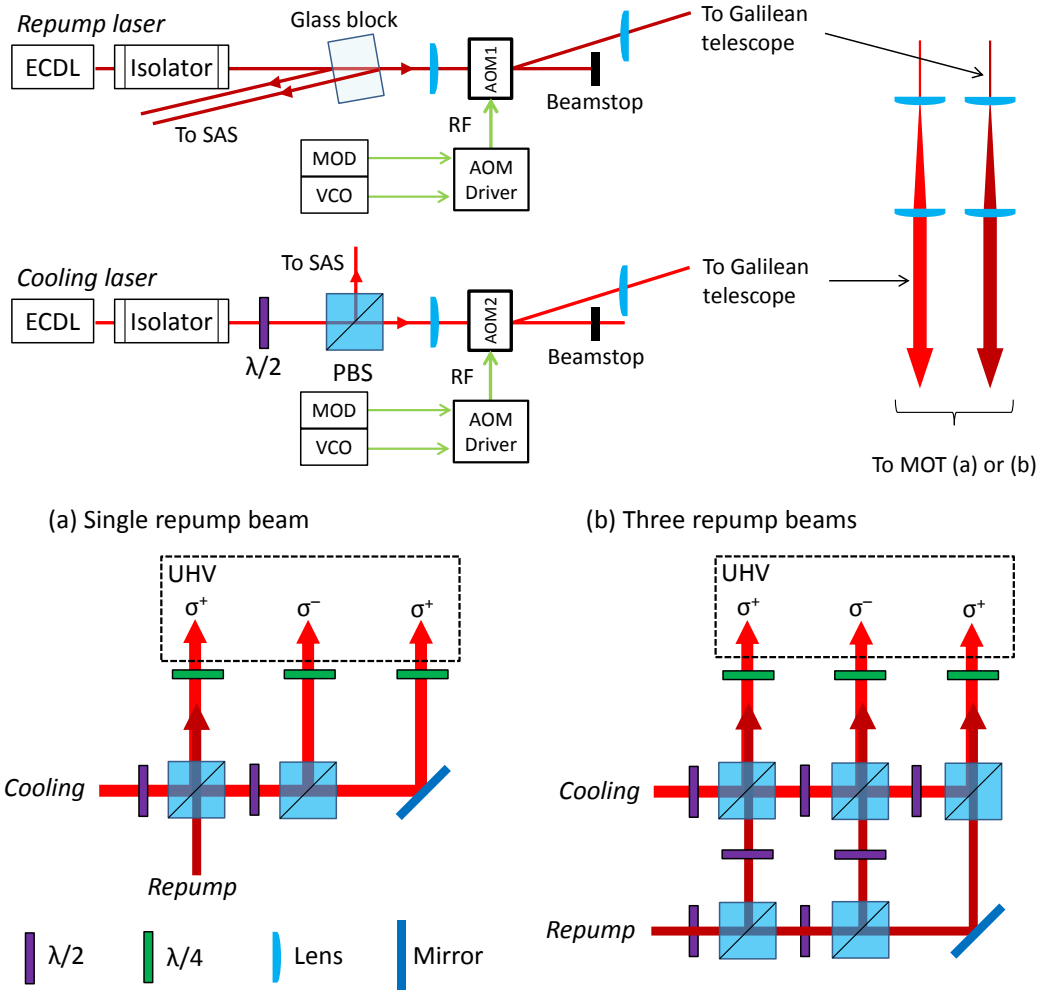

Figure 2.8: *Summary of MOT optics. Either a single or triple repump beam MOT could be arranged depending on the application.*

The electric coils are enamelled copper wire (200 windings) wound around aluminium frames and are positioned on either face of the MOT chamber. Custom-made copper wedges fix the coils in place. The coils have a radius of 75 mm and are separated by a distance of 90 mm. The coils are operated independently with currents of 3 to 6 Amps resulting in a magnetic gradient, in the trapping region, of 10-20 Gauss/cm. With independent control over the current in each coil, the minimum of the field can be translated along the z direction. The 3-dimensional profile of the magnetic field produced by the coils is given in Figure **??**. The four peaks are caused by the coils emerging from the xy-plane and indicate the position of the maximum field strengths in Figure **??**. The central dark region is the potential minimum where the atoms are confined during the operation of the MOT.

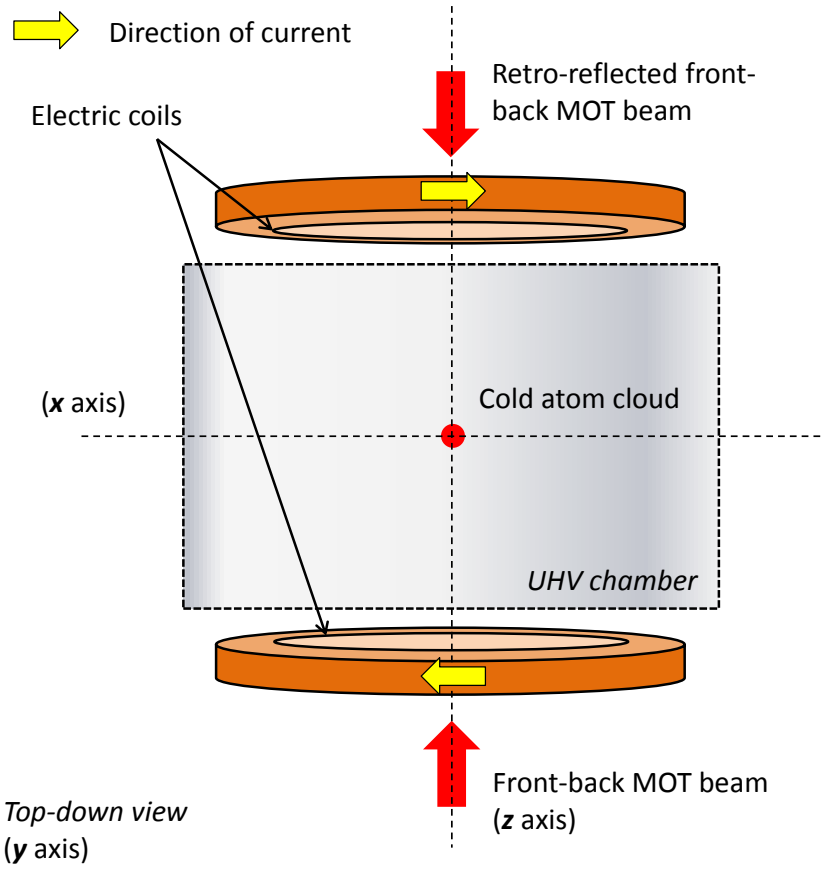

Figure 2.9: *Coils for creating a linear, inhomogeneous magnetic field in the region of the MOT laser intersection.*

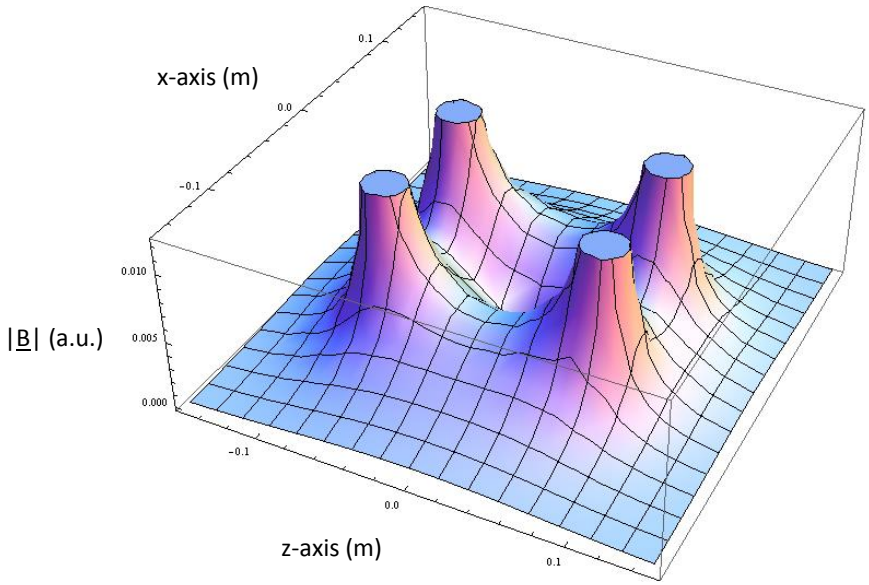

Figure 2.10: *Magnetic field strength of the quadrupole magnetic field used for this MOT.*

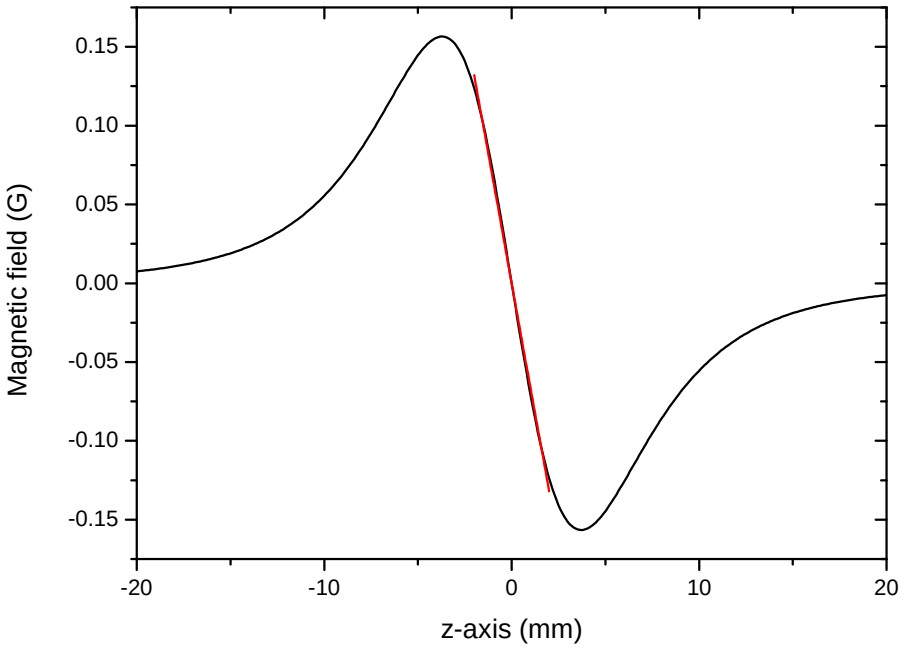

Figure 2.11: *Theoretical magnetic field produced by the coils along the z-axis. The red line is a linear fit to the data to provide an estimation of the magnetic field gradient.*

2.2.3 Ultra-high vacuum

Cooling and trapping neutral atoms with a MOT for more than a few seconds requires a vacuum of at least 10^{-7} mbar. The atom cloud must be isolated from the external environment which contains background gases that would collide with trapped atoms. With the UHV system described here, a base pressure of 5×10^{-10} mbar can be achieved.

A schematic diagram of the UHV system is shown in Figure **??**. The chamber itself is a stainless steel structure assembled with high purity, oxygen-free copper gaskets on all flanges. Prior to assembly, all vacuum components were thoroughly cleaned using lint-free cloth and acetone. The MOT chamber is an octagonal chamber with a 2.75″ CF port placed on each of the eight surfaces. Six of these ports are windows with anti-reflection coating optimised for transmission at 780 nm light. This permits optical access for the MOT beams and probe beams. A fibre feedthrough flange is attached to the top port, and a blank CF flange is secured to the bottom flange.[1] The fibre feedthrough flange has a Swagelok fitting which enables the fibre pigtails to be coupled through a Teflon ferrule while maintaining UHV. On the front and back surface, there are 4.5″ CF ports. A

[1]For some work contained in this thesis, these upper and lower flanges were swapped. Mounting the fibre from the top down was found to be experimentally easier than installing it from the bottom port.

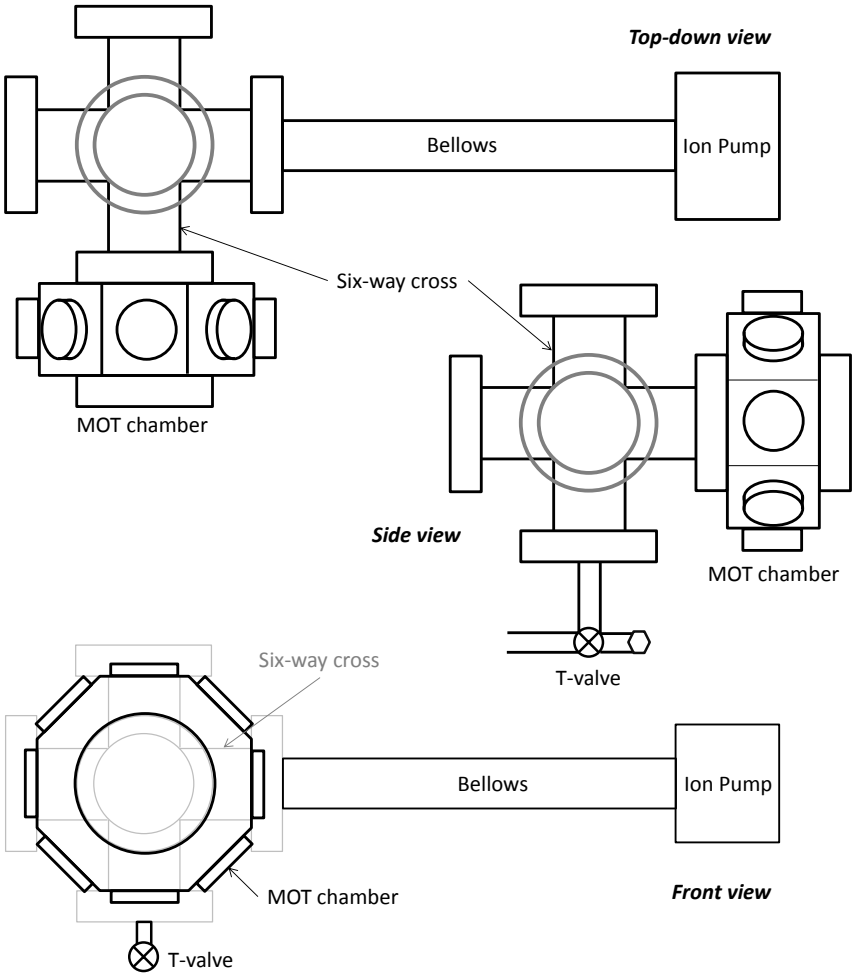

Figure 2.12: *Illustration of the vacuum system and chamber.*

viewport is attached onto one of these CF ports, while the other side is connected to a stainless steel six-way cross with a 4.5″ CF port on each arm. The chamber is secured to the optical bench with a pair of aluminium supports locked around two of the arms on the six-way cross. The first pump is an Ulvac GLD-136C rotary-vane pump (the RVP has a pumping speed of 136 litre/min) which is connected to the six-way cross using a flexible plastic bellows and a KF flange (rated to 10^{-8} mbar). The RVP is connected in series with a Varian TV-81-T turbomolecular pump (TMP) which rotates at 80,000 rpm. The TMP connects to the chamber via a 4.5″ CF flange below the six-way cross. The third pump is a Varian VacIon Plus Starcell 55 ion pump (IP) which pumps at 50 litres/sec. This is connected to the rightmost flange of the six-way cross via a 0.5 m long stainless steel bellows. This bellows is utilised to increase the distance between the MOT chamber and the strong magnets of the ion pump.

Central to the system is a T-valve (rated to 10^{-12} mbar) that provides isolation of

ion pump, MOT chamber and six-way cross from the TMP and RVP attachments. This valve is positioned on the lowest arm of the six-way cross. The top port of the six-way cross is a dual pressure gauge integrated into a single sensor head. A PM-PVB2 Pirani gauge is used to measure pressures from atmosphere down to 10^{-3} mbar. A PM-AIG17G ionisation gauge is used for pressures from 10^{-3} to 10^{-9} mbar.[2] Both gauges are connected to a NGC2 pressure gauge controller using a shielded cable which supplies and reads all voltages/currents required and displays the pressure measurement.

Rubidium is introduced to the chamber using dispensers (SAES getter, Rb/ NF /3.4/12 FT10+10) which are attached to the left port of the six-way cross. Electrical feedthroughs on this port connect the getters to a variable current supply which allows control of the amount of Rb vapour in the vacuum chamber. The getters are mounted so that they are not directly in line with the MOT to avoid high-velocity rubidium atoms colliding with the cold atoms in the MOT. Each getter is a metal strip that contains a mixture of rubidium-chromate (Rb_2CrO_4) plus a reducing agent. To activate a new getter, a process called 'burning in' must be peformed. This involves passing ever greater currents through the getter source for a short period of time until it is evident that rubidium is being released by resistive heating. When a high enough current is applied to the getter, a small slit on one side of the getter will open which allows the rubidium to be released. To test for the presence of rubidium, a laser tuned to one of rubidium's atomic transitions is passed through the chamber until fluorescence is observed using a CCD camera.

The pump-down procedure is as follows. The roughing pump (RVP) is connected to the back of the chamber and the T-valve is open. The gas is drawn from the chamber into the RVP and expelled through an Edwards FL20K foreline trap. After approximately 6 hours a pressure of $\sim 2 \times 10^{-2}$ mbar is achieved. This pressure is measured using the pirani gauge and read from the ionisation gauge controller. At this stage, with the T-valve still open, the turbo molecular pump (TMP) is switched on. Using the 'emission' function of the ionisation gauge controller, the pressure is monitored. At approximately 10^{-6} mbar, the ion pump (IP) is switched on. The three pumps work in unison for 5 minutes and the T-valve is closed. The chamber is now being pumped down solely with the ion pump. The RVP and TMP are deactivated to allow the rear section of the chamber to return slowly to atmospheric pressure. The pressure in the main

[2] In practise, the ionisation gauge is rarely used as it increases the vacuum pressure during operation. The ion pump current is sufficient to measure pressures from 10^{-2} to 10^{-10} mbar.

chamber is now read from both the ion pump current and from the ionisation gauge controller. A minimum pressure of $\sim 2 \times 10^{-7}$ mbar is usually obtained at this stage.

To reach lower pressures, contaminants from the inner chamber walls must be removed. These contaminants are usually water-based and can be removed via a process called bakeout. The MOT chamber, six-way cross, bellows and ion pump are wrapped with individual electrical heating straps and then covered with aluminium foil to provide insulation. Thermocouples are attached to each region with copper tape and are connected to a MA900 PID 15 temperature controller, which monitors and controls the temperature of each section using power relays to the heating tapes. The temperature is incremented/decremented in 10°C steps with 30 minutes of temperature-stabilisation in between to ensure the ion pump does not stop operating due to the increased level of outgassing. Additionally, the temperature change must not exceed 2°C/min as this can irreversibly warp chamber components, flanges and fittings due to thermal stress. The temperature of the entire system is maintained at 140°C for two days before reducing it back to room temperature using the same gradation of <2°C/min. After bakeout, the base vacuum pressure is always below 1×10^{-9} mbar.

2.3 Imaging optics for single atoms

The detection of small numbers of atoms and molecules via imaging techniques is highly desirable for modern atomic physics experiments. Collecting low levels of light and the imaging of small sources require a high numerical aperture and diffraction-limited performance, respectively. Often, in ion trapping experiments or laser cooling of neutral atoms, efficient imaging optics are required but must adhere to restrictions in working distance due to the already dense arrangement of optics, beam paths and mechanical structures. Commercially-available solutions for this application are either long working distance microscope objectives, which are relatively expensive, molded aspheric lenses with usually short focal lengths, or achromats, which have larger spot sizes. Thus, it is preferable to custom design an objective to suit the experimental system. With widespread availability of optics and mounting systems, this task is made easier.

A lens system is described here which fulfills the requirements of having a high numerical aperture, diffraction-limited performance and can be optimised using OSLO software to account for UHV chamber windows and the operational wave-

length. The design, optimisation and testing follow the procedures outlined by [**?**]. The objective described here is ideal for use with a caesium MOT (at an imaging wavelength of 852 nm) but can easily be re-positioned to compensate for chromatic shift to work with wavelengths between 400 and 1064 nm.

The lens array is designed with OSLO LT software by tracing a uniform parallel beam through a set of optics and the chamber window such that it focuses at the cloud position. Although four, five and six lenses were trialled, it was found that good designs could be made with just four lenses. The final lens surface, 8, was set to have fixed radius of curvature and focal distance in order to keep the distance between the cloud and objective constant. The radii of curvature and inter-lens distances are used as variables. The program minimizes the squared sum of the spherical aberrations up to 7^{th} order as well as 3^{rd} order coma and astigmatism. The four-lens design is shown in Figure **??**.

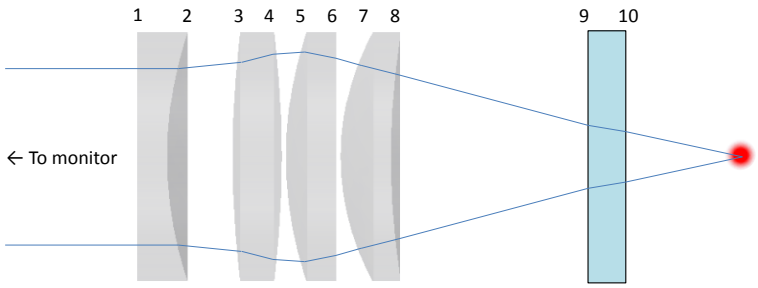

Figure 2.13: *Lens assembly for the objective.*

The lenses were chosen from the LENS-Optics GmbH catalogue[3] to closely match an OSLO-optimised lens array. Each lens is 25.4 mm in diameter, has a surface quality of $\lambda/4$, scratch-dig 20-10, centration <5 minutes of arc and anti-reflection coating for 650–1000 nm. A 25.4 mm lens tube and set of retaining rings (Thorlabs SM1L40) were used to secure the array in place.

A shear plate interferometer was used to test the objective design. A 852 nm laser beam was focused onto a 1 μm aperture to serve as a high NA point source. The transmitted light was collimated by the objective, sent to a shear plate and analysed with a monitor (Figure **??**). The resulting interference fringes give information about the wave front distortion from the objective [**?**]. The primary difficulty with this objective was found to be the play of lens positioning inside the tube. Although each component was machined to satisfy ± 0.1 mm in its dimensions, the tube itself allowed large movemements of the lenses when the

[3]LENS-Optics GmbH, Finkenweg 14a, 85391 Allershausen, Germany, http://www.lens-optics.de/

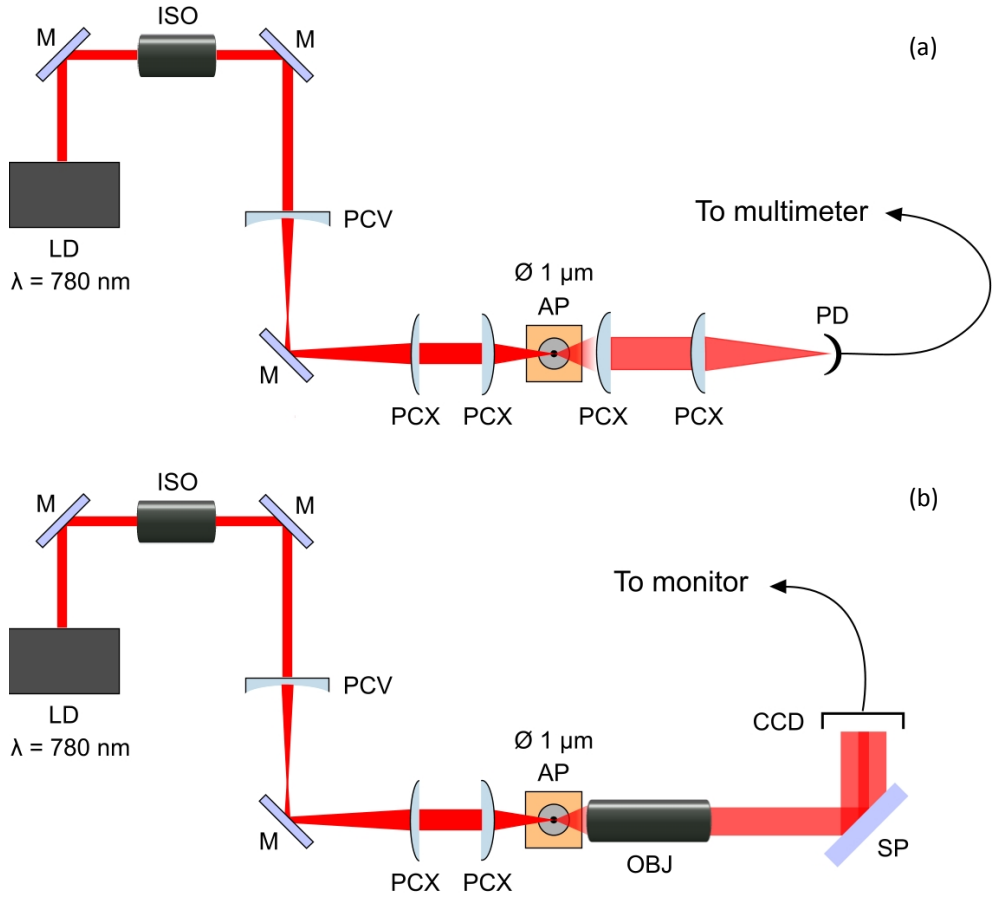

Figure 2.14: *Illustration of the testing method used for the objective. The upper panel (a) describes the method of aligning the 1-µm aperture (AP) with the focussed laser beam. Both the AP and PD (photodiode) are fixed to translation stages. The transmission of the laser beam through the AP is maximised iteratively. When the transmission reaches the highest value attainable, the objective is placed at its focal length after the AP (b). A shear plate is positioned at 90° to the expanded and magnified output beam and a CCD camera is used to examine the interferometric pattern.*

retaining rings were not secured. Thus, it was very difficult to place the lenses in the tube and ensure that they were all in line with each other along the central axis of the tube. To solve this problem, a custom tube was designed as shown in Figure **??**. Each lens is placed in its own individual lens tube and each tube can be screwed together using internal and external threading. The entire tube piece was fabricated from one solid aluminium piece to minimise diameter-mismatching.

Unfortunately, this design was complete a number of weeks after returning from the research group in Germany, so final shear plate interferometry tests were not carried out on this objective. However, this simple and effective objective can be used in the future for imaging the cloud of cold atoms.

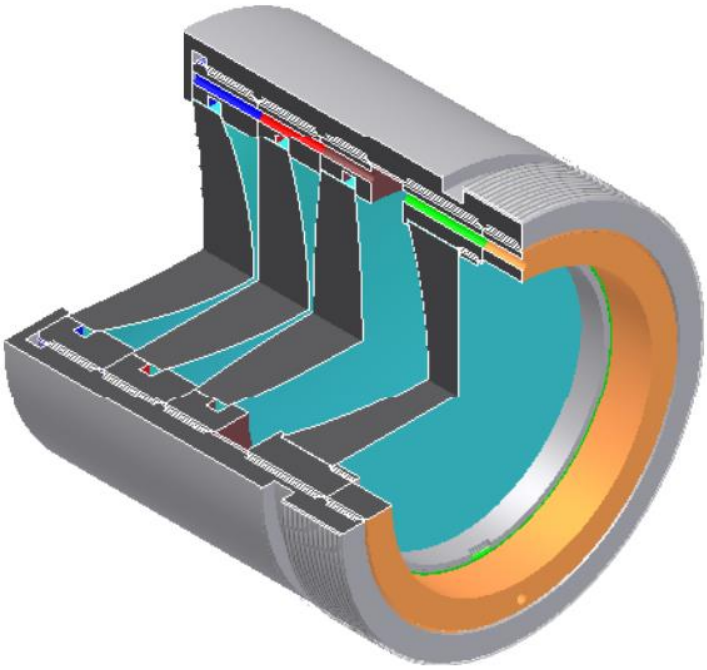

Figure 2.15: *A custom lens tube with individual lens holders which thread together to form the lens array illustrated in Fig.* **??**.

2.4 Conclusion

This chapter described the use of a magneto-optical trap to laser cool and spatially confine a sample of ^{85}Rb atoms. In the past decade, the MOT has made its way into undergraduate laboratories with the advance in inexpensive laser diodes and all-in-one frequency locking systems. In this system, three pairs of orthogonally-directed circularly polarised beams are aligned to intersect at the centre of a vacuum chamber. A pair of magnetic field coils in anti-parallel configuration creates a spherical quadrupole trap which has a minimum position aligned with the centre of the intersection point of the six beams.

Resolving the hyperfine spectrum of ^{85}Rb is necessary for frequency-stabilisation of the cooling and repumping laser. To lock the frequency of the cooling and repump laser, a saturated absorption spectroscopy setup is used and the resulting signal is sent to a DigiLock system to controllably frequency lock both lasers.

Work on a high resolution imaging objective has been presented. This system will be tested and utilised in the experiment in the future.

Chapter 3

Theory and fabrication of optical nanofibres (ONFs)

The optical fibre discussed in this thesis is commercially-fabricated, cylindrical, glass fibre designed to allow a single mode of light to propagate. The fibre consists of a glass inner core (typically made from germanium-doped silicon-oxide) and a surrounding glass cladding made from pure silicon-oxide (SiO_2). The presence of the doping element in the core generates the small difference in refractive index, n, between the core and cladding ($n_{clad} < n_{core}$), thus allowing light to be confined within, and propagate along, the fibre. The core size is designed so that the optical field intensity at the cladding-core interface is negligible. Tapered fibres are created by simultaneously heating and stretching such a step index optical fibre using a fibre pulling rig. If the taper is stretched enough so that the narrowest region has a submicron diameter, the waveguide is then called an optical nanofibre (ONF). In this chapter, the properties and characteristics of ONFs will be explained including theoretical considerations and experimental data. Consideration will be given to their use with a sample of cold rubidium atoms. The first section concentrates on the theory behind these waveguides. The final section returns to experimental work with ONFs and how they are fabricated with the fibre pulling rig. The advantages of the ONF as an atom probe and the nuances of installing it in UHV are also discussed.

3.1 ONF profile

A schematic diagram of a tapered fibre using 125 μm fibre with a 4.4 μm core diameter is shown in Figure **??**. The tapered fibre is a waveguide which has two segments of standard optical fibre (the *pigtails*) either side of a very thin length of fibre called the *waist*. Typically, the waist is a few mm in length. The *transition* regions join the pigtails to the waist to make a smooth change in diameter. The taper profiles in this work are exponential due to the stationary flame and limited stepping motor motion of the fibre pulling rig.[1] In the pigtails, the light mode propagates in the core due to the step in refractive index between the two media. In the transition region of the taper, both the core and cladding diameters decrease simultaneously. Eventually, the light mode will no longer be guided by the core and it will extend into the cladding via an evanescent field.[2] As the initial core diameter is already much smaller than the initial cladding diameter, the core essentially disappears. This results in a waveguide where the mode partially exists within the cladding (the new, smaller core) and partially as an evanescent field. Thus, the first transition region transforms the core-cladding guided mode to a cladding-environment mode while the second transition region does this process in reverse. The transition regions introduce/are associated with loss mechanisms for the mode and, therefore, in the following sections, the concept of an adiabatic transition region will be introduced and later considered in terms of the operation of the fibre pulling rig used in the Quantum Optics Laboratory.

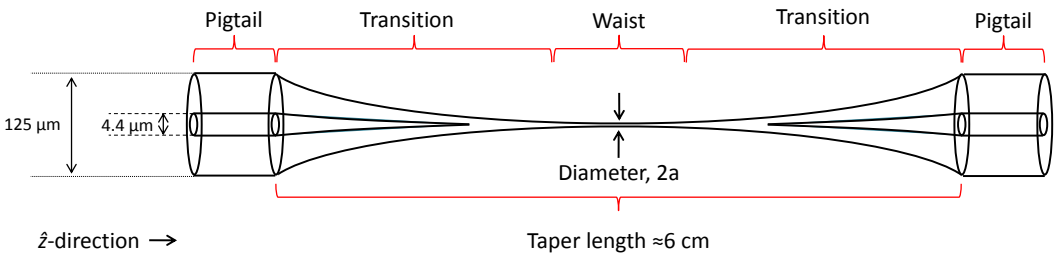

Figure 3.1: *Schematic illustration of an optical nanofibre. The narrowest region has a diameter, 2a in the range of hundreds of nanometers. Typical taper lengths are in the region of 6 cm. The $\hat{z}$-direction is along the fibre axis.*

[1] By using a narrow, movable flame, almost any taper profile can be obtained [**?**].

[2] At any total internal reflection event there will be an evanescent field, but in the case of usual core-cladding guidance, it will be negligible in terms of spatial extent and intensity.

3.2 Propagation of light in an optical fibre

Using cylindrical coordinates (r, ϕ, z), Maxwell's equations for an isotropic,charge-free, non-magnetic medium can be used to derive the dispersion equation for a step-index optical fibre (see Appendix A, [**?**] and [**?**]),

$$\frac{J_l'(ha)}{haJ_l(ha)} = -\frac{n_{core}^2 + n_{clad}^2}{2n_{core}^2}\frac{K_l'(qa)}{qaK_l(qa)} \pm R \tag{3.1}$$

where

$$R = \left[\left(\frac{n_{core}^2 - n_{clad}^2}{2n_{core}^2}\right)^2 \left(\frac{K_l'(qa)}{qaK_l(qa)}\right)^2 + \frac{l^2}{n_{core}^2}\frac{\beta^2}{k_0^2}\left(\frac{1}{q^2a^2} + \frac{1}{k^2a^2}\right)^2\right]^{1/2}. \tag{3.2}$$

Here, $k = \omega n/c = k_0 n$ is the wavenumber, n_{core} is the refractive index of the core and n_{clad} is the refractive index of the cladding material. The quantity l is an integer which determines the azimuthal properties of the fields and can be compared to a measure of "skewness" in the ray diagram picture. Both h $(= k^2 - \beta^2)$ and q $(= \beta^2 - k^2)$ depend on k and the propagation constant along the fibre axis, β. β is one of the most important quantities for determining the modal structure of light in a fibre.[3] The functions $K(ha)$ and $J(ha)$, and their derivatives, $K'(ha)$ and $J'(ha)$, are Bessel functions of the first kind and modified Bessel functions, respectively. The $\pm$ sign in Equation **??** denotes two sets of solutions: the HE $(-)$ and EH $(+)$ modes.[4] Equation **??** can be solved graphically for β by plotting the left and right-hand side and finding the coordinates of their intersections. An example of this is shown in Figure **??** for $-R$ (HE modes), $l = 1$.

[3]The fraction β/k_0 is often redefined as n_{eff}, the effective refractive index. To avoid confusion with the use of n_{eff} to describe the number of atoms emitting light into the ONF modes in later chapters, this definition is not used in this thesis.

[4]The naming of the modes is based on the contribution of E_z and H_z to the mode in comparison to the contributions from a transverse component: E_z makes a larger contribution than H_z for the EH modes, and E_z makes a smaller contribution than H_z for the HE modes [**?**] (this is true despite the different units of measurement for E_z and H_z).

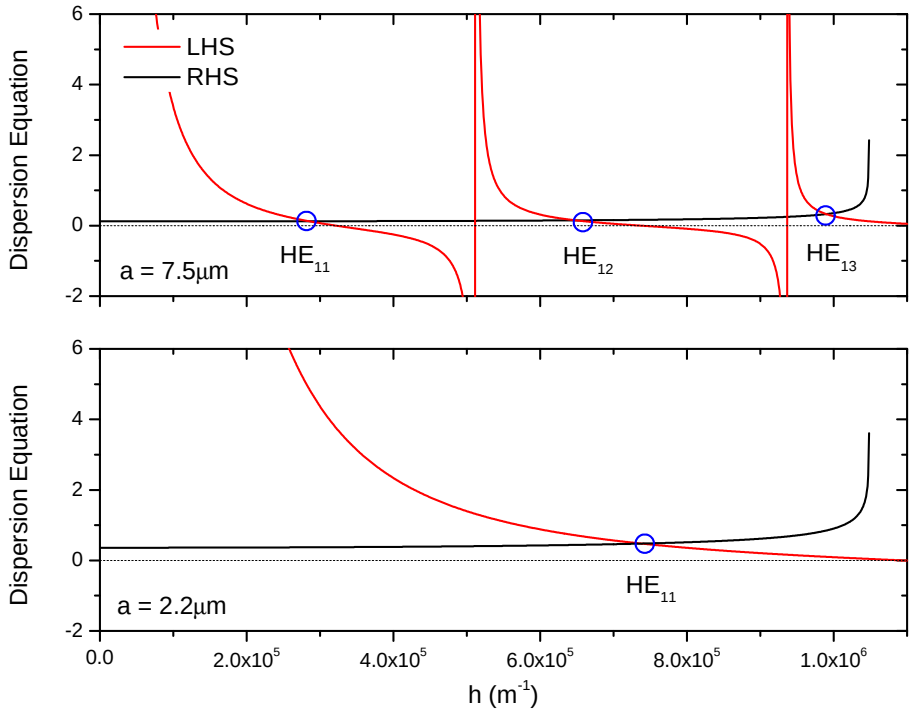

Figure 3.2: *Plot of the LHS (red, solid line) and RHS (black, solid line) of Equation* **??** *for* $l = 1$ *(hybrid modes) and* $-R$ *(using* $+R$ *yields the EH modes). Each intersection point yields a value for* β *via* $h = \sqrt{k^2 - \beta^2}$*. The upper panel shows three intersection points (*HE_{11}*,* HE_{12}*,* HE_{13}*) for a fibre with core radius 7.5* μm*,* $n_{core} = 1.4595$*,* $n_{clad} = 1.4537$ *(*$\lambda = 780$ *nm). The lower panel shows that for an optical fibre with core radius 2.2* μm *(*$n_{core} = 1.4595$*,* $n_{clad} = 1.4537$*,* $\lambda = 780$ *nm) only the* HE_{11} *mode can propagate.*

3.3 Guiding the fundamental mode in an ONF

Optical fibre can be designed to carry either one single mode of light (the fundamental mode) or multiple modes. To utilise a subwavelength optical fibre waveguide in a cold atom experiment, it should either operate efficiently as a single-mode device, or be designed to carry more than one mode through the pigtails, transition regions and waist, with minimal loss. Although the design of few-mode optical nanofibres has been demonstrated recently [**?**] in the Quantum Optics Laboratory, it is not trivial. For the work discussed in this thesis, only single mode ONFs were fabricated.

A characteristic of SMFs is that the transverse intensity profile at the fibre output has a fixed shape that is independent of the launch conditions and the spatial properties of the injected light, assuming that no cladding modes can carry substantial power to the fibre end. The launch conditions only influence the efficiency with which light can be coupled into the guided mode. This characteristic is im-

portant for (a) fluorescence coupling from atoms as the only parameters concerned are those associated with coupling efficiency between the atoms and waist, and (b) absorption studies of surrounding samples because the spatial extent and intensity of the evanescent field is critical.

Single-mode fibres are designed such that they support only a single propagation mode per polarization direction for a given wavelength. For most of the work presented in this thesis, the ONFs used were fabricated to satisfy this criterion. For step-index fibres (in this work, this includes both standard fibre (core-cladding) and tapered fibre (core-vacuum)), the condition for single-mode guidance can be formulated using the V-number, which can be calculated from the freespace wavelength, the core radius a, and the numerical aperture (NA) [**?**]:

$$V = \frac{k_0 a \sqrt{n_{core}^2 - n_{clad}^2}}{2} = \frac{2\pi a}{\lambda}\mathrm{NA}, \tag{3.3}$$

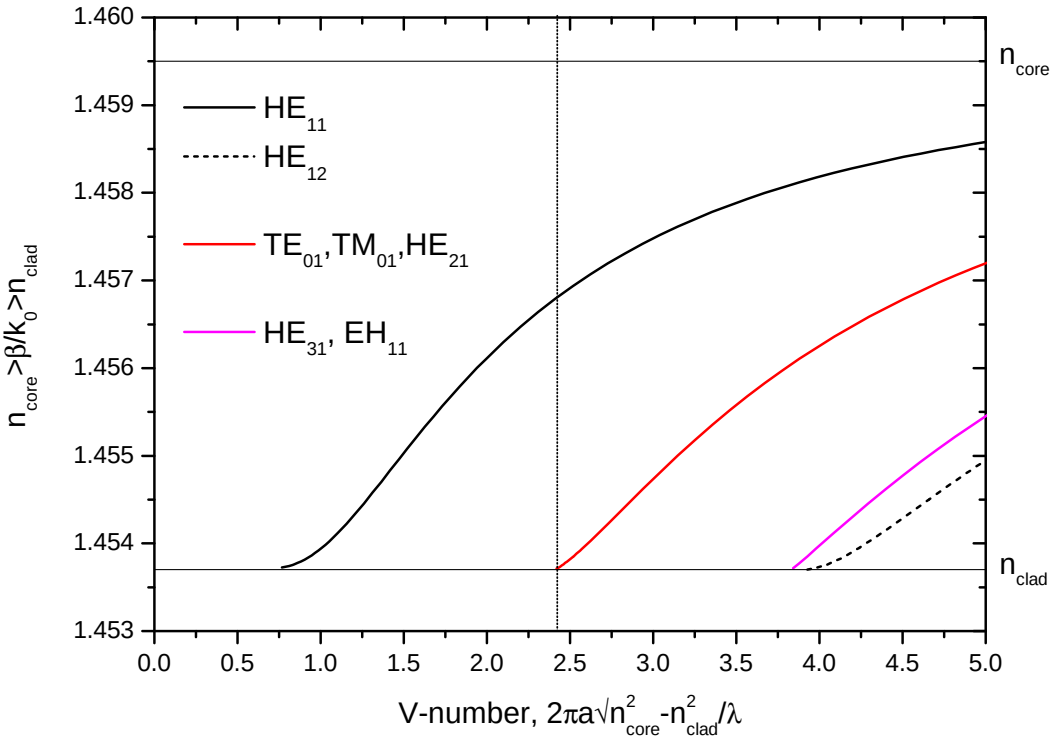

Figure 3.3: *A plot of the propagation constant, β (normalized to k_0) against V-number for an optical fibre with cladding and core refractive indices as 1.4537 and 1.4595, respectively. The small Δn implies that the weak guidance condition is fulfilled and the modes are described as linearly polarised (LP). The dashed, vertical line indicates the boundary between single- and multi-mode guidance in the waveguide ($V = 2.405$).*

where k_0 is the freespace wavenumber ($2\pi/\lambda$). Thus, SMFs usually have a relatively small core (with a diameter of only a few μm and a mode radius of a

few μm) and a small refractive index difference, $\Delta n \approx 0.006$, between core and cladding. This implies that the NA of the fibre is small ($\sim$0.1) and the paths of the rays inside the core are almost straight along the fibre axis (the $\hat{z}$-direction). Consequently, all the guided modes can be approximated as nearly TEM (transverse electric and magnetic) modes [**?**], since the $\hat{z}$-components of the $\underline{E}$ and $\underline{H}$ fields are negligible compared to the transverse components [**?**]. The modes resulting from this approximation are, therefore, called linearly polarised (LP) modes, since the fields are polarised transverse to the direction of propagation. Figure **??** is a plot of propagation constant against V-number for optical fibre with $\Delta n \approx 0.006$. The step-profile, circular cross-section fibre used in the following experiments is single-mode when $V \leq 2.405$. In this case, only the two polarised states of the fundamental mode can propagate.

In the case of an optical nanofibre, the weakly guiding condition no longer holds since Δn is much larger than for a standard fibre: $\mathrm{NA_{ONF}} = \sqrt{n_{core}^2 - n_{clad}^2} = \sqrt{n_{ONF}^2 - n_{vacuum}^2} = 1.055$. This causes the true fibre modes to separate out. A comparison of the modes in a standard core-clad fibre and those in an ONF is shown in Figs. **??** and **??**. Both plots show propagation constant against V-number. A considerably larger separation occurs between modes within the same group when compared to the standard fibre case.

As shown by Figure **??**, the single mode condition $V = 2.405$ generates a single-mode fibre diameter for the ONF of 566 nm using Equation **??**. Further, the single mode condition can be reached for any wavelength λ if the radius of the ONF is small enough to allow only the fundamental mode to propagate – see Figure **??**.

The V-number equation indicates that, in the case of this work, the only parameter we can control to ensure single-mode propagation in the ONF is the ONF diameter. In Chapter 8, the concept of customizing the taper shape for introducing few-mode propagation in the waist will be discussed. The work in this thesis is based on single mode propagation unless specified otherwise. Further, the evanescent field which exists outside a subwavelength tapered fibre has not yet been discussed here. For the following three chapters, fluorescence coupling is the primary concern. Absorption spectroscopy experiments are presented in Chapter 8 and evanescent field properties will be highlighted there.

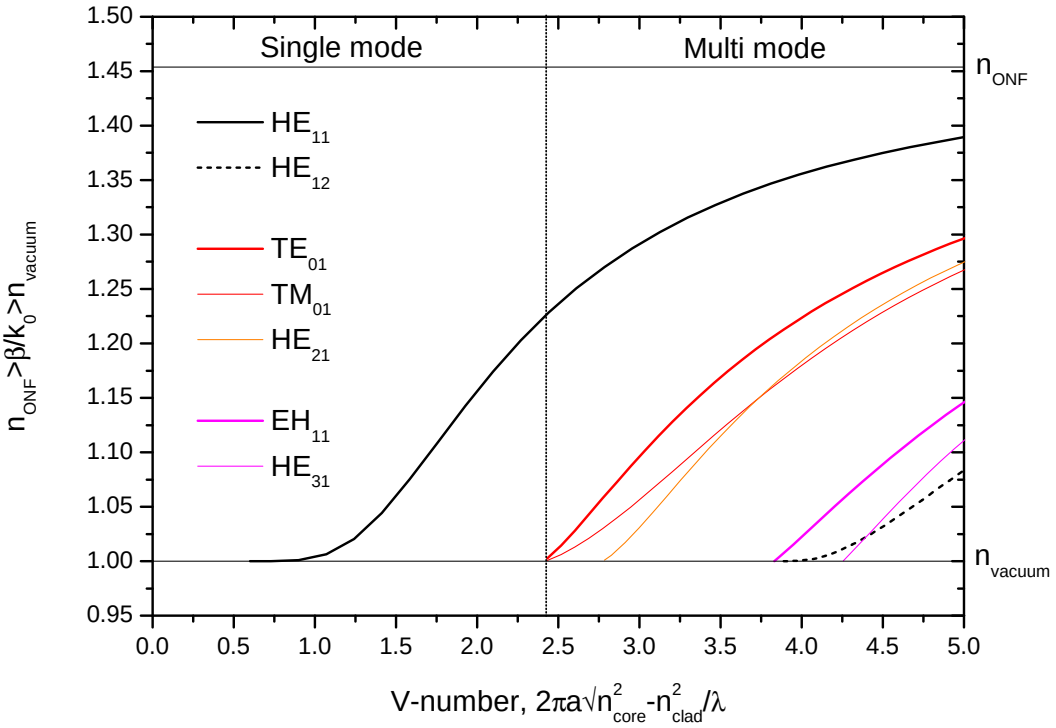

Figure 3.4: *A plot of the propagation constant, β (normalized to k_0) against V-number for an optical nanofibre (or microfibre for V-numbers above $\approx$4.5 with a fixed λ of 780 nm) with cladding (vacuum) and core refractive indices as 1 and 1.4595, respectively. The weak guidance condition is not applicable here as Δn is large. Thus, the LP modes separate out to reveal the exact modes. The dashed, vertical line indicates the boundary between single- and multi-mode guidance in the waveguide ($V = 2.405$).*

3.4 Fabricating ONFs with a fibre-pulling rig

Many variations of fibre pulling rig exist for different applications, for example, the CO_2 laser heater [**?**], the micro-furnace [**?**], electro-furnace [**?**] and the flame [**?**]. Each of these has their advantages and disadvantages; for example, there is an inverse square relationship between diameter and heating for a CO_2 laser heat source, while for a flame or furnace heat source there is simply an inverse relationship between heating and radius. This ultimately places a stricter limit on the minimum taper diameter attainable for a given CO_2 laser power as compared with a flame heat source.

The Quantum Optics pulling rig was developed over a number of years within the QOG by several students and researchers. Figures **??** and **??** show an illustration and photograph of the rig used. The fibre clamps are fixed to the top of steel posts which are, in turn, secured inside a pair of post-holders. The post-holders are fixed to the stepper motor stages (Standa). The stages are controlled by a PC via a USB port and have a stepping resolution of 1 μm. A pair of parallel, low-

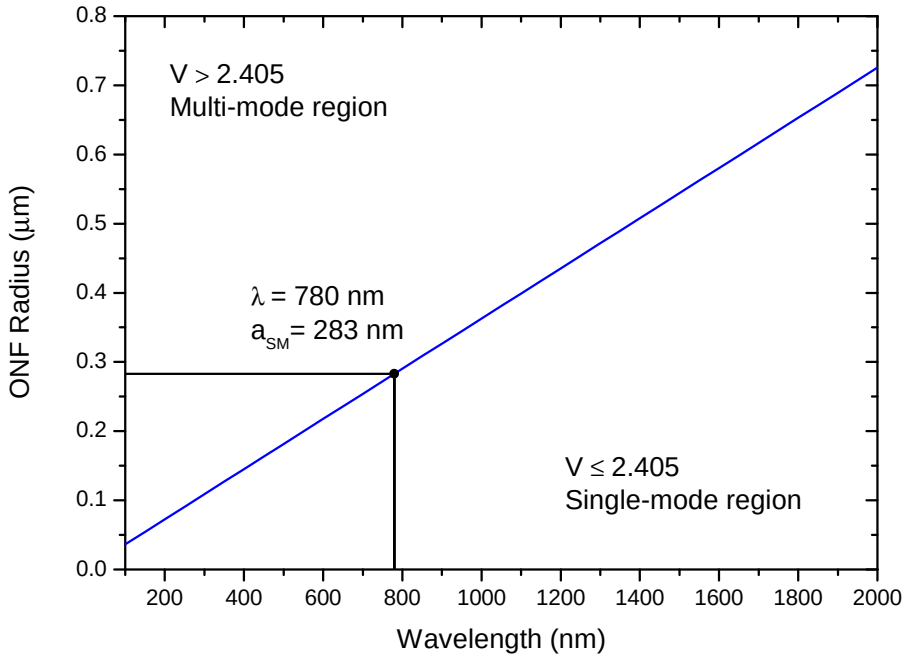

Figure 3.5: *Plot of ONF radius against wavelength of light for the single mode condition $V = 2.405$. The top region of the graph represents the few- and multi-mode regime of propagation while the bottom portion is exclusively single-mode propagation. The gridlines on the low left meet on the single mode line ($V = 2.405$) where $\lambda = 780$ nm $\Rightarrow a_{SM} = 283$ nm. It is assumed that the refractive index is constant through this range.*

friction rails are slotted through the clamp-post assembly. Grub bolts are used to fix the positions of the clamp-assembly on the rails to facilitate transportation of the ONF out of the rig once the fabrication is complete.

A hydrocarbon flame (oxygen and butane) is used to heat the fibre during stretching. Using flow controllers (Burkert S/N1000 for oxygen and Brooks Instrument 0151E for butane) the stoichiometric burning ratio of 13:2 is maintained. If the mixture is oxygen-starved, the flame has a yellow colour - this indicates that the flame temperature is not sufficient to burn all the hydrocarbons present and these deposit on the fibre surface as soot. The flame will burn blue when enough oxygen is present to completely burn off all the hydrocarbons. This prevents soot being deposited on the fibre surface and produces a suitable flame temperature. The temperature required to soften the fibre glass is 1300°C. The oxygen and butane are premixed in the torch head before burning at the nozzle. The flow rate of the gases must be kept to a minimum otherwise the pressure will push upwards on the fibre causing it to bend especially at low waist diameters. The nozzle has a rectangular slot 10 mm × 2 mm which creates a hot zone of about 1.2 cm long on the fibre. A tapered fibre with a diameter of 1 μm can be made with a pull

length of around 18 mm using this system.

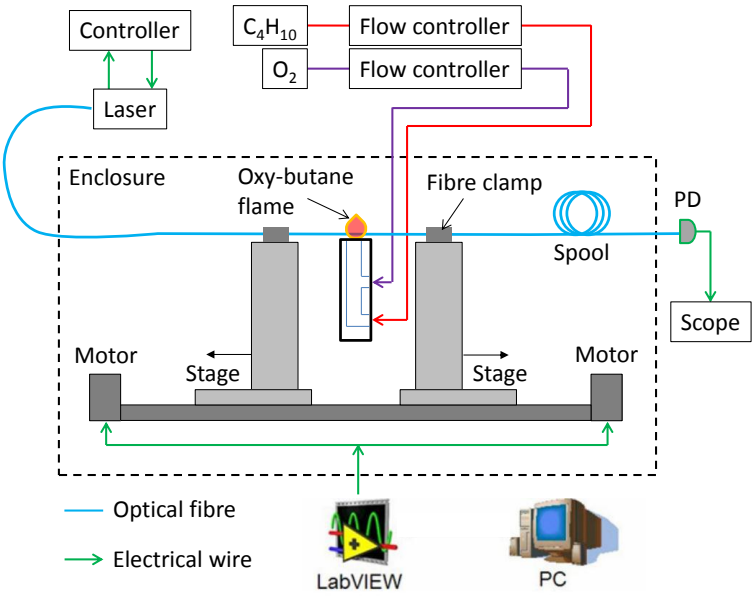

Figure 3.6: *Illustration of the fibre pulling rig. A flow-controlled oxygen-butane flame heats a portion of buffer-stripped optical fibre while two stepper motors stretch the fibre apart. A photodiode (PD) monitors the transmission of an optical signal through the fibre during stretching. The motor motion is controlled via a LabVIEW program. The rig is contained within an enclosure to minimise air currents and airbourne dust near the fibre. The spool of fibre – positioned after the ONF and before the PD – serves to irradicate any cladding modes that may exist after the tapered regions of the tapered fibre.*

To create a tapered fibre, the optical fibre is stripped of its buffer layer (usually a length of about 1 cm is stripped) and cleaned before being clamped between the two motorised pulling stages. The clamps (Fujikura, FH-100-250) hold the fibre taut and prevent slippage during stretching. The stages are fixed to a sliding platform so that the clamped fibre can be slid into position over the oxy-butane flame. A computer program[5] is then used to move the stages apart a particular distance at a specified speed. Typically, pull speeds of ∼0.01 mm/s are used for pull lengths of ∼28 mm to achieve submicron taper waists. After the tapering process, the clamps can be bolted to the rails to stop any further motion of the stages. The posts with the clamps attached can be removed from the post holders, leaving the ONF intact. With additional mechanical stages, the ONF can be placed under a microscope or glued to a u-shaped mount for installation in UHV. The mount used in this work is 90 mm in length which sets an upper limit on the length of taper.

[5]This program is supplied with the stepper motors.

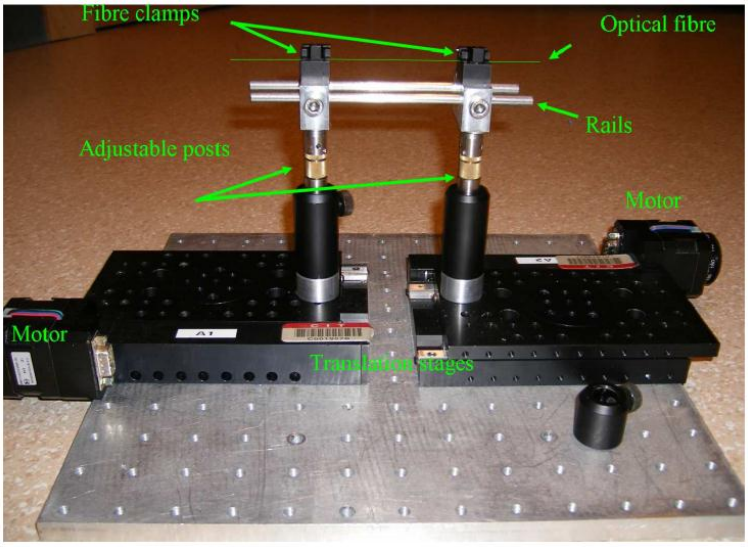

Figure 3.7: *Photograph of the clamp-post-stage assembly for the rig. Grub screws in the clamp-post assembly are loosened for the ONF fabrication process but can be tightened to fix the positions of the clamps along the rails and then transport the ONF to a microscope or experimental setup. (Image courtesy of Dr. Jonathan Ward.)*

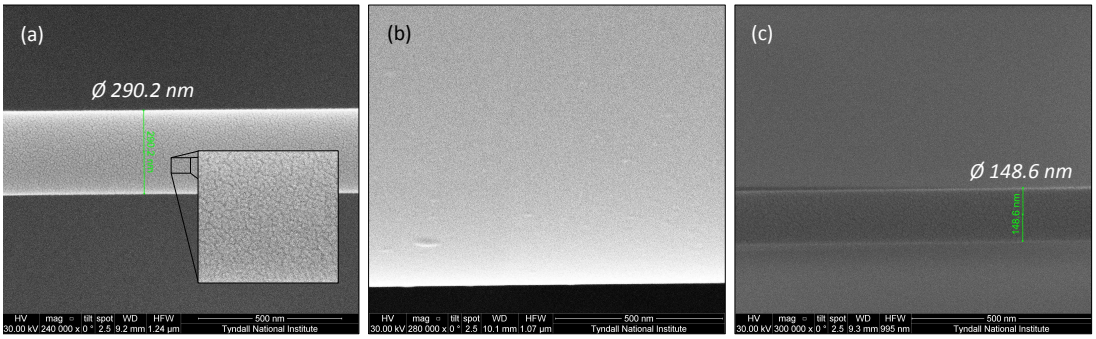

Figure 3.8: *SEM images of a selection of tapered fibres. (a) An ONF with waist diameter of 290 nm. The pattern visible on the surface is due to the sputtered gold layer on the fibre (zoom section). (b) Small irregularities on the fibre surface are present after removing the fibre from the vacuum chamber. This may be attributed to adhesion of moisture and rubidium. (c) An ONF with a waist diameter of 148 nm.*

The diameter of the ONF can be estimated with a microscope or with scanning electron microscopy (SEM). Figure **??** shows SEM images of three tapered fibres. In Figure 3.8(a), the ONF has a waist diameter of 290 nm. The pattern on the fibre surface is due to the layer of gold which is sputtered on the fibre before being placed in the SEM (see inset). This is irreversible which means that the ONF cannot be used in the cold atom experiment after the SEM. It has been observed that after removing the fibre from vacuum, small irregularities on the fibre surface are present. This may be attributed to adhesion of moisture during the vacuum

break and adhesion of rubidium due to the attractive van der Waals surface interaction. The panel on the right shows an ONF with a waist diameter of 148 nm. At such small diameters, the device is quite delicate. Though SEM imaging is destructive for the ONF, it does enable calibration with a $\times 100$ objective microscope with a graduated scale, facilitating the measurement of fibre waists by optical means with an accuracy of ± 0.1 μm.

3.5 Minimising transmission loss

The process of tapering an optical fibre can lead to transmission loss in a number of different ways. The transition regions may allow the light to couple to higher modes which do not exist in the waist or pigtails and, therefore, cannot propagate from the ONF onto a detector. The ONF must be fabricated in a clean environment as the presence of dust and impurities on the surface of the narrower regions can couple power out of the evanescent field. Additionally, because such high circulation intensities of light exist around an ONF, surface deposits can provide a sink for radiated heat. In UHV this can allow a small point on the waist region to reach temperatures above the softening point of the glass and the fibre will tend to break. This effect has been observed when the input optical power was as low as 300 μW. Transmission loss can also happen over a long period of time. Work by Fujiwara *et al.* [**?**] indicated that fractures and fissures can develop on the surface of the tapered fibre over time due to external strains and stresses on the structure. These effects are minimised when the ONF is mounted vertically, but often the process of threading the Teflon ferrule on to the pigtails, tightening the Swagelok nut and pumping the chamber down can be quite damaging. While some of these issues can be solved just by being dexterous, a clean room is not always available in which to fabricate tapered fibres. Fortunately, the most critical factor can be controlled: the transition regions can be made adiabatic during fabrication.

A tapered fibre is adiabatic if the taper angle is small enough at each point that the power lost from the fundamental mode is negligible [**?**, **?**]. This implies that, with a smooth transition gradient, a long tapered fibre can be made with very little loss. However, a short fibre is desirable as it is more rigid and is, therefore, experimentally easier to handle and less susceptible to environmental conditions such as vibrational effects from air currents.

By monitoring the transmission of light through the ONF during fabrication,

the adiabaticity of the transition regions can be gauged. Figure **??** shows a plot of ONF transmission while it is being heated and stretched. The features which occur between 50 and 100 seconds are indicative of mode beating - modes which begin to propagate via the cladding interfere with modes guided in the core of the tapered fibre. When this interference disappears, the waveguide has returned to single-mode behaviour. The presence of mode beating can be avoided by keeping the ONF as straight as possible. Figure **??** shows the decrease of ONF transmission over a long timespan. After approximately 47 minutes (2800 seconds) of steady decrease the transmission suffers a large drop to less than 20%. This may be attributed to dust landing on the ONF surface or the development of cracks and fissures in the waveguide [**?**] due to air currents and gravitational sag. Thus, the ONF must be installed in UHV in a vertical orientation as quickly as practicable.

The taper shape can be controlled using the flame-brushing technique while stretching the fibre [**?**, **?**]. In fact, flame brushing also allows complete rig calibration to be achieved [**?**]. For a fibre pulling rig with a pair of linear stepper motors and a stationary flame, the shape of the tapered fibre can be approximated by:

$$2a_f = 2a_0 e^{-z/L_{hot}}, \tag{3.4}$$

where $2a_0$ is the diameter of the untapered fibre, z is the position along the fibre and L_{hot} is the length of the hot zone of the flame. Thus, it is assumed that all tapers in this thesis have exponential taper profiles.

3.6 Installing an ONF in UHV for use with cold ^{85}Rb

The ONF must be positioned centrally in the chamber on a rigid support which allows unrestricted beam access. A solid, aluminium base and u-shaped mount were designed to secure the ONF in place and facilitate coupling to and from UHV. These are illustrated in Figures **??** and **??**. In preparing these components, UHV procedures are adhered to. In advance of fabricating the ONF, the entire fibre is swabbed with acetone. The fibre feedthrough flange, cylindrical base, mount, grub screws and M3 bolts are all cleaned in an ultrasonic bath and are stored in aluminium foil when not in use. During the gluing and mounting

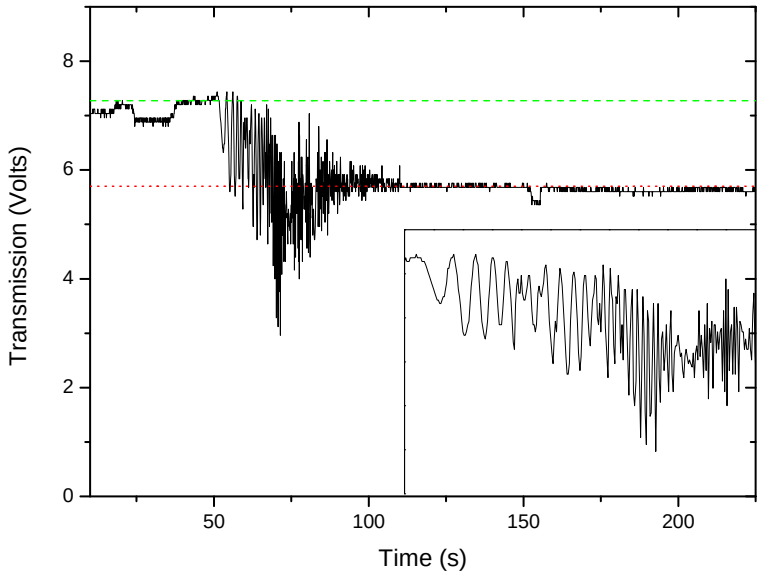

Figure 3.9: *Plot of ONF transmission during the course of approximately 200 seconds. Inset graph shows a zoom in of the mode beating during the initial tapering.*

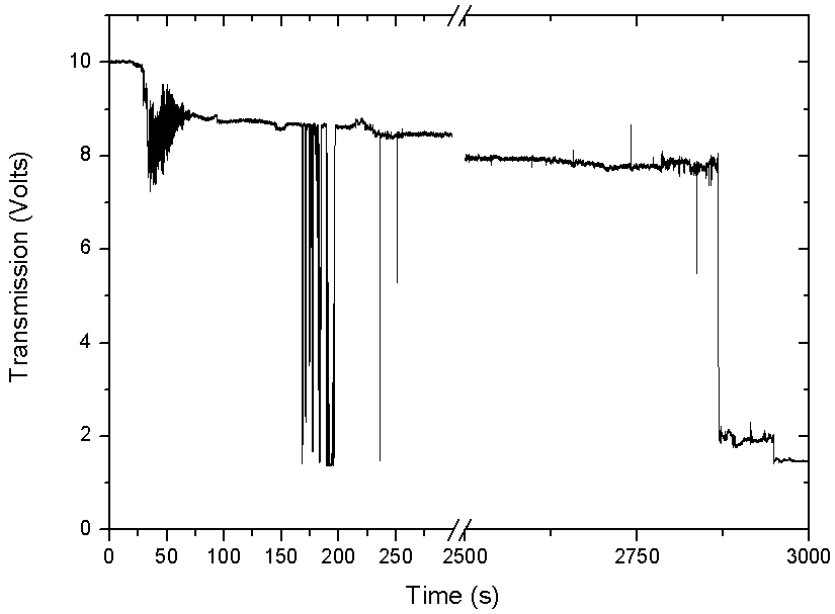

Figure 3.10: *Plot of ONF transmission during the course of 50 minutes.*

process, rubber gloves are worn. This prevents dirt/grease being transferred to the components when they are being handled.

After the ONF has been fabricated in the rig, the friction locks for the sliding rails are tightened so that the clamps and fibre can be removed from the rig and moved to a separate optical bench. The mount is fixed to a mechanical translation stage with a steel post and an M3 grub screw. The mount is positioned between the fibre clamps and carefully brought within a mm of the ONF while also ensuring

that the notches are at the narrowest region of the taper. Using UHV compatible glue which must be cured with UV light, the ONF is finally fixed to the mount ends. The mount is detached from the translation stage and slotted in to the cylindrical base. Here, a grub screw is tightened against the stub of the mount - as the mount is very light compared to the base, this single contact point is sufficient to stabilise the structure. The combined base and mount is fixed to the vacuum flange (which already has a copper gasket in place) with two long M3 bolts. At this point, the Teflon ferrule and Swagelok nut are threaded onto the pigtails. The nut is finger tightened temporarily. The structure is inserted from the bottom or top of the MOT chamber. The flange is rotated to ensure that the mount is at an angle of 45° to the front window to allow MOT beam access. The flange is bolted to the octagonal chamber in the normal manner. Finally, the Swagelok nut is tightened around the teflon ferrule.

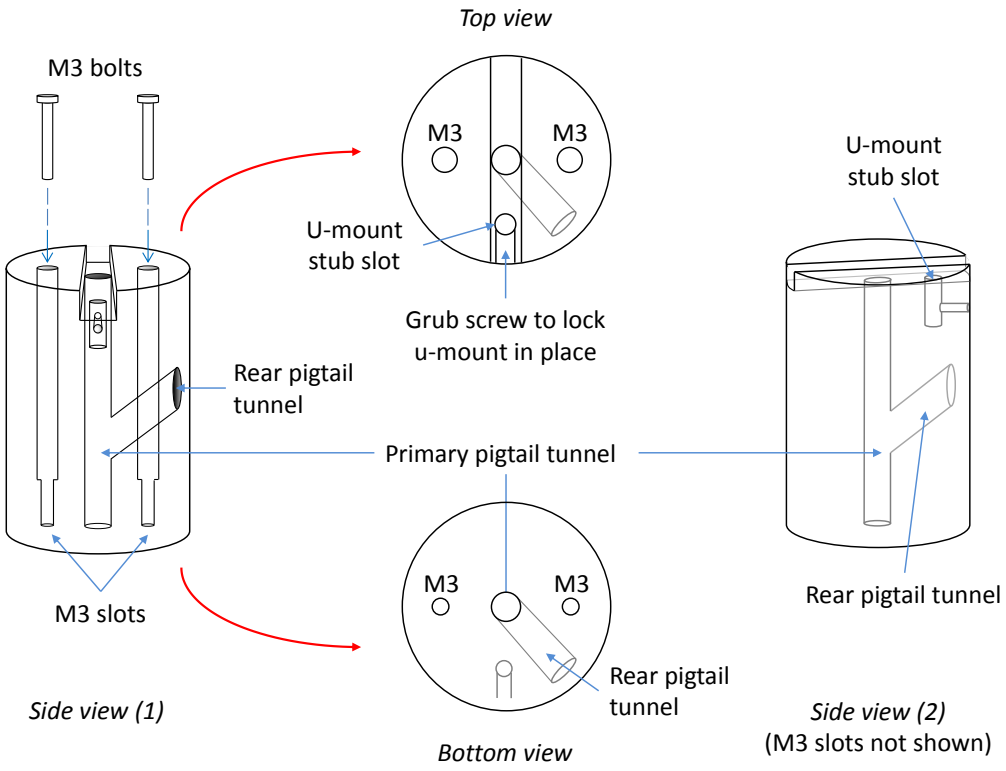

Figure 3.11: *Illustration of the aluminium cylinder used in the ONF mounting system. The top of the cylinder has a slot into which the mount fits (see Figure* **??***). A tunnel runs through the cylinder to bring the pigtails out of the vacuum chamber - a sloped tunnel joins with this to bring the rear pigtail to the centre of the cylinder. A pair of M3-sized slots allow the cylinder to be secured to the vacuum flange.*

The ONF fabricated by the rig must satisfy the following conditions in order to be used effectively in a cloud of cold ^{85}Rb:

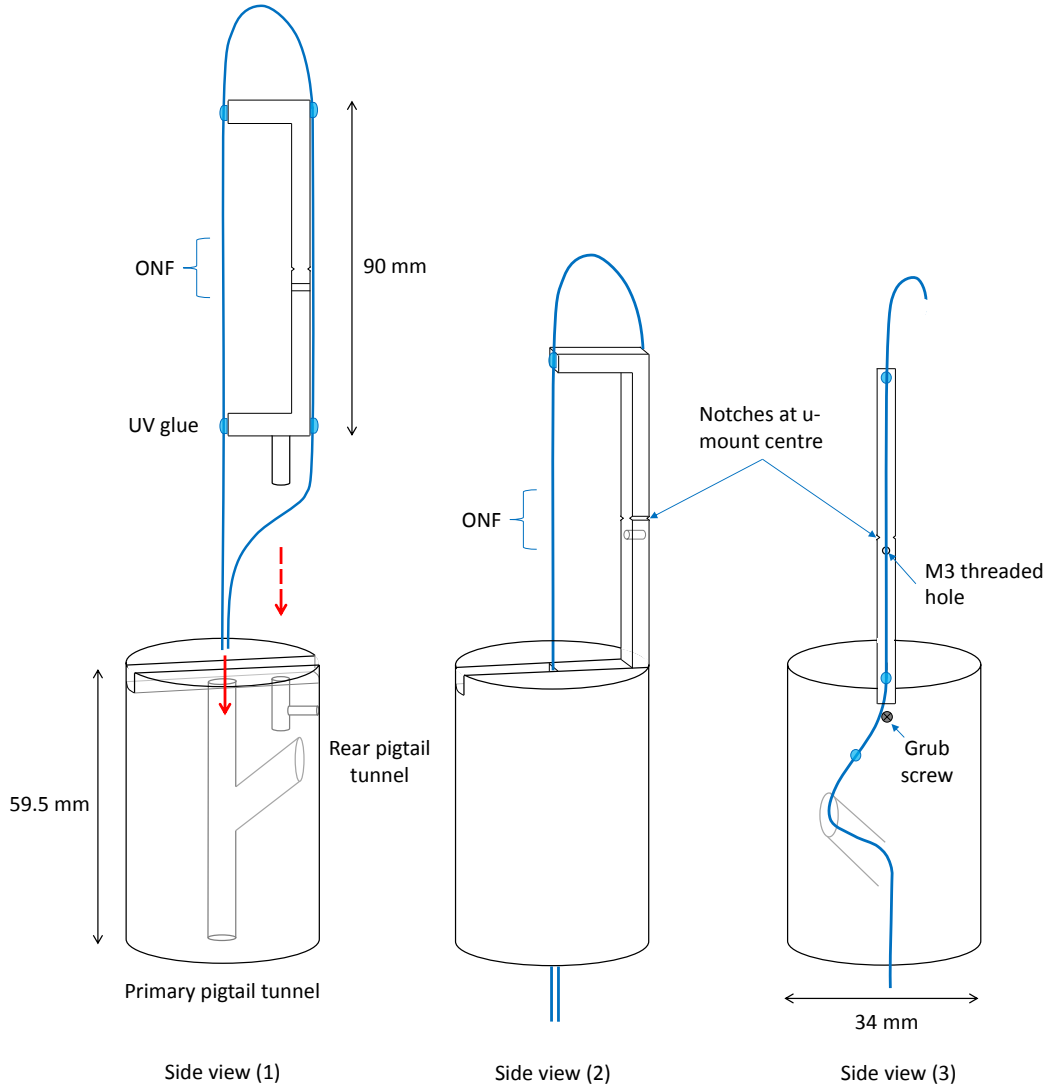

Figure 3.12: *Three perspectives of the ONF mounting system. The aluminium mount is secured to the cylindrical base by tightening a grub screw against the mount stub. The front pigtail is threaded through the primary pigtail tunnel while the rear pigtail is brought through the sloped rear tunnel to join the primary tunnel. The tunnel aligns directly with the fibre feedthrough, Teflon ferrule and Swagelok nut. Notches are engraved into the side of the mount to help in identifying where the ONF should be positioned during the gluing stage and during cloud-ONF alignment. A threaded M3 hole is positioned near the notches to allow the entire mount to be fixed to a mechanical translation stage for gluing.*

- To demonstrate ONF absorption with low input powers, the diameter should be significantly subwavelength in order to maximise the spatial extent of the evanescent field.
- The ONF diameter should be less than the maximum single-mode diameter to avoid loss due to higher mode coupling, i.e. $D_f < D_{SMF} = 566$ nm using $V = 2.405$;
- For maximum fluorescence coupling, the ONF radius should fulfill the condition $k_0 a = 1.45$.

Thus, the primary condition of $k_0 a = 1.45$ yields an optimum diameter for ^{85}Rb of 180 nm $\times$ 2 = 360 nm. Additionally, the length of the waist region should be sufficient to allow overlap with the cloud atom cloud. This turns out not to be a problem with the rig used in this work as, in general, long tapers are generated by default as a result of the chosen stretching parameters.

3.7 Conclusion

This chapter has described the theory and fabrication of the ONF. By solving the transendental equation for β, the propagation constant, the waveguiding properties of either a standard core-clad fibre or an ONF can be determined. In a standard fibre, the change in refractive index between the core and cladding is small and the weakly guiding condition holds. Thus, the linearly polarised mode approximation can be used. In an ONF, these linearly polarised modes become separated as the change in refractive index between the ONF glass (cladding glass) and the environment is large. The fundamental guided mode in an ONF is then the HE_{11} mode and higher modes such as TE_{01}, TM_{01} and HE_{21} are discussed in Chapter 8. To ensure single-mode-guidance in ONFs, the diameter must fall below the cut-off for that wavelength. In ^{85}Rb (780 nm), the cut-off diameter, a_{SMF} is approximately 566 nm as calculated with the V-number. The ONFs in this work are created using a home-made fibre pulling rig. The rig uses an oxygen-butane torch to melt the fibre glass while it is stretched apart using a pair of stepper motors. ONF transmission is monitored during stretching to ensure the transition regions maintain adiabaticity. SEM can be used to determine the diameter of the ONF. Typically, ONF transmissions of >70% can be achieved for ONF diameters of as low as ~150 nm. The challenging aspect of utilising the ONF is installing it in UHV for use with a cloud of atoms. A custom-designed

aluminium mount and cylindrical holder were fabricated to secure and position the ONF in UHV for long-term operation with the MOT. A Teflon ferrule is used with a Swagelok, fibre-feedthrough vacuum flange to couple the ONF pigtails out of the vacuum chamber without disrupting the quality of the vacuum.

Chapter 4

Theoretical studies of surface interactions for cold atoms near an optical nanofibre[1]

In this chapter, the lineshape of the fluorescence emitted by a cloud of optically excited, cold atoms coupled to an optical nanofibre is analyzed. There has been growing interest in the past decade in analysing the interaction between optically excited cold atoms and dielectric nanobodies. In fact, this problem is critical for developing schemes for an exchange of quantum information between single atoms, photons, and nanobodies [**?**, **?**]. The spectral dependence of the fluorescence intensity coupled into the dielectric nanobody may yield information about the interaction strength between the atoms and the nanobody surface. Specifically, this refers to the van der Waals and Casimir-Polder interactions [**?**]. Investigation of these potentials is of particular significance for developing techniques for trapping cold atoms around optical nanofibres [**?**, **?**, **?**]. For example, the studies presented here examine the interaction between a planar surface and an atom - an interaction which is siginificant for any waveguide structure used in atom chip work [**?**, **?**]. Recent work [**?**] studies precisely the interaction between an ONF and a sample of ^{85}Rb atoms. One important aspect of such an interaction is the resultant modification of the spontaneous emission rate of atoms located near nanobodies such as nano- and microfibres [**?**, **?**, **?**], nano- and microspheres [**?**, **?**], and nano- and microdisks [**?**]. Fluorescence radiation emitted by excited

[1]This work can be found in [**?**] - Russell, L., Gleeson, D. A., Minogin, V. G. and Nic Chormaic, S. Spectral distribution of atomic fluorescence coupled into an optical nanofibre. Journal of Physics B: Atomic, Molecular and Optical Physics 42, 185006 (2009).

atoms located near the nanobody and, subsequently, coupled *into* the nanobody should be considered in the context of entanglement between spatially separated atoms [**?**, **?**, **?**]. The lineshape of the fluorescence coupled into an optical nanofibre is generally influenced by both the van der Waals and Casimir-Polder redshifts and both effects must be considered for a complete evaluation.

The ability to fabricate optical nanofibres [**?**, **?**] has facilitated the growth of experimental studies into *atom & nanofibre* systems. Recent experimental observations have shown that, in these systems, the fluorescence excitation spectrum may exhibit either a well-pronounced, long tail at red detunings [**?**] or an asymmetry with a broadened red wing of the spectral line [**?**]. In [**?**], the long red tail of the spectrum was originally assigned to transitions between bound states of atoms in the van der Waals potential, and this was corroborated by theoretical studies [**?**, **?**]. However, in later work [**?**], it was highlighted that the long red tail was only observed when no specific measures were taken to clean the surface of the ONF prior to data acquisition. Subsequently, on cleaning the surface by ultra-violet light, the spectrum exhibited a well-pronounced asymmetry of the spectral line with a prevailing red side, rather than the previously reported and theoretically predicted long red tail [**?**, **?**].

The above observations clearly show that atom interactions with the surface of an ONF may depend strongly on the degree of cleanliness of the fibre surface. In terms of experimentally producing an ONF, a clean environment is paramount to ensuring the surface remains free of dust, moisture and surfactants which may compromise its transmission [**?**][2]. Here, for experiments on atom-fibre interactions, the contributions of basic physical mechanisms to the asymmetry of the fluorescence spectrum are evaluated, rather than the effects of a dirty surface. For clean surfaces, such basic mechanisms include the van der Waals and Casimir-Polder interactions.

The van der Waals interaction can be understood by imagining a single neutral atom placed in a vacuum. The presence of vacuum fluctuations induce a polarization of the atom's otherwise symmetric charge distribution. If a second atom is nearby this first atom, the second atom experiences a polarisation in sync with the polarization of the first atom. The Casimir-Polder force is a manifestation of the same effect except for the case when there is large separation between the two atoms. Thus, it is termed a 'retarded' effect due to the finite speed of light. The contribution of the van der Waals interaction to the redshift of the spectral

[2]A clean environment, ideally, is a clean room with humidity control etc.

line has already been observed in the selective-reflection spectroscopy of caesium vapour located near a dielectric surface [**?**], for example.

The purpose of this work is to show that, alongside the previously considered scenario whereby the fluorescence lineshape asymmetry is caused by the bound-to-bound transitions between the ground and excited state van der Waals potentials, another possible cause of the asymmetry may be an inhomogeneous broadening of the spectral line. This broadening arises from direct contributions of the van der Waals shift to the shape of the spectral line produced by a spatially extended ensemble of cold atoms. For completeness, the contribution of the Casimir-Polder redshift to the spectral dependence of the coupled fluorescent light is considered and, under realistic experimental conditions, it is shown that the Casimir-Polder contribution to the shape of the spectral line may be negligible.

In what follows, the coupling of light emitted by ^{85}Rb and ^{133}Cs cold atomic clouds - two atoms which are widely used in laser cooling experiments - is analysed. Specifically, the fluorescence spectrum emitted by optically-excited atoms into the fundamental guided mode of an optical nanofibre is evaluated. Results from our study show that, for typical radii of optical nanofibres in the range from 200 to 600 nm and atomic clouds that are tightly confined around the nanofibre, the fluorescence excitation spectrum exhibits a well-pronounced asymmetry with red-side broadening caused by the van der Waals redshifts and a shifting of the peak position to the red side of the spectrum. The inclusion of the Casimir–Polder effect has minimal influence on the asymmetry of the lineshape, but reduces the redshift of the peak position slightly.

4.1 Power of fluorescence coupled into the fibre

Consider a collection of cold, two-level atoms in the vicinity of an optical nanofibre as shown in Figure **??**. The atoms are excited by a laser field near-resonant to the atomic dipole transition and they emit fluorescent light, which partially propagates into the guided modes of the fibre. Consider the case where the frequency of the fluorescent light is below the cut-off frequencies of all modes apart from the fundamental, HE_{11}, mode, so that the fluorescent light can only ever propagate in the fundamental mode. The lower state of the atom is considered to be the ground state and we assume that the upper state can only decay to the ground state.

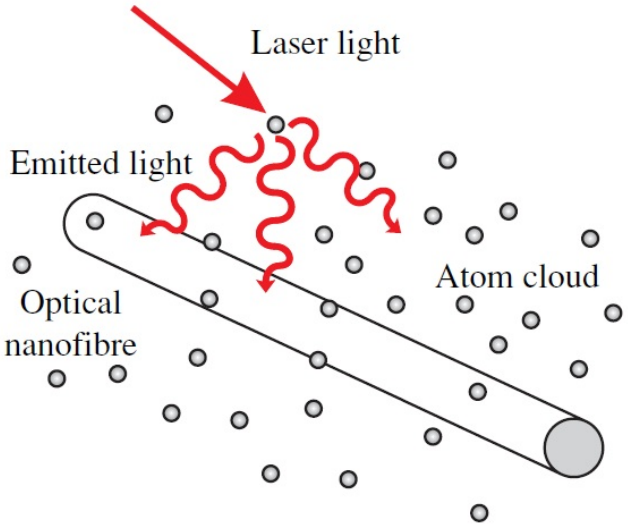

Figure 4.1: *Conceptual diagram of the setup with an optical nanofibre surrounded by an atom cloud, optically excited by near-resonant laser light.*

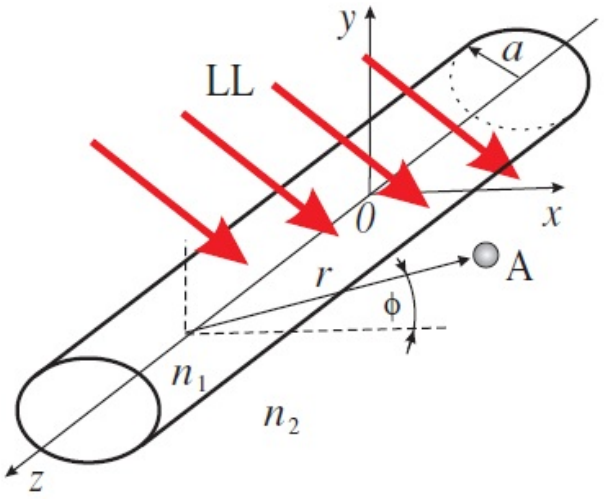

Figure 4.2: *An atom (A) at a position (r, ϕ) from the central axis, z, of an optical nanofibre with radius a. The atom is excited by laser light (LL). Due to the axial symmetry of the waveguide we use cylindrical coordinates (r, ϕ, z). The refractive indices of the environment and waveguide are given by n_{clad} and n_{core}, respectively.*

For a single, motionless, two-level atom placed near the optical nanofibre and excited by an external laser field near-resonant to the dipole optical transition (see Figure **??**) the probability of finding the atom in the upper excited state is

$$p_{\mathrm{e}} = \frac{1}{2} \frac{\Omega^2}{(\omega - \omega_0)^2 + \gamma^2 + \Omega^2}, \tag{4.1}$$

where $\Omega = dE_0/2\hbar$ is the Rabi frequency defined by the atomic dipole matrix element, d, and amplitude, E_0, of the exciting laser field, ω is the frequency of the laser light, ω_0 is the position-dependent atomic transition frequency, and γ is half the position-dependent total spontaneous decay rate, $W_{\rm sp} = 2\gamma$. In the case we are considering, the spontaneous decay rate is made up of the position-dependent decay rate, $\gamma^{(\rm g)}$, into the guided modes of the fibre and the position-dependent decay rate, $\gamma^{(\rm r)}$, into the radiation modes of the fibre, such that

$$W_{\rm sp} = 2\gamma = 2\gamma^{(\rm g)} + 2\gamma^{(\rm r)}. \tag{4.2}$$

For a single atom the probability of spontaneous photon emission into a guided mode of the fibre per unit time is proportional to the population, $p_{\rm e}$, of the excited atomic state and the rate of spontaneous emission, $2\gamma^{(\rm g)}$, into the guided mode,

$$W(r) = 2\gamma^{(\rm g)}(r)p_{\rm e}(r) = \frac{\gamma^{(\rm g)}(r)\Omega^2}{(\omega - \omega_0(r))^2 + \gamma^2(r) + \Omega^2}. \tag{4.3}$$

In the above equation we explicitly show that the atomic transition frequency and the spontaneous emission rates are functions of the atom's position, r. For an ensemble of motionless, two-level atoms distributed near the fibre with density $n(\mathbf{r})$, the light power coupled into the fundamental guided mode is accordingly defined by the volume integral [**?**]

$$P = \hbar\omega \int \frac{\gamma^{(\rm g)}(r)\,\Omega^2}{(\omega - \omega_0(r))^2 + \gamma^2(r) + \Omega^2} n(\mathbf{r})\, dV. \tag{4.4}$$

Hence, the power coupled into the optical fibre depends on the shape of the atomic cloud and its position with respect to the axis of the fibre. In the laboratory, usually just one pigtail of the fibre is connected to a detector and so a maximum of $P/2$ is detected.

In the following, we consider the case of weak optical saturation and neglect the Rabi frequency in the denominator of the excitation probability. We also neglect the short-range repulsive part of the surface potential that can influence a small fraction of the atomic ensemble and may produce a minor contribution to the shape of the spectral line. In its general form, the atomic transition frequency can be written as

$$\omega_0(r) = \omega_0^0 - \delta\omega(r), \tag{4.5}$$

where ω_0^0 is the unperturbed transition frequency and $\delta\omega(r)$ represents the shift that depends on the distance between the atom and the dielectric surface of the fibre $(r-a)$. At small distances $\delta\omega(r)$ is defined by the van der Waals interaction and can be evaluated from [**?**, **?**, **?**, **?**]

$$\delta\omega_{vdW}(r) = \frac{C_3}{(r-a)^3}, \tag{4.6}$$

where C_3 is the van der Waals constant for the atomic transition. At large distances, the shift originates from the Casimir-Polder potential and can be evaluated as

$$\delta\omega_{CP}(r) = \frac{C_4}{(r-a)^4}, \tag{4.7}$$

where the Casimir-Polder constant is given by

$$C_4 = \frac{3\gamma_0}{8\pi}\frac{\epsilon-1}{\epsilon+1}\left(\frac{\lambda}{2\pi}\right)^4 \phi(\epsilon). \tag{4.8}$$

In the above equations, γ_0 is half the natural linewidth for the free atom, ϵ is the static relative permittivity of the fibre material and $\phi(\epsilon)$ is a slowly varying function close to unity, $0.77 \leq \phi(\epsilon) \leq 1$. The explicit structure of the function $\phi(\epsilon)$ can be found in [**?**].

For a typical dipole transition where the wavelength, λ, lies in the visible to the near-infrared region, the border between the van der Waals and Casimir-Polder interactions usually occurs at a distance from the surface of $r - a \simeq \lambda/10 \simeq$50-80 nm. Van der Waals attractions primarily contribute at distances very close to the surface, i.e. at $r - a \leq \lambda/10$. At larger distances, i.e. $r - a \geq \lambda/10$, the Casimir-Polder interaction replaces the van der Waals potential and must be included in calculations. For illustrative purposes and in order to describe the shift for both short- and long-range distances, as well as intermediate distances, we adopt a simple equation such that

$$\delta\omega(r) = \frac{C_4}{(r-a)^3(C_4/C_3 + r - a)}, \tag{4.9}$$

which gives a unified description of the shift over all distances. At small distances, Equation **??** reduces to the van der Waals equation while at larger distances it reduces to the Casimir-Polder equation. One can show, by numerical evaluation, that Equation **??** reproduces the transition between van der Waals- and Casimir-Polder-dominant regions very well. For the numerical calculations which follow in Section 4.2, Equation **??** has not been explicitly used. Instead, either Equation **??** or Equation **??** has been used as the expression $\delta\omega(r)$ in Equation **??** depending on the integration limits. For example, when $r - a \leq \lambda/10$, $\delta\omega(r) = \delta\omega_{vdW}$ and when $r - a > \lambda/10$, $\delta\omega(r) = \delta\omega_{CP}$. In the case where only the van der Waals contribution is considered, $\delta\omega(r) = \delta\omega_{vdW}$ is used in Equation **??** from $r = a \to \infty$.

Finally, the power of the fluorescent light coupled into the guided fibre mode at weak optical saturation can be written as

$$P = \hbar\omega \int \frac{\gamma^{(\mathrm{g})}(r)\,\Omega^2}{\left[\omega - \omega_0^0 + \delta\omega(r)\right]^2 + \gamma^2(r)} n(\mathbf{r})\, dV. \tag{4.10}$$

A numerical evaluation of the integral defined by Equation **??** is given in the next section. Before presenting the numerical results, we will briefly discuss the spatial selectivity of the surface interactions and present numerical values of their corresponding redshifts.

Let us assume, for simplicity, that the ensemble of cold, two-level atoms placed around the ONF is spatially broad. In principle, every atom could be excited by the laser field and, subsequently, would be able to emit fluorescent light. However, the resonance condition restricts the spatial position of atoms which can, in reality, emit fluorescence. According to Equations 4.6 and **??**, for the case of the van der Waals interaction, the atoms are essentially excited at a mean radial position, $\overline{r}_{\mathrm{vdW}}$, given by

$$\overline{r}_{\mathrm{vdW}} \simeq a + \sqrt[3]{\frac{C_3}{\omega_0^0 - \omega}} \tag{4.11}$$

occupying a cylindrical shell coaxially positioned around the optical fibre as shown in Figure **??**. In a similar way, when the resonance condition is satisfied at long distances, the Casimir-Polder interaction is responsible for the excitation of atoms in a cylindrical shell with mean radial position, $\overline{r}_{\mathrm{CP}}$, given by

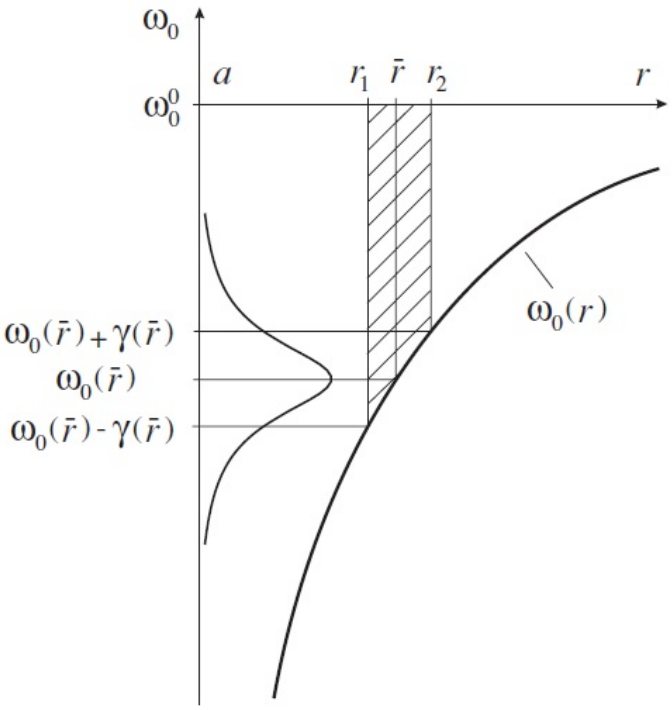

Figure 4.3: *Position-dependent optical absorption line. The shaded area indicates the position of the cylindrical shell containing the excited atoms.*

$$\overline{r}_{\mathrm{CP}} \simeq a + \frac{\lambda}{2\pi}\sqrt[4]{\frac{3\gamma_0}{8\pi\left(\omega_0^0 - \omega\right)}}. \tag{4.12}$$

The spatial width, δr, of the cylindrical shell containing excited atoms is defined by a position-dependent frequency width, $2\gamma(r)$, of an optical resonance. Assuming that at the edges of the shell the probability of atomic excitation is half that at the centre of the shell, one can evaluate the radii of the shell edges, r_1 and r_2, as roots of the equations

$$\omega_0\left(r_{1,2}\right) \simeq \omega_0\left(\overline{r}\right) \mp \gamma(r_{1,2}). \tag{4.13}$$

Hence, the spatial width of the cylindrical shell containing excited atoms is given by $\delta r = r_2 - r_1$. It can be easily shown that when the average frequency shift $\omega_0^0 - \omega_0(\overline{r})$ exceeds the natural linewidth $\gamma(\overline{r})$ the spatial width of the shell is small compared to the shell radii, i.e. $\delta r << r_{1,2}$, and can be evaluated by neglecting small variations in the spontaneous emission rate inside the shell, i.e. making the approximation $\gamma(r_{1,2}) \simeq \gamma(\overline{r}) \simeq \gamma_0$. For the van der Waals interaction this simplification results in an estimate of the spatial width of the shell that is given

by

$$\delta r_{\mathrm{vdW}} \simeq \frac{2(\overline{r}_{\mathrm{vdW}} - a)^4 \gamma_0}{3C_{3\mathrm{g}}}. \tag{4.14}$$

For the case of the Casimir-Polder interaction, the above simplification yields a characteristic width

$$\delta r_{\mathrm{CP}} \simeq \frac{2\lambda}{3} \left(\frac{2\pi(\overline{r}_{\mathrm{CP}} - a)}{\lambda} \right)^5. \tag{4.15}$$

The total power of the fluorescent light exciting the guided fibre mode is proportional to the volume, V, of the cylindrical shell with inner radius, r_1, and outer radius, r_2, i.e. the volume $V = \pi \left(r_2^2 - r_1^2\right) l \simeq 2\pi \overline{r} \delta r l$, where l is the spatial extension of the atomic ensemble along the fibre. Hence, the power of the fluorescent light coupled into the guided mode can be evaluated with

$$P = 2\pi\hbar\omega\gamma^{(\mathrm{g})}\left(\overline{r}\right) \frac{\Omega^2}{\gamma^2(\overline{r})} n(\overline{r}) \overline{r} \delta r l. \tag{4.16}$$

For the van der Waals and Casimir-Polder interactions, the mean radius and width of the shell containing excited atoms can be estimated from Equations (**??**), (**??**), (**??**), and (**??**).

Table 4.1: *Position and width of the cylindrical shell containing excited two-level atoms for van der Waals and Casimir-Polder interactions.*

ω	$\omega_0^0 - 2\gamma_0$	$\omega_0^0 - 3\gamma_0$	$\omega_0^0 - 4\gamma_0$
$\overline{r}_{\mathrm{vdW}} - a$ (nm)	74	64	58
δr_{vdW} (nm)	29	16	10
$\overline{r}_{\mathrm{CP}} - a$ (nm)	64	57	53
δr_{CP} (nm)	17	11	7

Numerical values of the mean radii and widths of the shells for the van der Waals and Casimir-Polder interactions for typical optical dipole transition parameters are given in Table **??**. The data has been calculated for a value of the van der Waals constant, $C_{3\mathrm{g}} = 2\pi \cdot 2\mathrm{kHz}(\mu\mathrm{m})^3$, a wavelength, $\lambda = 800$ nm, and for three values of the laser field frequency, $\omega = \omega_0^0 - n\gamma_0$, with $n = 2, 3, 4$ and $2\gamma_0 = 2\pi \cdot 5$ MHz chosen as a typical value of the natural linewidth for the optical dipole transition. The values shown in Table **??** indicate clearly that, for a typical dipole transition, the evaluations give very similar average regions of extent for

both the van der Waals and Casimir-Polder interactions. This implies that the Casimir-Polder contribution to the spectral lineshape is expected to be small when compared to that from the van der Waals interaction. In other words, the Casimir-Polder potential should yield a contribution comparable to that of the van der Waals potential only at such small distances where, physically, the van der Waals interaction exists.

4.2 Numerical evaluations

In Equation **??** there are two unknown quantities: the spontaneous emission rate into the guided mode and the spontaneous emission rate into the radiation modes. Of these two quantities, the more important for our analysis is the rate of spontaneous emission into the guided mode. This quantity varies sharply near the surface of the fibre and, therefore, strongly influences the rate of coupling of spontaneously emitted light into the fibre. The rate of spontaneous emission into the radiation modes changes weakly near the fibre, keeping its value approximately equal to the rate of spontaneous emission into free space. In the following analysis we will neglect the weak spatial dependence of the spontaneous emission rate into the radiation modes and consider only the position dependence of the spontaneous emission rate into the guided mode.

A complete evaluation of the spatial distribution of the evanescent light field of a fundamental guided mode and the spontaneous emission rate into the fundamental guided mode of an optical fibre is presented in Appendix A. Figure **??** shows the dependence of the spontaneous decay rate for a two-level atom as a function of distance between the atom and the optical nanofibre surface calculated according to Equation **??**.

The fluorescence emission line spectrum for ^{85}Rb and ^{133}Cs atoms can now be estimated. We assume the atoms emit fluorescence light into an optical fibre made of fused silica, with permittivity, $\varepsilon = 2.1$. The Rb atoms are assumed to be excited at the 5S-5P optical dipole transition, with a wavelength of 780 nm and a spontaneous decay rate of $2\gamma_0 = 2\pi\cdot$ 6 MHz [**?**, **?**] from the upper 5P state into free space. For this optical transition in Rb, the van der Waals constant is evaluated as $C_{3g} = 2\pi \cdot 3$ kHz$(\mu$m$)^3$ [**?**, **?**, **?**]. Cs atoms are assumed to be excited at the 6S-6P optical transition with a wavelength of 852 nm and a spontaneous decay rate of $2\gamma_0 = 2\pi\cdot$ 5.2 MHz [**?**] from the upper 6P state into free space. The van der Waals constant for this optical transition in the Cs atom is $C_{3g} = 2\pi \cdot 1.56$

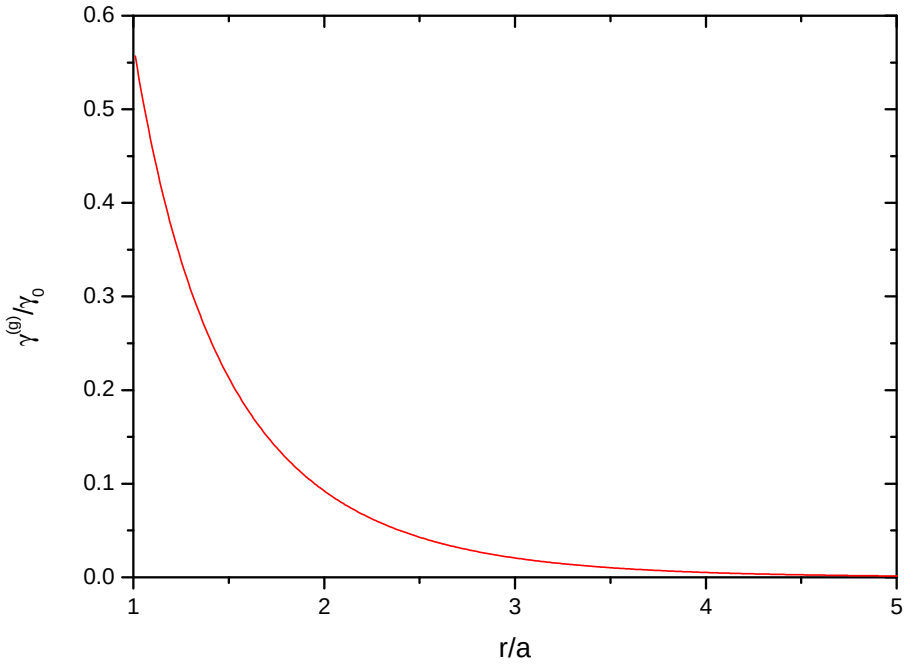

Figure 4.4: *Normalized spontaneous decay rate of a two-level atom into the fundamental guided mode HE_{11} as a function of distance between the atom and the axis of the optical nanofibre with radius $a = 200$ nm.*

kHz$(\mu$m$)^3$ [**?**, **?**, **?**]. For both optical transitions, with relatively close wavelengths, the refractive index of the fibre is chosen to be $n_{core} = 1.45$ and the refractive index of the outside medium is $n_{clad} = 1$.

We assume that the cold atoms are distributed in a spherically symmetric cloud of radius R centred symmetrically on the longitudinal axis of an optical nanofibre with radius a. The cloud has no atoms inside the cylindrical region occupied by the fibre, but in the region outside the fibre the cloud is assumed to have a Gaussian density distribution described with cylindrical coordinates, $n(z, r, \phi)$, as follows:

$$n(z, r) = \frac{N}{\pi\sqrt{\pi}R^3} \exp\left[\frac{a^2 - r^2 - z^2}{R^2}\right], \tag{4.17}$$

where N is the total number of atoms and is given by

$$N = 2\pi \int n(r) r \mathrm{d}r\mathrm{d}z. \tag{4.18}$$

It is worth noting here that, for the shape of atom cloud that we consider, i.e. a cloud with an empty internal volume, one can expect an increase in the strength

of the surface effects due to the increased ratio of the surface area to the cloud volume.

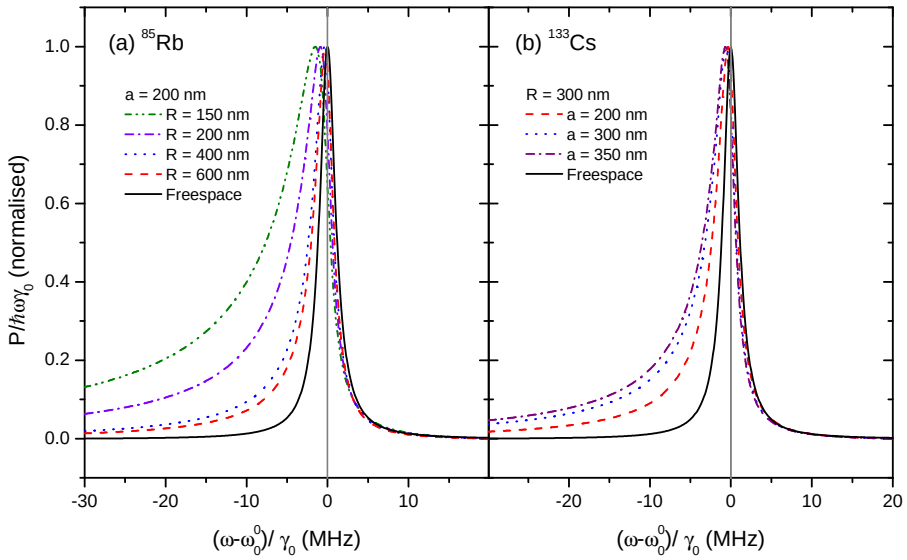

Figure 4.5: *Frequency-dependence of the fluorescence power from an atom cloud coupled into the optical nanofibre in the van der Waals approximation. (a) Rb atoms with fixed fibre radius $a = 200$ nm and an atomic cloud radius $R = 600$ nm, 400 nm, 200 nm and 150 nm. (b) Cs atoms with fixed cloud radius $R = 300$ nm and a nanofibre radius of 200 nm, 300 nm and 350 nm. The solid black line shows the free space lineshape. All lineshapes are normalized to a maximum value of 1 for ease of comparison.*

Figure **??** shows the estimated coupled fluorescence spectrum for rubidium and caesium atoms, calculated under the assumption that Equation **??** has the same form as Equation **??**, i.e. approximating the potential as the van der Waals shape only and neglecting the Casimir-Polder potential for the moment. Thus, the term $\delta\omega(r)$ in Equation **??** is given by only in Figure **??**. Figure **??**(a) demonstrates the frequency dependence of the lineshape for rubidium atoms as the atom cloud size varies and the fibre radius is kept constant. As one can see, the asymmetry of the fluorescence lineshape increases when the radius of the atomic cloud decreases. In other words, the tighter the cloud around the fibre, the more pronounced the asymmetry becomes. As the radius of the cloud increases the atoms located further from the nanofibre are less influenced by the change in the van der Waals frequency shift and, hence, the shape of the fluorescence spectrum approaches that of the symmetrical, free space distribution. In Figure **??**(b), we present the reverse situation for caesium atoms, i.e. the atom cloud size is kept constant while varying the size of the nanofibre. As can be seen, a very similar result is obtained. As we increase the fibre radius, more of the fluorescing atoms are close to the fibre surface and, as a result, the van der Waals potential affects a greater proportion of the total atoms in the cloud, leading to more pronounced

asymmetry in the lineshape.

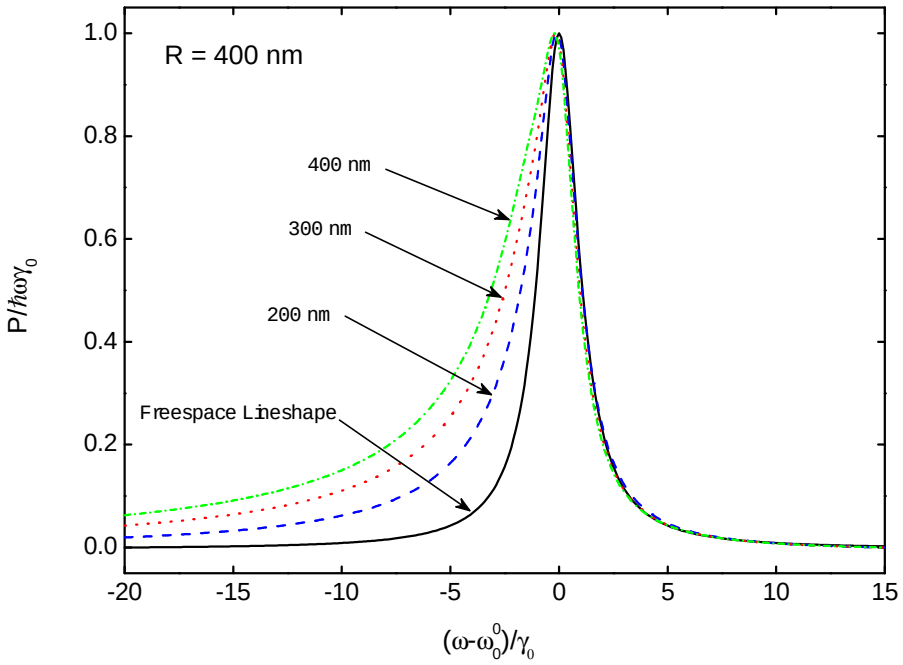

Figure 4.6: *Frequency dependence of the fluorescence power from a Cs cloud coupled into the optical nanofibre for redshift contributions from both the van der Waals and Casimir-Polder effects. The cloud radius is $R = 400$ nm and the nanofibre radius is varied. The solid black line represents the free space lineshape. All lines are normalized to a maximum value of 1 for ease of comparison.*

If we now consider a total surface potential (Equation **??**), which describes the van der Waals potential at short distances and the Casimir-Polder potential at larger distances, we see that a similar phenomenon is observed (Figure **??** for caesium atoms). The most pronounced effect occurs when the fibre radius approaches that of the effective cloud radius. This arises because there is a greater population of atoms fluorescing near the surface of the fibre under such conditions. In the case where the fibre radius and cloud radius are equal, the asymmetry is maximally evident, as shown in Figure **??** for $a = 400$ nm. Note that the inclusion of the Casimir-Polder potential at large distances has resulted in a slight reduction of the redshift of the peak position of the lineshape when compared to that for the van der Waals interaction alone (Figure **??**(b)). However, the overall asymmetry of the lineshape is still very clear at negative detunings. The reduction of the redshift can naturally be explained by an increased number of atoms with a reduced redshift value. In other words, the approximation $C_4 = 0$ slightly overestimates the value of the spectral line redshift.

This small reduction in the observable redshift due to the inclusion of the Casimir-Polder effect is evident from the plots in Figure **??**. Hence, while the van der

Waals interaction is clearly the dominant influence on the lineshape, the overall lineshape should include the contributions from the Casimir-Polder effect in order to obtain a precise prediction of the fluorescence coupled into a nanofibre. A comparative investigation of this behaviour for different values of a and R is given in order to determine under what conditions this change to the lineshape (arising from the Casimir-Polder effect) can be neglected. Irrespective of the values chosen for a and R no appreciable difference arises when one includes the Casimir-Polder effect. In fact, we see that the overall redshift *decreases* with increasing values of a and R. For $a = R = 200$ nm there is a small, but identifiable, difference between the two spectra as shown in Figure **??**(a). For larger values of R with respect to a (Figures **??**(b) and (c)), the difference between the lineshapes reduces as the spectra approach the freespace lineshape. Even for the case $a = R = 600$ nm (Figure **??**(d)), any difference between the two regimes is unresolvable. One explanation for this result is that, when $a = R$, very few atoms experience the Casimir-Polder interaction because the cloud density has decreased by a factor of $\exp\left(\left(a + 0.1\lambda/\right) R\right)$ in the region where the Casimir-Polder dominance begins. When $R \geq a$ the density of atoms has also reduced significantly at the crossover region, thereby yielding a very small contribution to the lineshape from the distant atoms.

Note that for ease of comparison, in Figures **??**, **??** and **??**, all powers coupled into the nanofibre have been normalised to a maximum value of 1. In reality, there are large differences in the actual amount of power coupled into nanofibres of different radii. In Figure **??** we plot the power coupled into a nanofibre as a function of nanofibre radius and, as expected, the power coupled reduces significantly with increasing fibre radius for a fixed atom cloud size.

4.3 Conclusion

We have examined the efficiency of coupling the fluorescence emitted from an ensemble of cold, two-level atoms into an optical nanofibre and we have calculated the frequency dependence of fluorescence power coupled into the fundamental guided mode of the optical nanofibre. The coupled fluorescence spectrum was evaluated by considering the total surface potential that describes the van der Waals effect at short atom-surface distances and the Casimir-Polder effect at larger atom-surface distances. These evaluations show that the van der Waals redshifts may be responsible for a pronounced asymmetry of the coupled fluores-

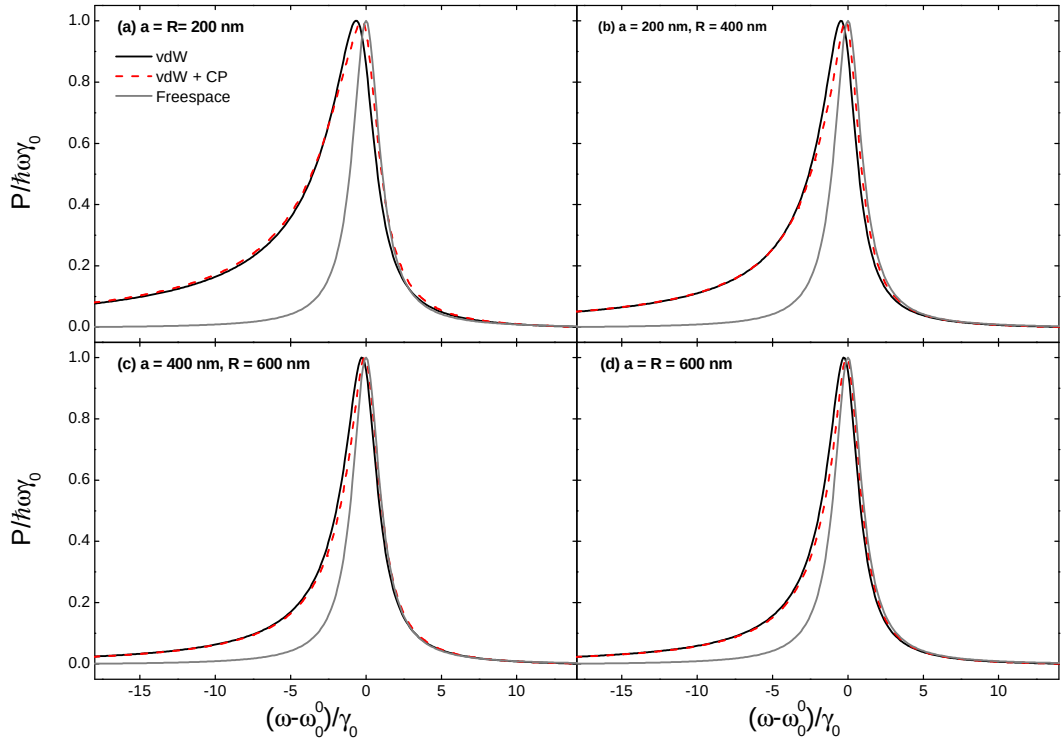

Figure 4.7: *Frequency dependence of the fluorescence power from a Cs cloud coupled into the optical nanofibre for different lineshape contributions: van derWaals effect only (solid, black line), Casimir–Polder + van der Waals (dashed, red line), for different cloud radii and fibre radii. All lines are normalized to a maximum value of 1 and the free space lineshape (solid, grey line) is provided for ease of comparison between the curves.*

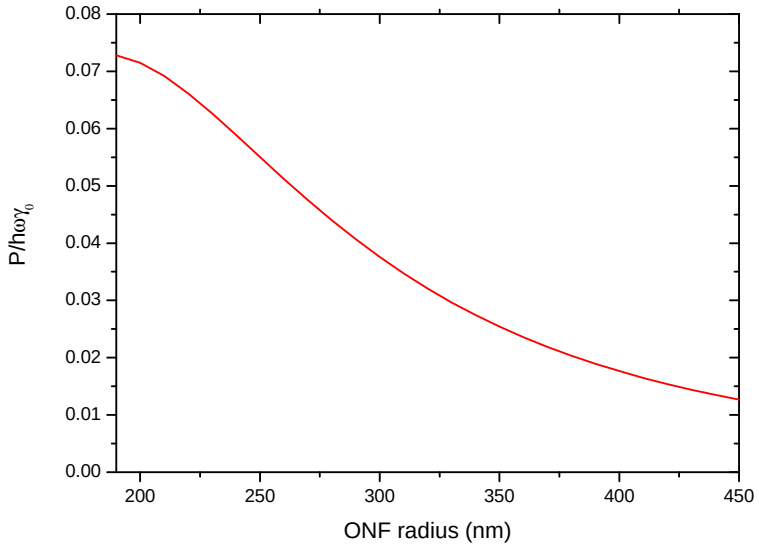

Figure 4.8: *Power coupled into a nanofibre as a function of fibre radius. The power shown is the maximum power for each value of the fibre radius. The data were plotted for a* ^{85}Rb *cloud with* $R = 5$ *mm.*

cence spectrum, whereas the Casimir-Polder redshifts may produce only a slight asymmetry of the spectrum. Furthermore, the asymmetry is more exaggerated for atomic ensembles that are tightly confined around the optical nanofibre. Additionally, the asymmetry of the lineshape increases as the fibre radius is increased and there is clear evidence of a long red tail. We conclude that, for a correct and accurate comparison of the experimentally obtained profile of the lineshape with the theoretical lineshape, one should consider the total surface potential by taking into account the van der Waals and Casimir-Polder redshifts. This is particularly important when considering atomic clouds which are tightly confined around the nanofibre surface [**?**]. In this work, the fibre was considered to be a flat surface when seen by the atoms due to the relatively short distances considered. A more realistic approach is to consider the cylindrical nature of the surface [**?**]. Earlier work has shown that the flat surface approach is a reasonable first approximation [**?**]. Note also that, if the power coupled into the fibre were monitored at both ends, quantum correlations between the modes emitted in opposite or equal directions could be studied. Nayak *et al.* [**?**] have conducted beautiful experiments based on this idea with laser-cooled Cs atoms. Using a Hanbury Brown-Twiss setup, the photon correlation was seen to change from anti-bunching to bunching as a function of increasing atom number when photons were propagating in the same direction in the fibre. In contrast, when the photons were detected at opposite ends of the nanofibre, antibunching was always observed. However, for this type of experiment, the van der Waals and Casimir-Polder effects are negligible since the photon count rate is the measured quantity rather than the emission spectrum [**?**].

Chapter 5

Fluorescence coupling experiments with an ONF[1]

In this chapter, experimental work using the atom and nanofibre system is presented. The first section outlines the process of coupling the atom cloud to the ONF and then summarises some typical measurements and quantities concerned with using a subwavelength waveguide detector embedded in the cloud. The final two sections in this chapter outline two methods of temperature measurement using fluorescence coupling.

Figure **??** illustrates the system which is utilised in this chapter: a laser-cooled cloud of ^{85}Rb atoms surrounding an optical nanofibre. The nanofibre waist can have a diameter in the range of a few microns down to a few tens of nanometers - anywhere in this range, there is some probability that the photons emitted from the surrounding atoms will couple to the waist and propagate in one of the two directions through the waveguide. This system is placed in an ultra-high vacuum chamber. The optical nanofibre pigtails are out-coupled from the chamber (as described in Chapter 3) and connected to a single photon counting module or a suitable avalanche photodiode detector. Recording the photon count rate with an SPCM, for example, enables an estimation of cloud temperature [**?**], allows calculations of cloud loading times and lifetimes [**?**] and studies of photon correlations from the resonance fluorescence of the cold atoms [**?**, **?**].

[1]Portions of this work can be found in [**?**] - Russell, L., Deasy, K., Daly, M. J., Morrissey, M. J. and Nic Chormaic, S. Sub-Doppler temperature measurements of laser-cooled atoms using optical nanofibres. Measurement Science and Technology 23, 015201 (2012); and [**?**]: Russell, L., Kumar, R., Tiwari, V. B. and Nic Chormaic, S. Measurements on release-recapture of cold Rb-85 atoms using an optical nanofibre in a magneto-optical trap, Optics Communications 309, 315-317 (2013).

In Chapter 8, the ONF is used as the carrier of a probe beam to perform absorption-based experiments on the surrounding cold cloud. Here, we are interested in the properties of the entire cloud rather than of the smaller numbers of atoms which are within the evancescent field of a probe beam in the ONF. Measurements presented here demonstrate the sensitivity of the ONF to MOT parameters such as cooling laser detuning and intensity.

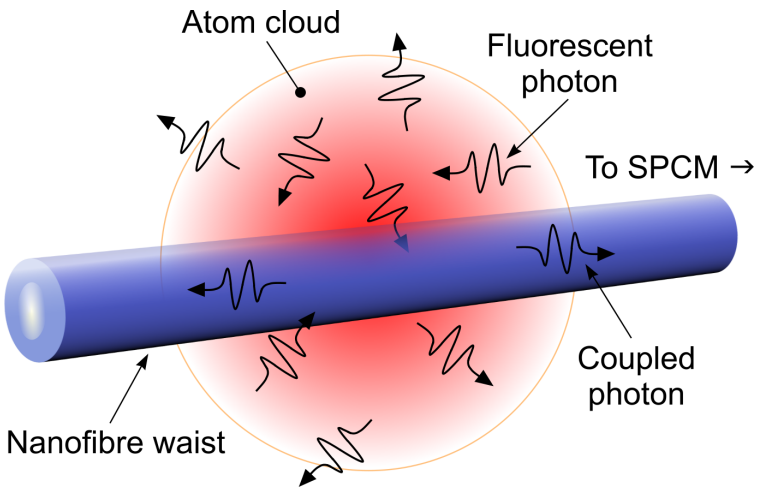

Figure 5.1: *Schematic of the atom cloud overlapping the nanofibre, illustrating the coupling of fluorescence photons to the guided mode of the fibre.*

5.1 ONF-cloud coupling

5.1.1 ONF-cloud alignment

The process of finding the best position of the cloud in relation to the ONF is repeated each time a new ONF is installed in the chamber. Vertical movement of the cloud is enabled by vertical magnetic compensation coils. These coils are set up as shown in Figure **??**: a vertical coil, with inner radius of 3.5 cm, sits on top of the chamber and a current of up to 3 A can be passed through it, vertically displacing the cloud up to 5 mm (the direction of the displacement depending on which direction the current is passed through the coil). A pair of coils sit opposite each other on the chamber, at 90° to the trapping coils. These also have an inner radius of 3.5 cm. These coils are connected in series and can both take a current up to 3 A which generates a horizontal displacement of the cloud of approximately 5 mm. This system of coils is essential because the waist of the nanofibre will not always be exactly at the centre of the MOT for two reasons: (a) during ONF fabrication, there may be uncontrolled motion of the pulling stages (see Chapter

3) and this creates non-symmetric tapers and (b) during the ONF gluing stage, the ONF will not necessarily be mounted such that the waist is at the mid-point of the mount (see Chapter 3). Full displacement of the cloud is rarely required, but if the cloud does need to be repositioned more than a few millimetres from the original zero point of the magnetic field, then full re-alignment of the MOT beams is necessary. More usually, vertical re-positioning along the ONF of 1 or 2 mm is performed, with small adjustments to the beam position to optimise the cloud shape and maximise the coupling of fluorescent photons.

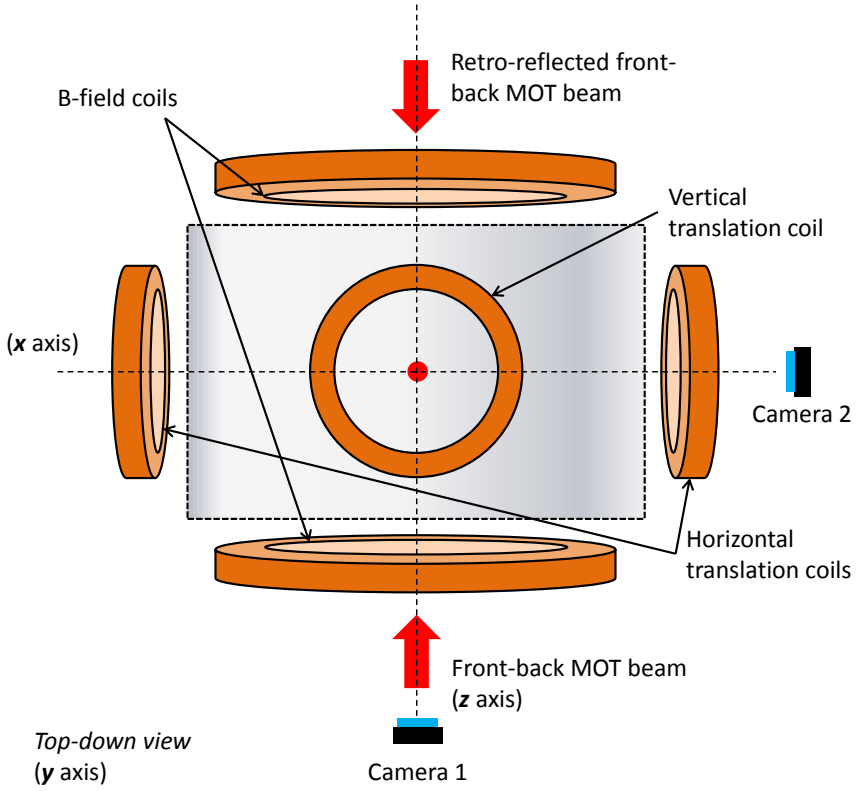

Figure 5.2: *Placement of translation coils and trapping coils around the vacuum chamber (top-down view). The horizontal, front-back MOT beam is indicated for clarity.*

For coarse alignment, two cameras monitor the cloud position with respect to the ONF. A Thorlabs USB CMOS camera (camera 1 – Thorlabs, DCC1545M) monitors vertical (y-axis) and horizontal alignment (x-axis) with the system of translation coils. In the mutually orthogonal direction (along the z-axis of the magnetic coils), a custom-made magnifying CCD camera (camera 2) monitors the secondary horizontal alignment of the cloud. The ONF is visible with camera 2 due to the scattering of the diagonal MOT beams off the ONF surface. At the front of the chamber, camera 1 cannot resolve the ONF: a software package is used to view the image from the camera and the ONF is illuminated with a

handheld torch in order to draw a vertical line from one side of the ONF to the other (see Figure **??**).

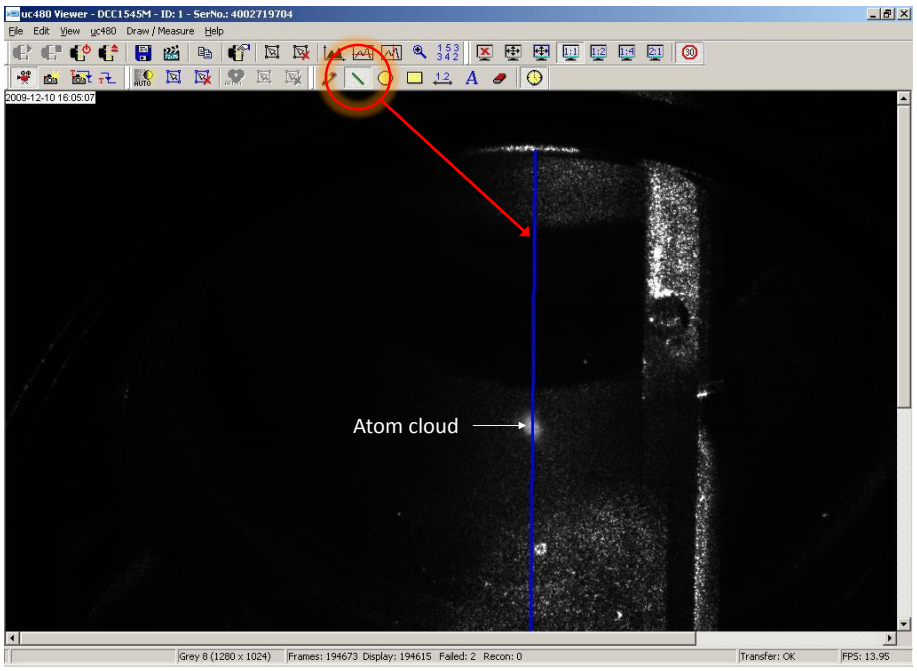

Figure 5.3: *Screenshot of uc480 software for camera 1 (see Figure* **??***). The ONF is highlighted by a vertical blue line which is created by the line tool (circled in red). The ONF is illuminated with a handheld torch in order to manually overlay the blue line on the camera image.*

Lastly, for fine alignment, an SPCM (Perkin-Elmer single photon counting module, model: SPCM-AQR-14[2]) is used to monitor the fluorescent photon count rate from the cloud via the ONF. By tweaking the coil currents the count rate is maximised and by adjusting MOT beam alignment both the background signal and, more importantly, the signal-to-noise ratio are optimised.

5.1.2 Measurements

When the MOT is switched on (i.e. when the cooling and repump laser are frequency-locked and a current is applied to the MOT coils) the number of atoms in the MOT increases during the *loading time*. The *loading curve* is characterised by the atom type, the capture velocity, the trapping volume and the average

[2]The SPCM has a dark count of 100 counts/s and quantum efficiency of 60% at 780 nm. For each photon detected, the SPCM will output a 35 ns TTL pulse, which is detected by a Hamamatsu C8855 counting unit, connected via a USB cable to a computer. This allows user-defined gating times to be set for the counting unit, with no dead time between the gated counting periods due to a dual counter incorporated into the C8855 counting unit. This lack of dead time is very advantageous for continuous measurement of the number of coupled photons.

initial atomic temperature of the atoms in the background vapour. When the capture rate and loss of the trap balance each other, the number of atoms in the MOT reaches a steady value. The capture rate, R, represents the number of atoms that enter the trap per second and is given by

$$R = \frac{1}{2} n v_c^4 V^{2/3} \left(\frac{m}{2 k_B T} \right)^{3/2}, \tag{5.1}$$

where n is the density of atoms in the vapour, v_c is the capture velocity, V is the trapping volume, m is the atomic mass, k_B is Boltzmann's constant and T is the atom temperature [**?**]. The loss rate of the trap Γ is described by the inverse lifetime, $1/\tau$ [**?**]:

$$\frac{1}{\tau} = n \sigma \left(\frac{3 k_B T}{m} \right)^{1/2}. \tag{5.2}$$

Here, σ is the cross-section for an atom in the background vapour to collide with an atom in the MOT and knock it out of the trap. Thus, the rate of change of atoms in the MOT is described by[3]

$$\frac{dN}{dt} = R - \frac{N}{\tau}. \tag{5.3}$$

where N is the number of atoms in the MOT. When the number of atoms reaches a steady state value some time after the MOT has been switched on, $N = N_s = R\tau$. Additionally, at $t = 0$, $N = 0$ and

$$N(t) = N_s \left(1 - e^{-t/\tau} \right). \tag{5.4}$$

To monitor the loading of the MOT, the fluorescent photons from the cloud can be imaged onto a photodiode (PD) (Figure **??**). The output voltage from the PD is proportional to the number of atoms trapped in the MOT (N_A) and can be used to trace the loading curve of the MOT: knowledge of the sensitivity of the PD makes it possible to convert from V_{PD} to detected optical power.

Figure **??** shows the number of photon counts per second coupled to the ONF from the atom cloud as recorded with an SPCM instead of a PD. The low count level ($< 2.5 \times 10^5$ counts/s) before the magnetic field is switched on arises from

[3]The form of this equation has a more complex form before making assumptions about background pressure and sample density. See, for example, [**?**].

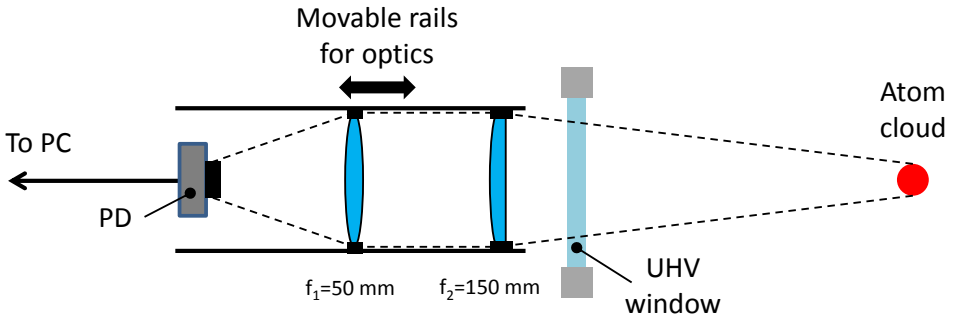

Figure 5.4: *An optical setup for imaging the cloud of cold atoms onto a photodiode (PD). The signal from the PD is sent to a computer so that the output voltage (which is proportional to cloud fluorescence) can be recorded.*

light coupling to the ONF from the cooling laser beams, repump laser beam, the various external light sources in the laboratory, and the dark count of the detector. When the magnetic field is switched on (dashed vertical line, Figure **??**) the atom cloud begins to load and the fluorescence level grows in proportion to the number of atoms captured by the MOT. In Figure **??**, loading curves for four different cooling laser intensities are plotted as recorded with the ONF and SPCM. It is interesting to note that a saturation effect is seen towards the higher values of intensity.

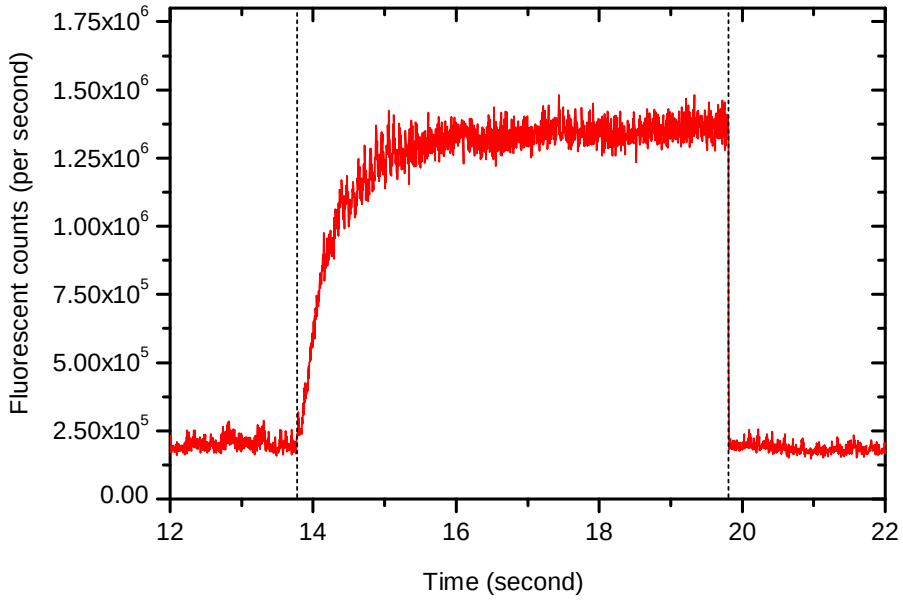

Figure 5.5: *Flourescent counts from the atom cloud per second. Signal-to-noise ratio is approximately 20.*

The count rate detected by the SPCM, R_{counts}, can be determined using the following formula:

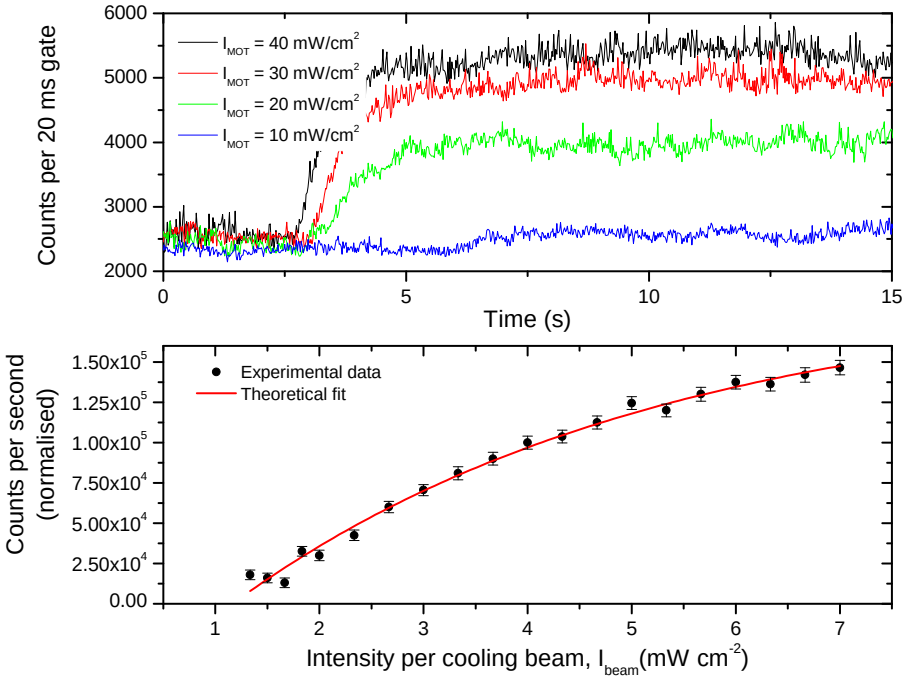

Figure 5.6: *Steady-state counts as a function of cooling laser intensity. The upper plot shows a series of loading curves (in terms of count rate per 20 ms gate time) using different values of cooling laser intensities (I_{MOT}). The lower plot shows the steady state counts per second as a function of I_{beam}.*

$$R_{counts} = n_{\text{eff}} \eta_f \gamma_{sc} Q_D T \tag{5.5}$$

where n_{eff} is the effective number of atoms contributing to the fluorescence signal, η_f is the average coupling efficiency of spontaneous emission into the guided modes of the fibre, Q_D is the quantum efficiency of the detector (60% at 780 nm), and T is the transmission through the ONF from its waist region to one end. The atomic scattering rate, γ_{sc}, can be written as a function of laser intensity and detuning of the cooling laser from the cooling transition [**?**],

$$\gamma_{sc} = \frac{\Gamma}{2} \frac{I/I_s}{1 + I/I_s + 4\left(\Delta/\Gamma\right)^2}. \tag{5.6}$$

To determine n_{eff} it was assumed that any atoms beyond a distance of 300 nm from the surface of the fibre have very little effect on the spontaneous emission detected by the photon counter. Work by Le Kien *et al.* [**?**] discusses this in detail - the majority of the fluorescence coupling occurs for atoms within 200-300 nm from the ONF surface for ONF radii of $\approx$ 200 nm. By overlapping this cylinder-shaped observation area (see Figure **??**), which has an inner radius of

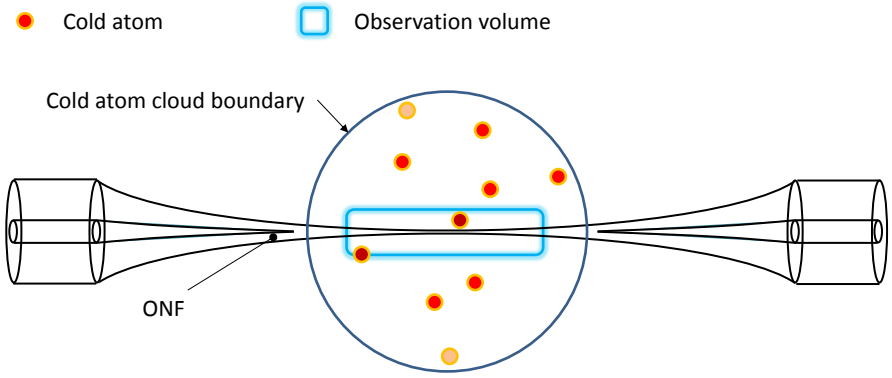

Figure 5.7: *Schematic of the experiment, illustrating how n_{eff} is determined.*

a, with the average density of the MOT, $\overline{\rho_{MOT}} = N_A V_{MOT}$, the effective number of atoms contributing to the spontaneous emission detected by the SPCM was calculated from the following equation

$$n_{\text{eff}} = \overline{\rho_{MOT}} \pi L_f \left(a^2 - r^2\right), \tag{5.7}$$

where L_f is the length of the TONF waist and is assumed to be greater than the diameter of the MOT, i.e. $L_f > D_{MOT}$ (which is generally correct: typical cloud diameters are approximately 1 mm and the waist length is usually several mm). In the case of an ONF with waist diameter of about 1 μm, n_{eff} is 0.4 and a maximum count rate of 2000 counts/s can be observed. For the count rate plotted in Figure **??** of ~6000 counts/s, the fibre diameter was approximately 600 nm. Using $\eta_D = 0.06$ (estimated using previous work based on ^{133}Cs [**?**]), we get $n_{\text{eff}} = 0.4$.

If n_{eff} is plotted against the observation cylinder radius (Equation **??**) it is clear that n_{eff} grows quadratically with increased ONF radius. This is, of course, not the case in reality as the coupled power will decrease with fibre diameter in accordance with Equation **??**. A weighting factor which follows the curve of this plot should be applied to the observation cylinder volume in order to more accurately predict n_{eff}. This is important for ONFs with diameters around and slightly above λ (780 nm) in particular. Figure **??** shows the predicted coupled fluorescent power as a function of nanofibre radius. Only the vdW-influenced spectral frequency shift has been used here as the Casimir-Polder effect is negligible in this case of millimetre-dimensioned clouds – as discussed in Chapter 4. The maximum of the coupled power curve occurs at $k_0 a = 1.45$, i.e. an ONF diameter of 360 nm in the case of ^{85}Rb. For the case of an ONF radius of 500

nm, high signal-to-noise ratios can be obtained with ease despite achieving much less coupled power compared to what can be achieved using an $r = 180$ nm ONF. This demonstrates the effectiveness of the nanofibre as a light detection tool. On the other hand, the spatial extent of the evanescent field at this large diameter (a few nanometres for a diameter of 1 μm) is very small and absorption via the nanofibre is challenging, if not impossible, without dramatically increasing the density and decreasing the spatial spread of the atom cloud. This necessitates the overall requirement of small diameter fibres in the range of 350 - 400 nm to satisfy the maximum coupling condition and to allow absorption techniques to be demonstrable. Table **??** describes two fitting functions which describe the change in the power coupled to the ONF as a function of ONF radius. These functions are solved for increasing values of ONF radius and plotted in Figure **??**.

Table 5.1: *Fitting functions to describe the change of coupled power to the ONF from the cold atoms as the ONF radius increases.*

For...	ONF radius < 180 nm	ONF radius ≥ 180 nm
Fitting function:	$y = A2 + \frac{A1-A2}{1+e^{\frac{x-x0}{dx}}}$	$y = y_0 + Ae^{-e^{-z^{0.7}}-z+1}$ $\left(z = \frac{x-xc}{w}\right)$

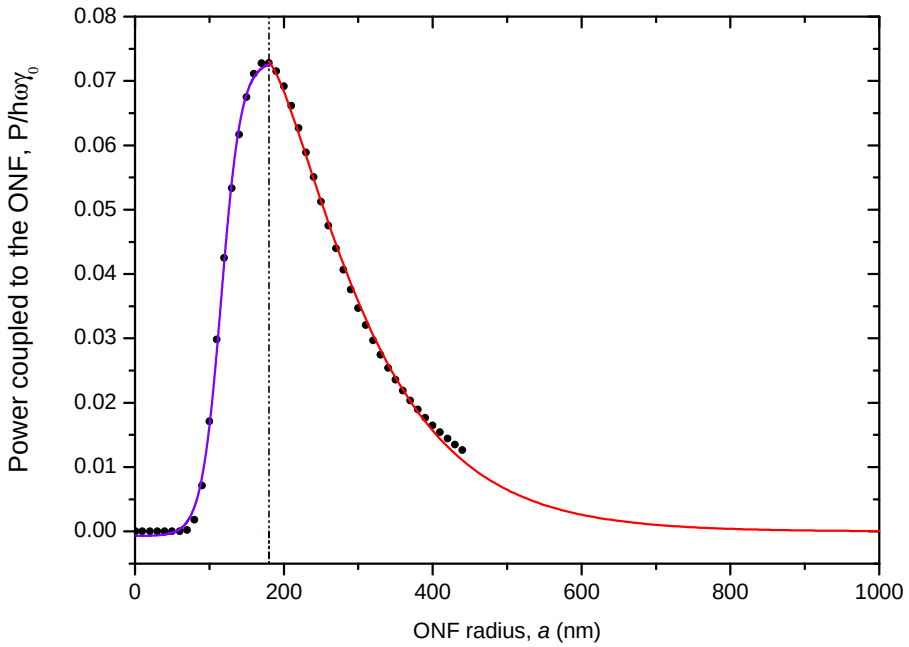

Figure 5.8: *Predicted power (normalised) coupled to a nanofibre as a function of increasing nanofibre radius. As expected from the optimum coupling condition ($k_0 a = 1.45$), the maximum coupled power is obtained when the ONF radius is 180 nm (black, dash-dot-dot line). The cloud radius was set to 0.5 mm in this simulation.*

A typical SMF (single-mode fibre) has approximately 80% of the light within

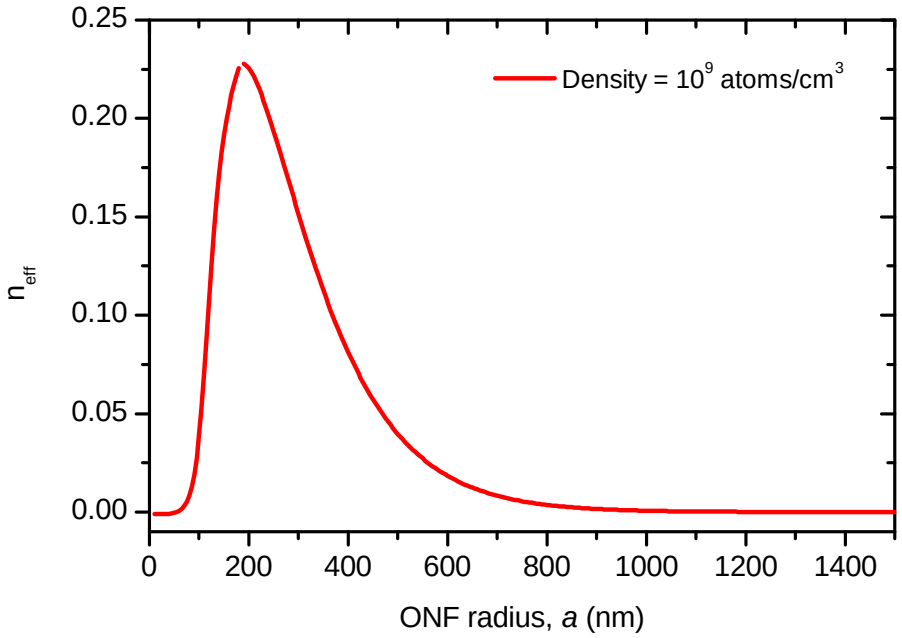

Figure 5.9: *n_{eff} as a function of nanofibre radius with a correction factor that includes the reduction of the evanescent coupling region for larger and large radii. Cloud density is 10^9 atoms/cm^3 and cloud radius was set to 0.5 mm in this simulation. The maximum coupled power is obtained when the ONF radius is 180 nm.*

the core and 20% of light extends beyond the core and into the cladding. The diameter of the entire mode (mode field diameter, MFD) includes the light within the cladding. The MFD[4] of 780 nm light in 780HP single mode fibre (core radius is 2.2 μm) is approximately 5 μm so it is clear that photons can couple to the ONF even when it is a couple of microns in diameter in accordance with Figure **??**.

n_{eff} depends on the cloud density, ONF diameter and ONF waist length. After fabrication, the latter two quantities are fixed and the cloud density can be increased. For example, Figure **??** shows the theoretical maximum value of n_{eff} when the cloud density is 10^9 atoms/cm^3. The plot in Figure **??** shows how the effective number of atoms can be dramatically increased by improving the cloud density.

5.1.3 Further comment about n_{eff}

When determining n_{eff} experimentally, a number of points must be taken account of. The SPCM measures the actual photon counts from various atoms throughout

[4]See http://www.thorlabs.com/Thorcat/6800/780HP-SpecSheet.pdf

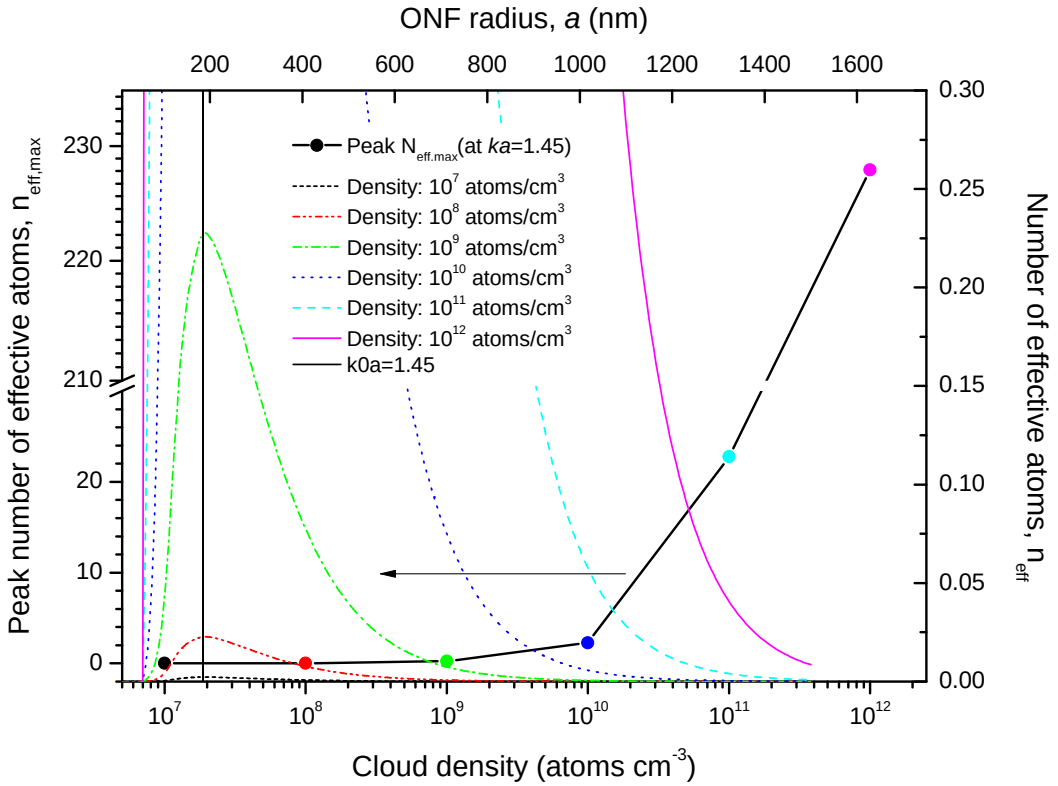

Figure 5.10: *This compound graph shows what the peak value of n_{eff} is at different values of the MOT cloud density. The left and bottom axes (coloured data points with a black spline fit to guide the eye) show the peak value of n_{eff} at a fixed ONF radius which satisfies the condition $k_0a = 1.45$. It is clear that, with increased density, a very large increase in n_{eff} is seen. Thus it is desirable to improve MOT density in order to improve optical density. The top and right axes relate the fluorescence coupling curves for varying cloud density as a function of ONF radius – for comparison, Figure* **??** *shows just one of these curves at 1×10^{10} atoms/cm^3 (green, dash-dot curve in this plot). Each of these curves peak at $ka = 1.45$ (indicated by the solid black line at a radius of about 185 nm). For example, with a cloud density of 10^{10} atoms cm^{-3} (green, dash-dot curve) and an ONF radius of 400 nm, the maximum n_{eff} that can be obtained is 0.04.*

the entire cloud. Here, Equation **??** is used to estimate the quantity $n_{eff,1}$ (see Figure **??**). This cannot be used to measure cloud density, but provides an interesting figure of merit which relates the density of atoms emitting photons into the guided mode of the ONF to the overall number of atoms in the MOT and the cloud volume.

If the 'usual' atom cloud density, ρ, is known then Equation **??** can be used to estimate the quantity $n_{eff,2}$ (see Figure **??**) with some fixed observation volume positioned symmetrically around the ONF. This will drastically overestimate the 'true' n_{eff} if ρ is multiplied by the volume of a 300-nm-wide observation cylinder surrounding the ONF, but for purposes of optimisation (e.g. cloud density, ONF

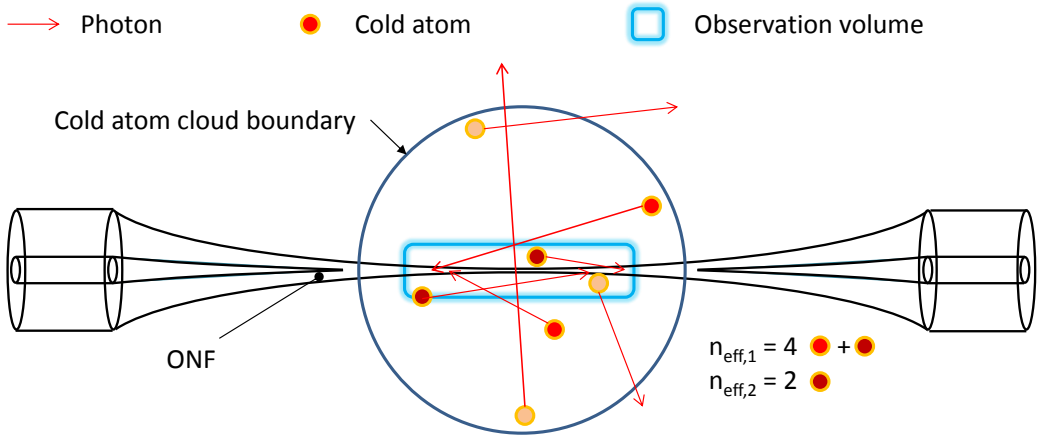

Figure 5.11: *Variations in the definition of n_{eff} due to the random direction of emission of fluorescent photons.*

dimensions) the small observation volume is sufficient.

If there is no knowledge of ρ, and Equation **??** is used to determine $n_{eff,2}$ (with V as the volume of the 300-nm-wide observation cylinder), the density of the cloud will be underestimated. This is summarised in Figure **??**.

5.2 Temperature measurements

Temperature is undeniably one of the most important characteristics of a laser-cooled sample of atoms that one can measure. By experimentally determining the ensemble temperature, T, quantities such as the spring constant and diffusion coefficient can be estimated [**?**, **?**], temperature and density regimes can be mapped out [**?**], and a wealth of information regarding the efficiency of the trapping, cooling and compression scheme can be revealed [**?**, **?**].

There now exist many temperature measurement techniques for cold atoms. Some novel methods have been implemented to match specific trapping techniques (for example, see [**?**, **?**]) but the most common methods use the thermal expansion of the cloud to estimate T [**?**, **?**, **?**]. These are called time-of-flight (TOF) measurements.

For temperatures at the Doppler limit (146 μK for ^{85}Rb) and above the release-recapture (RR) method is well-suited. At temperatures significantly below the Doppler limit, gravity begins to play a role in the thermal expansion of a cold cloud of atoms because the initial velocity of the atoms becomes small compared to the velocity acquired due to gravity during expansion. Both the cloud shape

and capture region must be known in order to fully analyse the characteristic release-recapture motion. Although TOF methods are generally destructive (i.e. the cloud must be destroyed to determine T), RR can be termed reconstructive as each sequence ends with the original cloud being recaptured (albeit for a finite time).

The behaviour of the cloud of atoms as a damped harmonic oscillator provides insight into the spring constant of the cloud and its temperature. The first demonstration of such a temperature measurement was by Steane and Foot [**?**] who used a pushing beam to impart oscillatory motion on the cloud. The authors remark that the pushing beam may affect the results by optical pumping. Thus, it is advantageous to use the magneto-optic field as the displacing force when performing forced oscillation. This magneto-optic-force-based oscillation technique was originally implemented for a conventional fluorescence imaging setup [**?**, **?**]. In this work, by imparting a one-dimensional oscillatory motion to the magnetic trap, the phase difference between the oscillations of the trap and the oscillations of the atom cloud can be determined by measuring the photon count rate at one end of the nanofibre. This measurement technique is highly sensitive to just a few atoms and has distinct advantages over alternative temperature measurement techniques since the nanofibre method is non-destructive.

In general, the trapped atoms under study – either via their fluorescence signal or by using a resonant probe beam – are those that are located closest to the centre of the MOT where the nanofibre is positioned and are the coldest atoms. External observation using a photodiode gives a view of the whole cloud and no access to the inner distribution. However, the nanofibre is ideal for probing small numbers of atoms located near the nanofibre and in the central region of the trap.

In the following two sections, we focus on the method of forced oscillations (FO) and the release-recapture method (RR), respectively.

5.2.1 Method of forced oscillations[5]

As mentioned, the first demonstration of the forced harmonic magneto-optical trap method [**?**] used the radiation force of an additional laser beam to push the trapped atoms away from the trap centre. However, three-dimensional sub-

[5]This work can be found in [**?**]: Russell, L., Deasy, K., Daly, M. J., Morrissey, M. J. and Nic Chormaic, S. Sub-Doppler temperature measurements of laser-cooled atoms using optical nanofibres. Measurement Science and Technology 23, 015201 (2012).

Doppler theory was required to calculate the pushing force. The motion of the atom cloud in this current work is restricted to one dimension, allowing straightforward analysis using the well-established forced harmonic oscillator model.

To measure the temperature of a cold atom cloud, the system is viewed as isolated from the surrounding environment. This allows us to define the temperature, T, in terms of the average kinetic energy, $\langle E_k \rangle$, of the atomic sample [**?**]:

$$\frac{1}{2}k_B T = \langle E_k \rangle \tag{5.8}$$

where k_B is Boltzmann's constant. An atom trapped in the oscillating MOT behaves as a damped harmonic oscillator [**?**], the motion of which is described by

$$m\ddot{x} = -\kappa x - \lambda \dot{x}, \tag{5.9}$$

where m is the atomic mass, x is the atom's position, κ is the spring constant and λ is the damping coefficient. We have neglected stochastic heating of the cloud due to the low atomic density.

In thermal equilibrium, the atom cloud has a thermal energy given by [**?**, **?**]:

$$k_B T = \kappa \langle r_x^2 \rangle = m \langle v^2 \rangle \tag{5.10}$$

where $\langle r_x^2 \rangle$ is the $1/e^2$ radius of the atom cloud along the direction of forced oscillation and $\langle v^2 \rangle$ is the mean square atomic velocity. To measure κ the cloud is forced to oscillate in the x-direction. The periodic motion of the trap centre is given by $\Delta x(t) = \xi_0 cos(\omega t)$, where ξ_0 is the maximum displacement of the trap centre and ω is the applied oscillation frequency. By ensuring the maximum displacement of the cloud is small, it remains within the linear regime of the trap and the motion of an atom within the trap is described by $x(t) = A(\omega)\cos(\omega t - \phi)$, where

$$A(\omega) = \frac{\omega_n^2 \xi_0}{\sqrt{(\omega_n^2 - \omega^2)^2 + \gamma^2 \omega^2}} \tag{5.11}$$

and

$$\phi(\omega) = \frac{\pi}{2} - \tan^{-1}\left(\frac{\omega_n^2 - \omega^2}{2\gamma\omega}\right). \tag{5.12}$$

Here, ω_n is the natural frequency of the trap and is related to the spring constant by $\kappa = m\omega_n^2$, and $\gamma = \lambda/2m$ is the damping constant. Therefore, by measuring the phase, $\phi(\omega)$, we can obtain κ allowing the temperature to be determined from Equation **??**. It can be seen from Equation **??** that the natural frequency and oscillation frequency are equal when $\phi(\omega) = \pi/2$.

To carry out forced oscillation temperature measurements, typical methods of forcing the MOT to oscillate are using either a pushing laser beam [**?**] or superimposing a small oscillating magnetic field [**?**] on the main trapping field of the MOT. In the latter technique the current supplied to a pair of translation Helmholtz coils is modulated, causing the atom cloud to oscillate and the motion is that of a forced, damped harmonic oscillator. Fluorescent photons from the atom cloud are focused onto a photodiode producing a sinusoidal output signal, which can be frequency analyzed using a spectrum analyzer. A plot of phase, $\phi(\omega)$, versus applied oscillation frequency, ω is generated and the natural frequency is equal to the applied frequency when $\phi(\omega) = \pi/2$, as seen from Equation **??**. Once the natural frequency is known, the spring constant can be determined since $\kappa = m\omega_n^2$. The radius of the cloud is found by imaging it with a CCD camera.

In the setup described here, the current to just one of the electric coils is modulated so that the minimum of the magnetic field oscillates over a small, 1-dimensional spatial range, which is less than the radius of the atom cloud. The decision to modulate the current to a trapping coil rather than the smaller compensation coils was a technical one, based on the quality of the power supplies in use. Unlike conventional fluorescence detection schemes [**?**], an optical nanofibre is utilised instead of a photodiode (PD). The optical nanofibre passes vertically through the central region of the stationary trap and is connected to an SPCM. For comparison, we also make a single temperature measurement using the photodiode detection system similar to that described in [**?**].

We assume that the atom cloud has a Gaussian density profile and the number of photons coupled into the nanofibre is proportional to the atom density at any point in the cloud, as previously shown in [**?**]. The atom cloud and nanofibre are overlapped, with the nanofibre slightly off-centre within the cloud, as shown in Figure **??**(a). During the forced oscillation of the atom cloud the nanofibre re-

mains stationary. As the current in the coils reaches its maximum and minimum values, I_{max} and I_{min}, the displacement of the atom cloud is largest after a particular length of time which depends on the frequency of the current modulation. These points of maximum displacement are illustrated in Figure **??**(a), with the corresponding points detailed on the density profile of the atom cloud shown in Figure **??**(b). If we assume that the oscillations of the cloud are small, the change in the density profile of the cloud can be assumed to be linear over this variation in position and a similar variation will occur in the number of photons coupled into the nanofibre. Hence, sinusoidal oscillations of the atom cloud across the nanofibre will lead to a sinusoidal variation in photon counts as detected with the SPCM. This is illustrated in Figure **??**(c).

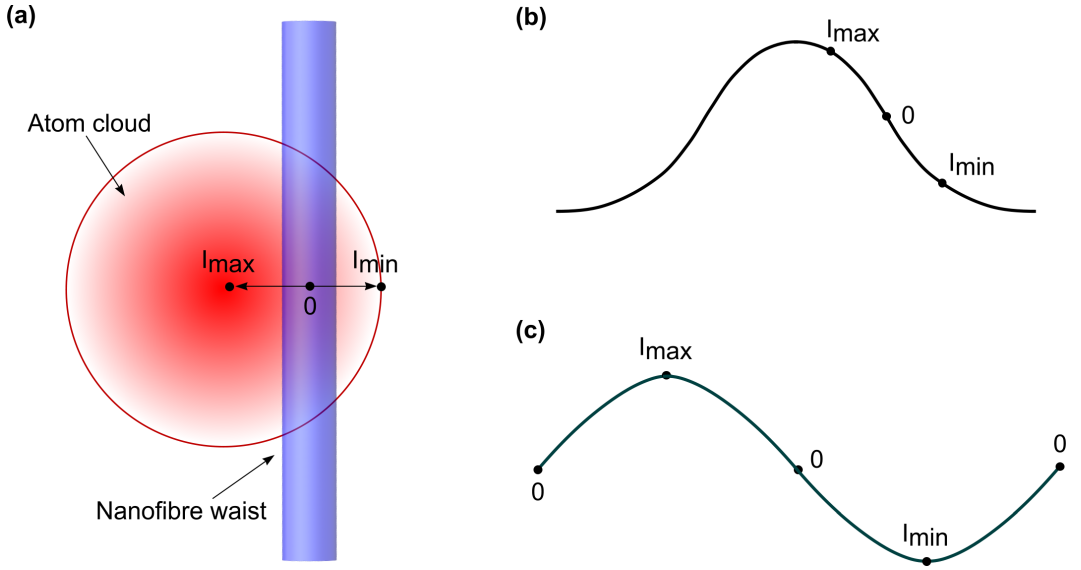

Figure 5.12: *(a) Nanofibre positioned off-centre within the atom cloud, (b) Gaussian density profile of the atom cloud, (c) Qualitative sketch of the nanofibre output for a sinusoidal oscillation of the atom cloud across the fibre.*

A schematic diagram of the setup used for the forced oscillation temperature measurement is shown in Figure **??**. To determine the radius of the atom cloud, it is magnified and imaged on a CCD camera, which was calibrated using objects of known dimensions. The output of the CCD camera is sent to a TV monitor for real-time viewing and a video card for recording and imaging.

To take a single phase measurement, function generator 1 is set to a fixed oscillation frequency, ω, causing the atom cloud to oscillate. At the same time, the function generator outputs a TTL signal that is in phase with the oscillating output, as shown in Figure **??**. The TTL signal is split between a transistor switch and a data acquisition (DAQ) card. Initially, the transistor switch is closed and

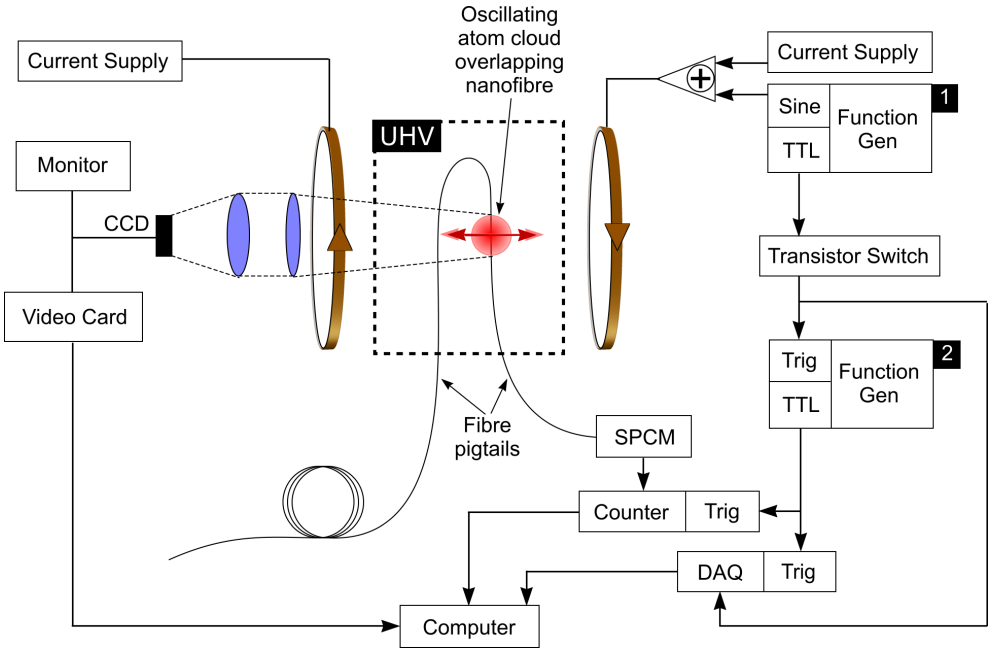

Figure 5.13: *Schematic diagram of the experimental setup for carrying out temperature measurements using the forced oscillation technique. Only the nanofibre detection scheme is shown. SPCM: single photon counting module; DAQ: data acquisition card; UHV: ultra high vacuum; CCD: charge coupled device camera.*

does not allow the TTL signal to pass. When the switch is opened the TTL signal triggers function generator 2, which outputs a burst of 1000 TTL pulses of variable width depending on ω. This TTL signal is then used to trigger the counter of the SPCM and the DAQ card so that both measurements are synchronised. The DAQ card measures the applied modulation signal (reference) and the SPCM counter measures the modulated photon count rate (signal) through the nanofibre.This timing sequence is illustrated in Figure **??**. The phase between the reference and signal yields the natural frequency from Equation **??**.

Initially, a reference result was taken for the temperature of the cold atom cloud using the photodiode setup as mentioned. Figure **??** is a plot of phase versus applied oscillation frequency as measured directly using a spectrum analyzer. When the phase is 90°, the natural frequency is equal to the applied frequency (see Equation **??**) of 25.2 Hz. This is determined by fitting a non-linear curve to the data points (red curve in Figure **??**). The $1/e^2$ radius was measured to be 1.01 mm and, using Equation **??**, an ensemble temperature of 260 μK was determined. The largest source of error in the temperature for both the PD and nanofibre techniques originates from measuring the radius of the atom cloud. Using a Gaussian fit to the cloud profile, the maximum error on the radius, Δr_x, is 0.5 pixels, equivalent to 0.023 mm in real space. Therefore, to determine the

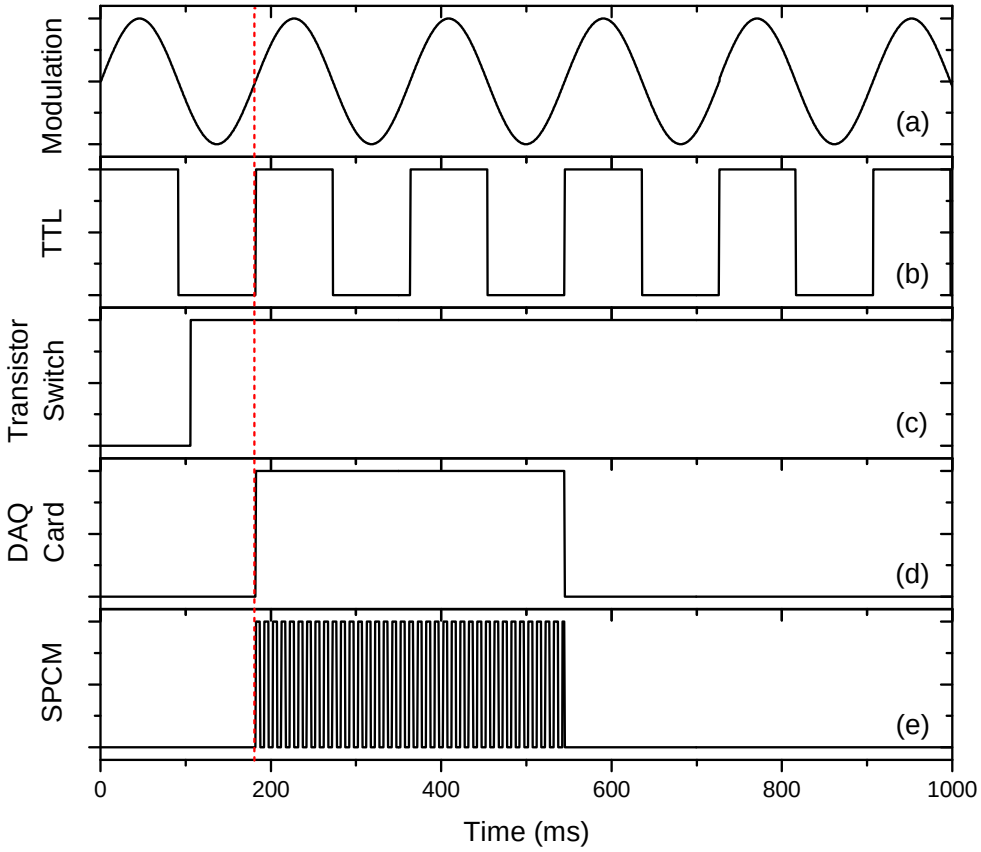

Figure 5.14: *Timing diagram for the experiment.*

error for each temperature value, the following empirical formula was used:

$$\text{Error} = \left(2\frac{\Delta\omega_n}{\omega_n} + 2\frac{\Delta\langle r_x \rangle}{\langle r_x \rangle} \right) T \tag{5.13}$$

A sinusoidal fit was applied to each set of data in order to find the natural frequency. Figures **??**(a) and **??**(b) show two examples of the photon count rates obtained at one end of the fibre for two different applied modulation frequencies of 10 Hz and 50 Hz, respectively. This data was then compared to the actual modulation data as measured using the DAQ card in order to determine the phase between the two signals.

For increasing oscillation frequency, an increase in the phase is observed as shown in Figures **??** and **??**. In Figure **??**, the normalized raw data from the SPCM is plotted against the phase angle for two complete oscillations of the cold atom cloud. For each increment in the oscillation frequency the phase increases further away from the input modulation. In Figure **??**, the phase shift is plotted against the modulation frequency. Each point on this plot represents an averaged value of

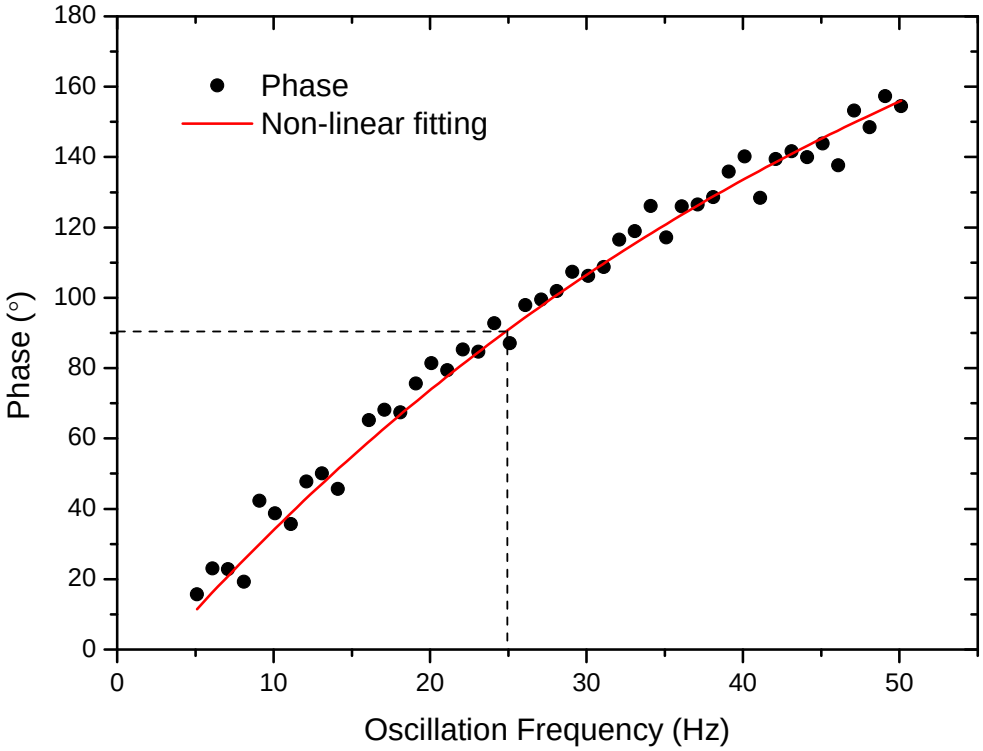

Figure 5.15: *Plot of phase against oscillation frequency using a photodiode and spectrum analyzer. This provides a reference value for the cold atom temperature as measured with a nanofibre.*

phase, calculated from a number of readings for each oscillation frequency. The experiment was repeated for frequencies ranging from 5 to 50 Hz and varying cloud radius and these results are presented in Table **??**. The natural frequency was determined by averaging over a large number of readings for each oscillation frequency and error approximation based on the standard deviation yields an uncertainty of 2.5% for ω_n. This corresponds to a maximum uncertainty of 1° on the phase, $\phi(\omega)$.

Table 5.2: *Estimated temperature values obtained for an atom cloud of varying radius and modulation frequency for a fixed laser detuning of -12 MHz.*

Detection Method	Frequency (Hz)	Spring constant (10^{-21} kg/s^2)	Radius (mm)	Temperature (μK)
PD (reference)	25.2	3.56	1.01	260 ± 33
Nanofibre	25.2	3.56	1.15	338 ± 40
Nanofibre	26.8	4.02	1.29	482 ± 53
Nanofibre	28.2	4.45	0.64	130 ± 19

By increasing the red-detuning of the cooling laser from the cooling transition, further cooling of the trapped atoms in the MOT can be achieved [**?**]. To investigate if the forced oscillation setup using the nanofibre can detect such changes

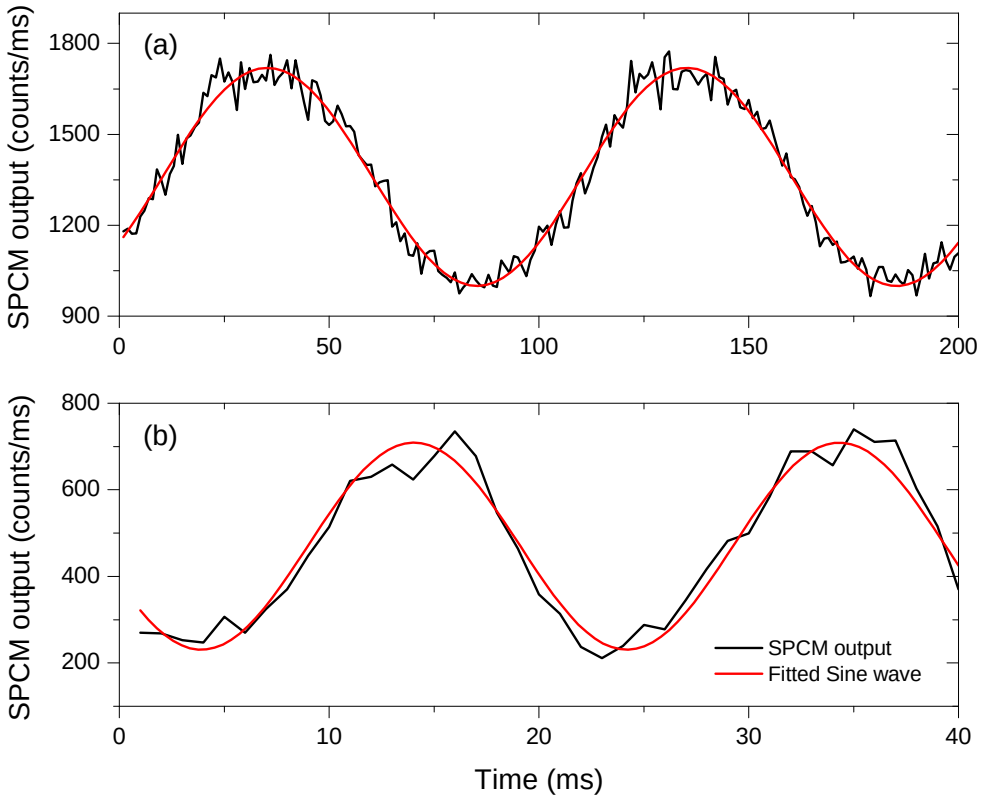

Figure 5.16: *Plot of SPCM counts and fitted sine wave against time, for an oscillation frequency of (a) 10 Hz and (b) 50 Hz.*

in the temperature of the atom cloud, temperature measurements were made for various red-detuning values of the cooling laser. Figure **??** is a plot of phase versus oscillation frequency for different red-detunings. The natural frequency can be obtained and, along with the radius of the atom cloud, the temperature can be determined. These results are presented in Table **??** and Figure **??**.

As there exists some ambiguity in the literature concerning the appropriate definition of radius for an atom cloud[6], we have analysed our system using, additionally, the $1/e$-radius and Gaussian full-width at half-maximum (FWHM). Figure **??** plots the temperature of the atom cloud as a function of detuning for the three standard radius definitions used.

The results presented in Table **??** and Figure **??** are in agreement with the expected trend, showing a decrease in the atom cloud temperature with increased red-detuning from the cooling transition, regardless of which cloud radius definition is used. This consideration of cloud radius is particularly relevant when discussing the effect which the hot surface of the nanofibre has on the surrounding cold atoms. Importantly, we have observed a sub-Doppler temperature at large

[6]See for example: [**?**] ($1/e^2$), [**?**] ($1/\sqrt{e}$), [**?**] (σ_{rms})

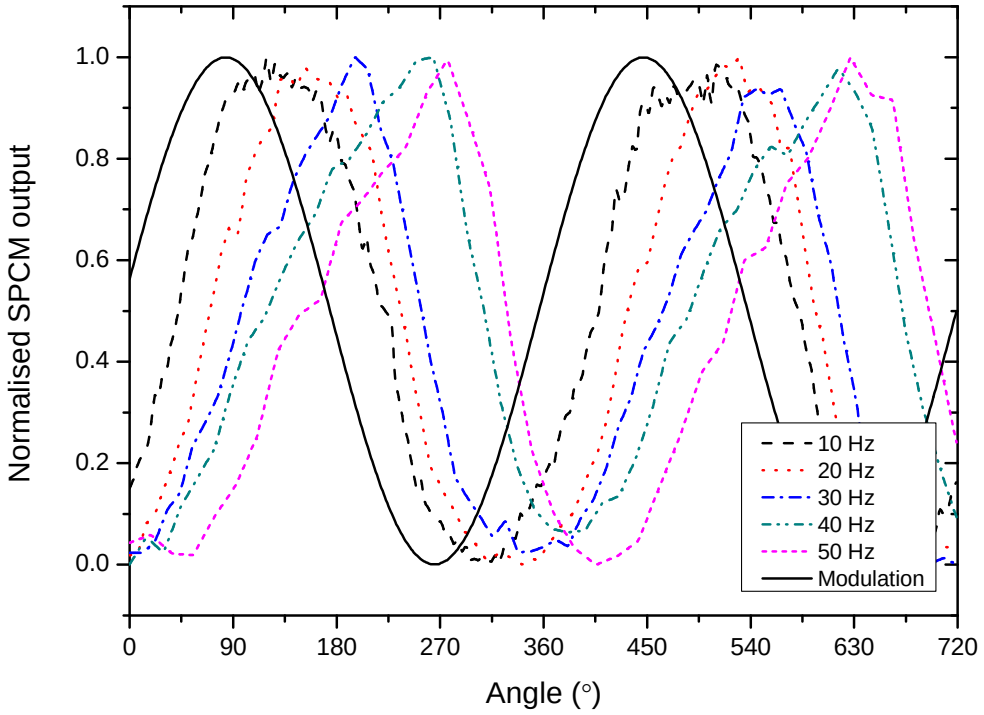

Figure 5.17: *Plot of normalized SPCM output against rotation angle for various oscillation frequencies, showing the changing phase shift due to the modulation as the frequency increases.*

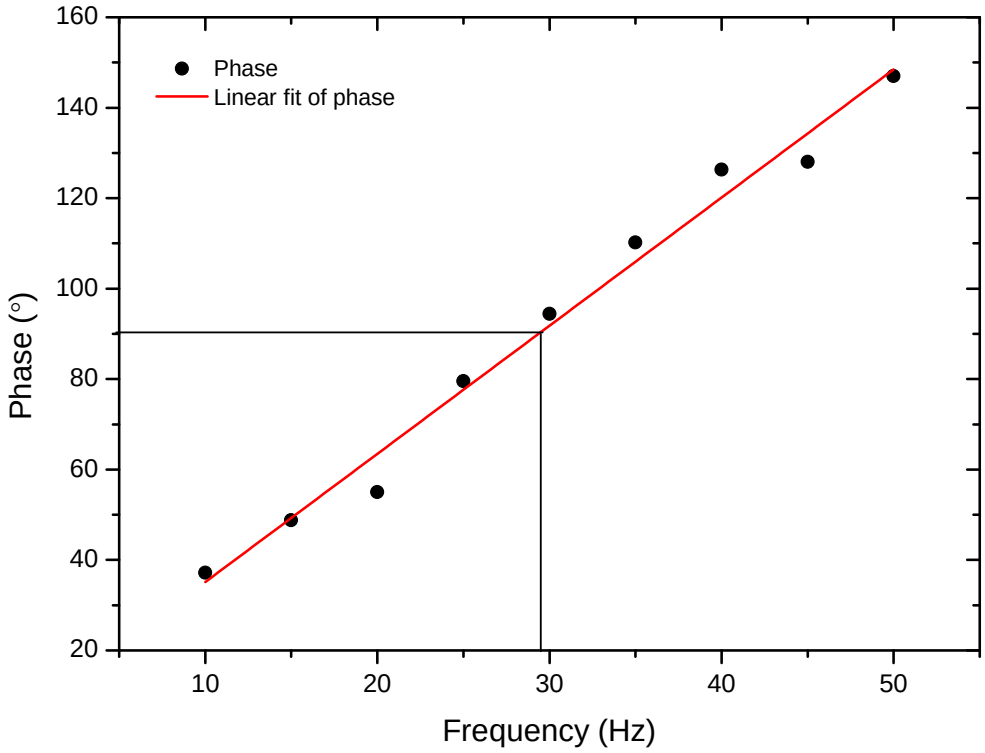

Figure 5.18: *Plot of phase against oscillation frequency as determined from data taken using the nanofibre.*

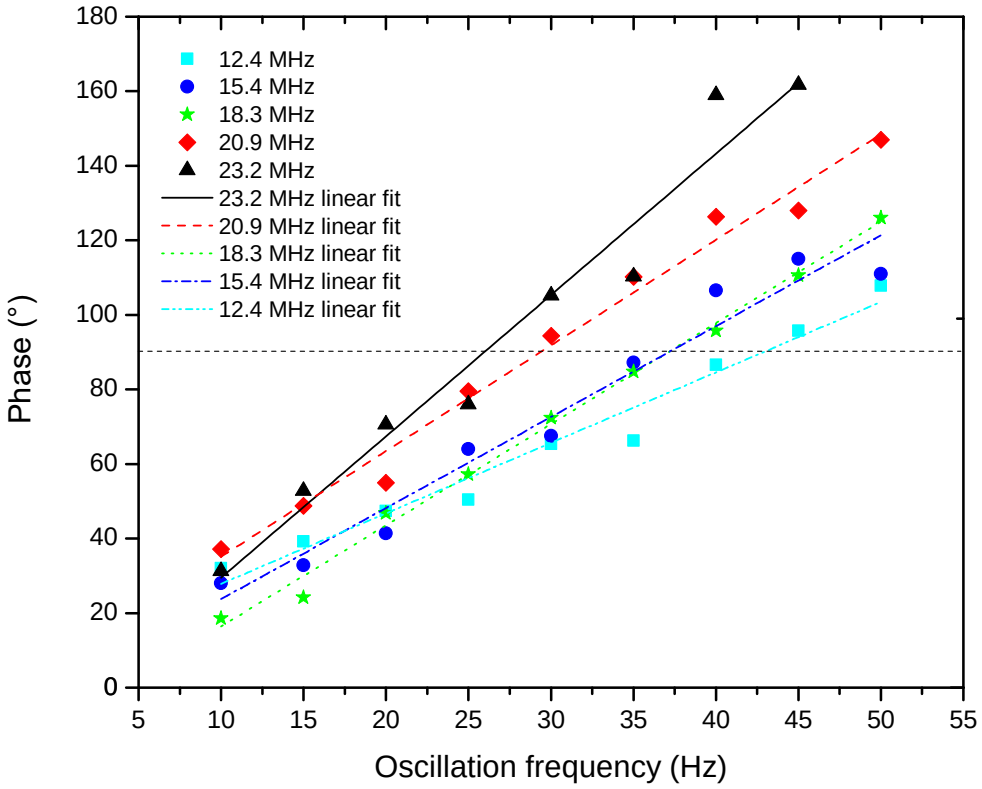

Figure 5.19: *Plot of phase against oscillation frequency for various red-detunings from the cooling transition of* ^{85}Rb.

Table 5.3: *Values of decreasing temperature for increasing red-detuning of the cooling laser based on the* $1/e^2$ *cloud radius.*

Detuning (MHz)	Frequency (Hz)	Spring constant (10^{-21} kg/s^2)	Radius (mm)	Temperature (μK)
12.4	43.1	10.4	1.14	973 ± 85
15.4	37.2	7.75	1.08	653 ± 63
18.3	37.2	7.75	0.82	374 ± 41
20.9	29.5	4.87	0.73	185 ± 24
23.4	26.0	3.79	0.57	89 ± 14

enough detuning, regardless of radius definition, thereby indicating that such low temperatures can be reached even with the hot fibre being present in the cloud. For the lower red-detuning values in Table **??** and Figure **??**, radiation pressure forces may inflate the temperatures achieved as higher atom numbers would have been present under these conditions. The system is optically thin (<0.3). It has been shown that one may see significant effects of radiation trapping when the resonant optical depth is of the order of 1 [**?**] or even a factor 10 lower [**?**]. Therefore, further analysis incorporating radiation trapping and heating effects will be the focus of future discussion.

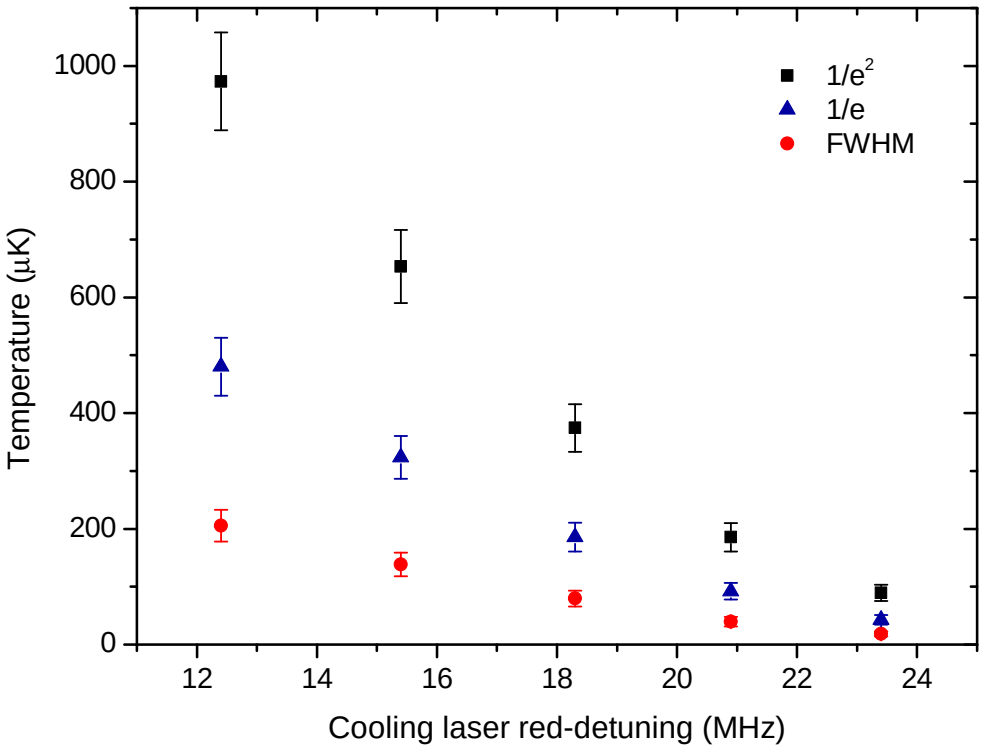

Figure 5.20: *Plot of atom cloud temperature against detuning for three different definitions of cloud radius.*

5.2.2 Release-recapture method[7]

If a spherical cloud of atoms, with a Gaussian velocity distribution, is allowed to expand homogeneously from an initial finite diameter, the fraction of atoms remaining after the release time, Δt_2, is given by

$$f_r = \frac{1}{\pi^{3/2}} \int_0^{v_c/v_T} e^{-u^2} u^2 du.4\pi, \tag{5.14}$$

where $u^2 du.4\pi$ is the spherical polar coordinate for velocity. The thermal velocity of the atoms in the MOT at a temperature T is $v_T = \sqrt{2k_B T/m}$ and $v_c = R_c/\Delta t_2$ is the velocity at which the atoms just reach a position R_c in the time interval Δt_2. The capture region is characterised by the radius of the MOT beams, R_c. Integrating Equation **??** yields:

$$f_r = -\frac{2e^{-\frac{v_c^2}{v_T^2}} v_c}{\sqrt{\pi} v_T} + \mathrm{Erf}\left[\frac{v_c}{v_T}\right]. \tag{5.15}$$

[7]This work can be found in [**?**]: Russell, L., Kumar, R., Tiwari, V. B. and Nic Chormaic, S. Measurements on release-recapture of cold Rb-85 atoms using an optical nanofibre in a magneto-optical trap, Optics Communications 309, 315-317 (2013).

Equation **??** describes f_r as a function of Δt_2. This equation is fitted to the experimental data by taking R_c is known and v_T is the fitting parameter.

For these experiments, the transmission of the ONF was ∼60% and the waist diameter was ∼ 1μm (as determined with SEM). The cooling laser beams were switched on and off with an AOM in order to achieve the desired loading, release and recapture sequence (see Figures **??** and **??**). A recapture time, Δt_3, of 50 ms was used to ensure that no background vapour atoms were recaptured by the MOT. The loading time of the MOT was typically ∼1 second. The magnetic field remained on at all times.

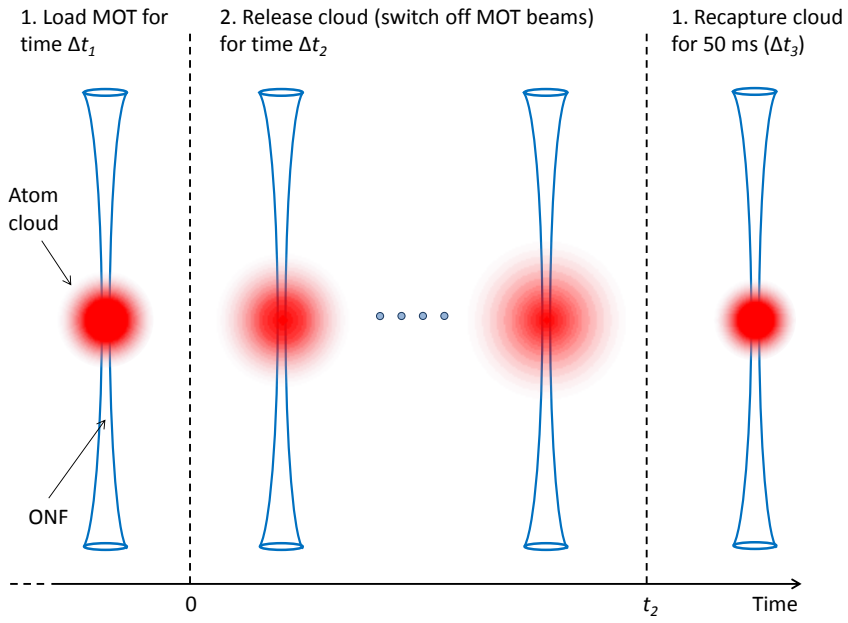

Figure 5.21: *Illustration of the release and recapture sequence as a function of time. The cloud is positioned centrally around the ONF. The cloud is loaded for a time* Δt_1 *and then released from the trap for a time* Δt_2*.* Δt_2 *is varied from sequence to sequence to build up a profile of the velocity of the atoms in the MOT. The recapture time,* Δt_3*, is set to 50 ms. The cloud is then released once more for 50 ms, before repeating the entire sequence.*

To perform a temperature measurement, the cloud of atoms was loaded for 10 seconds (Δt_1) to ensure a steady-state number of atoms was reached. Then, the cooling laser was switched off using the AOM for a time Δt_2 to allow the cloud to expand freely. Δt_2 is varied each time the sequence is repeated: Δt_2 = 5 ms, 10 ms, 20 ms, ... 150 ms. After the release time has passed, the cooling laser is switched on for Δt_3=50 ms to recapture the cloud. The cooling beams are switched off again with the AOM for 50 ms to provide a suitable contrast between the signal from the recaptured atoms and the background level. The

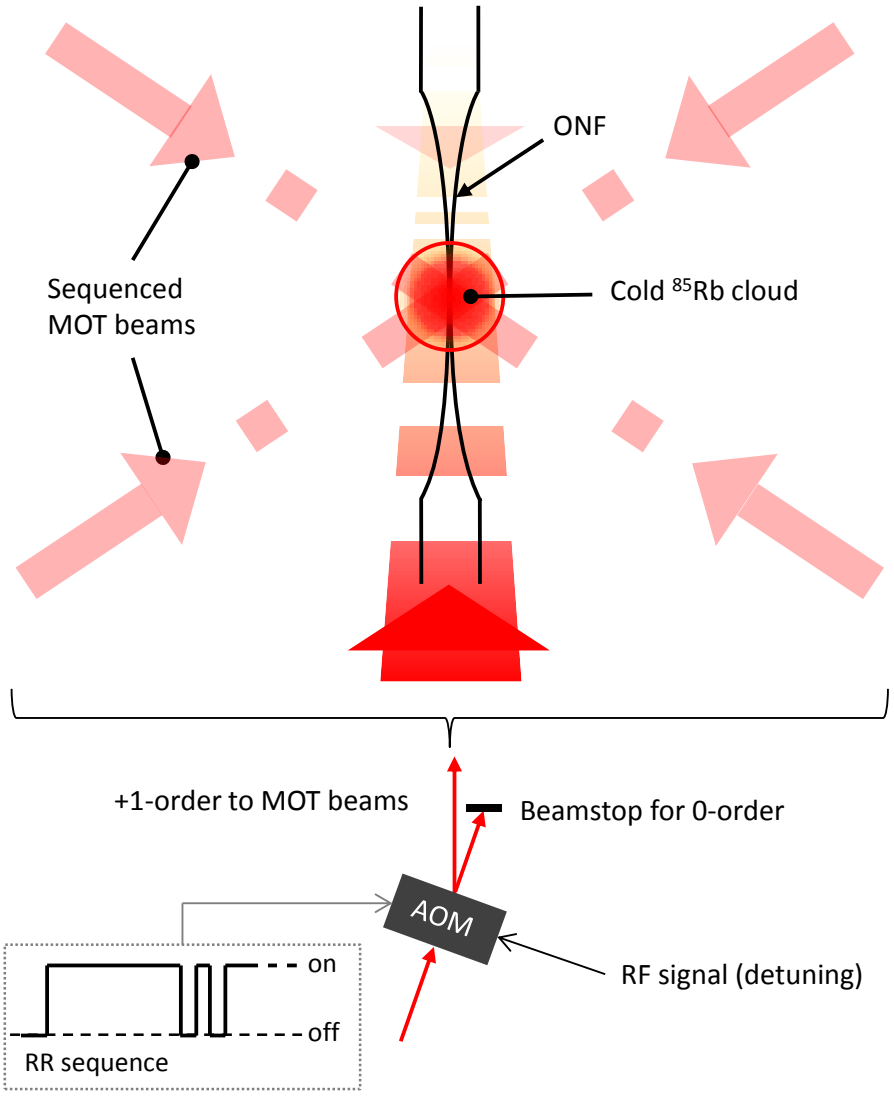

Figure 5.22: *Illustration of the experimental setup. The 1st-order beam from an AOM is expanded and split into three equal-intensity cooling beams for the MOT. The ^{85}Rb cloud is positioned centrally around the ONF. The cooling beams are switched on and off according to the sequence shown here with an AOM. Beam detuning is controlled via the tunable RF input on the AOM.*

sequence is recommenced for the next value of Δt_2. An image of the cloud is recorded using a CMOS camera and image analysis is performed to estimate the cloud radius.

Following this release and recapture process, fast atoms escape the MOT after a short release time and slower atoms are lost only after longer release times. To estimate the temperature of the atoms, the fraction of remaining atoms is calculated as a function of Δt_2. This is proportional to the fluorescence coupled into the nanofibre. This method is sensitive to the velocity distribution of the

cloud.

Temperatures approaching the Doppler limit have been observed at moderate detunings when the alignment of MOT beams has been particularly good. For example, for a detuning of -2.6Γ (where $\Gamma = 2\pi \times 5.9$ MHz is the natural linewidth of the $5^2S_{1/2} \rightarrow 5^2P_{3/2}$ transition in ^{85}Rb) with a cooling laser intensity per beam, I_{beam}, of $2.9I_s$ (where I_s=1.6 mW/cm^2 for $\sigma^{\pm}$-polarised light on the ^{85}Rb cooling transition), T is estimated to be 167 μK (Figure **??**). Poor MOT beam alignment would mean that atoms may leave the capture region in a non-isotropic way, the signature of which is an immediate and sharp decrease in recaptured atoms. The importance of precise optical alignment and power equalisation in the MOT beams is well known [**?**, **?**]. For example, [**?**] reports a temperature and associated variation of (147±25) μK depending on the alignment of the laser beams. By using the ONF as the detection tool, the effect of beam misalignment and power mismatching is detectable with a greater sensitivity than with fluorescence imaging techniques.

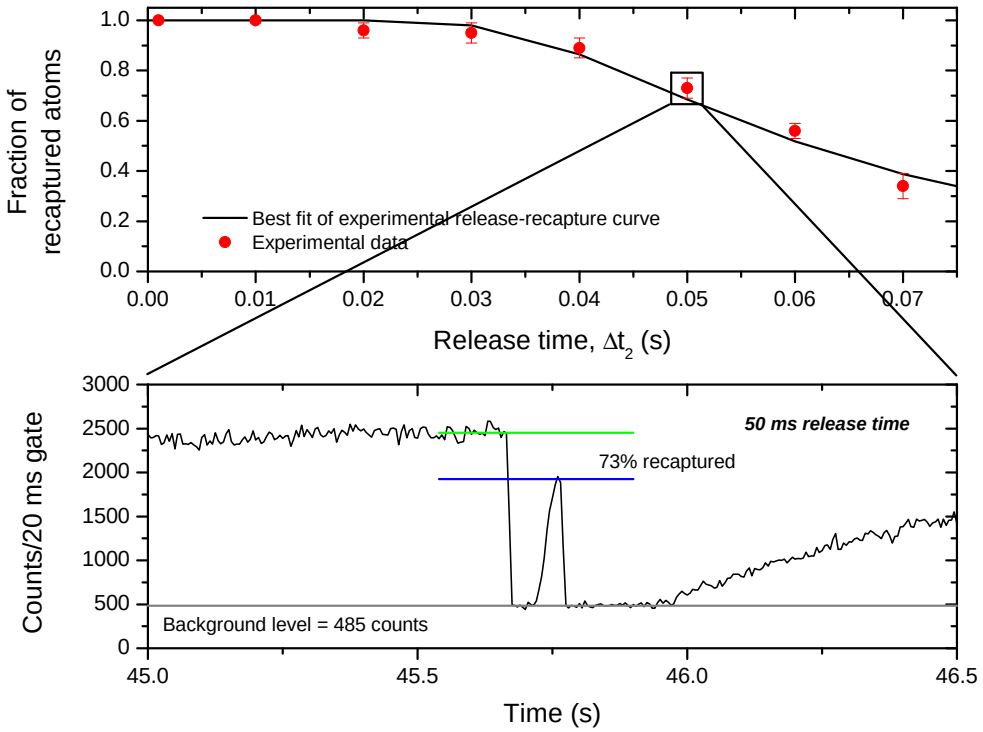

Figure 5.23: *Fraction of recaptured atoms estimated from the fluorescence data obtained from an optical nanofibre placed near the cold cloud of atoms. For a release time, Δt_2, of 50 ms, 73% of the expanded cloud was recaptured with δ=2.6Γ and cooling laser intensity of $2.9I_s$ (4.6 mW/cm^2) per beam.*

The temperature of the cold atoms as a function of I_{beam} was investigated (see Figure **??**) and measurements show that a span of a few hundred μK can be

observed when varying I_{beam} from 2.5 mW/cm^2 to 6.7 mW/cm^2 at a constant cooling laser red-detuning of $\sim 2\Gamma$. As expected, the temperature reduces as laser intensity is reduced [**?**].

Traditionally, R_c is the quantity with the greatest uncertainty. A small change in R_c ($\sim$ 2.5 mm) when fitting Equation **??** to the data results in a temperature shift of the order of the error bars seen in Figures **??**–**??**.

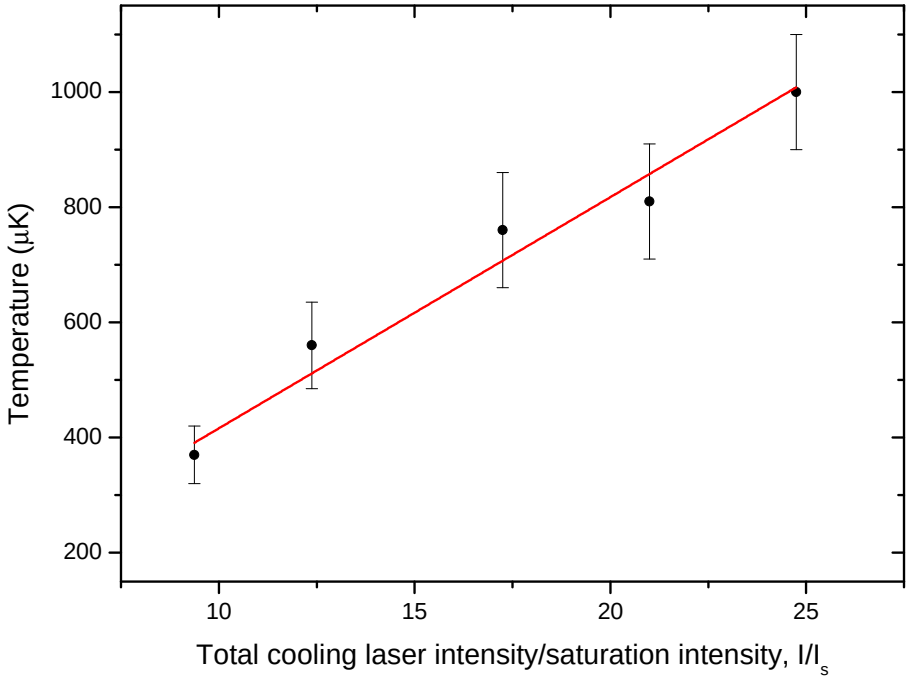

Figure 5.24: *Temperature as a function of cooling laser intensity normalised to the saturation intensity, I_s (δ=-2Γ). The solid red line is a linear fit to the experimental data.*

In order to compare the RR temperature measurements with another technique, we have taken data directly from previous work which used the method of forced oscillations to estimate cloud temperature (see [**?**] for full details). Table **??** presents a comparison of results for temperature as a function of cooling laser red-detuning. The results found using each technique correlate quite well. In particular, for higher detunings, the T values which have been estimated with each method agree more strongly. Lower values of red-detuning were not easily examined with the ONF used for RR as the sacrifice in N_A was sufficient to lower the fluorescence coupling signal siginificantly.

Figure **??** shows that temperatures obtained with RR increase linearly with the dimensionless light-shift parameter $\Omega^2/|\delta|\Gamma$ as expected [**?**]. The spring constant, κ, which describes the restoring force in the MOT and is particularly relevant in compressing atoms to high density, can be inferred from these temperature

Table 5.4: *Variation of temperature with cooling laser red detuning in units of the natural linewidth using two different measurement techniques. I_{beam} was approximately 2.2I_s for release-recapture and 1.3I_s for forced oscillation. Forced oscillation data are taken directly from [?].*

Method	Red Detuning Γ	Temperature mK
Release recapture	1.1	1.80±0.20
	2.0	0.56±0.13
	3.5	0.23±0.03
Forced oscillation	2.1	0.97±0.08
	2.6	0.65±0.06
	3.1	0.37±0.04
	3.5	0.18±0.02

values. To determine κ, it is assumed that, in thermal equilibrium, the atom cloud has a thermal energy given by $k_BT = \kappa\langle r^2\rangle = m\langle v^2\rangle$, where T is the experimentally-determined cold atomic cloud temperature, k_B is Boltzmann's constant, r is the radius of the atom cloud, and $\langle v^2\rangle$ is the mean square atomic velocity [?, ?]. For each red-detuning, the cloud radius is estimated using image analysis. Figure ?? shows that the spring constant increases with intensity at low intensity or detuning values and then levels off at some critical value of the light-shift parameter. Wallace *et al.* [?] report that the spring constant is not independent of I_{beam} until a moderately high value of the light-shift parameter is reached. It is interesting to observe that, as evident in Figure ??, κ levels off above light-shift parameter values of ≈1. As the most dense part of the cloud is being studied with the ONF, this may be an interesting observation compared to measurements done with photodiodes.

As the atom number is increased in the MOT, the regime of operation transitions from temperature-limited (TL) to multiple-scattering (MS) [?, ?, ?]. In the TL regime, the cold atoms are essentially non-interacting because N_A is small (typically less than 10^4) and the density is low. The cloud acts as an ideal gas in this regime, and, as more atoms are loaded into the trap, the size of the cloud remains the same while the density increases linearly and its distribution remains Gaussian [?]. For larger N_A ($\geq 10^5$) the cloud begins operating in the MS regime and the density becomes largely independent of N_A [?]. Two effects are seen in this regime. Firstly, repulsive forces caused by the re-absorption of scattered photons lead to an increase in the cloud size while the density remains constant. This radiation trapping effect determines the density and temperature of cold atoms [?, ?]. For example, at $N_A \sim 10^7$ the cloud density is maintained and the optical

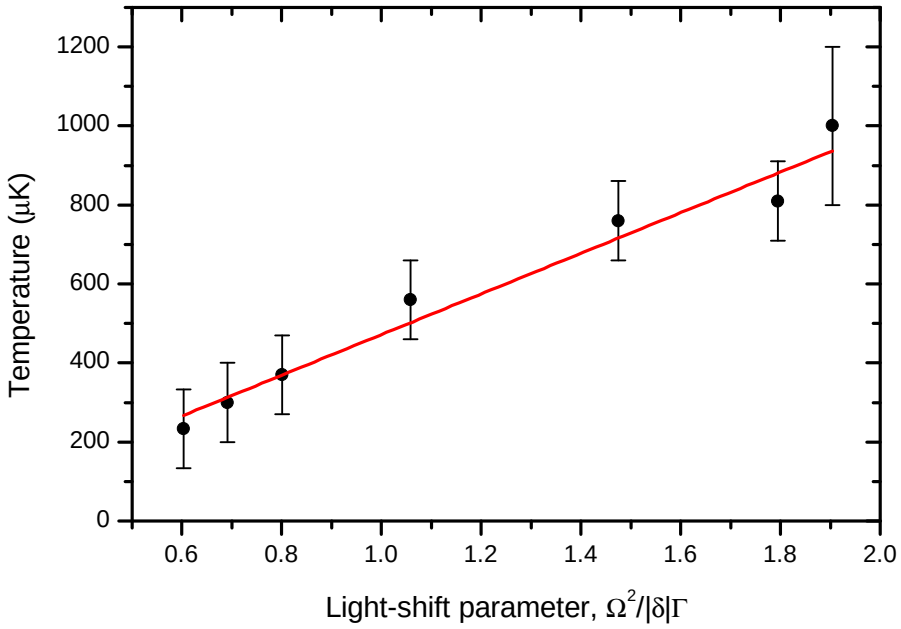

Figure 5.25: *Temperature of the cloud as measured with RR plotted against the dimensionless light-shift parameter* $\Omega^2/|\delta|\Gamma$ *(black circles) and a linear fit (red line) to the data.*

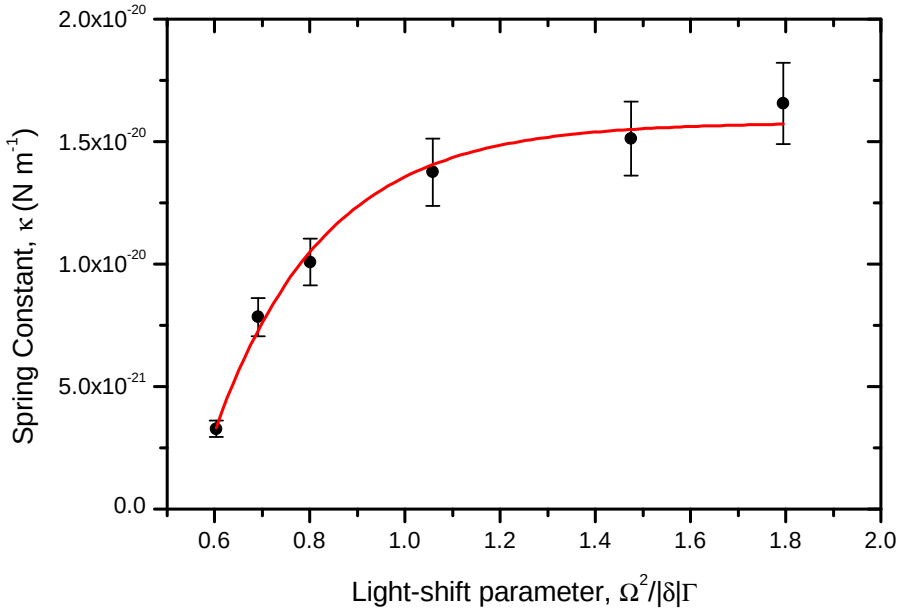

Figure 5.26: *Spring constant against dimensionless light-shift parameter* $\Omega^2/|\delta|\Gamma$ *(black circles) with a fit for a guide to the eye (red, solid line).*

thickness is such that, on average, each photon absorbed from the cooling laser beams will, after re-emission, scatter no more than once on its way out of the cloud. This determines the spatial growth of the cloud as N_A increases beyond 10^7 [**?**]. The second effect is due to an attenuation force which arises from the intensity gradients in the MOT beams and the absorption of such by the atoms

[?, ?]. This results in spatial compression of the cloud and a small reduction in spring constant of the trap [?]. When the MOT transitions from the TL to the MS regime, the atom distribution may or may not change from Gaussian to flat-topped. Thus, at higher cloud densities, cloud images may not be a direct indicator of density. Measurements using an ONF negate the use of imaging analysis to estimate cloud volume (for example, [?]) making it simpler to observe regime-change in the MOT via fluorescence coupling.

By considering an observation volume surrounding the ONF, the cloud density can be studied as the light-shift parameter is varied. It is assumed that atoms within a hollow observation cylinder with an outer radius equal to the ONF radius + 300 nm are most likely to emit fluorescence into the guided mode of the ONF [?, ?]. This number of effective atoms, n_{eff}, can be estimated at one end of the ONF using $n_{eff} = 2C_P/R_{sc}\eta_{ONF}Q\eta_{QD}$ where R_{sc} is the atomic scattering rate, η_{ONF} is the average coupling efficiency of photons into the guided ONF mode in one direction (estimated at 2% using previous work based on ^{133}Cs [?]), Q is the ONF transmission from the middle of the ONF waist to the detector (the transmission through the entire length of fibre is 60% so Q=77% for half the fibre length), and η_{QD} is the quantum efficiency of the SPCM (60%). The quantity C_P is the fluorescent count rate obtained by the SPCM and is obtained from the RR raw data. The scattering rate, R_{sc} is described by [?]

$$R_{sc} = \frac{\Gamma}{2}\frac{C_1^2\Omega_{tot}^2/2}{\delta^2 + \Gamma^2/4 + C_2^2\Omega_{tot}^2/2}. \tag{5.16}$$

Here, Ω_{tot} is the Rabi frequency for all MOT beams and is found from six times that of any one of the trapping beams. C_1 and C_2 are average Clebsch-Gordan coefficients for the transition between the initial (subscript "1") and final (subscript "2") state. Here, the values of C_1^2 and C_2^2 are assumed to be equal due to optical pumping among the Zeeman sub-levels in the presence of strong coupling between atoms and the radiation field as discussed in [?].

If n_{eff} is plotted as a function of light-shift parameter, saturation of the atom number commences from $\Omega^2/|\delta|\Gamma \sim 1.2$ onwards (see Figure ??). As the observation volume is fixed by the ONF radius, this saturation effect is due to the spatial expansion of the cloud while it maintains constant density and may also indicate the onset of the MS regime in the MOT.

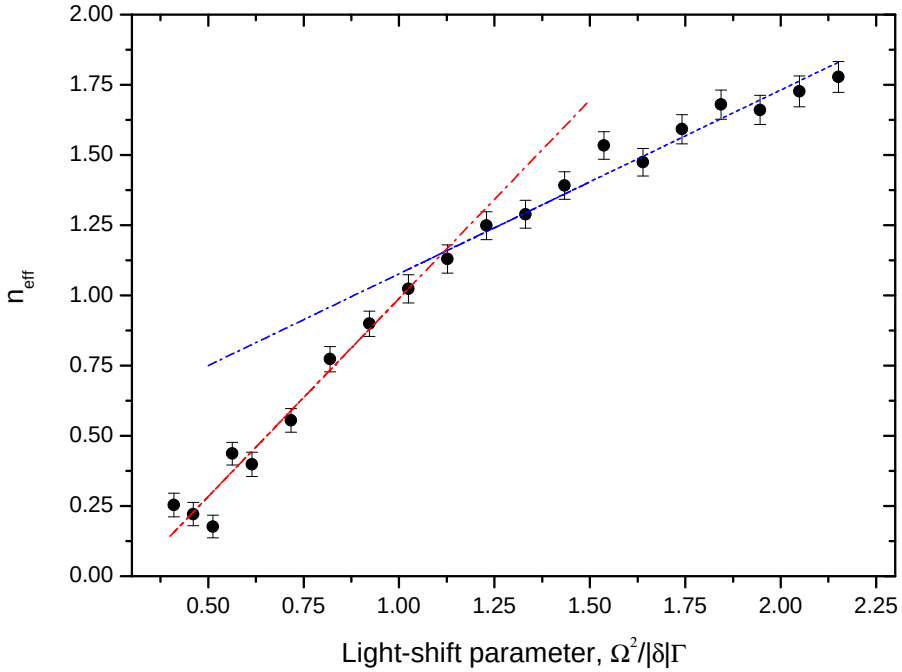

Figure 5.27: *Estimation of effective atom-number, n_{eff}, with increasing dimensionless light-shift parameter $\Omega^2/|\delta|\Gamma$ (black circles) with two linear fits to indicate the change in slope around a light-shift parameter 1.2.*

5.3 Conclusion

This chapter has summarised the fluorescence-based experiments performed with the atom cloud + ONF system. Alignment of the cloud around the ONF is easily achieved with a system of orthogonal CCD cameras and an SPCM. Very high signal to noise ratios can be achieved with good alignment making the system extremely sensitive to even low N_A small fluctuations in laser powers or other MOT parameters. The quantity n_{eff} gives an estimation of how many atoms are coupling fluorescence into the guided mode of the ONF. This number is affected strongly by the ONF radius, a – to maximise n_{eff}, a must satisfy $k_0 a = 1.45$. Additionally, by increasing the cloud density, dramatic increases in n_{eff} can be seen.

Two techniques for measuring the temperature of a cloud of cold ^{85}Rb atoms in a MOT with the ONF-coupled fluorescence are experimentally demonstrated. The first method used is that of forced oscillations, which takes advantage of the mechanical properties of the MOT. The fluorescence photons from the trapped atoms were detected using an optical nanofibre, which was placed within the atomic sample. Good agreement was found between temperature measurements made using the optical nanofibre and the conventional fluorescence imaging method with a

photodiode and, in each case, the forced oscillation technique was used. As expected, a decrease in atom temperature was observed for increased red-detuning of the cooling laser beams regardless of the definition of cloud radius used. The nanofibre-based temperature measurements yield marginally higher results than the corresponding fluorescence imaging method and this may be attributed to the effect which the relatively hot surface of the nanofibre has on nearby laser-cooled atoms.

Prior to this, two other significant non-destructive temperature measurement techniques have been reported [**?**, **?**], both of which are performed in-situ. In [**?**], atom numbers ranged from 10^5 to 10^7 and, for lower numbers, intensity correlation signals become quite small. In the course of the work reported here, it was found that, for lower atom numbers, it was more difficult, albeit not impossible, to achieve fluorescence coupling. Further studies will investigate the lower limit on the atom number within the system that still attains efficient fluorescence coupling into the nanofibre.

It is worth reiterating that sub-Doppler temperatures were observed for large red-detunings from the rubidium cooling transition. On this basis, it would be worthwhile investigating the influence of the optical nanofibre on the formation of even colder atomic systems, e.g. Bose-Einstein condensates, and such a study is crucial for determining the functionality of optical nanofibres in hybrid quantum systems for quantum communication schemes [**?**].

The temperature of a cold ensemble of ^{85}Rb atoms was estimated using the release-recapture method with a nanofibre. The RR sequence was applied to an AOM which allowed rapid switch of the MOT beams. This results coincide with those found by other methods and again reinforce the viability of placing the ONF in yet colder atomic samples. Furthermore, this work has highlighted the sensitivity of the cloud temperature to small changes in beam misalignment, detunings and intensities and demonstrated the ability to detect these temperature changes with the ONF. It should now be possible to conduct a systematic temperature measurement while exploring the entire parameter space using a sensitive detector which can be positioned anywhere in the cloud.

Free-space RR measurements show that, with the same variation in laser cooling intensity as used here, a few hundred μK span can be observed. The results presented here display this trend and, additionally, provide detailed information about the velocity distribution of the atom cloud. In particular, with the release-recapture method it is necessary to be sensitive to the initial velocities of nearby

(near-surface) atoms and through data analysis create a decay curve which shows how fast nearby atoms leave the capture region and cease to fluoresce into the ONF's guided mode.

Chapter 6

Experiments with a dark magneto-optical trap[1]

The density of atoms n in a magneto-optical trap is limited to approximately $\sim 10^{11}$ atoms/cm^3 for two reasons. Firstly, a transfer of kinetic energy occurs when a ground-state (F) atom collides with an excited state atom (F'). This leads to a trap loss rate of βn per atom where $\beta \approx (1-5) \times 10^{11}$ cm^3/s. The second limitation is due to laser-cooled atoms in the MOT reabsorbing scattered photons, a phenomenon known as *radiation pressure*. The outward radiation pressure of the fluorescent light balances the confining forces of the trapping laser beams at a particular density and, at this point, if the number of atoms is increased, the atom cloud will grow in spatial extent rather than density. For the ONF, this is a major consideration. If we wish to do an absorption-based experiment, as many atoms as possible are required to fill the evanescent region around the ONF to improve signal quality dramatically.

Work published in 1993 by Ketterle *et al.* [**?**] demonstrated a new style of magneto-optical trap which confined sodium atoms in a dark ground hyperfine level, unperturbed by the cooling beams and thus free from the density limitations of a standard *bright* MOT. By reducing the intensity of the repumping light for sodium, the dark spontaneous-force optical trap transferred almost all the atoms from the upper (bright) hyperfine level to the lower (dark) hyperfine level. As the atoms are no longer cycled by the cooling laser to an excited hyperfine state, there is no fluorescence from the atoms which leads to the terminology of "dark MOT". Although a small excitation rate is optimal for confining large numbers

[1]This work is in preparation for publication in Measurement Science and Technology under the title "Investigation of a ^{85}Rb-dark magneto-optical trap using an optical nanofibre"

of atoms at high density, the maximum possible excitation rate is required to efficiently capture atoms from a thermal vapour and load them into a MOT. By using a bright trapping region and dark trapping region in the MOT beams, both of these requirements can be fulfilled. A doughnut-shaped repumping beam can be used to create a bright outer MOT and a dark inner MOT. An atom which encounters the region with negligible repump intensity will spend a very short time in the cooling cycle before being shelved into the dark hyperfine level, i.e. $F = 2$ for ^{85}Rb (see Figure **??** for the energy level diagram of ^{85}Rb).

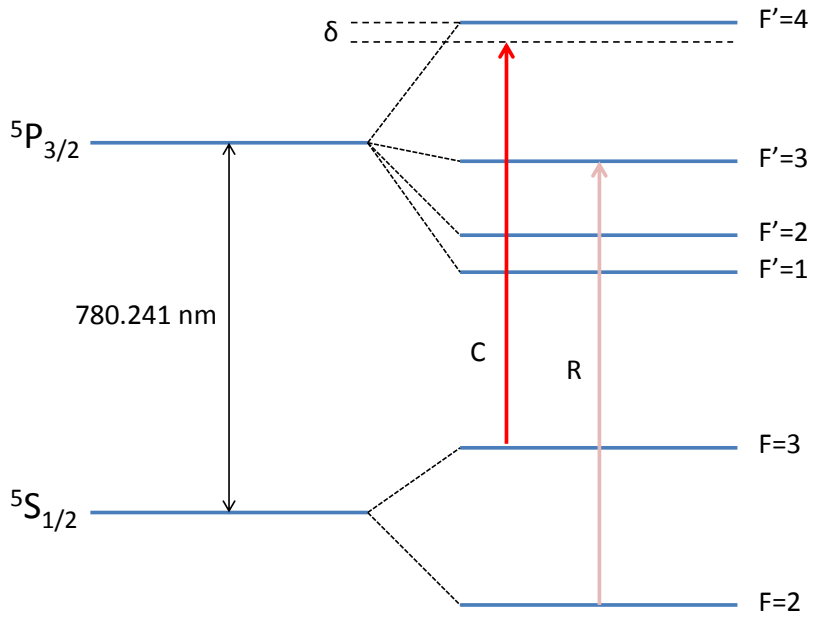

Figure 6.1: *The basic DMOT energy level scheme for ^{85}Rb. The intensity of the repump beam (R) is reduced to allow atoms to accumulate in $F = 2$. The cooling beam (C) is tuned, as normal, near the transition $F = 3 \rightarrow F' = 4$.*

The bright (BMOT) and dark MOT (DMOT) can also be separated temporally by using triggered mechanical shutters and AOMs. The spatial dark MOT is experimentally more advantageous as the dark atoms can be continuously loaded into the dark trap from the outer bright trap. In the bright region of the MOT things work as normal. In fact, although the inner dark region is not really a *trap* anymore, the outer bright region still captures background atoms and feeds the dark section. In other words, experimental parameters for the atoms at the trap centre can be monitored and adjusted while simultaneously maintaining the high loading rate of the MOT. This is possible because the trapped atom cloud is localized near the minimum of the magnetic field whereas the capture of atoms occurs throughout the whole intersection volume of the cooling beams. This arrangement is very appealing for ONF-based work. For example, the possibility

of continuous (i.e. non-sequenced) absorption measurements via an ONF probe would be available. Permyakova *et al.* [**?**] report that even with moderate beam powers (of the order of 6 mW) the dark MOT can capture large numbers of atoms and generate optical densities as high as 9. Thus, by using low cooling laser intensities (for confining large numbers of atoms at high density) in a DMOT scheme, high signal-to-noise ratios for the fluorescence coupling can be achieved as well as the freedom to use minimal input absorption beam powers. This leads to the demonstration of non-linear effects in the cloud with very little laser power expenditure.

Townsend *et al.* [**?**] published work in the mid 1990's which demonstrated atom densities of nearly 10^{12} cm^{-3} in a dark MOT for caesium. Prior to this work, no report of similar density enhancements in MOTs for elements other than sodium had been reported. The larger hyperfine splittings found in the ground states of heavier alkali-metal atoms (such as caesium and rubidium) means that the dark MOT technique is not as straightforward as it is for sodium which has much smaller hyperfine level splittings. A rubidium atom will undergo many cooling cycles ($F = 3 \rightarrow F' = 4$) before falling to the dark ground state ($F = 2$) due to spontaneous Raman processes. This cycling time can be shortened by using additional 'depumping' light, tuned to the $F = 3 \rightarrow F' = 3$ transition. The depumping light is used to take advantage of the hyperfine structure splitting between the two upper excited states (i.e. $F' = 3$ and $F' = 4$ are split by 120 MHz) and the lower ground state splitting (i.e. $F = 2$ and $F = 3$ are split by $\approx$ 3 GHz). On the other hand, the probability for an Na atom to scatter from the cooling cycle into the dark ground state unaided by depumping light is higher than that for Rb to scatter from its cooling cycle to $F = 2$. Thus, this transition must be forced with a depumper tuned to $F = 3 \rightarrow F' = 3$. This increases the probability of the bright $F = 3$ atoms to scatter to $F = 2$ due to selection rules. The experimental setup described in [**?**] employed two hollow repumping beams and a depumping beam to put the caesium atoms into the lower ground state. The experimental setup used in the Quantum Optics Laboratory will be described in the next section.

In this chapter, the work described was performed to see if improvements in density could be made for the MOT. Although it turns out that no density increase was observed, characterisation experiments were perfomed to see if there were effects in the DMOT from the ONF. In this work, only the spatial dark MOT is considered.

6.1 Experimental setup

The repump beam is initially expanded in a telescope setup to a diameter of 25 mm (see Figure **??**). A separate unity magnification telescope is used to place a shadow in the beam and project it on to the cold cloud. This setup is shown in Figure **??**; a glass slide with an opaque circle is placed near the focal point of the telescope and aligned to create a hollow repump beam at the MOT. The circle has a transmission of 10^{-4} as determined experimentally. If the circle were placed in the beam without being incorporated in a telescope system, Fresnel diffraction effects would occur at the trap centre. This would diminish the ability of the perturbed dark region to collect atoms in the $F = 2$ state.

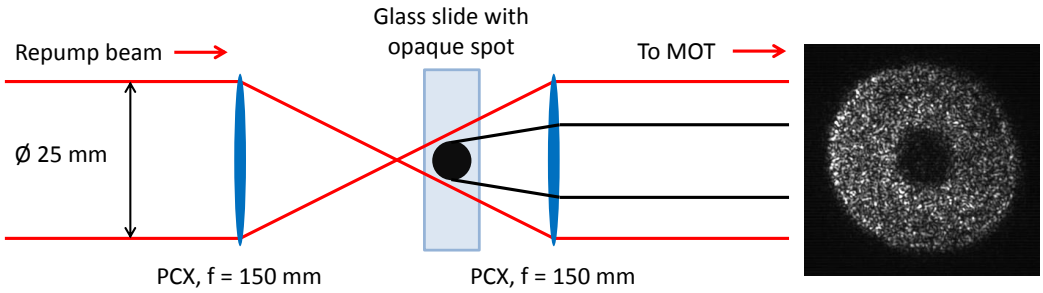

Figure 6.2: *The hollow repump beam is created using a unity magnifier with an opaque circle positioned near the centre of the two lenses. This imaging setup reduces Fresnel diffraction in the beam at the position of the MOT.*

For the rubidium atom, simply having a hollow repump beam is not enough to generate a large dark state fraction [**?**]. In sodium, the splitting between the ground state levels is small enough to ensure that off-resonant scattering from the F' level to the lowest ground state occurs regularly over many cooling cycles. In ^{85}Rb, the splitting between the hyperfine levels of the ground state, $F = 2$ and $F = 3$, is approximately 3 GHz and so a region of negligible repump beam is simply not sufficient. In this setup, a depumping beam, tuned near $F = 3 \rightarrow F' = 3$, has been used to force many atoms into $F = 2$. In fact, the depumper can be used on its own (with a normal repump beam) to reach a moderate fraction of $F = 2$ atoms. The combination of the two allows one to reach very dark MOTs. The complete energy level scheme with the three laser frequencies is shown in Figure **??**.

Rather than directing the repump beam along a path which copropagates with a cooling beam (as described in previous chapters for different experimental work), a separate path is used. The reason for this is due to the retroreflecting mirrors in the cooling beam path. If the repump beam is aligned such that it passes

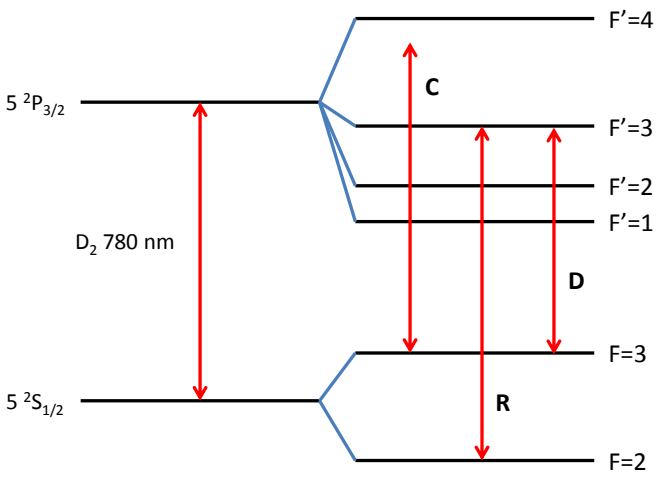

Figure 6.3: *Energy levels utilised in the dark MOT for* ^{85}*Rb. 'C' is the cooling laser, 'R' is the hollow repump beam and 'D' is the depumping light.*

centrally through the cloud, but reflects back off the retroreflecting mirror, in general, the back-reflected dark spot does not align with the forward propagating one. Thus, the dark MOT quality is greatly compromised.

To quantify how "dark" the trap is, Ketterle *et al.* [**?**] used the parameter p to denote the fraction of atoms in the bright state,

$$p = \frac{N_b}{N_b + N_d} \tag{6.1}$$

where N_b is the number of atoms in the bright state, $F = 3$, and N_d is the number of atoms in the dark state, $F = 2$. The fluorescence collected by the ONF is proportional to the numbers of atoms in whichever state is being probed so p is easily measurable from SPCM count rates. Additionally, p can be estimated from the magnitude of the absorption dips. This is demonstrated in the following section.

6.2 Free-space spectroscopy of the DMOT

A free-space probe beam is passed through the atom cloud to perform absorption spectroscopy. The probe beam is dervied from a third ECDL (Toptica DL100) operating in scanning mode and frequency tuned via its own saturated absorption

spectroscopy setup. The beam, after passing through the cloud, is directed (in freespace) to a Hamamatsu avalanche photodiode (model[2]: C5460-01). This is not as sensitive as the SPCM but does have some advantages. The APD outputs an analogue voltage signal proportional to the intensity of the light incident upon it rather than a series of TTL pulses requiring a counting unit. This output can be viewed and stored in the same manner as the photodiode signal for conventional imaging techniques. Here, the output signal is sent to a PC where it is monitored and recorded with a LabVIEW program (see Appendix B). This setup is illustrated in Figures **??** and **??**.

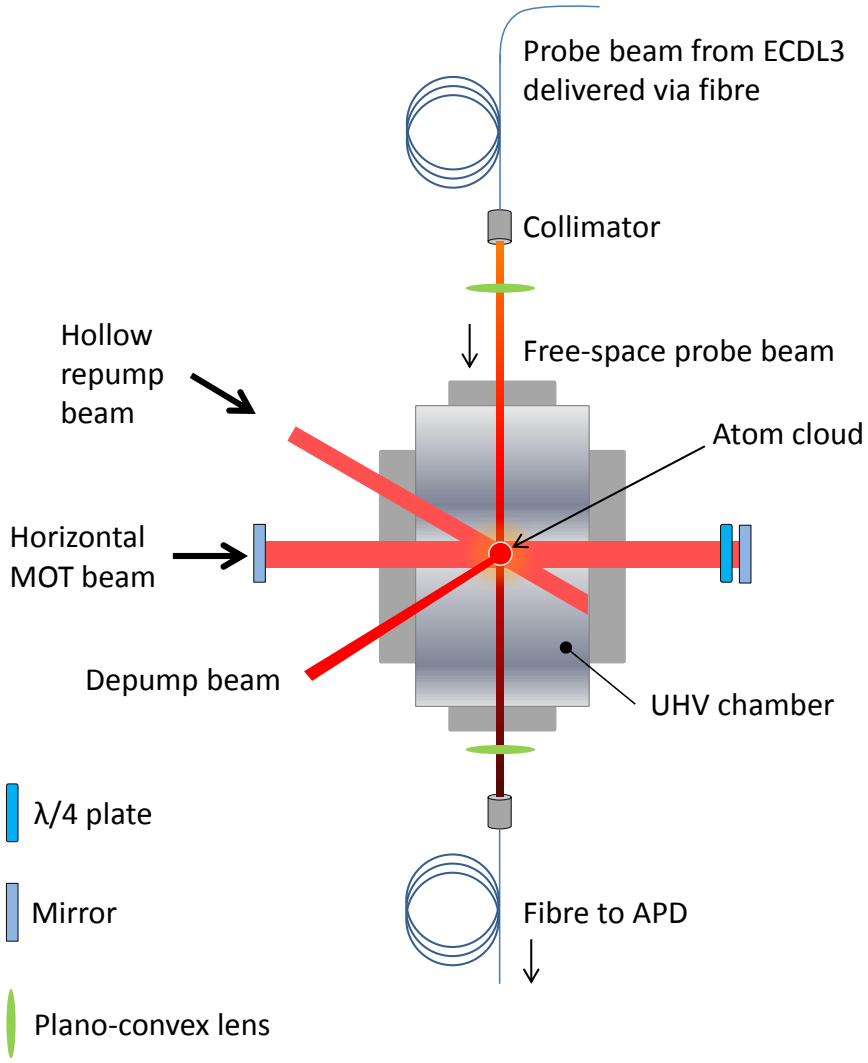

Figure 6.4: *Experimental setup for free-space spectroscopy on the DMOT.*

As noted in the previous section, placing a shadow directly into the repumping

[2]The C5460-01 APD has a photoelectric sensitivity of -1.5×10^8 V/W at λ=800 nm, and a noise equivalent power of 0.02 pW/Hz$^{1/2}$

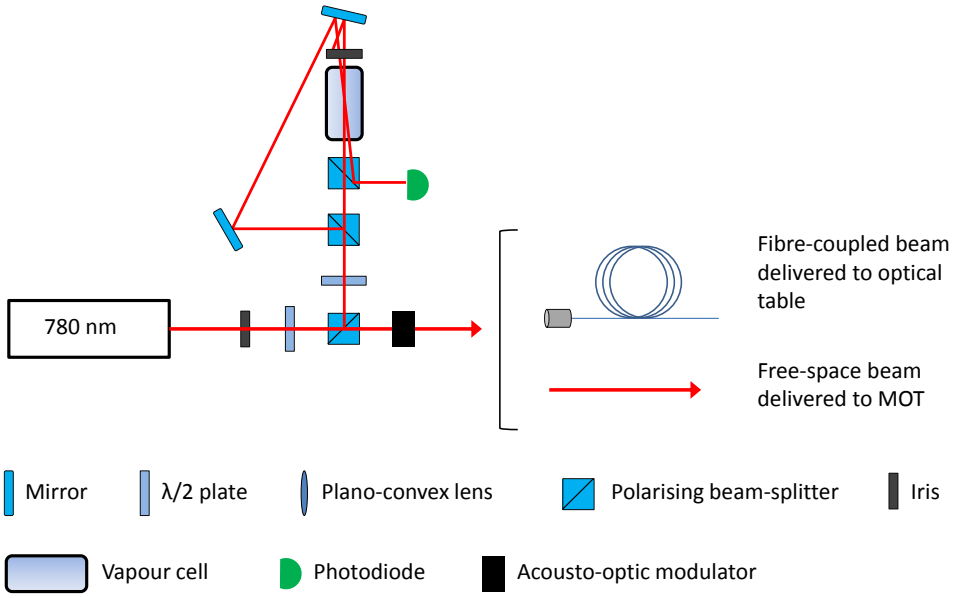

Figure 6.5: *SAS setup and optical preparation for ECDL3.*

beam path leads to Fresnel diffraction at the atom cloud position. Of course, one of the underlying restrictions in many laser cooling experiments is the design of the vacuum chamber. In most setups, the beam path length for MOT beams and probe beams must be large to accommodate the large chamber size. Figure **??** shows a spectrum collected for a bright MOT and a dark MOT generated by simply positioning the shadow in the repumping beam. Here, only a small percentage of the total population is transferred to the lower ground state.

A forced dark MOT (FDMOT) can also be created by applying the depumper to the BMOT. Figure **??** shows the effect of blocking and unblocking the depumper, which is tuned close to $F = 3 \rightarrow F' = 2$ and has an intensity of 120 mW/cm^2 at the cloud. The DMOT actually allows more $F = 3$ atoms in the trapping region than the FDMOT as the depump beam, when aligned correctly, only affects the atoms which move into the dark repumping region. The DMOT is advantageous in this case as the outer region feeds the inner dark region. In other words, having a large population of $F = 3$ atoms around the $F = 2$ atoms is better for the atom number throughout the cloud. Refer to Figure **??** to see the subtle differences between both types of dark MOT.

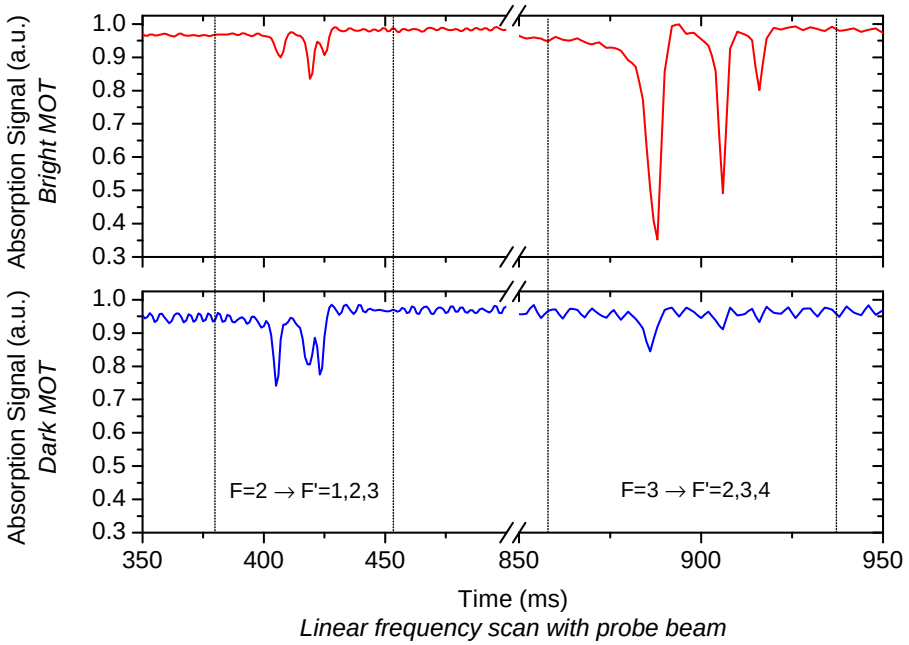

Figure 6.6: *Normalised absorption profiles of the dark and bright MOT using a 4 mm shadow placed directly in the repumping beam. Fresnel effects dominate the resulting repump beam profile at the position of the cold cloud and diminish the shape and intensity of the dark region. Thus, weak population transfer to $F = 2$ is observed as well as a dramatic loss of atoms from the $F = 3$ state.*

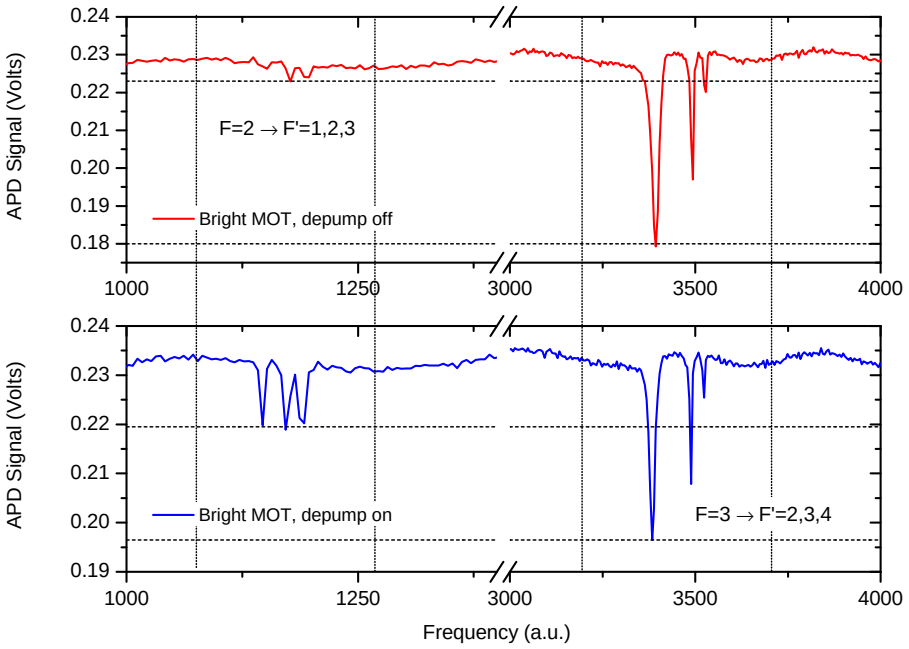

Figure 6.7: *By sending the depumping beam to the BMOT, a siginificant transfer of atoms from $F = 3$ to $F = 2$ can be achieved. Probe beam intensity = 75 $\mu W/cm^2$, depump intensity = 120 $\mu W/cm^2$ and the depump is tuned close to $F = 3 \rightarrow F' = 2$.*

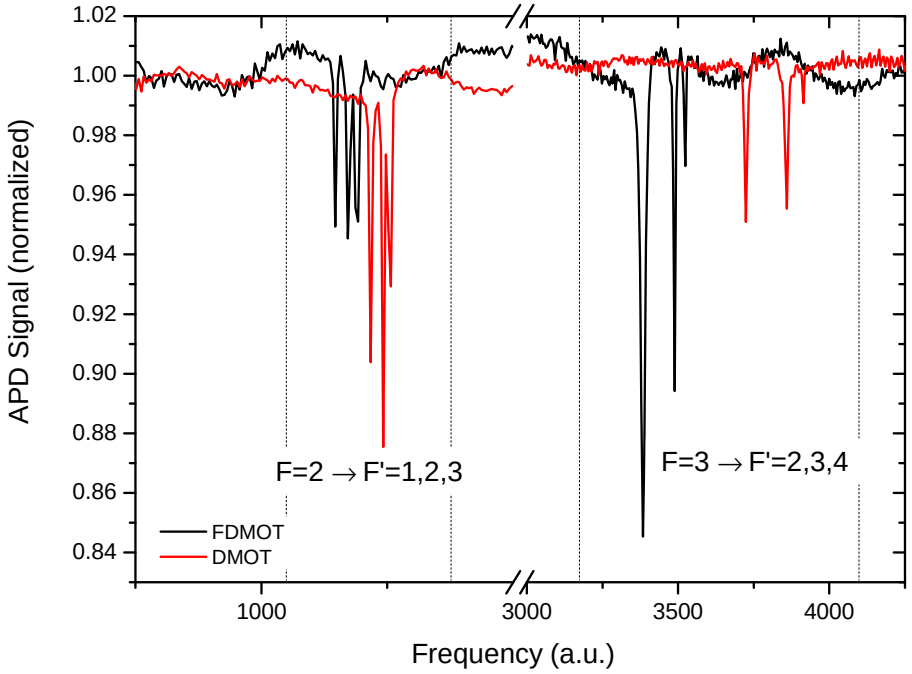

Figure 6.8: *Comparison between FDMOT (black plot) and DMOT (red plot). Although the FDMOT allows a large number of atoms to remain in $F = 3$, the DMOT is advantageous as much lower p values can be achieved.*

6.2.1 Effect of shadow shape and size on the DMOT

Three different shadow shapes were compared to see which was the most effective at producing a DMOT. Figure **??** shows freespace spectra for (a) an elliptical shadow and (b) a square shadow. The elliptical shadow does not match well with the geometry of the MOT and a large loss in atom number is observed. The square shadow is marginally better; not as many $F = 3$ atoms are lost with the square DMOT compared to the elliptical DMOT. The circular shadow is the optimal shape for a DMOT. Figure **??** shows the best combination of shadow shape and dimensions.

6.2.2 Measurement of thermal velocity of DMOT with transient absorption

The thermal velocity distribution of the cloud can be estimated using single parameter transient absorption [**?**]. This is a destructive method and relies on the monitoring of a low-intensity probe beam passing through the cloud during free expansion. These data are taken with the probe beam tuned to $F = 2 \rightarrow F' = 1$ in the FDMOT with a range of depump powers. A 1 Hz repetition rate was used

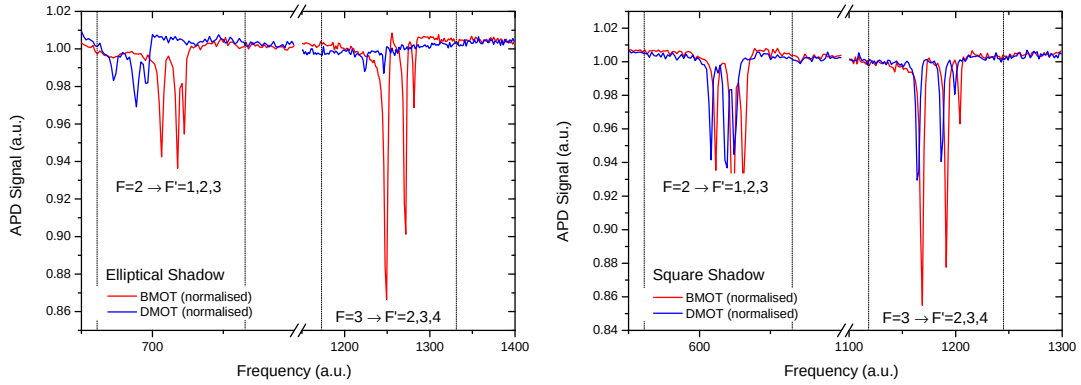

(a) *Elliptical shadow* **(b)** *Square shadow*

Figure 6.9: *Two different shadow shapes showing influence of shape on populations in different levels.*

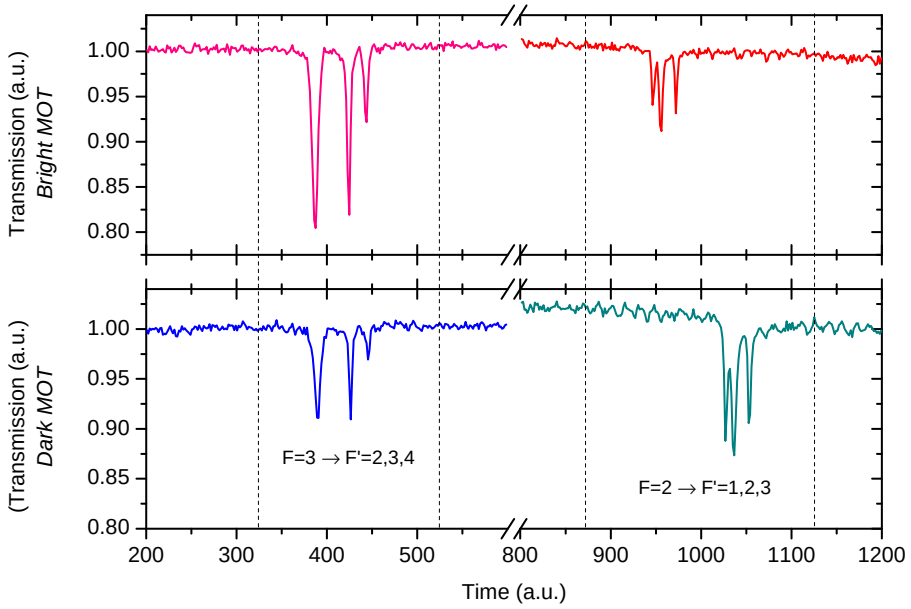

Figure 6.10: *Freespace spectroscopy of a BMOT (upper plot) and a well-optimised DMOT (lower plot) created with a circular shadow in the repump beam. Unlike in previous figures, the cooling transitions appear on the left-hand side in these plots.*

for a 10 ms off/measurement time.

Figures **??** and **??** illustrate the disruptive effect which the depumping light has on the MOT. The velocity distribution increases with increasing depumping intensity levels. These data are purely illustrative as the probe beam dimensions are not precisely known. Thus, temperatures cannot be readily extracted from the transient curves. However, the effect of the depumper on the MOT is clear from the curves. Knowledge of the number of atoms in the laser-cooled sample would allow estimation of T via fitting the first derivative of the transient curve

using the derivative of

$$\frac{I}{I_0} = exp\left[\frac{\sigma N}{\pi\left(t_m^2\bar{v}^2 + t_m\bar{v}\sqrt{4t_m^2\bar{v}^2 - 2\frac{\sigma N}{\pi} + \bar{v}^2t^2}\right)}\right], \tag{6.2}$$

where $\bar{v}$ is the parameter to be determined. Thus, T can be calculated with $T = m\bar{v}/3k_B$.

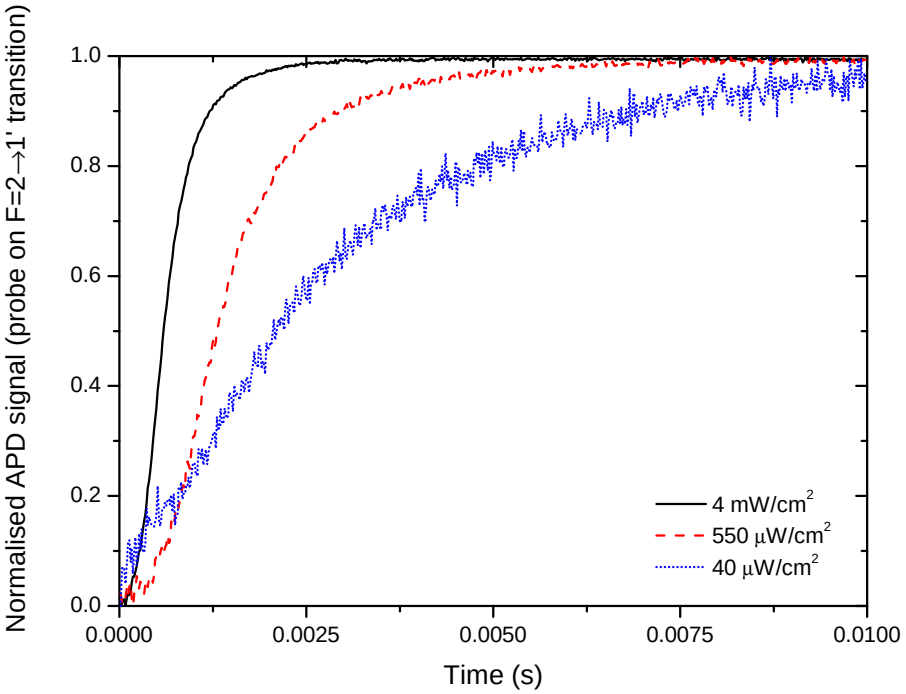

Figure 6.11: *Transient absorption of a FDMOT for varying depump powers: 4 mW/cm^2 (black, solid line), 550 $\mu W/cm^2$ (red, dashed line), 40 $\mu W/cm^2$ (blue, dotted line). The probe beam is tuned to $F = 2 \rightarrow F' = 1$.*

6.3 Characterising the DMOT with an ONF

By using beam stops to block and unblock the depumper and/or the repump probe, the different populations of atoms in $F = 2$ and $F = 3$ can be probed. In the previous section, a probe beam generated by an ECDL was used. From this section onwards, the probe beam is derived from the repump beam of the MOT and aligned, in free-space, with the centre of the atom cloud (Figure **??**). The frequency of this probe beam is fixed with an AOM and tuned to the repump transition of ^{85}Rb. Additionally, to facilitate rapid swapping from a DMOT to a BMOT, the shadow in the optical path of the repump MOT beam can be easily

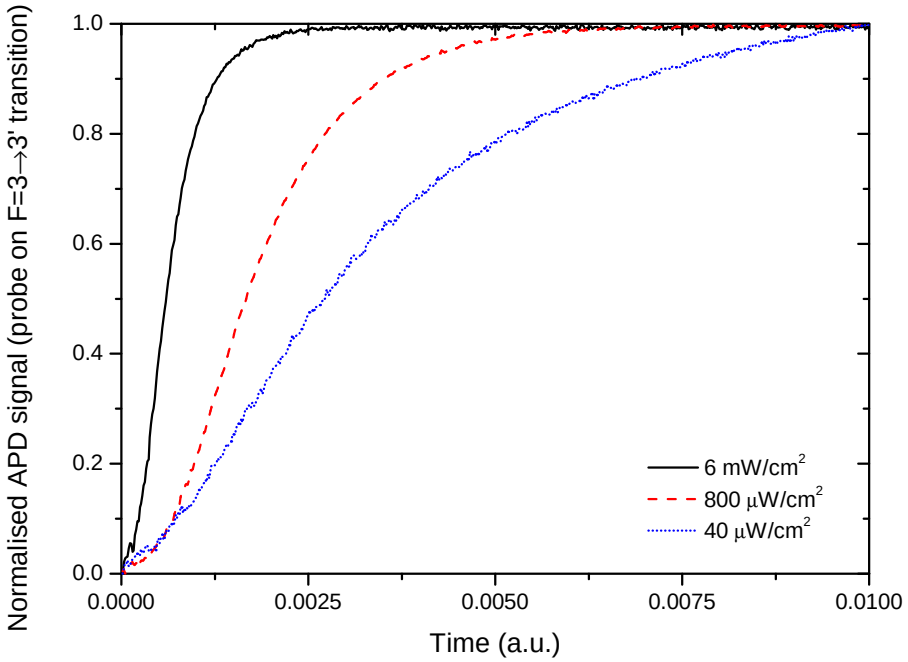

Figure 6.12: *Transient absorption of a FDMOT for varying depump powers: 6 mW/cm^2 (black, solid line), 800 $\mu W/cm^2$ (red, dashed line), 40 $\mu W/cm^2$ (blue, dotted line). The probe beam is tuned to $F = 3 \rightarrow F' = 3$.*

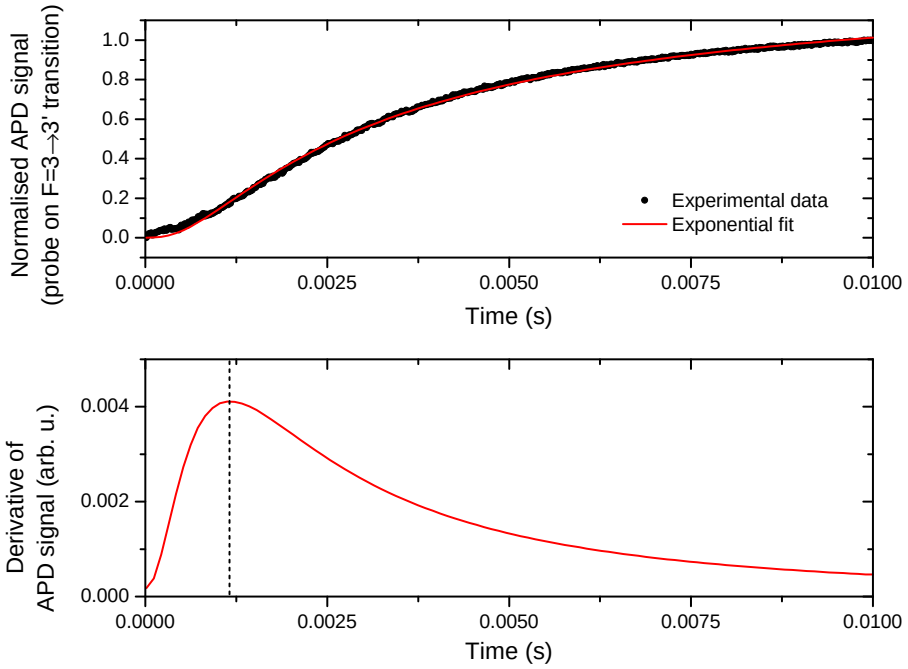

Figure 6.13: *Transient absorption of a FDMOT for a 40 $\mu W/cm^2$ depump beam. The probe beam is tuned to 3-3'. The peak of the derivative occurs at 1.18 ms.*

unclipped from its holder and removed.

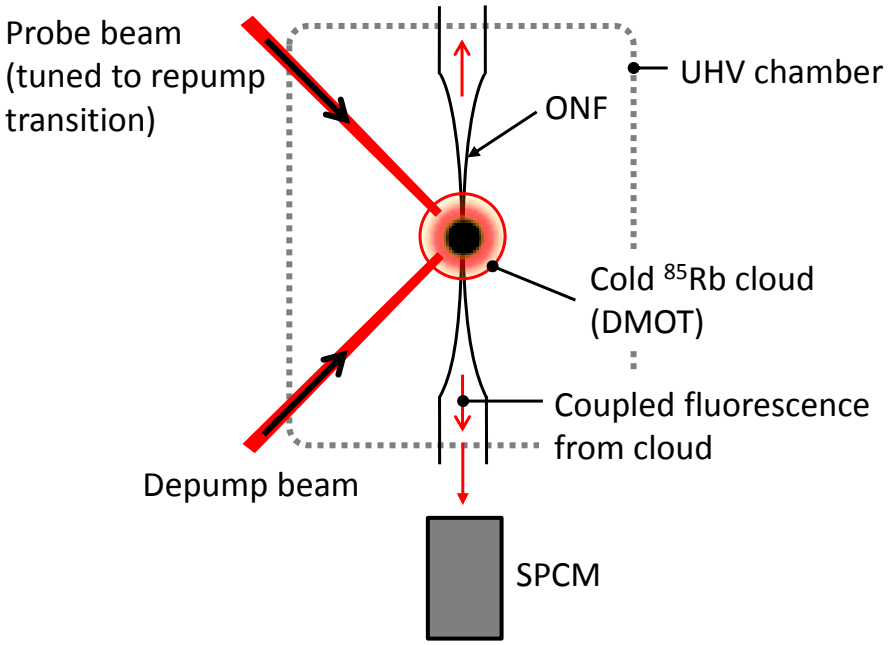

Figure 6.14: *The experimental setup used to study the DMOT with the ONF. The probe beam in this case is derived from the repump MOT beam and frequency tuned to the repump transition of ^{85}Rb. The probe is aligned with the centre of the cloud so that the central dark region can be illuminated when the DMOT is in use. The hollow repump MOT beam and the depumper are used in the same way as in the previous sections.*

Figure **??** shows two loading curves: the upper (black) plot is for a BMOT and the lower (red) plot is for a DMOT. The DMOT in this instance has no depumper shining on it and, thus, it is not extremely dark (i.e. p is not very low). This explains why the resulting coupling is relatively large ($\sim$ 750 counts/5 ms gate) compared to the coupling from the BMOT ($\sim$ 2000 counts/5 ms gate). The steady state count rate for both curves is proportional to the number of atoms in $F = 3$ although, the distribution of atoms between both hyperfine ground states, $F = 2$ and $F = 3$, is different in each case. However, these two sets of data are not enough to determine the population of each ground state or how dark the DMOT is (i.e. the value of p). To determine what the value of p is with the SPCM and ONF, three different fluorescence levels produced by different laser beam configurations must be recorded and analysed. This will be discussed in the following section.

Figure **??** shows two different sets of data. The upper plot shows the fluorescence signal from a DMOT created using just the hollow repump beam (i.e. no depumper is being used). The fluorescence level from this DMOT is 1750 counts/5

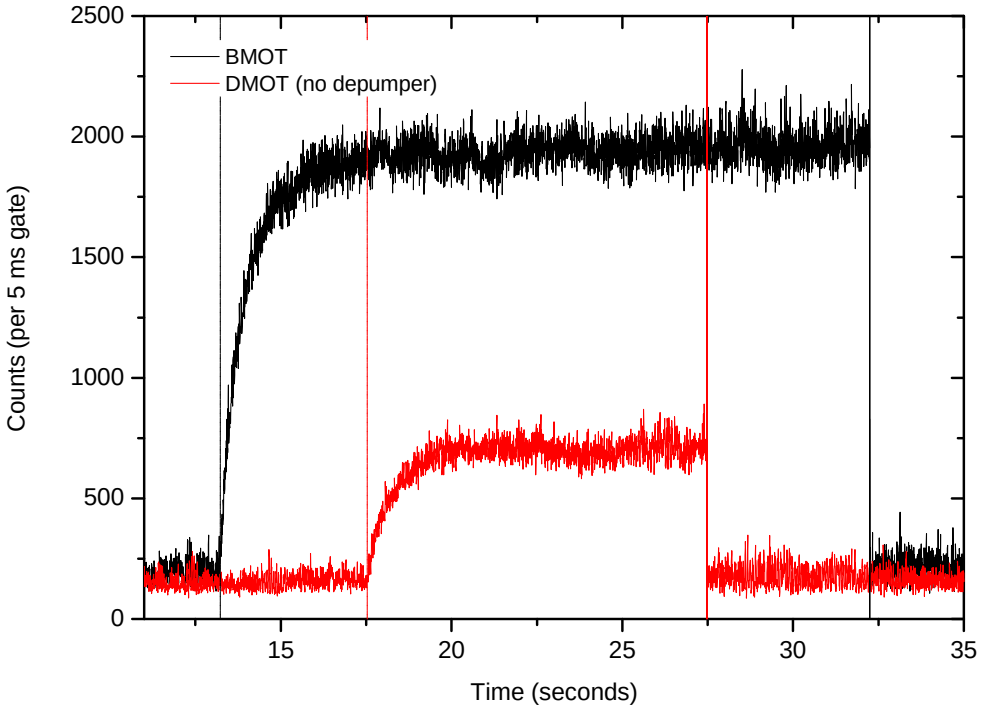

Figure 6.15: *This plot shows the residual fluorescence coupling that can be obtained with a DMOT of modest p value. The background level is approximately the same in both cases. Small variations are typical of that from laser drift over many tens of seconds (the time in which it takes to either remove or replace the dark spot into the optical path to change from DMOT to BMOT and vice versa).*

ms. By shining the probe beam on the DMOT, the dark shadow in the repump beam can be "filled in." In this plot, the probe beam is switched on for 100 ms every 1 second to produce the periodic spikes in the signal. The peak fluorescence level due to the "filling in" action of the probe beam is approximately equal to the steady-state fluorescence level of the BMOT which is shown in the lower plot (Figure **??**(b)). This BMOT is created simply by removing the dark shadow from the MOT repump beam. There is a small discrepancy between the steady state fluorescence level seen from the BMOT and the level of the peaks from the probed DMOT. This can be atributed to misalignment of the probe beam and/or a small loss in atom number due to the placement of the shadow in the path of the repump beam.

The presence of the depumper in the DMOT is investigated with the ONF+SPCM in Figure **??**. The upper left panel displays a loading curve for a DMOT created with a hollow repump beam and no depumer. This is qualitatively the same type of plot shown in Figure **??** (red curve). The experimental loading curve in Figure **??**(a) is highlighted by a red theoretical growth curve for clarity because the signal to noise ratios are poor for such dark clouds (i.e. a DMOT with low p is equivalent

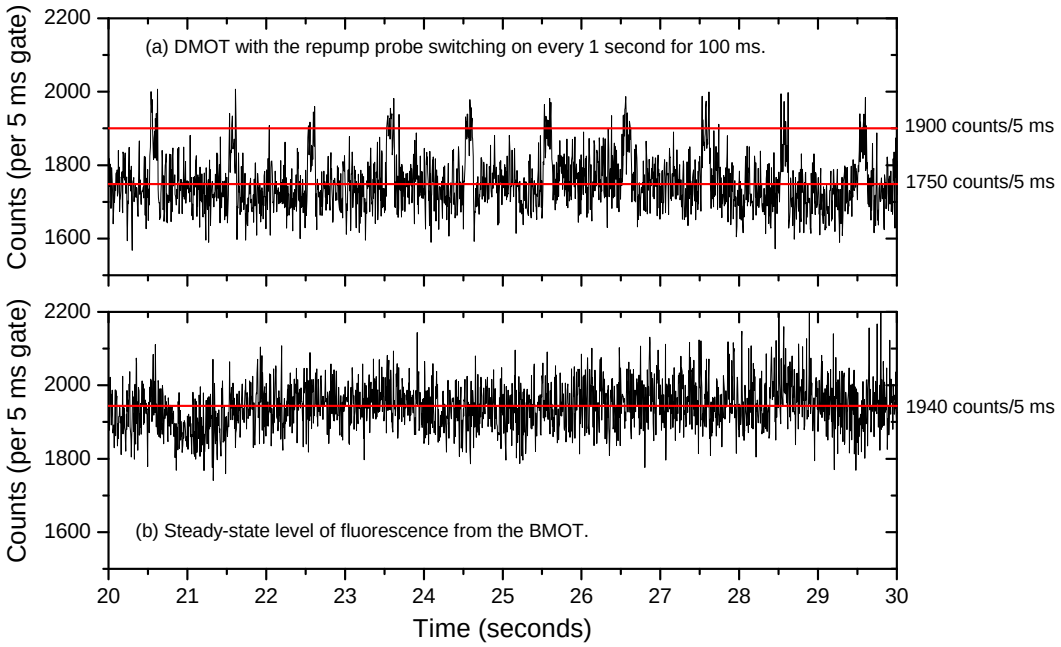

Figure 6.16: *The upper plot is the fluorescence from a DMOT created with just a hollow repump beam and with no depumper present. A probe beam (tuned to the repump transition) illuminates the dark region of the DMOT for 100 ms every 1 second to produce the spikes in the coupling signal. The probe beam "fills in" the hollow section of the repump beam to recreate the laser configuration of a BMOT. The lower plot shows the fluorescence signal from the same MOT configuration with the shadow removed from the repump beam. There is a small discrepancy between the steady state fluorescence level seen from the BMOT and the level of the peaks from the probed DMOT. This can be atributed to misalignment of the probe beam and/or a small loss in atom number due to the placement of the shadow in the path of the repump beam.*

to a BMOT with low atom number, N_A). Figure **??**(b) shows that the background level of the DMOT (125 counts/2 ms) is about the same as the background level when the magnetic field of the MOT is switched off (so that no cloud can form). During the 100 ms while the depumper is off, the fluorescence level recovers to $\sim$ 275 counts/2 ms, matching the steady-state level of the signal in the upper left panel (Figure **??**(a)). The two lower panels of Figure **??** introduce the probe beam. On the lower left (Figure **??**(c)), the signal from the DMOT is recorded while two things happen simultaneously: as before, the depumper is sequenced to switch off for 100 ms every 1 second. In addition, during this 100 ms, the probe beam is switched on. The simultaneous absence of the depumper and presence of the probe beam (acting as a "filling in" beam) recreates a BMOT for the atoms. For this particular set of data, the steady-state fluorescence of the BMOT was recorded and found to be approximately 1300 counts/2 ms. This matches quite well with the observed fluorescence level obtained during each 'spike' in Figure **??**(c). Finally, the lower right panel, (d), shows the solo effect of the probe beam

on the DMOT. In Figure **??**(d), the depumper is blocked and the probe beam is sequenced to switch on for 100 ms duration every 1 second. The background level count rate is approximately the same as the count rates reached by the peaks in Figure **??**(b), i.e. 275 counts/2 ms.

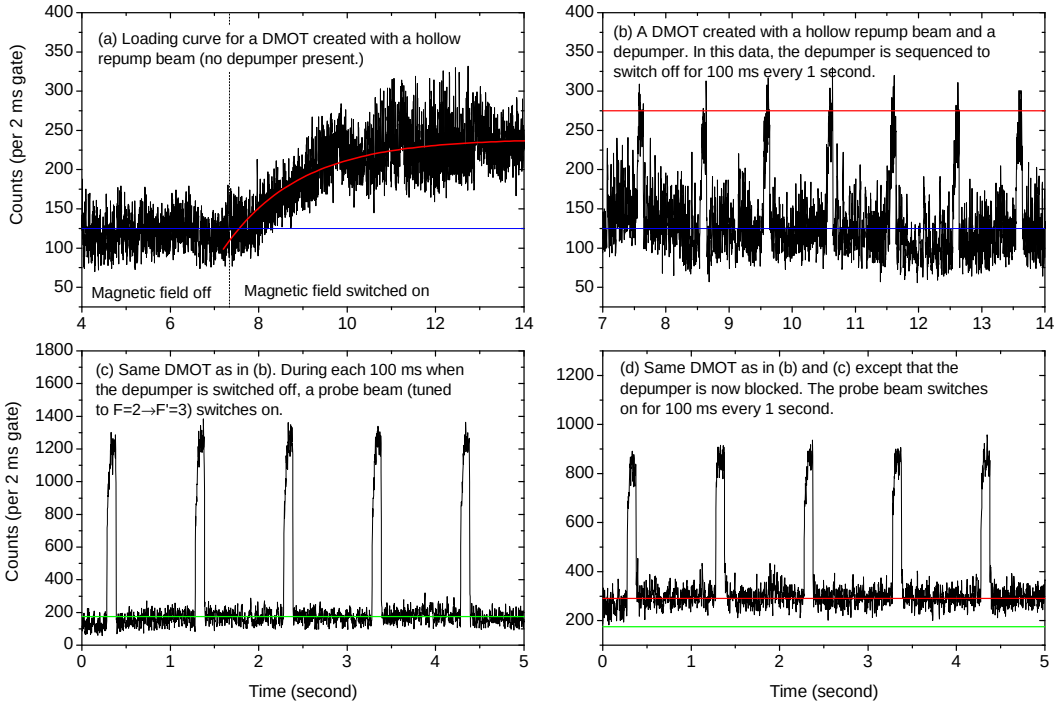

Figure 6.17: *A series of data sets for the DMOT under different conditions. (a) A loading curve for a DMOT which was created with a hollow repump beam and no depumper. The experimental loading curve is highlighted by a red theoretical growth curve. The steady-state fluorescence level after loading is between 250 and 300 counts/2 ms. (b) This DMOT is created with a hollow repump beam (as in (a)) and a depumper. The depumper is sequenced to switch off for 100 ms every 1 second. This results in the spikes in the fluorescence signal up to* $\sim$ *275 counts/2 ms, matching the steady-state level of (a) thus showing the effectiveness of the depumper. (c) the same DMOT as in (b) with the same depumper sequencing. In addition, the probe beam (tuned to* $F = 2 \rightarrow F' = 3$*) is aligned with the dark region of the cloud and is switched on for 100 ms (using an AOM) at the same time that the depumper switches off. Thus, the probe beam acts as a "fill in" beam which allows a BMOT configuration to be recreated for 100 ms. The maximum fluorescence level reaches 1300 counts/2 ms. (d) The DMOT in this dataset is created with the hollow repump beam only. The depumper is blocked and the probe beam follows the same sequence as that for (c). The presence of the probe beam generates a spike in the fluorescence signal as it acts to repump many of the atoms in* $F = 2$ *to* $F = 3$*. By taking the ratio of the baseline counts in (a) to the peak heights in (c), the value for p is determined to be* $\sim$*0.10. However, by including the depumper, p is determined using the baseline of (c) (green line): 50/1150*$\sim$*0.04.*

As mentioned earlier, to estimate p from the ONF setup, two sets of data are taken. These two datasets can be found in Figure **??**(a) and (c). Figure **??**(a) shows the fluorescence count rate through the ONF for a loading DMOT created

with a hollow repump beam (no depumping beam). At ∼7.5 s, the magnetic field is switched on and the DMOT loads. The fluorescence level increases from 125 counts/s (blue line - background) to approx. 275 counts/2 ms due to the residual bright atoms in the DMOT, i.e. the $F = 3$ atoms contribute 150 counts/2 ms to the signal. This is the numerator of p (Equation **??**) for the DMOT created with just a hollow repump beam. In Figure **??**(c), the fluorescence signal is recorded for a DMOT which is created with a hollow repump beam and depumper. This yields the baseline count rate of 175 counts/2 ms (green line) and, thus, the numerator of p in this case is 50 counts/2 ms. Furthermore, in this plot, the probe beam is added to the optical configuration. This probe beam is tuned to the repumping transition of ^{85}Rb and aligned with the dark region of the cloud. Thus, it "fills in" the dark central region of the doughnut-shaped repump beam, thereby recreating a standard BMOT configuration. The probe switches on for 100 ms at 1 Hz repetition rate, while the depumper switches off at the same time and rate. The observed spikes in the fluorescence count rate (∼1150 counts/2 ms) coupled to the ONF is from atoms in both the ground state hyperfine levels, $F = 2$ and 3. This is the denominator of p. By taking the ratio of the baseline in Figure **??**(b) (i.e. the red line) to the peak counts in Figure **??**(c), and correcting for the background level (the blue line), the value for p is calculated as ∼0.1. However, with the inclusion of the depumper, p becomes 50/1150=0.04.

6.3.1 DMOT loading times

Loading curves can be analysed for the DMOT and BMOT via the ONF. Figure **??** shows a loading curve for a BMOT (upper panel) and a loading curve for a DMOT (lower panel). The BMOT curve yields a loading rate, R_B, of 15.4×10^4 counts/s by fitting it with $N(t) = R/\Gamma\left(1 - e^{-\Gamma t}\right)$ where $\Gamma = 1/\tau$ is the collisional loss rate in the MOT (Equation **??**). The curve in the lower panel is the loading curve for a DMOT which has been created with a hollow repump beam and a depumper. The spikes in fluorescence occurring at 1 Hz (for a 100 ms duration) are due to the simultaneous switching off of the depumper and switching on the probe beam. As discussed previously, these conditions (no depumper and probe on) recreate the conditions for a BMOT and provide a measurement of the denominator of p. These peaks in the DMOT curve reach values of $\sim 1 \times 10^5$ counts/s, matching the steady state count rate of the upper (BMOT) loading curve. The baseline curve of the DMOT plot represents the loading curve of the fraction of $F = 3$ atoms present in the DMOT. The DMOT does not help the

loading process so the loading rate cannot be larger in the DMOT than in the BMOT. In Figure **??** we see that the loading rate of the DMOT, R_D, is $\approx 0.2 R_B$. For this DMOT, p=0.22.

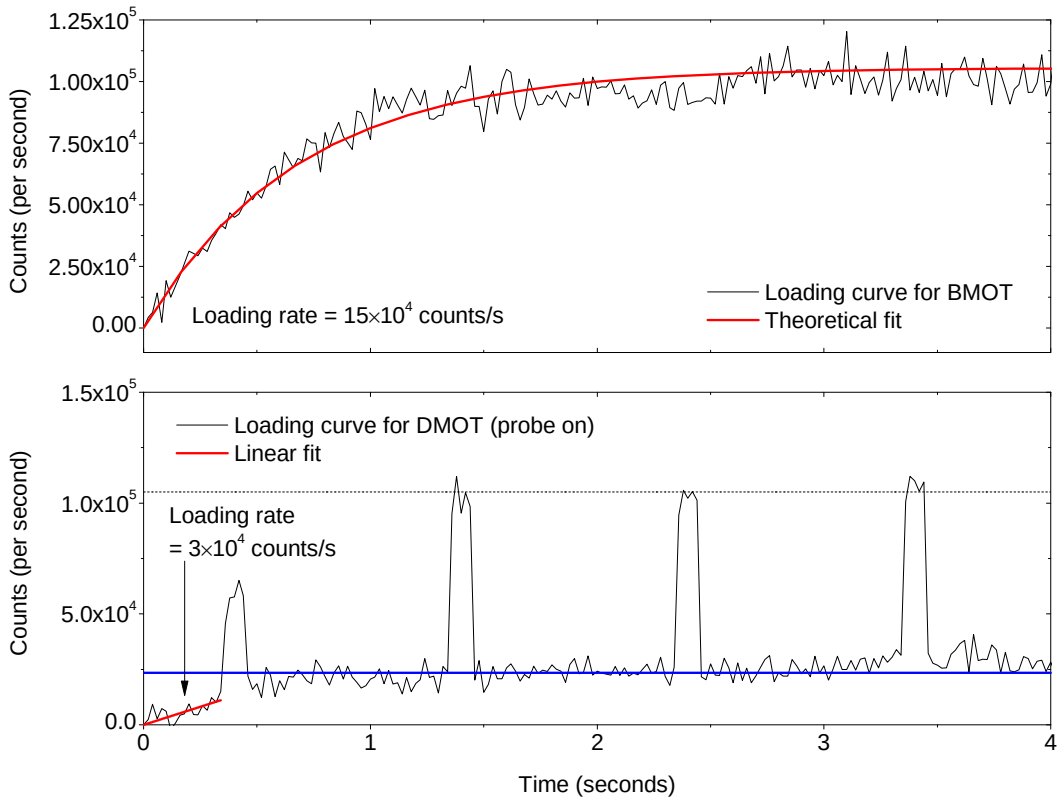

Figure 6.18: *The upper panel shows a typical BMOT loading curve with a loading rate of 15.4×10^4 counts/s. The red curve is the theoretical loading curve fit, $N(t) = R/\Gamma(1-e^{-\Gamma t})$, to the experimental data (black plot). The lower plot is the loading curve of a DMOT created with a hollow repump beam and a depumper. The spikes in the signal are due to the simultaneous switching off of the depumping beam and switching on of the probe beam. These spikes are then due to the atoms in both $F = 2$ and $F = 3$ as discussed in the previous section. The baseline (blue line) represents the loading curve of the residual bright ($F = 3$) atoms in the DMOT. In this case, $p = 0.22$. As the DMOT does not aid the loading process, the loading rates in both cases differ by an order of magnitude.*

Loading rates for the BMOT and DMOT can be explored by varying the cooling laser intensity and recording the same data as shown in Figure **??** for each I_{beam}. This study is shown in Figure **??**. The DMOT loading rate, R_D, is consistently lower than the BMOT loading rate R_B. The change in R_D can be also be examined as a function of p. In Figure **??**, p is varied (using different depumper intensities) over the range 0.08 to 0.50. The loading rate of the DMOT decreases for lower p values as expected [**?**]. The error in both R_D and p in this plot is due to the SPCM signal noise.

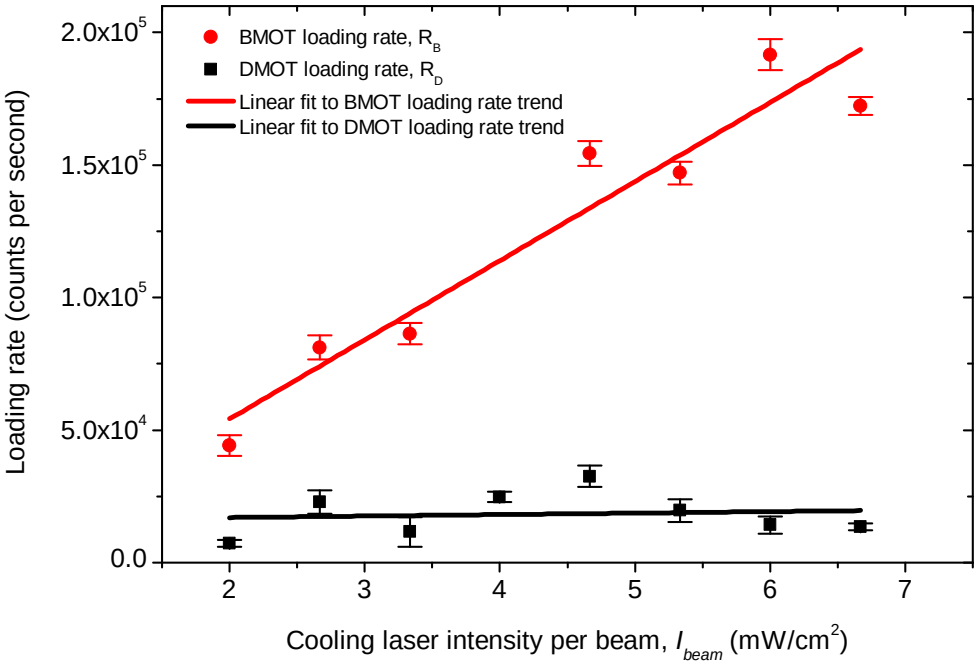

Figure 6.19: *The red (black) data points show the trend in loading rates for the BMOT (DMOT) while varying the cooling laser intensity. As the hollow repump beam and the depumper do not help the loading process, the loading rates for the DMOT are lower than those of the BMOT. Linear fits have been applied to each series as a guide to the eye. The error bars are calculated from the loading curve fits.*

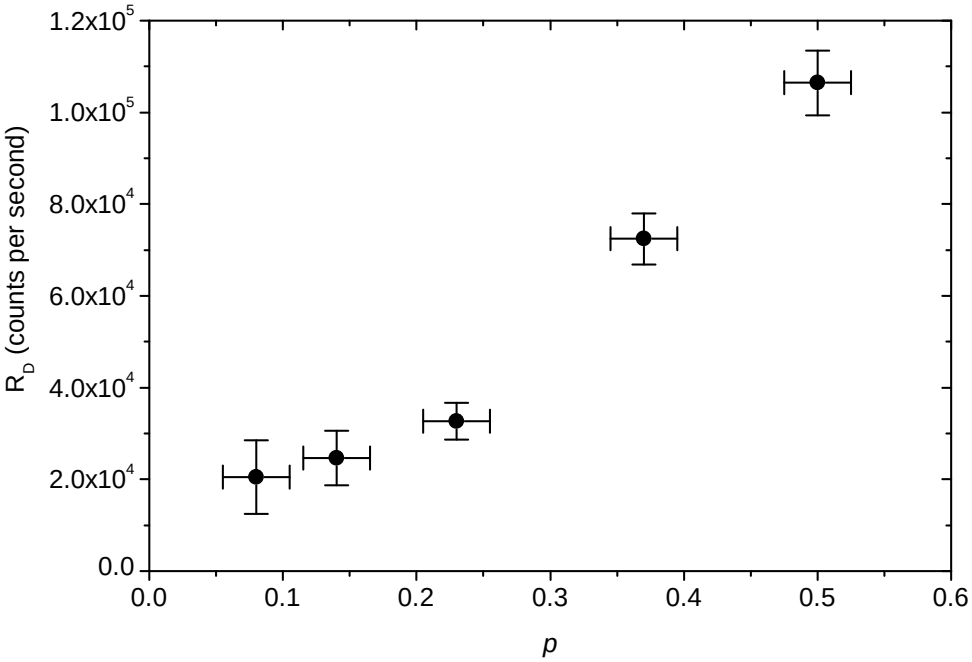

Figure 6.20: *Loading rate, R_D, for a DMOT (created with a hollow repump beam and a depumper) as a function of p. The error in both R_D and p in this plot is due to the SPCM signal noise.*

6.3.2 Effect of cooling laser intensity on the DMOT

Townsend *et al.* [**?**] report slightly reduced values of p for reduced cooling beam intensity. This trend is explored with an ONF in Figure **??**. One reasoning behind the approximately constant behaviour of Figure **??** is that, while the cooling laser intensity increases, both the bright and dark regions of the DMOT will experience the same increase in N_A. This implies that the ratio of the numbers of atoms in $F = 2$ and $F = 3$ will remain the same. This measurement took place over four hours so some uncertainty in the data is due to long-term laser power drifts which generate different noise levels in the fluorescence signal. With a high-transmission ONF having a radius fulfilling $k_0 a = 1.45$, and improvements to the laser stability and output power, it should be possible to measure p values for $I_{MOT} = I_{sat}$ (where $I_{MOT} = 6I_{beam}$) and even below this to much greater accuracy.

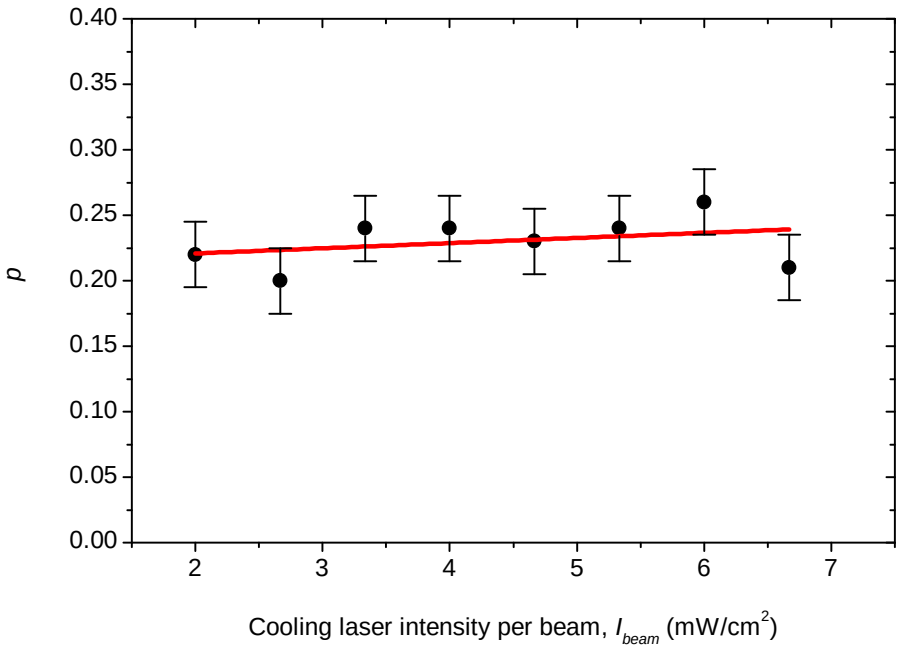

Figure 6.21: *Variation in p with increasing cooling laser intensity. The trend is approximately linear and nearly constant. The error for each data point represents the quality of the fluorescence coupling signal during each dataset.*

6.4 Conclusion

In conclusion, this work examined the implementation of a DMOT in order to circumvent the density-limitations of a BMOT. The low density of atoms in a

BMOT is a property that is limited by (a) reabsorption of emitted photons within the cloud, and (b) collisions between F and F' atoms which lead to kinetic losses. For the ONF, this is a major consideration. If one wishes to do an absorption experiment, by encouraging as many atoms as possible to fill the evanescent region around the ONF, the signal quality will improve dramatically. Although there will still be collisional loss in a DMOT (unless $p = 0$), the reabsorption of scattered photons is no longer a dominant problem. By packing more atoms in closer to the ONF surface, the evanescent field of a probe beam is easily absorbed by nearby atoms. A cloud density improvement is therefore critical for high optical density, allowing non-linear demonstrations such as EIT and slow light [**?**, **?**, **?**, **?**]. The DMOT was created with a hollow repump beam and an additional depumping beam. The DMOT was characterized with a free-space probe beam using absorption spectroscopy and probed with an ONF. Loading rates of the DMOT were measured and compared with those of the BMOT. For lower p values, the loading rate of the DMOT was correspondingly lower because the presence of the hollow repump beam and the depumer does not aid the loading process. The variation in p for different cooling laser intensities was measured via the ONF, with slightly lower values of p obtained for the lower intensities.

Chapter 7

Atomic absorption studies with an ONF

The strong evanescent field surrounding the waist of a sub-wavelength tapered fibre when light propagates through it allows light-matter interaction, not only with surface-adsorbed species and micro-particles in solution, but also with media surrounding the fibre. In-fibre spectroscopy can be performed on hot and cold atomic vapours. In the case of a hot vapour, transit-time broadening results in significantly broadened lineshapes as a thermal atom will pass through the evanescent field in under 1 nanosecond. This effect is reduced in a cold atomic gas. Here, where thermal velocities are of the order of a few centimeters per second, the atoms transit the evanescent field in much longer times ($\sim$ a few μs) allowing increased spectral sensitivity [**?**].

This chapter is largely concerned with the optical density (OD) of the cloud of ^{85}Rb atoms.The OD describes how optically thick a medium is: the more optically dense a material is, the slower an electromagnetic wave will move through that material. An optically dense atom cloud is desirable in many experiments, not least because it can enhance the signal-to-noise ratio of even the weakest transition in high-precision spectroscopy. In particular, for the ONF-cloud system, a significant increase in the efficiency of low-light-level nonlinear optics can be achieved with high OD. Also, a light pulse can be entirely stored only in a medium with a large enough OD in the experiments of storage and retrieval of light [**?**, **?**, **?**].

In the multiple scattering regime of the MOT [**?**, **?**], as the number of trapped atoms increases, the atomic density remains fixed and the spatial dimensions of

the atom cloud increases with $N^{1/3}$. Hence, a factor 2.7 increase in the OD would require a factor of 20 increase in the atom number [**?**]. In general, for fluorescence coupling studies, atom number is significant rather than simply the cloud density. However, for ONF absorption, it is the cloud density which should be maximised. Practically, the atomic cloud size will not be as small as the evanescent field volume so atom number is not the critical parameter.

Whereas in previous chapters the focus has been on n_{eff}, which is the number of atoms contributing to the fluorescence that is coupled to the guided mode of the ONF, here the quantity N_{eff} is introduced to measure the number of atoms in the evanescent field of the probe beam. Only a fraction of N_{eff} will experience van der Waals interactions as the spatial reach of the van der Waals force is $\sim \lambda/10$. Generally, for ONFs with large diameters (780 nm $< d <$1.5 μm) the value of n_{eff} will be larger than that of N_{eff}. The inverse becomes true for very small diameter ONFs where the evanescent field becomes large in spatial extent and intensity thereby reaching more and more atoms in the cloud (see Figure **??**).

In this chapter, an outline of our current work on absorption techniques is discussed. With the inherent limitations of our fibre pulling rig, these results indicate the potential of the technique rather than a complete study. We compare our own results with those found theoretically and the work done by a handful of other international groups.

7.1 Theoretical background

For light to be confined in the core of an optical fibre, the field must be evanescent in the cladding. This is true for core-clad fibre and for ONFs where the cladding is the vacuum. This implies that there must be (a) a decaying function in the cladding, and (b) the solution in the core needs to be continuous and finite everywhere. The fields are summarised as follows: (see Appendix A, [**?**] and [**?**])

In the core, $r < a$,

$$
\begin{aligned}
E_r &= \frac{-i\beta}{h^2}\left[AhJ_l'(hr) + \frac{i\omega\mu_0 l}{\beta r}BJ_l(hr)\right]e^{i(l\phi+\omega t-\beta z)} && (7.1)\\
E_\phi &= \frac{-i\beta}{h^2}\left[\frac{il}{r}AJ_l(hr) - \frac{\omega\mu_0}{\beta}BhJ_l'(hr)\right]e^{i(l\phi+\omega t-\beta z)} && (7.2)\\
E_z &= AJ_l(hr)e^{i(l\phi+\omega t-\beta z)} && (7.3)\\
H_r &= \frac{-i\beta}{h^2}\left[BhJ_l'(hr) + \frac{i\omega\epsilon_0 n_{core} l}{\beta r}AJ_l(hr)\right]e^{i(l\phi+\omega t-\beta z)} && (7.4)\\
H_\phi &= \frac{-i\beta}{h^2}\left[\frac{il}{r}BJ_l(hr) - \frac{\omega\epsilon_0 n_{core}}{\beta}AhJ_l'(hr)\right]e^{i(l\phi+\omega t-\beta z)} && (7.5)\\
H_z &= BJ_l(hr)e^{i(l\phi+\omega t-\beta z)}. && (7.6)
\end{aligned}
$$

In the cladding (or vacuum, in the case of the ONF), $r > a$,

$$
\begin{aligned}
E_r &= \frac{i\beta}{q^2}\left[CqK_l'(qr) + \frac{i\omega\mu_0 l}{\beta r}DK_l(qr)\right]e^{i(l\phi+\omega t-\beta z)} && (7.7)\\
E_\phi &= \frac{i\beta}{q^2}\left[\frac{il}{r}CK_l(hr) - \frac{\omega\mu_0}{\beta}DqK_l'(qr)\right]e^{i(l\phi+\omega t-\beta z)} && (7.8)\\
E_z &= CK_l(qr)e^{i(l\phi+\omega t-\beta z)} && (7.9)\\
H_r &= \frac{i\beta}{q^2}\left[DqK_l'(qr) + \frac{i\omega\epsilon_0 n_{clad} l}{\beta r}CK_l(qr)\right]e^{i(l\phi+\omega t-\beta z)} && (7.10)\\
H_\phi &= \frac{i\beta}{q^2}\left[\frac{il}{r}DK_l(qr) - \frac{\omega\epsilon_0 n_{clad}}{\beta}CqK_l'(qr)\right]e^{i(l\phi+\omega t-\beta z)} && (7.11)\\
H_z &= DK_l(qr)e^{i(l\phi+\omega t-\beta z)}. && (7.12)
\end{aligned}
$$

In the equations above, ϵ_0 is the permittivity of free space and A, B, C and D are constants to be determined via boundary conditions. By requiring the fields tangential to the core/cladding boundary to be continuous, a set of simultaneous equations for A, B, C and D are found,

$$
\begin{aligned}
AJ_l(ha) - CK_l(qa) &= 0\\
A\left[\frac{i(\pm l)}{h^2 a}J_l(ha)\right] + B\left[-\frac{\omega\mu_0}{h\beta}J_l'(ha)\right] + C\left[\frac{i(\pm l)}{q^2 a}K_l(qa)\right] + D\left[-\frac{\omega\mu_0}{q\beta}K_l'(qa)\right] &= 0\\
BJ_l(ha) - DK_l(qa) &= 0\\
A\left[\frac{\omega\epsilon_1}{h\beta}J_l'(ha)\right] + B\left[\frac{i(\pm l)}{h^2 a}J_l(ha)\right] + C\left[\frac{\omega\epsilon_2}{q\beta}K_l'(qa)\right] + D\left[\frac{i(\pm l)}{q^2 a}K_l(qa)\right] &= 0.
\end{aligned}
$$

A non-trivial solution exists only when the determinant of these coefficients vanishes and this yields the dispersion equation (see Equation **??**), which determines the propagation constant, β. The field equations also allow modelling of the field inside and outside the fibre. For each value of the ONF radius, a value for the propagation constant can be calculated (see Figure **??**). Figure **??** shows the intensity distribution inside and outside the ONF for four different radii. For very small ONF diameters, the evanescent field has an extremely large spatial extent and high intensities. Although an evanescent field does exist for larger diameters (e.g. for an ONF with diameter of $\sim$1 μm), it is of low intensity and has small spatial extent. To deliver a probe beam (evanescent field) to atoms surrounding an ONF, the probability of atomic absorption by many atoms is enhanced if one uses small diameter ONFs.

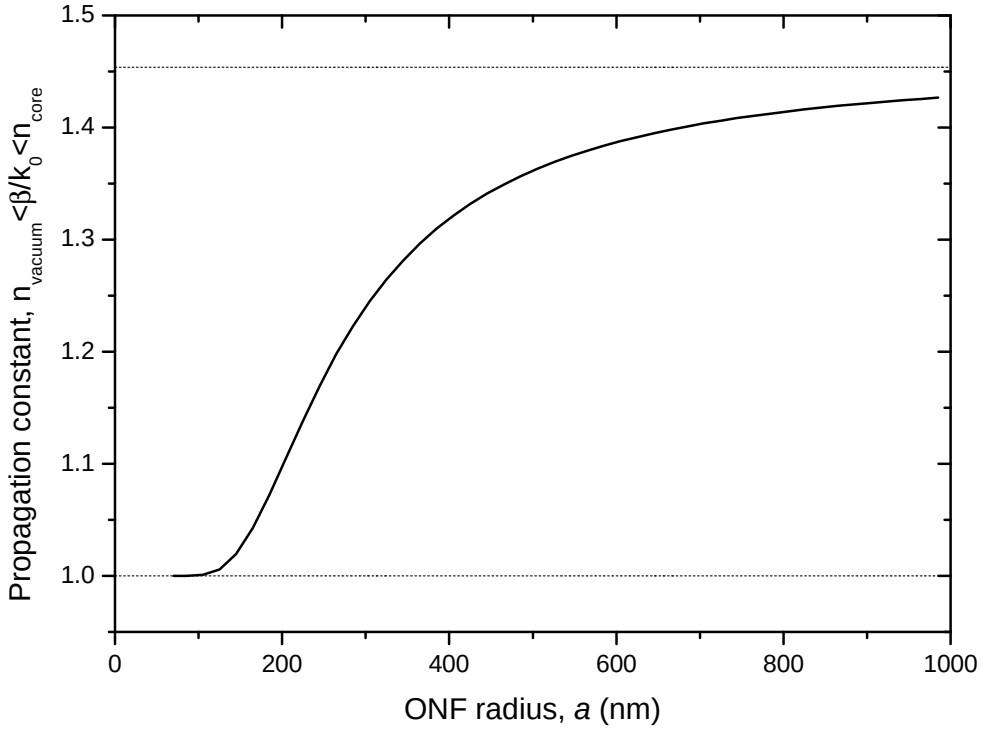

Figure 7.1: *A plot of propagation constant, β, versus the radius, a, of the ONF for $n_{core} = 1.4537$ and $n_{clad} = n_{vacuum} = 1$, $\lambda = 780$ nm.*

Absorbance, or optical density (σ), is the logarithmic ratio between the radiation incident on a material and the radiation transmitted through a material,

$$A = \sigma = -ln(T) = -ln\left(\frac{I_{on}}{I_{off}}\right) \tag{7.13}$$

where I_{on} is the intensity of the light that has passed through the material (trans-

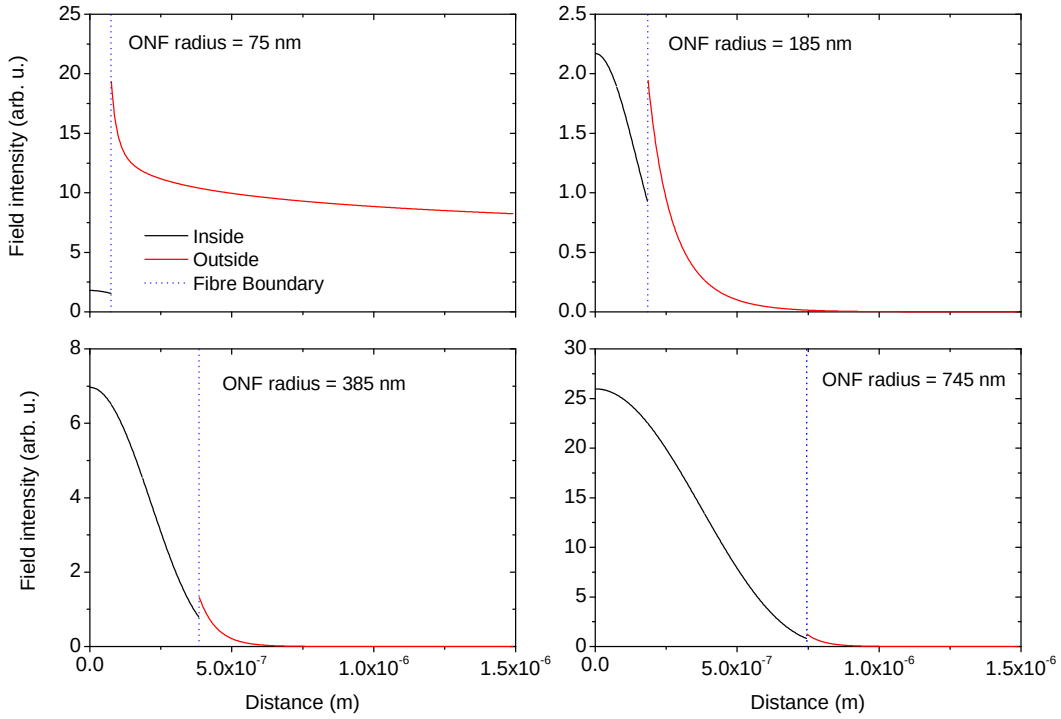

Figure 7.2: *The intensity of the HE_{11} mode along the radial direction in four different ONFs. The black, solid line is the intensity inside the ONF and the red, solid line is the intensity distribution that exists in the vacuum.*

mitted radiation), and I_{off} is the intensity of the radiation before it passes through the material (incident radiation). Specifically, for our measurements, these quantities refer to the power level of the probe beam when the MOT is *on* and when it is *off*, respectively.

The absolute absorption is found by dividing the intensity of the probe signal while the MOT is on by that when the MOT is off, and subtracting from 1, i.e. $1 - T = 1 - (I_{on}/I_{off})$. A plot showing both quantities for the same set of data is displayed in Figure **??**.

7.2 Experimental Procedure

The MOT is created in the usual way and the cloud is aligned around the ONF using the imaging and detection methods described in Section 5.1. Generally, atom numbers and cloud densities are of modest values: 10^7 atoms and 10^{10} atoms/cm^3, respectively. Figures **??** and**??** show the setup used for triggering the data acquisition for single-photon absorption. A square wave generator was used to switch the probe beam on and off before it entered a double-pass AOM

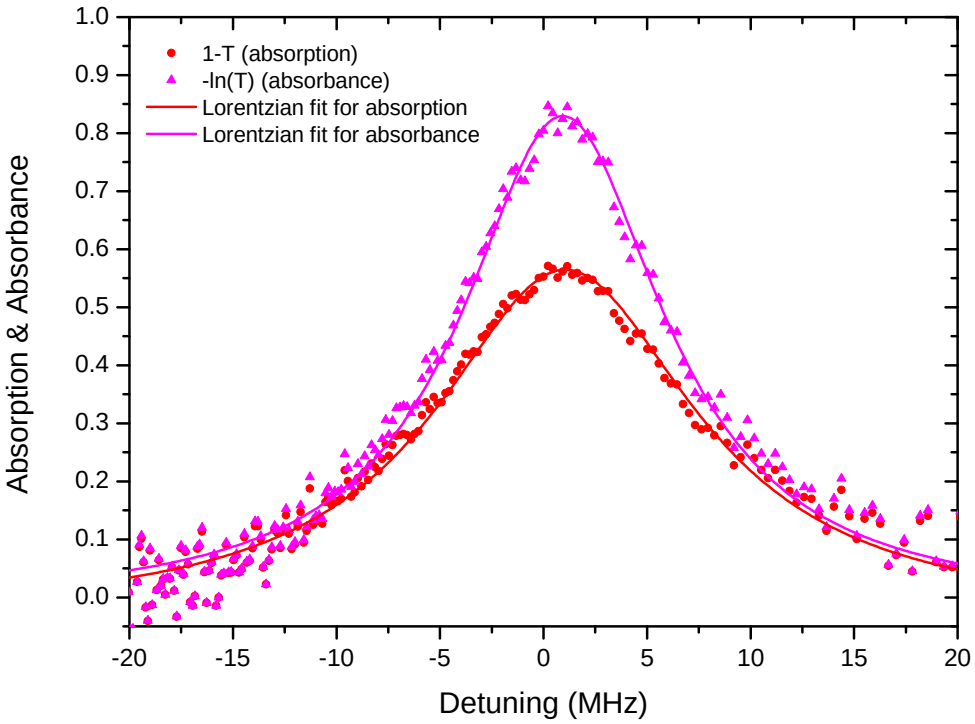

Figure 7.3: *Absorbance (optical density) and normalised absorption curves for a particular set of data. The optical density reaches a peak of about 0.8. The absolute absorption is 0.55. The N_{eff} for this experiment was approximately 1.5.*

system – see Figure **??**. To ensure that the spectroscopy is performed while the cooling laser and repump laser are off, the square wave generator was also used to supply 0 V or +1 V to the AOM drivers for the cooling and repump laser. After adjusting the time delay, the cooling beam and repump beam were shut off while the nanofibre probe beam was ramped across the ^{85}Rb cooling transition (see Figures **??** and **??**). An avalanche photodiode (APD) was placed at the opposite end of the fibre and the output signal was sent to a PC.

The nanofibre probe beam was prepared by coupling a small percentage of the zero-order cooling beam into a double-pass AOM setup [**?**] (**??**). This was necessary because AOM1, on its own, was not sufficient to frequency shift the probe beam to the vicinity of a hyperfine transition in ^{85}Rb (see Figure **??**). To reach F=3→4' while remaining locked to the crossover peak of (2,4), a frequency shift of 92 MHz is needed. Additionally, to scan around this transition it is necessary to shift from 72 MHz to 112 MHz (or some reasonable range to obtain a clear signal and background).[1] The resulting probe beam was then scanned across the

[1]It is also possible to lock the cooling laser to the (3,4) crossover and then shift the probe beam from 40 MHz to 80 MHz, for example. This was not feasible in our setup as the highest efficiency (>75%) of AOM1 lies in the mid-voltage (3-7 V) range and we want to avoid using very low detunings of around 40-50 MHz for the high quality MOT beams. Additionally, that

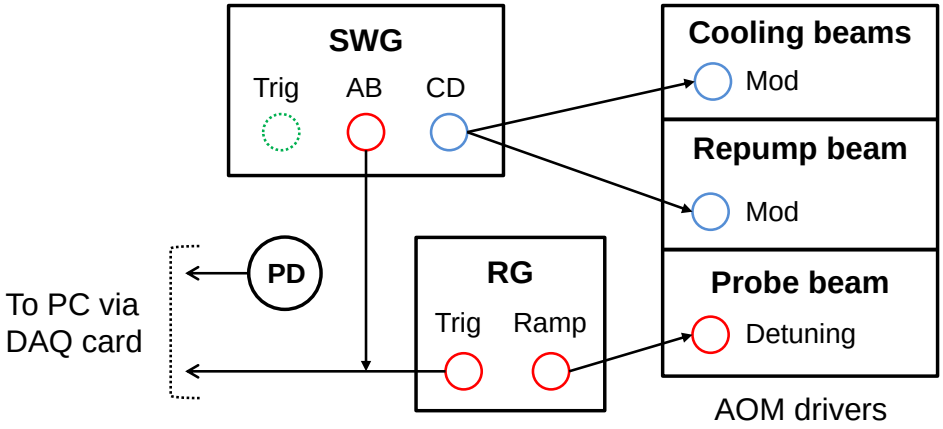

Figure 7.4: *Triggering scheme used for single-photon absorption experiments. SWG = square wave generator, RG = ramp generator, AOM = acousto-optic modulator, DAQ = data acquisition card, PD = photodiode. The SWG is triggered internally and is used directly to switch off and on the MOT beams while simultaneously switching on and off the probe frequency scan. Using a LabVIEW programme the APD is triggered with the SWG AB output through a DAQ board. The resulting sequence is shown in Figure* **??**.

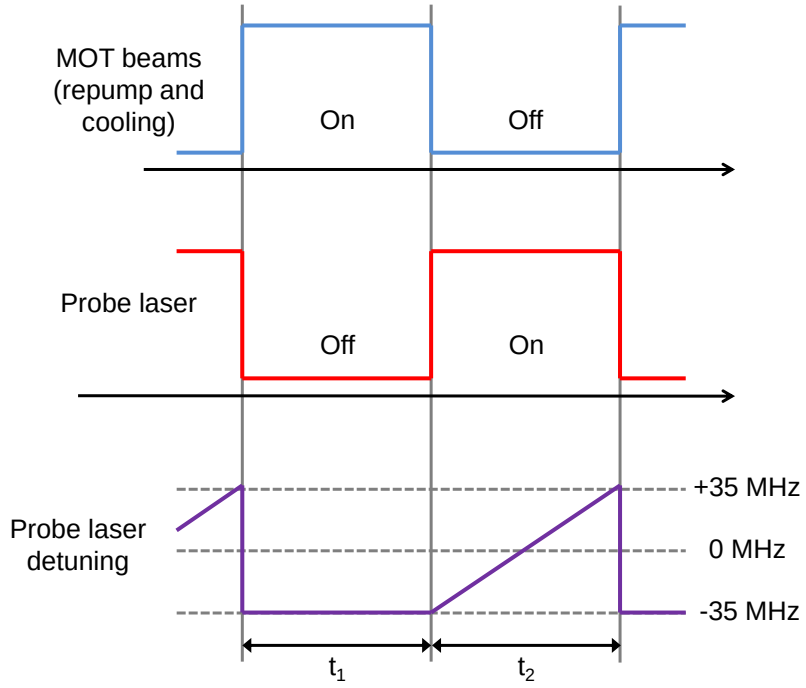

Figure 7.5: *Timing scheme for single-photon absorption generated by the setup displayed in Figure* **??**.

cooling transition of ^{85}Rb from -30 MHz to +60 MHz. This was achieved by applying a sawtooth voltage signal to the AOM VCO (voltage controlled oscilla-

would require the probe beam to be obtained in single-pass mode through the AOM which introduces angular changes during the frequency ramp.

tor) to ramp the beam detuning across the transition frequency. A typical power spectrum and the VCO ramp that generates it is shown in Figures **??** and **??**.

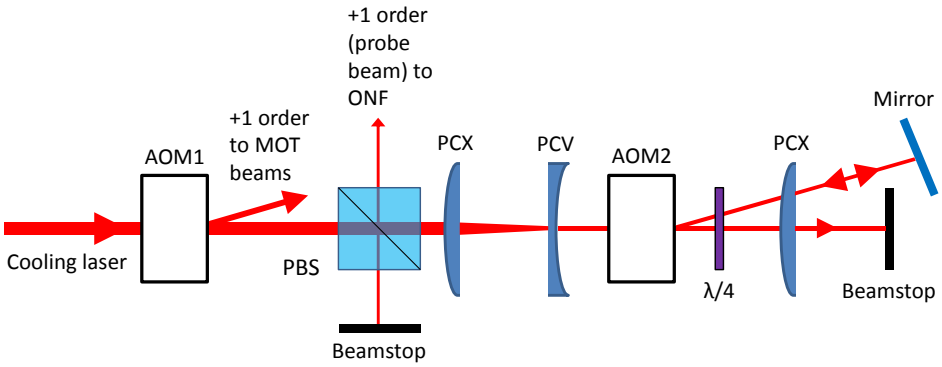

Figure 7.6: *Double-pass AOM setup. PBS = polarising beam splitter, PCX = plano-convex lens, PCV = plano-concave lens.*

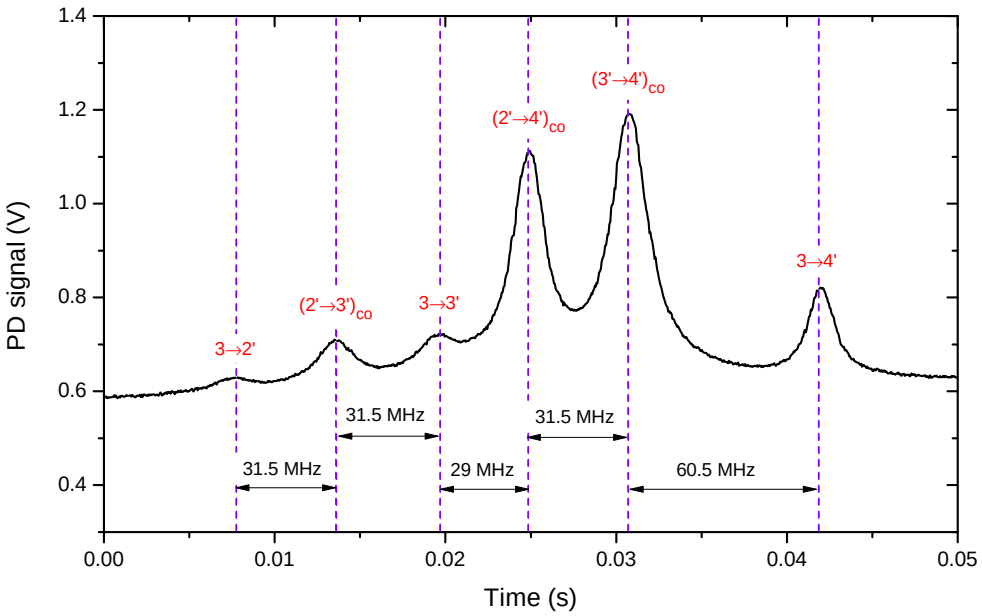

Figure 7.7: *Hyperfine spectrum of the cooling transition of ^{85}Rb indicating relative frequency positions of the transitions from F=3→F'=2,3,4. The x-axis, represented in time here, is a linear scan of PZT voltage which scans the ECDL frequency over this spectrum in 50 ms (se Chapter 2 for full details).*

The probe beam was coupled from free space to the pigtail of the ONF. The double-pass setup had to be resilient to angular movement of the probe beam during the frequency scan of the AOM. The power of the probe beam as a function of detuning (i.e. the intensity variation of the coupled signal during the ramp) was indicative of the quality of the double-pass setup and thus the free-space coupling of the probe into the ONF.

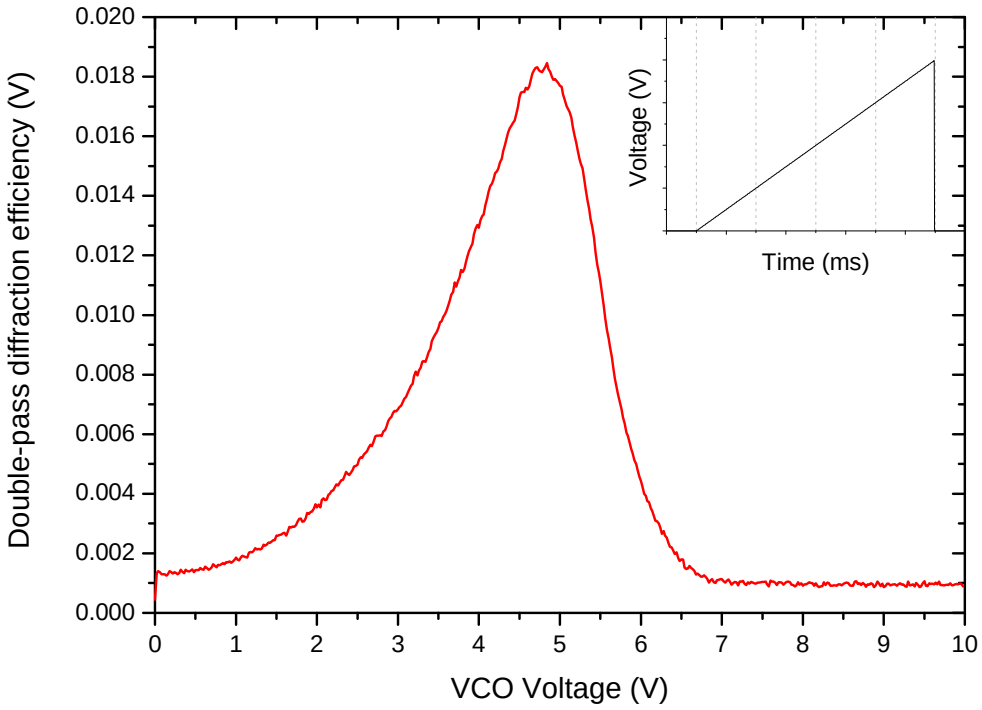

Figure 7.8: *As the VCO voltage is ramped from zero to 10 V (see inset) the probe beam undergoes a change in diffraction coupling efficiency through the double-pass setup. This power curve is maximum around the mid-voltage values, where absorption on the F=3→4 transition is expected to be observed.*

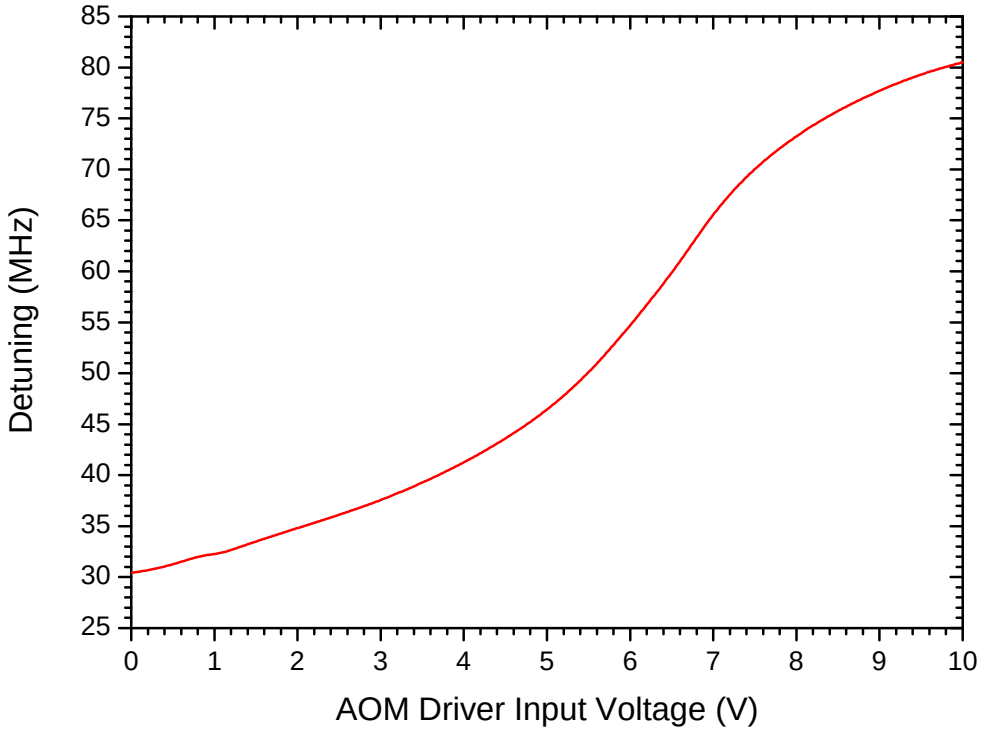

Figure 7.9: *AOM calibration curve for probe beam detuning.*

To perform a single photon absorption experiment as a function of probe beam detuning, the magnetic field for the MOT was switched on and a number of data sets were accumulated successively and averaged, while the probe beam was ramped from negative to positive detuning. The magnetic field and rubidium source were then switched off to record a set of reference signals. By comparing the probe signal while the MOT was on to that when it was off the transmission profile could be obtained.

7.3 Results

A comprehensive example of the experimental data obtained is shown in Figure **??**. An asymmetric absorbance profile centred on the cooling transition of ^{85}Rb is observed and this is shown by the blue data points and the solid black line in Figure **??**. To calibrate the x-axis of this plot in terms of probe beam detuning, the AOM calibration curve (Figure **??**) was used to map the AOM VCO to values of frequency in MHz.

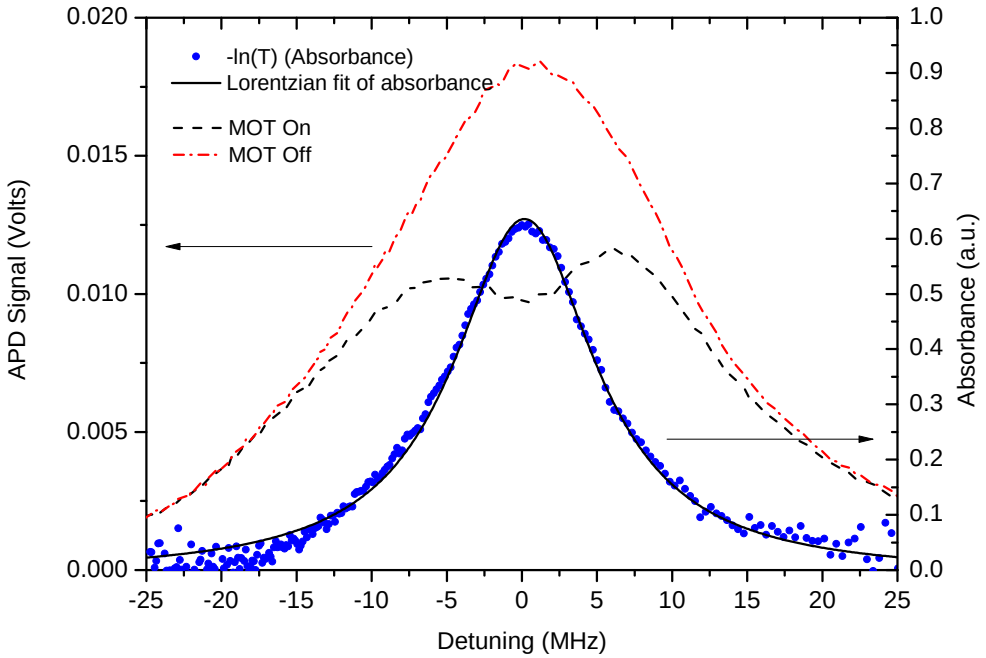

Figure 7.10: *Transmission data from a single photon absorption experiment using an input probe beam power of approximately 125 pW. The upper two lines (dot-dash red and dashed black) show the absorption of the probe beam by the cold atoms surrounding the nanofibre. The blue scatter plot is the absorbance, i.e. the negative logarithm of the transmission, T (i.e. MOT on / MOT off). The x-axis is calibrated in terms of positive and negative detuning centred on the peak of the absorbance plot. The black solid plot is a Lorentzian fit to the absorbance.*

The Lorentzian fit for the spectrum in Figure **??** yields an estimation of (11 ± 1) MHz for the linewidth, γ. This is significantly larger than the natural linewidth of 6 MHz for the cooling transition in ^{85}Rb. In this case, the input probe beam power was approximately 125 pW. By varying the input power, a variation in linewidth is evident as demonstrated in Figures **??** and **??** below. Even with low probe beam powers, large intensities of this light will exist at the nanofibre waist allowing the electronic transition to be easily saturated. With larger saturation parameters, S_0, the linewidth will be broadened according to $\gamma\sqrt{1+S_0}$. Thus, with lower probe powers and suitable detectors, it is possible to retrieve lineshapes which are almost free from power broadening.

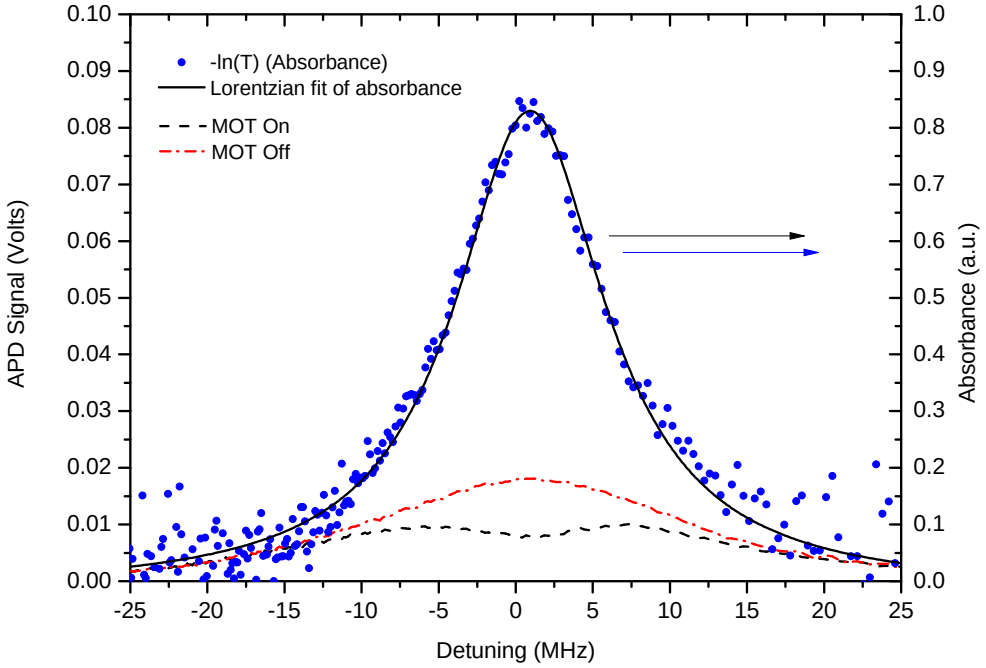

Figure 7.11: *Data for cold atom absorption. The lower curves show the probe transmission while the MOT is off (red, dash-dot curve) and while the MOT is on (black, dash curve) and are linked to the left y-axis. The probe beam input power = 150 pW. Absorbance plot (blue data points and solid, black fit linked to the right y-axis) shows a FWHM = (12±1) MHz.*

In [**?**] the measured linewidths for caesium approach 6.2 MHz for vanishing powers. This result exceeds the natural Cs D_2 linewidth in free space by almost 20%. This broadening can be explained by surface interactions, i.e., the van der Waals shift of the Cs D_2 line and the modification of the spontaneous emission rate of the atoms near the fibre.

One would expect to observe inhomogeneous broadening on the red side of the absorbance spectrum (see Chapter 4). In our system, the evanescent coupling region extends from the nanofibre surface radially outwards to a distance of about

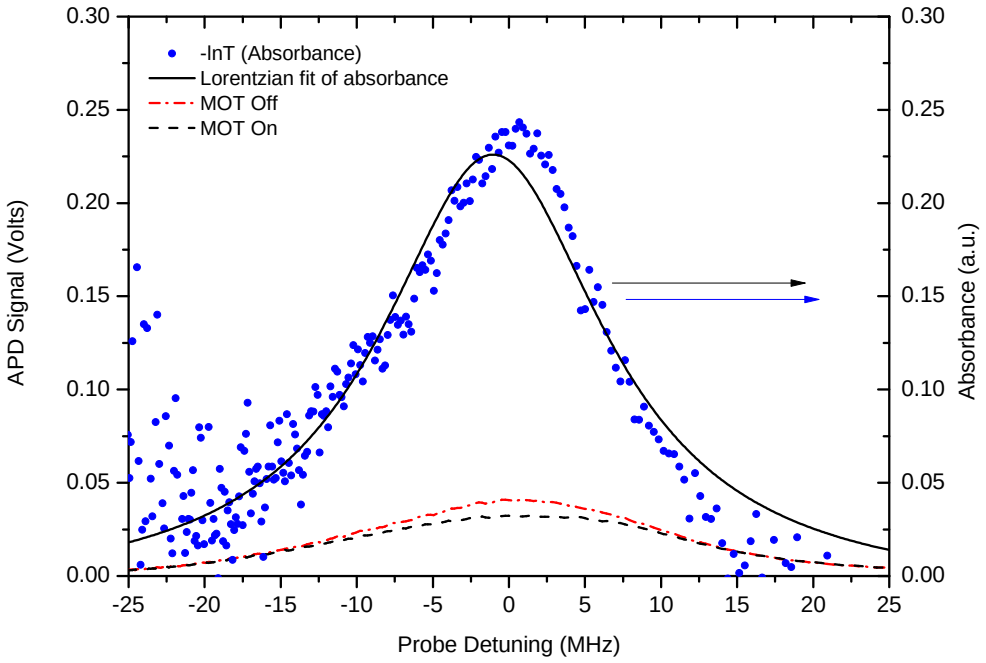

Figure 7.12: *Data for cold atom absorption. The lower curves show the probe transmission while the MOT is off (red, dash-dot curve) and while the MOT is on (black, dash curve) and are linked to the left y-axis. The probe beam input power = 273 pW. Absorbance plot (blue data points and solid, black fit linked to the right y-axis) shows a FWHM = (18±1) MHz.*

300 nm. On the other hand, the van der Waals interaction is dominant for a fraction of this distance – up to $\lambda/10$ from the nanofibre surface. The spatial $1/e$ extent of the evanescent field is approximately 70 nm for a 500 nm ONF (see Figure **??**). The corresponding hollow cylinder volume is 3.8×10^{-10} cm^3 and $N_{\text{eff}} = 4$. Thus, one can assume that four atoms are contributing to the absorbance lineshape and, as they are within $\lambda/10$ nm of the surface, they may experience van der Waals interactions with the ONF. All atoms which are within the evanescent field have some finite probability of coupling to the nanofibre. Only four of those atoms are within the region of significant surface interactions and contribute to an asymmetric lineshape. With a hollow cylinder volume of 2.3×10^{-9} cm^3 (using the full extent of the evanescent field, 300 nm), N_{eff} is 23. Thus, there are many more atoms outside the range of van der Waals interactions which contribute to the lineshape. This leads to the observation of symmetric profiles for "large" clouds.

In work by Nayak *et al.* [**?**], they estimate that there were 10 atoms near the ONF. In that work, the probe laser power is ∼10 fW (∼25 nW/cm^2), i.e. low enough not to saturate the atoms. The absorption reaches 65% at the line centre for a small number of atoms which implies that the photoabsorption for one

atom is approximately 10%. Furthermore, this value is five times smaller than the theoretically estimated value for one atom sitting *on* the nanofibre surface. Therefore, the atoms may be located around 100 nm away from the surface (see [?, ?, ?]).

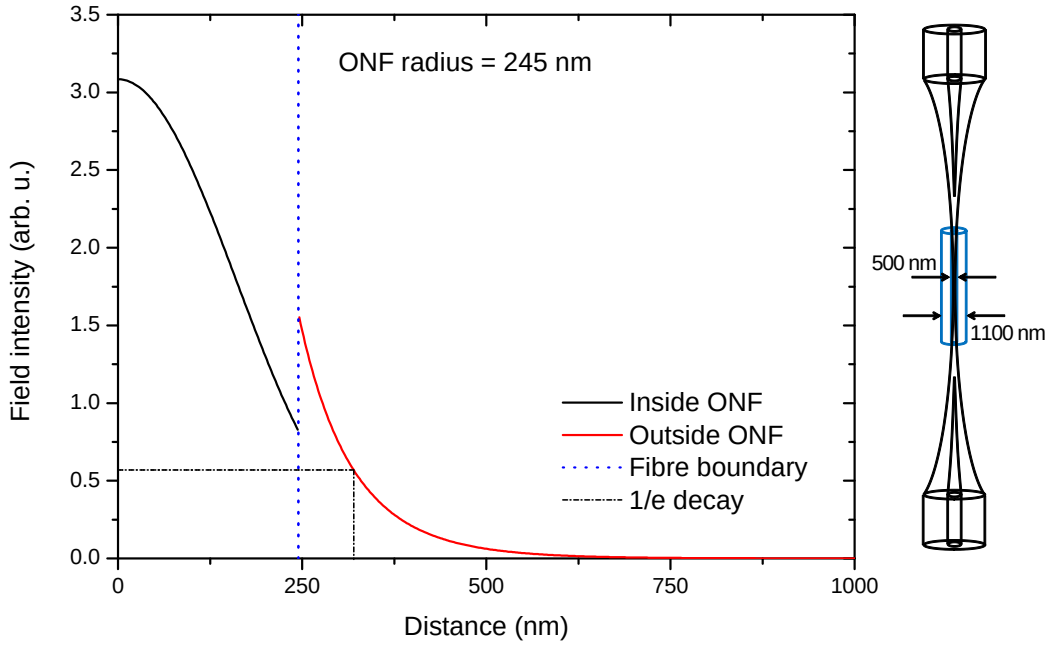

Figure 7.13: *A plot showing the intensity of the HE_{11} mode inside and outside the ONF. The evanescent field intensity approches zero around 600 nm, or 350 nm from the surface of the ONF. The distance at which the initial intensity is reduced to 1/e (37% of 1.56) is 320 nm from the surface.*

Without knowledge of the ONF diameter, the true value of N_{eff} is unknown and values given here are speculation. Chapter 8 discusses the limitations of the fibre pulling rig used in this work and how improvements will lead to prior knowledge of the ONF diameter.

Lineshapes have been observed with various different broadenings as seen in Figures **??**, **??**, and **??**. Between Figures **??** and **??**, only the MOT beam alignment was changed which indicates that the natural linewidth can be resolved easily with correct cloud alignment. Furthermore, it is not clear what influences the lineshape to exhibit blue or red-side broadening as seen in Figures **??**-**??**.

7.4 Conclusion

In this chapter, the ONF has been used to carry a probe beam through the central region of the cloud of cold ^{85}Rb to probe the cooling transition absorption

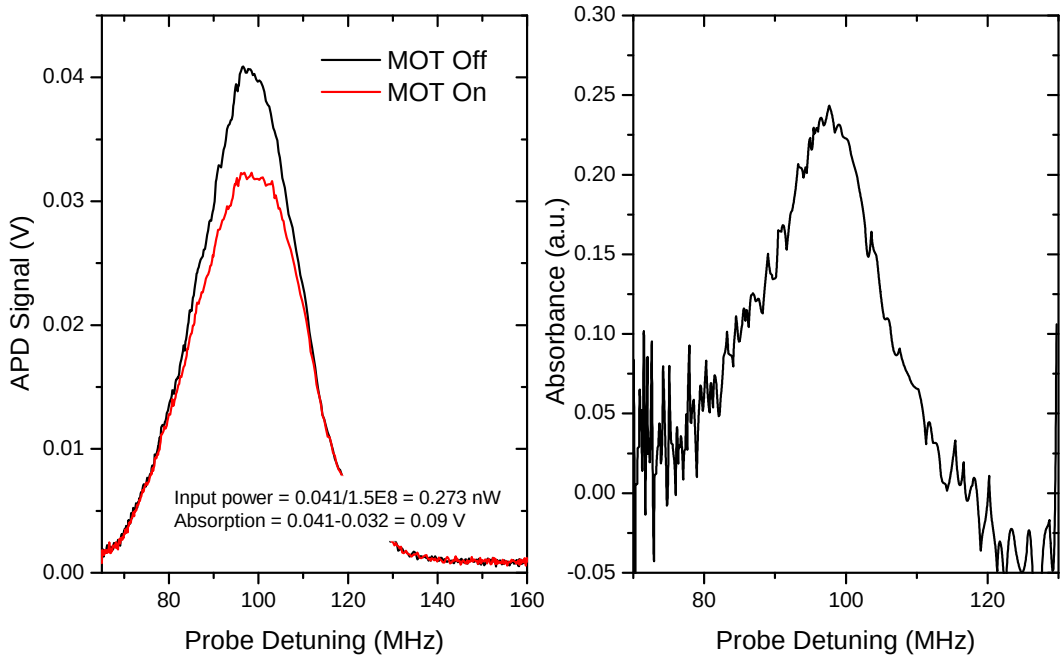

Figure 7.14: *Left panel: Raw data for cold atom absorption. Right panel: Absorbance profile. Linewidth is (18±4) MHz with 24% absorbance (25% absorption). This profile shows red-side broadening. Input power 273 nW.*

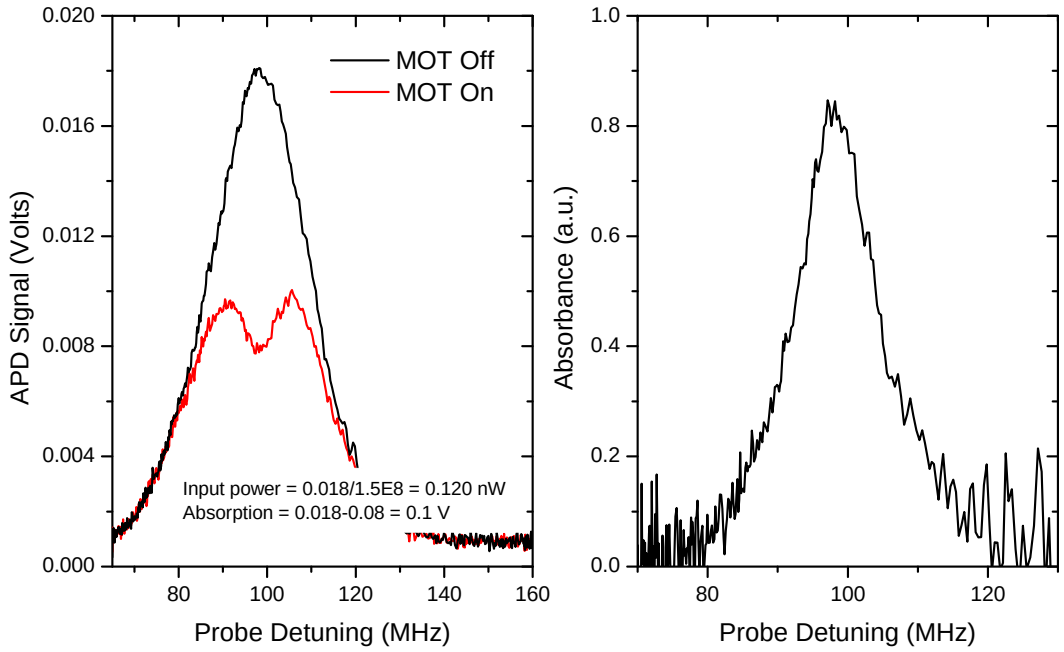

Figure 7.15: *Left panel: Raw data for cold atom absorption. Right panel: Absorbance profile. Linewidth is (14±1) MHz with 83% absorbance (66% absorption). This lineshape displays blue-side broadening. Input power is 120 nW.*

spectrum. Absorbance levels of over 80% have been reached with a modestly dense MOT ($\sim 10^{10}$ atoms/cm^3.). The width of the lineshapes was seen to vary with MOT beam alignment and input probe power. The natural linewidth of the

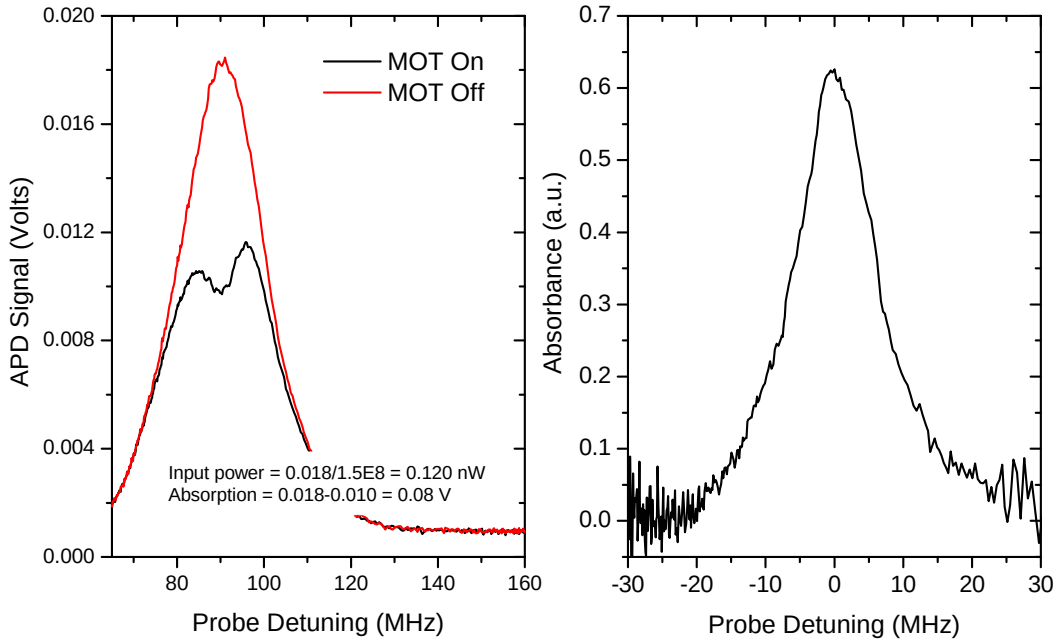

Figure 7.16: *Left panel: Raw data for cold atom absorption. Right panel: Absorbance profile. Linewidth is (5.7±0.2) MHz with 65% absorbance (50% absorption). This lineshape displays blue-side broadening. Input power is 120 nW.*

cooling transition, 5.7 MHz, was observed with an input beam of 120 nW.

To demonstrate absorption, small ONFs are necessary. For an ONF with radius in the region of 100 nm, not only is the power carried in the evanescent field large, but the spatial extent of the evanescent field is impressive. The primary issue in creating these small waveguides is accurate fabrication.

This chapter also reports the first demonstration of in-ONF absorption spectroscopy of ^{85}Rb – previously, similar demonstrations have been seen with Cs [**?**, **?**]. With advances in the fibre pulling rig, ONF absorption could be *de rigueur* for this experimental work as it offers not just the possibility of probing the atom cloud anywhere within the MOT boundaries, but also the ability to probe a specified number of atoms (by changing MOT parameters).

Chapter 8

Conclusions, Limitations and Proposals

In this final chapter, a conclusion which summarises this work and its context in the field is given followed by a number of experimental proposals. The foundation of these proposed studies is the optical nanofibre: the ability to fabricate a high-transmission ONF with a particular waist diameter is paramount to the development of cold atom + ONF experiments.

8.1 Conclusion

The body of work presented in this thesis focused on the integration of optical nanofibres (ONF) with a laser-cooled sample of ^{85}Rb atoms. This atom+nanofibre system was investigated experimentally and theoretically. Cold ^{85}Rb atoms were produced with a magneto-optical trap (MOT) in ultra-high vacuum (Chapter 2). The MOT is now a well-established tool for producing cold atomic samples with sub-Doppler temperatures less than 1 mK. To configure the MOT, three orthogonal laser beams of equal intensity were retro-reflected upon each other to form an intersection of six cooling beams. These beams then converged at the zero point of a quadrupole magnetic field, within a vacuum chamber, where the cold atom cloud was formed from a background vapour of rubidium. The resulting cloud was found to have a temperature in the range of 100-900 μK depending on MOT parameters, a diameter of 1.5 mm and a steady-state population of 10^8 atoms.

Usually, free-space probe beams and external imaging devices are used to mea-

sure typical MOT characteristics. The final section in Chapter 2 describes a high-quality imaging objective for applications involving imaging atomic clouds produced in MOTs. This work shows how ONFs can be used extremely effectively as probes in the atomic sample to investigate parameters such as trap loading times, density and temperatures. The nanofibre probe not only allows better understanding of the operation of a MOT, but may also act as a tool in quantum technologies. The principle behind the integration of the nanofibre and atomic cloud is that, provided the nanofibre diameter is suitably small (i.e. of the order of the wavelength of light it should carry and less), the fluorescence from the cold atoms can couple to the guided mode of the nanofibre. Placing a detector at either end of the nanofibre allows one to record the photon counts or fluorescence signal from the atom cloud at the nanofibre. The number of coupled photons is related to the atomic density of the atom cloud in the vicinity of the fibre. The optical nanofibres were fabricated from commercially-available, single-mode optical fibre using a heat-and-pull technique. Chapter 3 describes the setup in detail. A clean and stable oxygen-butane flame is used to heat the fibre while it is being controllably stretched. This has the effect of reducing the diameter of the heated region. Using this technique, fibres with transmissions of up to 99% and diameters approaching just 100 nm have been fabricated.

A comprehensive theoretical study of the surface interactions between the nanofibre and surrounding cold atoms was presented in Chapter 4. This work demonstrates that the signatures of the van der Waals and the Casimir-Polder interactions can be found in the fluorescence emission spectrum of the cold ^{85}Rb placed near the nanofibre. To the author's best knowledge, this work is the first comprehensive study of the Casimir-Polder effect in this system. The fluorescence spectrum from the cold atoms displays a red-shift of the peak as well as red-side broadening. The physical interpretation of this asymmetric broadening effect is not yet fully understood. The van der Waals force dominates in the region from the nanofibre surface out to a radial distance of $\approx \lambda/10$ and then the Casimir-Polder force becomes important. However, the spectrum itself is broadened and shifted primarily by the van der Waals interaction. As shown for the first time for the ^{133}Cs-ONF and ^{85}Rb-ONF system, the inclusion of the Casimir-Polder effect introduces very little additional broadening and adds a small blue-shift on to the red-shift of the spectrum. These interactions are stronger for smaller clouds with radii approaching that of the nanofibre.

In Chapter 5, a number of experiments were carried out using the nanofibre to collect the fluorescence from the cloud. The procedure of cloud-nanofibre align-

ment is carried out with a pair of CCD cameras and an SPCM. The relationship between the coupling efficiency and the size of the nanofibre was explored theoretically for different cloud densities for the first time in the history of cloud-ONF publications. Achieving a higher cloud density dramatically improves the number of atoms coupled to the nanofibre. The remainder of Chapter 5 explores two complementary temperature measurement techniques which exclusively use the nanofibre. To the author's best knowledge, this work is the first demonstration of such comprehensive temperature measurements in the cloud-ONF system and is, therefore, critical in our understanding of the ONF as a probe placed inside an extremely cold atomic sample. Firstly, the temperature of the cold atom cloud is measured using the method of forced oscillations. Over the course of a number of experiments, with the cooling laser detuned from the cooling transition by 12.4 MHz, results having the temperature of the cloud both above and below the Doppler limit were observed. This proved to be in good agreement with a temperature measurement carried out using a conventional photodiode for detection, which gave a result of $\sim$130 μK. Using the ONF, sub-Doppler temperatures were observed for smaller clouds, i.e. those with fewer trapped atoms. Furthermore, the trend of reduced temperatures for increased red-detuning was observed and it was found that the temperature of the atoms only went below the Doppler limit for very high values of red-detuning. Coupling this with the other results it appears the presence of the ONF may increase the temperature of the trapped atoms. Yet by reducing the number of atoms in the cold atom cloud or by using greater red-detuning (which also reduces the number of trapped atoms) the effect of the ONF can be reduced. This then allows sub-Doppler temperatures to be achieved in the presence of the ONF.

To address the possibility of density improvements in the MOT to increase atom-ONF coupling, a dark MOT (DMOT) was implemented. The DMOT utilises a hollow repump beam which allows atoms at the centre of the MOT to accumulate in the lower hyperfine ground state. In this so-called "dark" state, the atoms do not experience the density-limiting effects of a usual high-N_A MOT such as radiation pressure. Due to the large frequency separation of the two lower hyperfine ground states of ^{85}Rb, a depumping beam is necessary to achieve very dark DMOTs. The effects of the repump beam shadow shape and the depumper were investigated with freespace absorption spectroscopy. Using transient absorption curves, temperature increases were observed for high intensity depumping beams as expected. The remainder of the chapter was concerned with the first experimental implementation of a DMOT and ONF. To measure the 'darkness' of the

DMOT the quantity p was determined using the ONF. To estimate p, the fluorescent counts from the atoms in the upper "bright" hyperfine level $F = 3$ are divided by the counts from atoms in $F = 2$ and $F = 3$. The variation in p is explored with and without the inclusion of the depumper. The ONF was then used to examine the loading time of the DMOT as a function of p yielding the known result that, for darker DMOTs, the loading rate is reduced. Finally, it was found that p remains approximately constant for changing cooling laser intensity. Overall, the density of the DMOT was not improved beyond that of the BMOT, but with slight experimental adjustments to ensure the correct N_A regime is in effect, density improvements should be possible which will be beneficial for increasing the optical density ofthe system. These studies demonstrate that the ONF can be used to sensitively examine either population ($F = 2$ or $F = 3$) of atoms in the MOT.

Chapter 7 explores the use of the ONF as the carrier of a probe beam. Furthermore, this work is the first example of ONF absorption using ^{85}Rb. When light is coupled into an ONF, a significant portion of the light is guided within the evanescent field around the narrowest region. Absorption of the evanescent field component of the guided light can take place by atoms or molecules surrounding the ONF and this absorption in a probe signal passing through the fibre can be detected using an avalanche photodiode at the fibre output.This probe beam interacts via the evanescent field with the atoms around the ONF allowing in-fibre absorption spectroscopy. An AOM was used to perform a frequency scan of the probe around the $F = 3 \rightarrow F' = 4$ transition in ^{85}Rb to map out the absorption spectrum. With the lowest probe beam powers, the natural linewidth of the cooling transition can be resolved (6 MHz). Some lineshapes displayed asymmetric broadening indicating the presence of surface interactions but as these were not consistent, further exploration is necessary to determine which parameters are optimal for revealing such interactions.

It is clear that ONFs are an extremely versatile tool for probing atoms whether they are used as collectors or deliverers of light. The research in this thesis show how the ONFs allow a number of cold atom cloud characteristics to be determined, exhibiting great sensitivity to very low numbers of atoms in the vicinity of the ONF. While the MOT itself is relatively straightforward to implement, the key to this work and to its future role in quantum technologies is ensuring that the ONFs used are fabricated such that they are the correct diameter and continually maintain high transmission.

8.2 Limitations of ONFs

An ONF can be fabricated using the most basic equipment. In the work presented in this thesis, fabrication requirements are stringent. In fact, for use with a ^{85}Rb MOT, the ONF should be close to 180 nm in radius, have close to 100% transmission (which implies high adiabaticity) and have exemplary surface uniformity and smoothness. Most of the results presented in this thesis have been obtained because the ONF was suitable at that time. During the course of this work, while three different ONFs were used to generate data for Chapter 4, 5 and 6, at least an order of magnitude more ONFs were created, trialled and ultimately failed in UHV. The cost of fabricating, installing and then removing a broken or zero-transmission fibre from UHV is inexpensive for modern scientific standards, but extremely time-consuming and frustrating. The limitations of the work so far lie solely in the fibre pulling rig. A new rig has been built for a new incarnation of the cold atom experiment described here. The new rig should improve the quality of the ONFs produced for the ^{85}Rb MOT as it has individually controllable stages and utilises flame brushing. This enables custom taper shapes and sizes as well as back-calibration of the pull parameters with an SEM to achieve a specified waist diameter. In the following sections, the ONF diameter is assumed to be 360 nm and its transmission is assumed close to 100% such that there is no restriction on fluorescence signal collection and delivery of a probe beam to the atomic sample.

8.3 Two-photon absorption by cold ^{85}Rb via an ONF

Two-photon absorption (TPA) using an optical nanofibre in a rubidium vapour has been demonstrated recently [**?**]. In that work, TPA was observed with probe beam powers of less than 150 nW, which corresponds to less than 20 photons on average in the waist region of the nanofibre at any time. At low power levels, TPA may be useful for optical switching or for quantum logic gates based on the Zeno effect in the context of trapped atoms along a nanofibre [**?**, **?**].

We propose doing a similar experiment with laser-cooled ^{85}Rb using the scheme illustrated in Figure **??**. A 780 nm photon is detuned from the resonant frequency of the first atomic transition by an amount δ, producing a virtual population of the second atomic state. A second photon at 776 nm gives a detuning of the sum

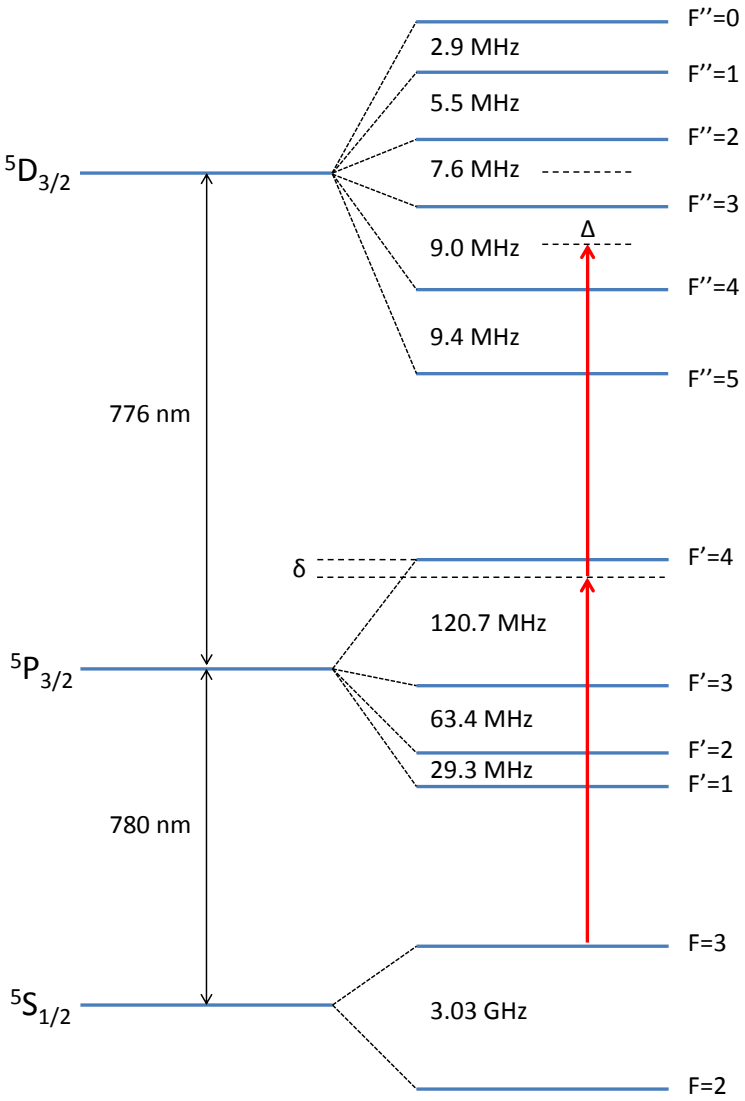

Figure 8.1: *Probe beam frequencies for TPA in cold ^{85}Rb via an ONF. A virtual population of the intermediate state will be generated by the cooling laser, while a scan over the final state, $^5D_{3/2}$, by a detuning Δ, is done with a second laser tuned to 776 nm.*

of the photon energies from the energy of the upper atomic state. By scanning Δ (i.e. the laser is scanned over the 776 nm transition) TPA can be observed as a decrease in the transmission of the 776 nm light. The colour of the fluorescent emission by the atoms using a spectrometer can also be monitored.

The proposed setup is shown in Figure **??**. The probe beam wavelength is monitored with a wavemeter during the experiment. Triggering is performed using the trigger input on the piezo control module. For small diameter nanofibres (≈400 nm), a significant fraction of the probe beam propagates in the evanescent field surrounding the cylindrical dielectric. For an atom in a vapour, transit-time

broadening due to the atom's limited interaction time with the evanescent field will be pronounced. We expect this contribution to be reduced in the case of atoms in a thermal cloud.

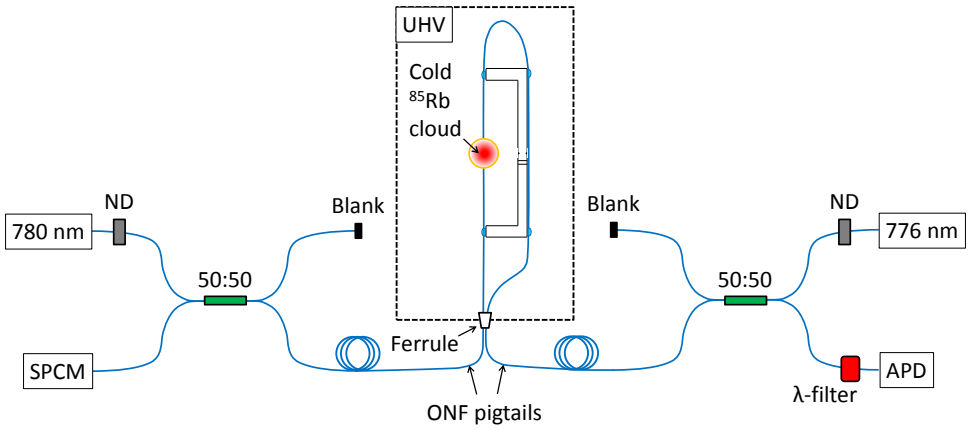

Figure 8.2: *The setup proposed to observe Doppler-free, TPA in an optical nanofibre.*

8.4 Simultaneous measurements of temperature and number of atoms via an ONF

Many modern laser-cooling setups perform experiments in a sequenced fashion with a temperature measurement (e.g. using time-of-flight) after the primary sequence. It is advantageous to collect temperature and number of atom data simultaneously (or, at least, within a short timespan of each other) as it provides the relevant MOT parameters rather than those found from a measurement later in the day when experimental parameters may have changed. In 2006, work by Silva *et al.*, [**?**], demonstrated a simple technique for measuring the temperature of a cloud of cold atoms using a freespace probe beam and an expansion period. In fact, their method was used for a DMOT. The advantage in using this technique for the DMOT is that one can really measure the temperature of just the dark region of the cloud by making sure the probe beam is much smaller than the cloud and passes through the dark region. Alignment with the dark region can be verified by a large frequency scan of the probe beam over the repump and cooling transitions to check population levels.

The proposed procedure is as follows. An on-resonance probe beam is sent towards the centre of the MOT and a suitable photodiode collects the signal. After loading the MOT until N_A reaches a steady state value, the MOT is switched off

and the cloud is allowed to expand. The resultant absorption signal diminishes as a function of time in a fashion similar to Figure **??**. The derivative of the absorption signal is taken and the maximum of the derivative occurs at some time t_m. Knowledge of the number of atoms and t_m allows the derivative to be fitted with the derivative of [**?**]

$$\frac{I}{I_0} = exp\left[\frac{\sigma N}{\pi\left(t_m^2\bar{v}^2 + t_m\bar{v}\sqrt{4t_m^2\bar{v}^2 - 2\frac{\sigma N}{\pi}} + \bar{v}^2t^2\right)}\right] \tag{8.1}$$

where $\bar{v}$ is the parameter to be determined. Thus, T can be calculated with $T = m\bar{v}/3k_B$.

This experiment can potentially be performed with the evanescent field of an ONF with some modifications to the model. In this case, one still has a weak,[1] narrow probe beam passing through the centre of an atomic cloud. As the diameter of the probe beam is much smaller than the extent of the cloud, one can treat it as a line source. The atomic density must be modified to account for the presence of the ONF using a "shadowing factor" g given by [**?**]

$$g(r) = 1 - \frac{\sin^{-1}(a/r)}{\pi}. \tag{8.2}$$

where a refers to the ONF radius and r is the radial distance between the atom and centre of the ONF. Thus, at the ONF surface, $g(r = a) = 1/2$. This factor is applied to the time derivative of the cloud density.

Additionally, for small times, gravity can be neglected as the isotropic expansion of the cloud is dominant compared to the centre-of-mass motion due to gravity. This is partricularly true for ONF absorption where one is measuring the signal from a just a few atoms which are closest to the fibre surface and are in the coldest region of the MOT. Figure **??** shows the theoretical absorption signal for a 75 μK cloud during expansion from the ONF surface ($a = 180$ nm). The signal returns to 0 within 5 ms.

Figures **??** and **??** illustrate the theoretical effect of using different ONF diameters and measuring different temperatures. As discussed previously (see Section 7.1), smaller diameter ONFs are better for absorption studies. The smaller the ONF,

[1] If necessary, to avoid saturation of the near-surface atoms, a power restriction can be incorporated into the sequence using amplitude control of an AOM via an AOM driver or with a mechanical filter.

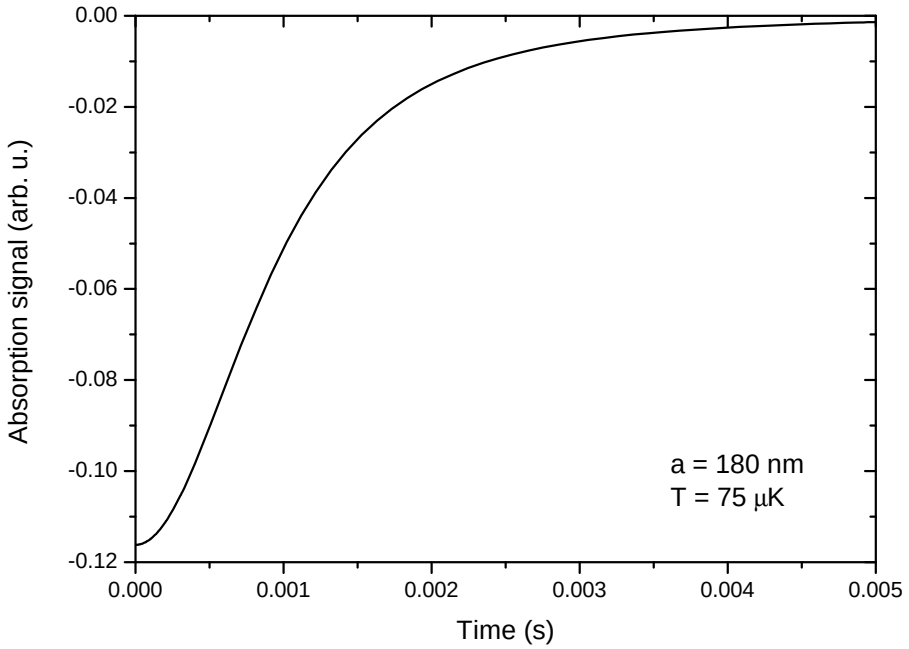

Figure 8.3: *Transient absorption signal for $a = 180$ nm, T=75 μK. ($N_A = 10^8$). This plot is obtained from calculations performed by Ravi Kumar in the QOG.*

the larger the absorption signal is. However, by changing the cloud temperature, Figure **??** shows that the position of the derivative peak, t_m, changes.

Work by Chen *et al.* [**?**], inspired by Gibble *et al.* [**?**], used optical pumping to acurately determine the number of cold atoms in the MOT. The linearly-polarized probe field in this method drives the $5^2S_{1/2}F = 2 \rightarrow 5^2P_{3/2}F' = 2$ transition of ^{87}Rb and the measurement is based on the following reasoning: the population in $F' = 2$ has the probability of one half to spontaneously decay to $F = 2$ and one half to spontaneously decay to $F = 1$. On average, each atom prepared in $F = 2$ initially can be optically pumped to $F = 1$ by absorbing two probe photons. Once the atom is in $F = 1$, it will not interact with the probe field. The transmission of the probe field is measured with a calibrated photodiode. The absorption energy of the probe field divided by the energy of *two* photons is the direct measurement of the atom number. Thus, the measured absorption energy does not depend on parameters such as detuning, polarization, intensity, and linewidth of the probe laser, population distribution among Zeeman sublevels, and Zeeman shifts induced by the magnetic field in the environment.

The sequence of the experiment is to switch off (for example, with an AOM) the cooling beams and then switch off the repump beam(s) after a time long enough to ensure all atoms are in $F = 2$. The probe laser is then switched on for a period of time anywhere between 5 to 500 μs. The area below the resulting absorption

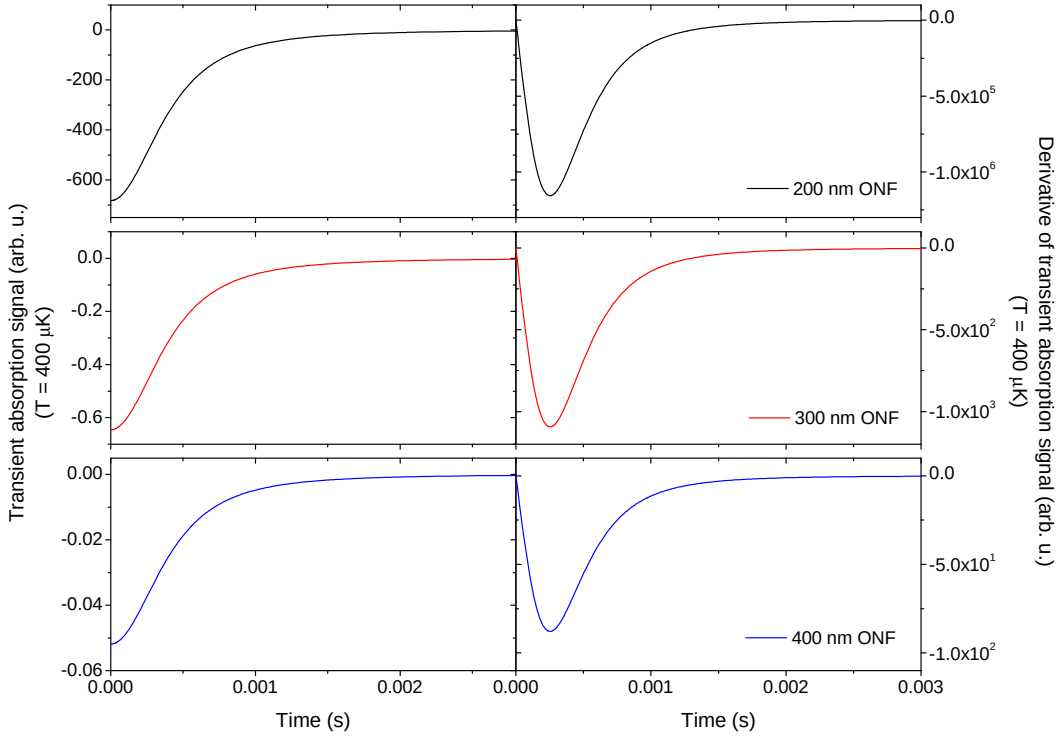

Figure 8.4: *Transient absorption signals and their derivatives for three different ONF radii (top: $a = 100$ nm, middle: $a = 150$ nm, bottom: $a = 200$ nm). While the position (in time) of the minimum of the signal does not change, the absorption depth does. This is due to the changing spatial extent of the evanescent field for different ONF radius – the smaller the ONF is, the further the evanescent field reaches. More atoms can absorb the probe beam around a smaller ONF. These data model the signal for $N_A = 10^8$ and $T = 400$ μK. These plots are obtained from calculations performed by Ravi Kumar in the QOG.*

profile yields the atom number.

Each measurement typically takes about 1 ms. During the optical-pumping process, each atom only absorbs two photons on the average and cannot be knocked away by the probe field. Atoms in $F = 1$ will be immediately recaptured once the MOT is turned on. Therefore, the measurement disturbs the MOT very little. The authors of [**?**] also recommend leaving the magnetic field on throughout the measurement as its presence during the process of optical pumping can minimize the population trapping of the dark state and avoid potential errors in determination of atom number.

If the density of the atom cloud is large enough to allow significant radiation trapping to occur or if the spontaneously emitted photon can be absorbed by another atom, the delay time before the probe pulse commences should be increased. This allows the atom cloud to expand and lowers the density. Then, the effect of the radiation trapping on the measurement of atom number can be

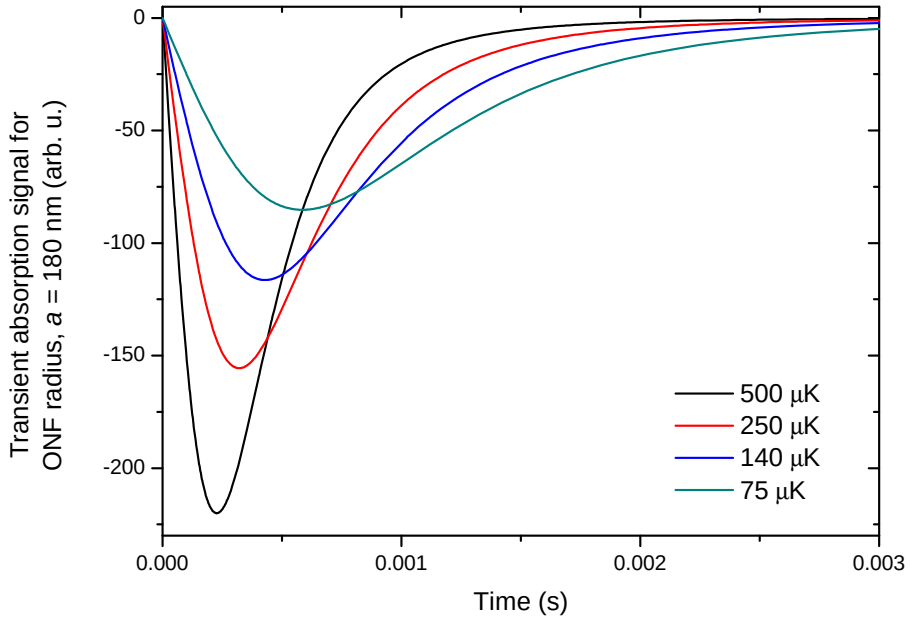

Figure 8.5: *Transient absorption derviative signals for four different temperatures: 500 μK (black), 250 μK (red), 140 μK (blue), 75 μK (green). The ONF here has a radius of 180 nm. These plots are obtained from calculations performed by Ravi Kumar in the QOG.*

minimized.

These two measurements of atom number and temperature are of critical importance in this work with cold atoms and an ONF as they can provide an insight into the behaviour of near-surface atoms. If the ONF diameter is known, the evanescent field spatial decay length is also known and these two experiments can be perfomed to yield a direct measurement of atom number, n_{eff}, atom density and atom temperature near the fibre. Knowldge of the temperature of such atoms is desirable as it will definitively answer the question about heating of atoms near the fibre surface.

8.5 Higher mode propagation in an ONF

Theoretical work in 2004 [**?**] proposed a scheme whereby a two-colour evanescent field around an ONF could be designed to create optical potential wells for use as atom traps. The two wavelengths are sent through the ONF in opposite directions and are both far detuned from the atomic resonance – one to the blue side and the other to the red. The atoms after loading can then be coupled to, and trapped near, a dielectric nanostructure without the need of additional external light fields.

For the caesium atom, the authors of [**?**] show that the light shifts of the $6^2S_{1/2} \leftrightarrow 6^2P_{3/2}$ transitions can be minimized by tuning one trapping beam to around 934.5 nm in wavelength (central red-detuned magic wavelength) and the other light to around 685.5 nm in wavelength (central blue-detuned magic wavelength).

Due to the small thickness of the ONF, the far-off-resonance fields have substantially differing evanescent decay lengths to produce a net potential with a large depth, a large coherence time, and a large trap lifetime. For example, [**?**] found that for a 0.2-μm-radius silica ONF carrying 30 mW of 1.06-μm-wavelength light and 29 mW of 700-nm-wavelength light, both fields circularly polarized at the input, gives for caesium atoms a trap depth of 2.9 mK, a coherence time of 32 ms, and a recoil-heating-limited trap lifetime of 541 s. In this particular case, the atoms are trapped at a distance of $\sim$200 nm from the ONF surface. Furthermore, various optical potential configurations can be designed by controlling the input polarisations of the two fields. When both input light fields are circularly polarized, a set of trapping minima of the total potential in the transverse plane is formed as a ring around the ONF. This design allows confinement of atoms to a cylindrical shell around the ONF. When one or both of the input light fields are linearly polarized, the total potential has two local minimum points in the transverse plane. This design allows confinement of atoms to two straight lines parallel to the ONF axis. Spatial positioning of cold atoms in well-defined optical potentials around an ONF has applications in quantum information processing, whereby the trapped atoms could be entangled using photons passing through the fibre.

While two-colour trapping has been demonstrated with caesium atoms around an ONF [**?**, **?**], a more graceful approach exists which has not yet been demonstrated. Figure **??** is a plot of propagation constant, β/k_0, versus V-number for an ONF. The range $0 < V < 2.4$ is single mode, while three modes can propagate in the region $2.4 < V < 3.8$: TE_{01}, TM_{01}, and HE_{21}. By choosing the ONF diameter carefully, both the HE_{11} mode and higher modes can be excited in the waveguide.

In [**?**] a novel type of blue-detuned evanescent field trap for cold neutral atoms based on two-mode interference in ONFs was presented. The ONF considered was designed such that only the four lowest order modes propagate: the fundamental mode (HE_{11}) and the first three higher order modes (TE_{01}, TM_{01} and HE_{21}). If the modes are coherently excited, they will yield a stationary interference pattern while co-propagating in the fibre due to their different phase velocities. This is of critical interest for generating unique trapping geometries, not just for laser-

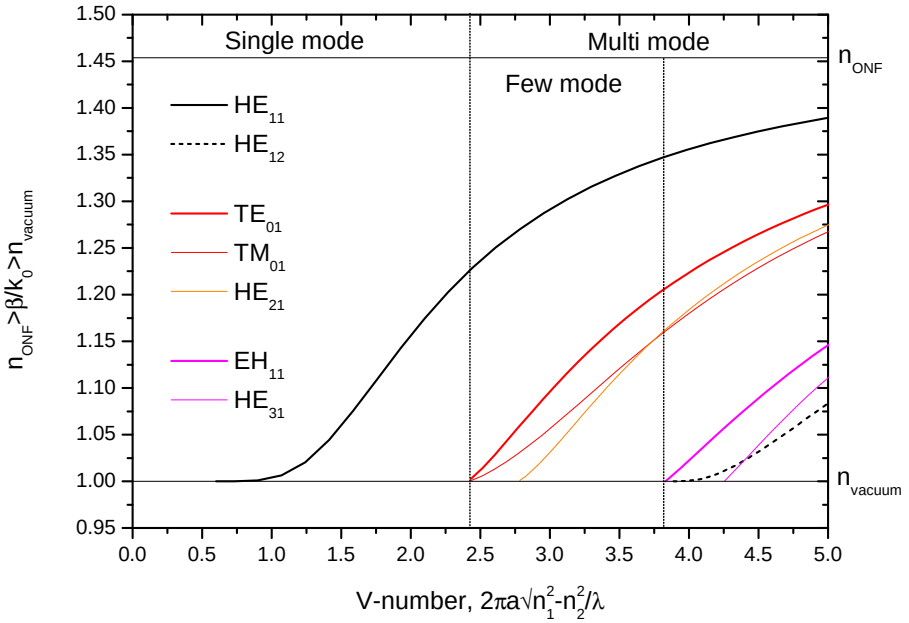

Figure 8.6: *A plot of the propagation constant, β (normalized to k_0) against V-number for an optical nanofibre (or microfibre for V-numbers above $\approx$4.5 with a fixed λ of 780 nm) with cladding (vacuum) and core refractive indices as 1 and 1.4595, respectively. The weak guidance condition is not applicable here as Δn is large (1$\leftrightarrow$1.4537). Thus, the LP_{11} modes separate out to reveal the exact modes. The dashed, vertical lines indicate the boundary between single- and multi-mode (including few-mode) guidance in the waveguide ($V = 2.405$).*

cooled atoms, but also for colloidal particles [**?**, **?**].

In 2012, our group published experimental work on higher mode propagation in ONFs [**?**]. A Laguerre–Gaussian beam was created in free space using a spatial light modulator (SLM)[2] and coupled to a few-mode fibre. This device allows convenient switching between the fundamental and LP_{11} fibre modes. By selecting a few-mode fibre with a relatively low cladding-core ratio, the propagation of the LP_{11} mode down to a submicron waist was maintained. Furthermore, by observing the transmission profile during tapering, it is possible to decisively terminate the pulling process in order to eliminate the two degenerate HE_{21} modes of the LP_{11} mode (Figure **??**). As a result, a nanofibre can be fabricated through which only the TE_{01} and TM_{01} components of the LP_{11} mode propagate. With advances in the fibre pulling rig, creating higher modes in an ONF should become routine.

[2]A spatial light modulator is an electronic device which modulates the phase, or intensity, or both, of light. The SLM used here was a phase only, reflective, liquid-crystal-on-silicon SLM (Holoeye Pluto NIR HEO1080HP) with a resolution of 1920×1080 pixels and an active area of 15.36×8.64 mm^2, designed for near infrared wavelengths around 1064 nm.

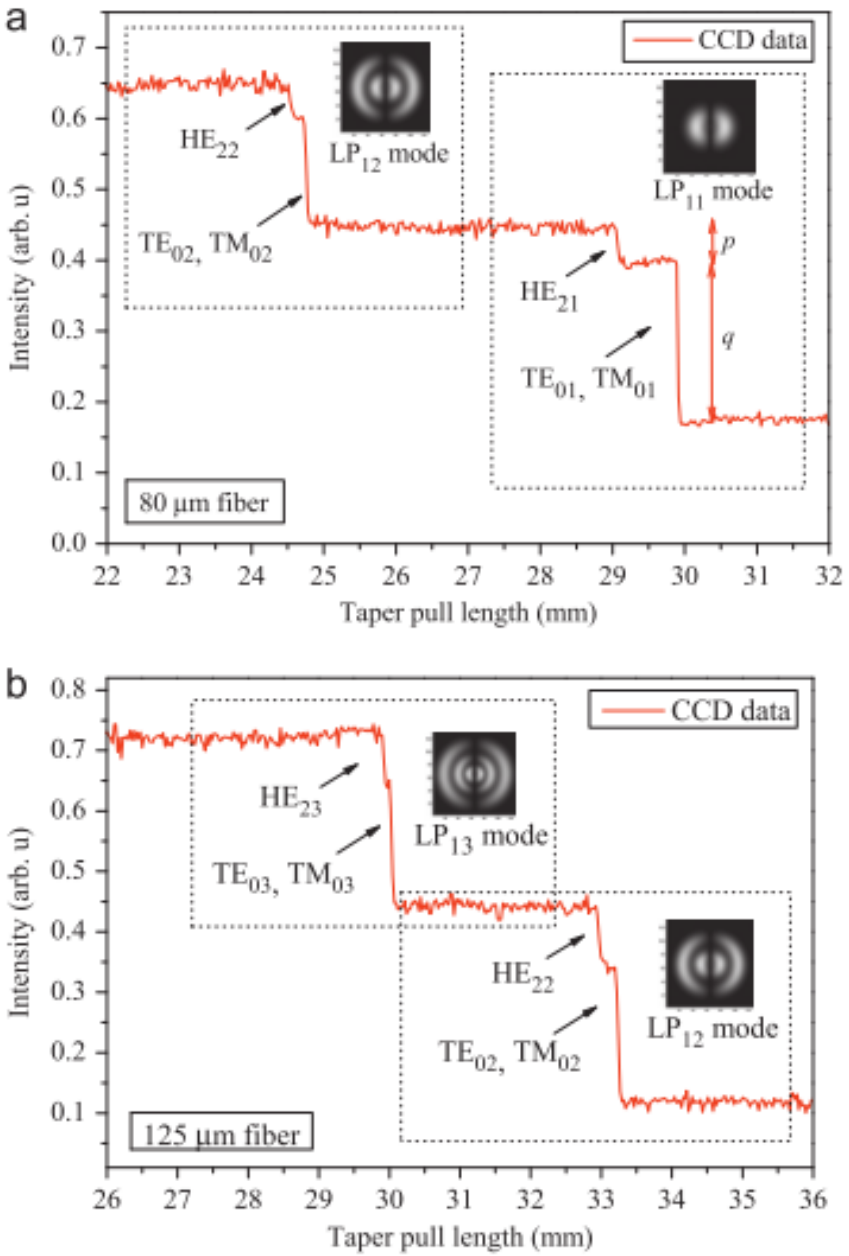

Figure 8.7: *From [?]: (a) This plot highlights the individual mode losses from each LP_{lm} set. Here p and q are the intensity drops due to the loss of the HE_{21} modes and the TE_{01} and TM_{01} modes, respectively. (b) Comparative plot of the mode drops when a similar tapering process is conducted with Thorlabs 1310BHP 125 mm fibre, but highly saturated at the start of tapering to highlight the mode drops. This shows loss into higher cladding modes (LP_{13}), due to stronger non-adiabatic behavior of the fibre taper.*

Higher modes offer a wide variety of trapping geometries that will lend themselves to future work on atom interfacing via waveguide structures where only one laser is required. Recent work by Masalov and Minogin [?] showed that excitation

rates for higher-order modes can be about 5–10 times higher than that for the fundamental mode. The high pumping rate of the higher-order modes in optical nanofibers may find important applications in quantum optics and metrology, including the creation of new trapping geometries for atoms, new types of coupling with microresonators, new schemes for evanescent field sensing of atoms and high-accuracy position detection of atoms around nanofibers.

8.6 Final remark

At the closing of the work described in this thesis, the Quantum Optics Group transformed into the Light-Matter Interactions Unit and set up a new home at the Okinawa Institute of Science and Technology Graduate University (OIST) in Japan. During my short stay at OIST, the university wrote an article profiling our research group to highlight our activities and fields of interest. I had the opportunity to help produce a simplified scientific illustration of the MOT - this is shown in Figure **??**. The full article can be found at https://www.oist.jp/press-room/news/2012/11/30/new-unit-profile-shedding-light-light-and-matter

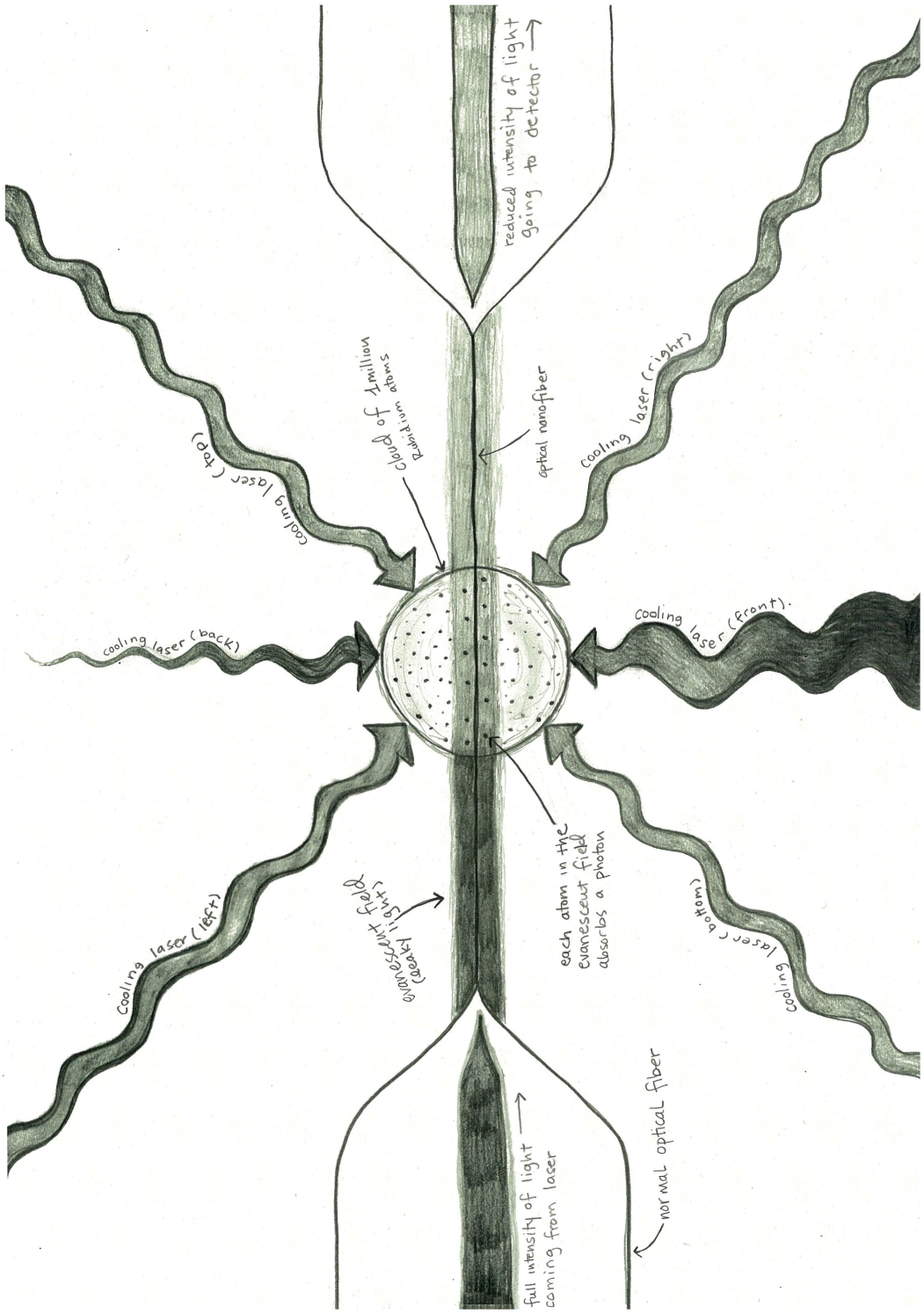

Figure 8.8: *Pencil illustration of the MOT and ONF created for a Unit Profile at Okinawa Institute of Science and Technology. (©V. Schipani)*

Appendix A

Electric field analysis of HE_{11} for an ONF

A.1 Spatial distribution of the electric field for the fundamental guided mode, HE_{11}, of an optical nanofibre

The following appendix appeared with [**?**]. We represent the operator of a quantized vacuum electric field of the guided modes of a nanofibre in a standard form.

$$\mathbf{E} = \sum \boldsymbol{\mathcal{E}}_\lambda a_\lambda + \text{h.c.}, \tag{A1}$$

where $\boldsymbol{\mathcal{E}}_\lambda$ is the electric field of a single vacuum guided mode, a_λ is the photon annihilation operator, and index λ describes the direction of propagation and polarization of a single vacuum guided mode. The electric field of a single guided mode can be represented as [**?**]

$$\boldsymbol{\mathcal{E}}_\lambda = i\sqrt{\frac{\hbar\omega_\lambda}{2\varepsilon_0 L}}\,\tilde{\mathbf{e}}_\lambda \mathrm{e}^{i\beta_\lambda z + im\varphi}, \tag{A2}$$

where ω_λ is a mode frequency, β_λ is a propagation constant, $\tilde{\mathbf{e}}_\lambda = \tilde{\mathbf{e}}_\lambda(r,\phi)$ is a normalized amplitude of the electric field, m is a quantum number of the mode angular momentum, and L is the length of a one-dimensional "box" which is defined by a spatial periodicity of the field. The electric field amplitude of a

single guided mode is normalized as

$$\int_0^{2\pi}\int_0^{\infty} n^2(r)\left|\widetilde{\mathbf{e}}_\lambda\right|^2 d\varphi r dr = 1, \tag{A3}$$

where $n(r)$ is the value of the refractive index equal to n_{core} inside the fibre and $n_{clad} = 1$ outside the fibre. The above representation of the vacuum field corresponds to a standard form of the vacuum field Hamiltonian

$$H_{\text{vac}} = 2\varepsilon_0\varepsilon\sum\int dV\left|\boldsymbol{\mathcal{E}}_\lambda\right|^2\left(a_\lambda^\dagger a_\lambda + \tfrac{1}{2}\right) = \sum\hbar\omega_\lambda\left(a_\lambda^\dagger a_\lambda + \tfrac{1}{2}\right). \tag{A4}$$

For the fundamental guided mode, HE_{11}, the propagation constant β is defined by the eigenvalue equation as

$$\begin{aligned}\frac{J_0(ha)}{haJ_1(ha)} = &-\left(\frac{n_{core}^2 + n_{clad}^2}{2n_{core}^2}\right)\frac{K_1'(qa)}{qaK_1(qa)} + \frac{1}{h^2a^2}\\ &-\left[\left(\frac{n_{core}^2 - n_{clad}^2}{2n_{core}^2}\right)^2\left(\frac{K_1'(qa)}{qaK_1(qa)}\right)^2\right.\\ &\left.+\left(\frac{\beta}{n_{core}k}\right)^2\left(\frac{1}{h^2a^2} + \frac{1}{q^2a^2}\right)^2\right]^{1/2},\end{aligned}$$

where J_m are Bessel functions of the first kind, K_m are modified Bessel functions of the second kind, $k = \omega/c$, and

$$h = \sqrt{n_{core}^2k^2 - \beta^2}, \qquad q = \sqrt{\beta^2 - n_{clad}^2k^2}.$$

We note that there are four different field distributions for the fundamental mode HE_{11}: two with opposite directions of propagation and two with opposite circular polarizations. In what follows, we write the field distribution for a guided mode with positive propagation constant and positive circular polarization using decomposition over cylindrical unit vectors

$$\widetilde{\mathbf{e}} = \mathbf{e}_r\widetilde{e}_r + \mathbf{e}_\varphi\widetilde{e}_\varphi + \mathbf{e}_z\widetilde{e}_z.$$

The cylindrical components of a normalized electric field amplitude for the HE_{11}

mode in the core region are given by [**?**]

$$\begin{aligned}
\widetilde{e}_r &= iA\frac{q}{h}\frac{K_1(qa)}{J_1(ha)}\left[(1-s)J_0(hr)-(1+s)J_2(hr)\right], \\
\widetilde{e}_\varphi &= -A\frac{q}{h}\frac{K_1(qa)}{J_1(ha)}\left[(1-s)J_0(hr)+(1+s)J_2(hr)\right], \\
\widetilde{e}_z &= 2A\frac{q}{\beta}\frac{K_1(qa)}{J_1(ha)}J_1(hr),
\end{aligned}$$

and outside of the core region are given by

$$\begin{aligned}
\widetilde{e}_r &= iA\left[(1-s)K_0(qr)+(1+s)K_2(qr)\right], \\
\widetilde{e}_\varphi &= -A\left[(1-s)K_0(qr)-(1+s)K_2(qr)\right], \\
\widetilde{e}_z &= 2A\left(q/\beta\right)K_1(qr).
\end{aligned}$$

In the above equations s is a dimensionless parameter such that

$$s=\frac{1/h^2a^2+1/q^2a^2}{S},$$

where the denominator is as

$$S=J_1'(ha)/haJ_1(ha)+K_1'(qa)/qaK_1(qa),$$

The normalization constant defined from Eq. (**??**) is

$$A=\frac{\beta}{2q}\frac{J_1\left(ha\right)/K_1\left(qa\right)}{\sqrt{2\pi a^2\left(n_{core}^2N_1+n_{clad}^2N_2\right)}}, \tag{A5}$$

where

$$\begin{aligned}
N_1 = \frac{\beta^2}{4h^2}&\left\{(1-s)^2\left[J_0^2\left(ha\right)+J_1^2\left(ha\right)\right]\right. \\
&\left.+\left(1+s\right)^2\left[J_2^2\left(ha\right)-J_1\left(ha\right)J_3\left(ha\right)\right]\right\} \\
&+\frac{1}{2}\left[J_1^2\left(ha\right)-J_0\left(ha\right)J_2\left(ha\right)\right],
\end{aligned}$$

$$N_2 = \frac{J_1^2(ha)}{2K_1^2(qa)}\left\{\frac{\beta^2}{2q^2}\left[(1-s)^2\left[K_1^2(qa)-K_0^2(qa)\right]\right.\right.$$
$$-(1+s)^2\left[K_2^2(qa)-K_1(qa)K_3(qa)\right]\Big]$$
$$\left.-K_1^2(qa)+K_0(qa)K_2(qa)\right\}.$$

The intensity distribution of the electric field inside the core is defined by a quantity

$$|\widetilde{\mathbf{e}}(r)|^2 = 2A^2\frac{K_1^2(qa)}{J_1^2(ha)}\left\{\frac{q^2}{h^2}\left[(1-s)^2J_0^2(hr)+(1+s)^2J_2^2(hr)\right]+\frac{2q^2}{\beta^2}J_1^2(hr)\right\}, \tag{A6.a}$$

and outside the core it is defined by the quantity

$$|\widetilde{\mathbf{e}}(r)|^2 = 2A^2\left[(1-s)^2K_0^2(qr)+(1+s)^2K_2^2(qr)+\frac{2q^2}{\beta^2}K_1^2(qr)\right]. \tag{A6.b}$$

A.2 Evaluation of the spontaneous decay rate into the fundamental guided mode

The following appendix appeared with [**?**]. The following derivation of the spontaneous emission rate follows a standard approach based on the Hamiltonian for a system "two-level atom + vacuum field" given by

$$H = \hbar\omega_0 b^+ b + \sum_\lambda \hbar\omega_\lambda\left(a_\lambda^+ a_\lambda + \tfrac{1}{2}\right) - \mathbf{d}\cdot\sum_\lambda\left(\boldsymbol{\mathcal{E}}_\lambda b^+ a_\lambda + \boldsymbol{\mathcal{E}}_\lambda^* b a_\lambda^+\right), \tag{A7}$$

where b^+ and b are the atomic excitation and de-excitation operators, a^+ and a the creation and annihilation operators, and $\mathbf{d}$ is a matrix element of the atomic dipole moment. For the Hamiltonian (**??**) the equations for probability amplitudes for the simplest case of a vacuum field initially in the vacuum state are

$$\dot{c}_{e,0} = \frac{i}{\hbar}\sum_\lambda \mathbf{d}\cdot\boldsymbol{\mathcal{E}}_\lambda \mathrm{e}^{-i\Delta_\lambda t}c_{g,1_\lambda}, \tag{A8.a}$$

$$\dot{c}_{g,1_\lambda} = \frac{i}{\hbar}\mathbf{d}\cdot\boldsymbol{\mathcal{E}}_\lambda^* \mathrm{e}^{i\Delta_\lambda t}c_{e,0}, \tag{A8.b}$$

where $c_{g,1_\lambda}$ are the probability amplitudes of the states which include the ground atomic state and the state of the vacuum field with one photon in mode λ and

$c_{e,0}$ is a probability amplitude of the state which includes the excited atomic state and the state of the vacuum field with zero photon numbers in all the modes.

Taking a formal solution of the second equation in the above set

$$c_{g,1_\lambda} = \frac{i}{\hbar}\mathbf{d}\cdot\boldsymbol{\mathcal{E}}_\lambda^* \int_{t_0}^{t} \mathrm{e}^{i\Delta_\lambda t'} c_{e,0}(t')dt', \tag{A9.a}$$

and substituting it into the first equation one can obtain an equation which describes the spontaneous decay of the upper atomic state

$$\dot{c}_{e,0} = -\frac{1}{\hbar^2}\sum_\lambda |\mathbf{d}\cdot\boldsymbol{\mathcal{E}}_\lambda|^2 \int_{t_0}^{t} \mathrm{e}^{i\Delta_\lambda(t'-t)} c_{e,0}(t')dt'. \tag{A9.b}$$

An application of the above equation to the vacuum modes of free space gives a well-known decay equation

$$\dot{c}_{e,0} = -\gamma_0 c_{e,0}, \tag{A10}$$

where γ_0 is half the spontaneous decay rate into free space,

$$W_{\mathrm{sp}} = 2\gamma_0 = \frac{1}{4\pi\varepsilon_0}\frac{4d^2\omega_0^3}{3\hbar c^3}. \tag{A11}$$

We now apply basic equation (**??**) to the fundamental guided mode HE_{11} of the vacuum field. The vacuum field of a single guided mode can be considered as periodic with spatial period, L, and the periodicity condition can be written as $\beta_\alpha L = 2\pi n_\alpha$, where $n_\alpha = 1, 2, 3, ...$ defines different values of the propagation constant, β_α. By making use of the periodicity condition, the sum over discrete numbers, n_α, in Eq. (**??**) can be replaced by an integral such that

$$\sum \to \frac{L}{2\pi}\int d\beta.$$

Taking into account a one-to-one correspondence between values of the propagation constant and frequencies of the vacuum modes, $\beta = \beta(\omega)$, one can replace $d\beta$ by $d\beta = \widetilde{\beta}' d\omega$, where $\widetilde{\beta}' = d\beta/d\omega$. This gives

$$\sum \to \frac{L}{2\pi}\int \widetilde{\beta}' d\omega.$$

Next, integrating Eq. (**??**) over frequency and time and using an equation

$$\int \mathrm{e}^{i(\omega-\omega_0)(t'-t)} d\omega = 2\pi\delta(t-t'),$$

while taking into account that the fundamental mode HE_{11} has two directions of propagation and two polarizations, Eq. (**??**) can be rewritten as

$$\dot{c}_{e,0} = -\gamma^{(g)} c_{e,0}, \tag{A12}$$

where $\gamma^{(g)}$ is half the spontaneous decay rate into the guided mode

$$W_{sp}^{(g)} = 2\gamma^{(g)} = \frac{\omega_0 \widetilde{\beta}'}{\varepsilon_0 \hbar} \left| \mathbf{d} \cdot \widetilde{\mathbf{e}} \right|^2 . \tag{A13}$$

In the last equation $\widetilde{\mathbf{e}}$ is an amplitude of the guided mode with a positive propagation constant and positive circular polarization. Note that Equation **??** coincides with a corresponding equation from [**?**].

Assuming $d = d_+$ is a spherical component of the atomic dipole moment one can finally rewrite the spontaneous decay rate into the fundamental guided mode HE_{11} as

$$W_{sp}^{(g)}(r) = 2\gamma^{(g)} = 2A^2 \frac{d^2 \omega_0 \widetilde{\beta}'}{\varepsilon_0 \hbar} \left[(1-s)^2 K_0^2(qr) + (1+s)^2 K_2^2(qr) + \frac{2q^2}{\beta^2} K_1^2(qr) \right], \tag{A14}$$

where the constant A is defined by Eq. (**??**). Equation (**??**) can be rewritten in a convenient form by introducing a dimensionless derivative, $\beta' = d\beta/dk = c\widetilde{\beta}'$, and making use of Eq. (**??**) for the spontaneous decay rate into free space,

$$W_{sp}^{(g)}(r) = 2\gamma^{(g)} = \gamma_0 \frac{3A^2 \lambda^2 \beta'}{\pi} \left[(1-s)^2 K_0^2(qr) + (1+s)^2 K_2^2(qr) + \frac{2q^2}{\beta^2} K_1^2(qr) \right]. \tag{A15}$$

Appendix B

LabVIEW Programmes

The author wishes to to acknowledge M. Daly and W. Cotter for help in designing these LabVIEW programmes.

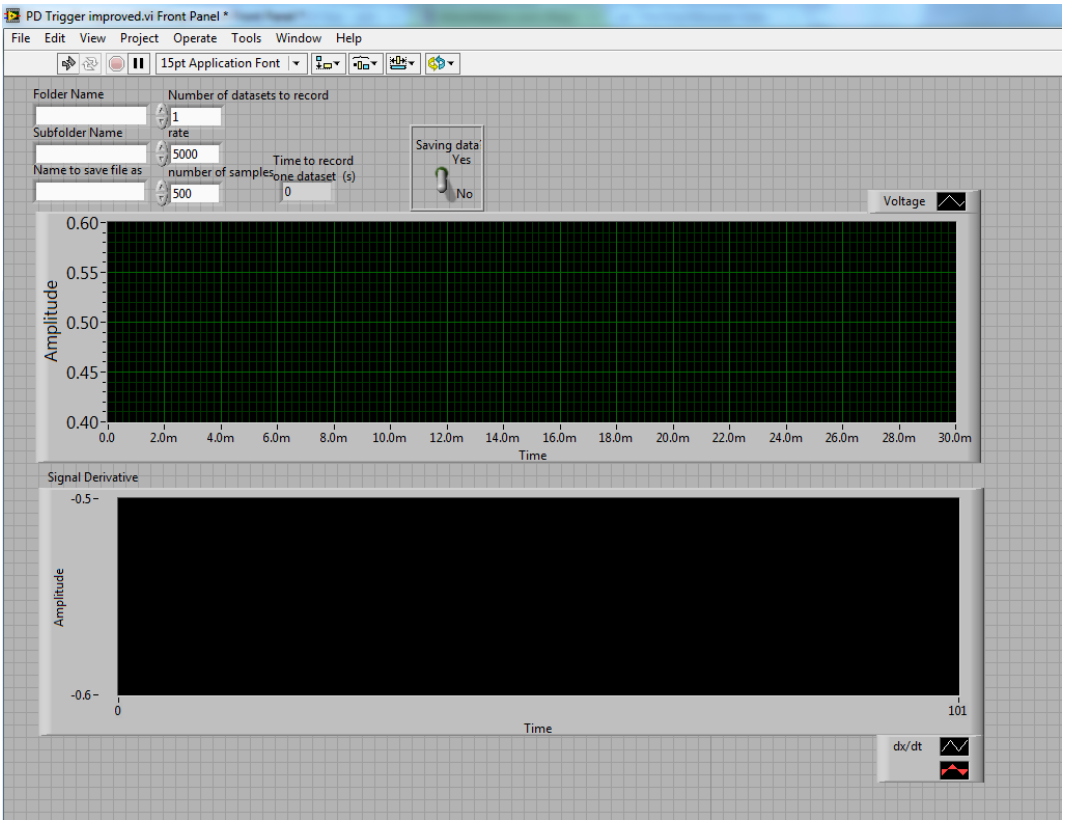

Figure B.1: *The PD trigger (front panel) which records the output signal from the APD.*

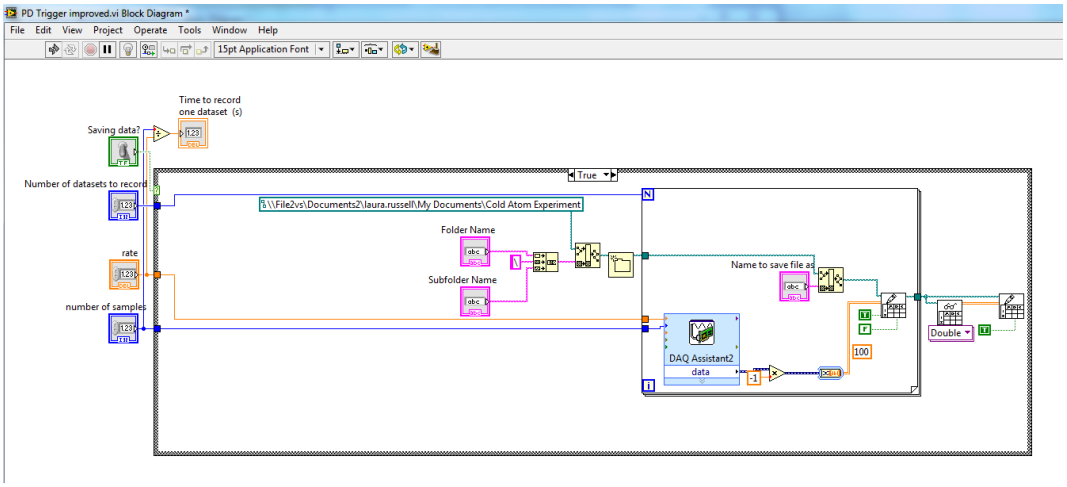

Figure B.2: *The PD trigger (back panel - "true" clause) which records the output signal from the APD.*

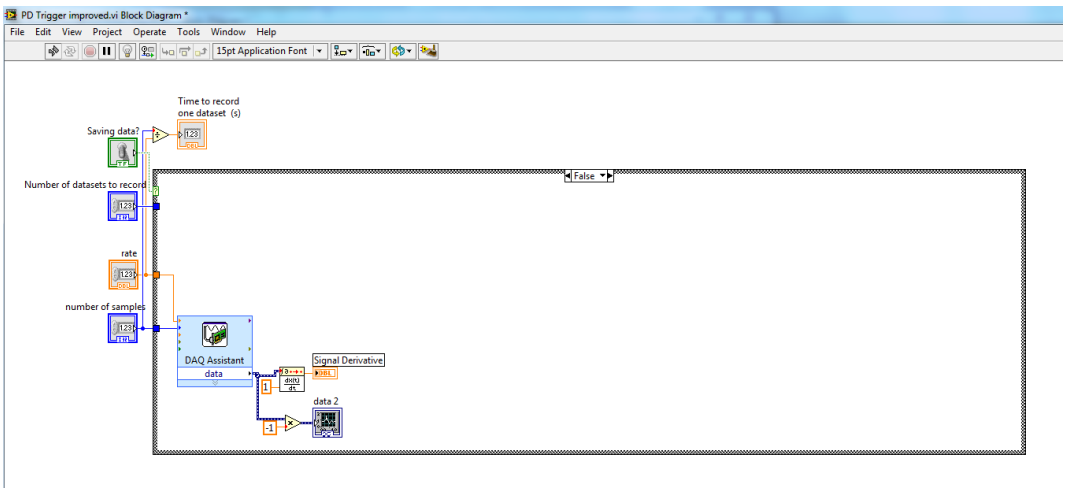

Figure B.3: *The PD trigger (back panel - "false" clause) which records the output signal from the APD.*

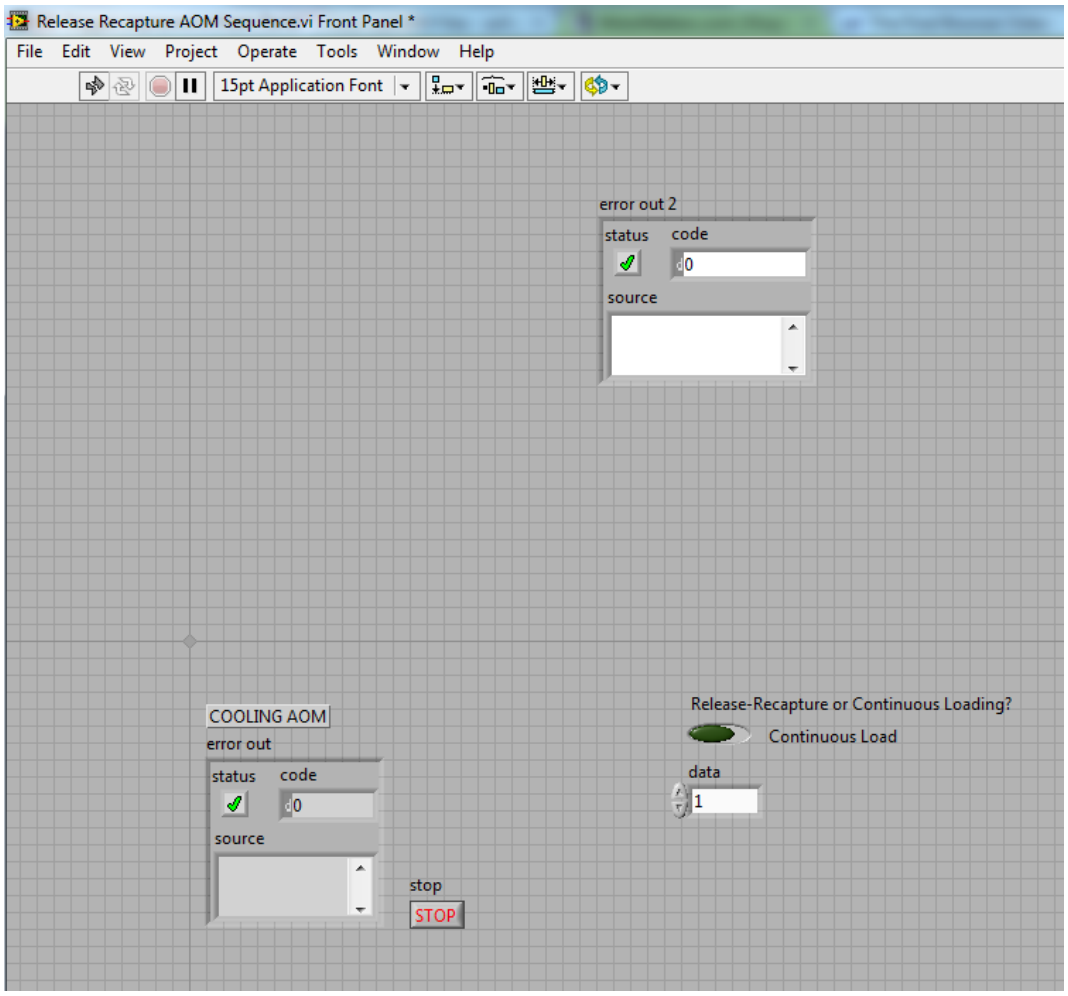

Figure B.4: *The RR AOM sequence which applies a series of square waves to the cooling laser AOM for specified time durations.*

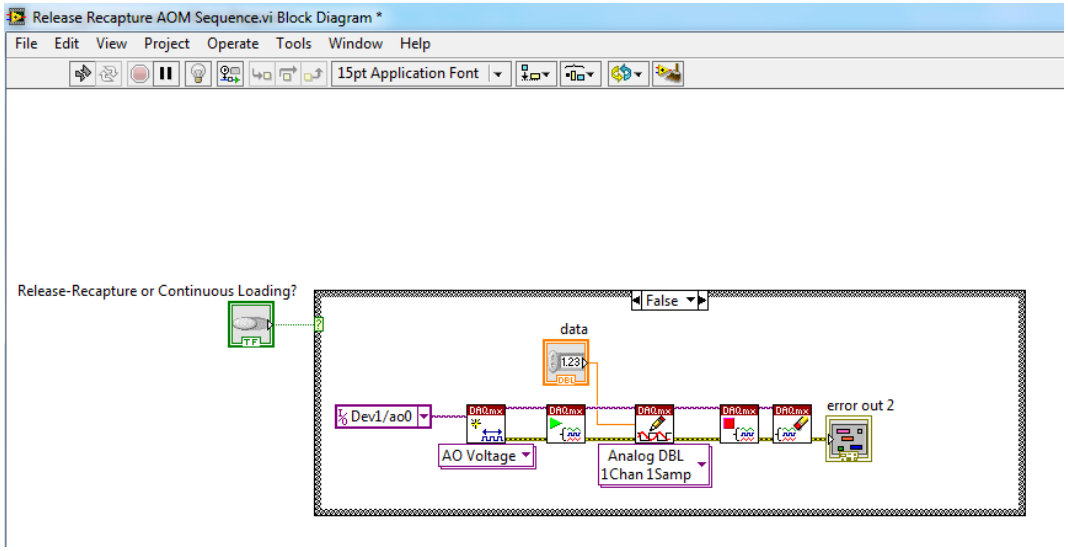

Figure B.5: *The RR AOM sequence which applies a series of square waves to the cooling laser AOM for specified time durations. The "false" clause activates the sequence, while "true" switches the AOM on continuously for normal MOT operations.*

Appendix C

Publications

IOP PUBLISHING JOURNAL OF PHYSICS B: ATOMIC, MOLECULAR AND OPTICAL PHYSICS

J. Phys. B: At. Mol. Opt. Phys. **42** (2009) 185006 (9pp) doi:10.1088/0953-4075/42/18/185006

Spectral distribution of atomic fluorescence coupled into an optical nanofibre

L Russell[1,2], D A Gleeson[1,2], V G Minogin[2,3] and S Nic Chormaic[1,2]

[1] Physics Department, University College Cork, Cork, Ireland
[2] Photonics Centre, Tyndall National Institute, Lee Maltings, Cork, Ireland
[3] Institute of Spectroscopy Russian Academy of Sciences, 142190 Troitsk, Moscow Region, Russia

E-mail: s.nicchormaic@ucc.ie

Received 5 May 2009, in final form 28 June 2009
Published 9 September 2009
Online at stacks.iop.org/JPhysB/42/185006

Abstract

We analyse the lineshape of the fluorescence emitted by a cloud of optically excited cold atoms and coupled into an optical nanofibre. We examine the efficiency of the fluorescence coupling and describe the asymmetry of the lineshape caused by the redshifts arising from both the van der Waals and Casimir–Polder interaction of the atoms with the surface of the optical nanofibre. We compare the contributions of the van der Waals and Casimir–Polder redshifts and show that the lineshape of the fluorescence coupled into an optical nanofibre is, basically, influenced by the van der Waals redshift and is characterized by a long tail on the red side of the spectrum. We conclude that a measurement of the lineshape of the coupled fluorescence could be used to characterize the strength of the interaction of atoms with dielectric surfaces and for the detection of atoms using nanofibres.

(Some figures in this article are in colour only in the electronic version)

1. Introduction

Over the past decade, there has been heightened interest in the interactions between optically excited, cold atoms and dielectric nanobodies, such as optical nanofibres, nanospheres and nanodisks. This is primarily due to the potential such systems offer for controlling and manipulating single particles, thereby providing tools for quantum information technologies. Progress in the fabrication of optical nanofibres in a standard laboratory environment [1, 2] has resulted in experimental studies in this area concentrating on the 'atom + nanofibre' interaction, in particular. One well-known outcome of this interaction is the resulting modification to the spontaneous emission rate of the atoms [3–6] that leads to enhanced coupling into the fibre guided modes for atoms close to the surface. Another important aspect that merits consideration is the spectral distribution of the fluorescence radiation emitted by excited atoms located near and, subsequently, coupled into the nanofibre [7–9]. An experimental observation of the optical coupling efficiency and the spectral dependence of the fluorescence intensity should facilitate a determination of the interaction strength between the atoms and the dielectric surface, including the influence of the van der Waals and Casimir–Polder potentials [10]. This problem is of particular significance for developing techniques for trapping cold atoms around optical nanofibres [11–13] for single particle manipulation and for engineering bipartite (or, indeed, multipartite) entanglement between two (or more) distant trapped atoms via the guided modes of the nanofibre [14, 15].

Recent observations have shown that the lineshape of the fluorescence excitation spectrum coupled into the fibre is not consistent and substantially differing lineshapes have been obtained under varying experimental conditions. In general, the observed lineshape exhibits either a well-pronounced, long tail at red detunings [8] or an asymmetry with an increased red wing of the spectral line [16]. In [8], the long red tail of the spectrum was assigned to the bound-to-bound transitions of atoms between the van der Waals potentials for the ground and excited atomic states and was further corroborated by theoretical studies [17, 18]. However, in later experimental work [16], the authors highlighted that the long red tail was

only observed when the nanofibre was not cleaned prior to data acquisition. On cleaning the surface by violet light, the spectrum exhibited a well-pronounced asymmetry of the spectral line with a prevailing red side [16], rather than the previously reported long red tail, in stark contrast to the theoretical predictions [17, 18].

The above observations clearly show that atom interactions with the surface of a nanofibre may depend strongly on the cleanliness of the nanofibre surface. It is, therefore, of principal importance for experiments on atom–fibre interactions to evaluate the contributions of basic physical mechanisms to the asymmetry of the fluorescent excitation spectrum, rather than the relatively uninteresting effects of a dirty surface. For clean surfaces, such basic mechanisms may include the van der Waals and Casimir–Polder interactions. The contribution of the van der Waals interaction to the redshift of the spectral line has already been observed in the selective-reflection spectroscopy of caesium vapour located near a dielectric surface [19], for example.

The purpose of this work is to show that, alongside the previously considered scenario, whereby the fluorescence lineshape asymmetry is caused by the bound-to-bound transitions between the ground and excited state van der Waals potentials, another possible cause of the asymmetry may be an inhomogeneous broadening of the spectral line. This broadening arises from direct contributions of the van der Waals shifts to the shape of the spectral line produced by a spatially extended ensemble of cold atoms. For completeness, we also consider the contribution of the Casimir–Polder redshifts to the spectral dependence of the coupled fluorescent light and show that, under realistic experimental conditions, the Casimir–Polder contribution to the shape of the spectral line may be negligible.

In what follows, we analyse the coupling of light emitted by ^{85}Rb and ^{133}Cs cold atomic clouds. We choose ^{85}Rb and ^{133}Cs for our evaluations since these elements are widely used in cold atom experiments. Specifically, we evaluate the fluorescence spectrum emitted by optically excited atoms into the fundamental guided mode of an optical nanofibre. Results from our study show that for typical radii of optical nanofibres in the range from 200 to 600 nm, and atomic clouds that are tightly confined around the nanofibre, the fluorescence excitation spectrum exhibits a well-pronounced asymmetry with red-side broadening caused by the van der Waals redshifts and a shifting of the peak position to the red side of the spectrum. The inclusion of the Casimir–Polder effect has minimal influence on the asymmetry of the lineshape but reduces the redshift of the peak position slightly.

2. Power of fluorescence coupled into the fibre

We consider a collection of cold, two-level atoms in the vicinity of an optical nanofibre as shown in figure 1. The atoms are excited by a laser field near-resonant to the atomic dipole transition and they emit fluorescent light which partially propagates into the guided modes of the fibre. We consider the case where the frequency of the fluorescent light is below the cut-off frequencies of all modes apart from the fundamental mode, HE_{11}, so that the fluorescent light can only ever propagate in this mode. The lower state of the atom is considered to be the ground state and we assume that the upper state can only decay to the ground state. The two-level atom model is partially justified by the fact that, for degenerate optical transitions, different magnetic sublevels have very similar spontaneous decay rates [6].

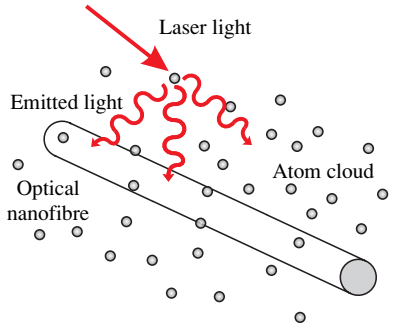

Figure 1. Conceptual diagram of the setup with an optical nanofibre surrounded by an atom cloud, optically excited by near-resonant laser light.

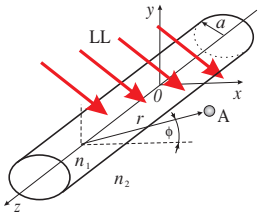

Figure 2. Position of the atom (A) near an optical nanofibre and excited by laser light (LL).

For a single, motionless, two-level atom placed near the optical fibre and excited by an external laser field near-resonant to the dipole optical transition (cf figure 2) the probability of finding the atom in the upper excited state is

$$p_e = \frac{1}{2}\frac{\Omega^2}{(\omega-\omega_0)^2+\gamma^2+\Omega^2}, \tag{1}$$

where $\Omega = dE_0/2\hbar$ is the Rabi frequency defined by the atomic dipole matrix element, d, and amplitude, E_0, of the exciting laser field, ω is the frequency of the laser light, ω_0 is the position-dependent atomic transition frequency and γ is half the position-dependent total spontaneous decay rate, $W_{sp} = 2\gamma$. In the case we are considering, the spontaneous decay rate is made up of two position-dependent decay rates, $\gamma^{(g)}$ into the guided modes of the fibre and $\gamma^{(r)}$ into the radiation modes of the fibre, such that

$$W_{sp} = 2\gamma = 2\gamma^{(g)} + 2\gamma^{(r)}. \tag{2}$$

For a single atom the probability of spontaneous photon emission into a guided mode of the fibre per unit time is proportional to the population, p_e, of the excited atomic state

and the rate of spontaneous emission, $2\gamma^{(g)}$, into the guided mode,

$$W(r) = 2\gamma^{(g)}(r)p_e(r) = \frac{\gamma^{(g)}(r)\Omega^2}{(\omega - \omega_0(r))^2 + \gamma^2(r) + \Omega^2}. \quad (3)$$

In the above equation, we explicitly show that the atomic transition frequency and the spontaneous emission rates are functions of the atom's position, r. For an ensemble of motionless, two-level atoms distributed near the fibre with density $n(\mathbf{r})$, the light power coupled into the fundamental guided mode is accordingly defined by the volume integral [20]

$$P = \hbar\omega \int \frac{\gamma^{(g)}(r)\,\Omega^2}{(\omega - \omega_0(r))^2 + \gamma^2(r) + \Omega^2} n(\mathbf{r})\,\mathrm{d}V. \quad (4)$$

Hence, the power coupled into the optical fibre depends on the shape of the atomic cloud and its position with respect to the axis of the fibre. Note that the power considered is the *total* power coupled into the nanofibre. If one were to monitor the power output at one end of the fibre, the observed power would be half the total power.

In the following, we consider the case of weak optical saturation and neglect the Rabi frequency in the denominator of the excitation probability. We also neglect the short-range repulsive part of the surface potential that can influence a small fraction of the atomic ensemble and may produce a minor contribution to the shape of the spectral line. In its general form, the atomic transition frequency can be written as

$$\omega_0(r) = \omega_0^0 - \delta\omega(r), \quad (5)$$

where ω_0^0 is the unperturbed transition frequency and $\delta\omega(r)$ represents the shift which depends on the distance, $r - a$, between the atom and the dielectric surface of the fibre. At small distances $\delta\omega(r)$ is defined by the van der Waals interaction and can be evaluated from [21–25]

$$\delta\omega_{\mathrm{vdW}}(r) = \frac{C_3}{(r-a)^3}, \quad (6)$$

where C_3 is the van der Waals constant for the atomic transition. At long distances the shift comes from the Casimir–Polder potential and can be evaluated from

$$\delta\omega_{\mathrm{CP}}(r) = \frac{C_4}{(r-a)^4}, \quad (7)$$

where the Casimir–Polder constant is given by

$$C_4 = \frac{3\gamma_0}{8\pi}\frac{\varepsilon - 1}{\varepsilon + 1}\left(\frac{\lambda}{2\pi}\right)^4 \varphi(\varepsilon). \quad (8)$$

In the above equation, γ_0 is half the natural linewidth for the free atom, ε is the static relative permittivity of the fibre material and $\varphi(\varepsilon)$ is a slowly varying function close to unity, $0.77 \leqslant \varphi(\varepsilon) \leqslant 1$. The explicit structure of the function $\varphi(\varepsilon)$ can be found in [21, 22].

For a typical dipole transition where the wavelength, λ, lies in the visible to the near-infrared region, the border between the van der Waals and Casimir–Polder interactions usually occurs at a distance from the surface of $r - a \simeq \lambda/10 \simeq$ 50–80 nm. Van der Waals attractions contribute primarily at distances very close to the surface, i.e. at $r - a \leqslant \lambda/10$. At larger distances, i.e. $r - a \geqslant \lambda/10$, the Casimir–Polder interaction replaces the van der Waals potential and, therefore,

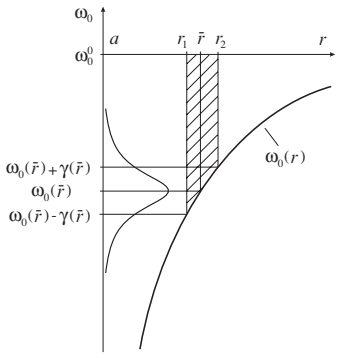

Figure 3. Position-dependent optical absorption line. The shaded area indicates the position of the cylindrical shell containing the excited atoms.

must be included in evaluations. In order to describe the shift for both short- and long-range distances, as well as intermediate distances, we adopt a simple phenomenological equation such that

$$\delta\omega(r) = \frac{C_4}{(r-a)^3\,(C_4/C_3 + r - a)}, \quad (9)$$

which gives a unified description of the shift over all distances. At small distances, equation (9) reduces to the van der Waals equation (6) while at larger distances it reduces to the Casimir–Polder equation (7). One can also show, by numerical evaluation, that equation (9) reproduces the transition between the van der Waals and Casimir–Polder shifts reasonably well.

Finally, the total power of the fluorescent light coupled into the guided fibre mode at weak optical saturation can be written as

$$P = \hbar\omega \int \frac{\gamma^{(g)}(r)\Omega^2}{\left[\omega - \omega_0^0 + \delta\omega(r)\right]^2 + \gamma^2(r)} n(\mathbf{r})\,\mathrm{d}V. \quad (10)$$

A numerical evaluation of the integral defined by equation (10) is given in the following section. Before presenting the numerical results, we will briefly discuss the spatial selectivity of the surface interactions and present numerical values of their corresponding redshifts.

Let us assume, for simplicity, that the ensemble of cold, two-level atoms placed around the optical fibre is spatially broad. In principle, every atom could be excited by the laser field and, subsequently, would be able to emit fluorescent light. However, the resonance condition restricts the spatial position of atoms which can, in reality, emit fluorescence. According to equation (10), when the resonance condition occurs at short distances, i.e. in the case of the van der Waals interaction, the atoms are essentially excited at a mean radial position, $\bar{r}_{\mathrm{vdW}}$, given by

$$\bar{r}_{\mathrm{vdW}} \simeq a + \sqrt[3]{\frac{C_3}{\omega_0^0 - \omega}}, \quad (11)$$

occupying a cylindrical shell coaxially located around the optical fibre as shown in figure 3. In a similar way, when the

Table 1. Position and width of the cylindrical shell containing excited two-level atoms for van der Waals and Casimir–Polder interactions.

ω	$\omega_0^0 - 2\gamma_0$	$\omega_0^0 - 3\gamma_0$	$\omega_0^0 - 4\gamma_0$
$\overline{r}_{\rm vdW} - a$ (nm)	74	64	58
$\delta r_{\rm vdW}$ (nm)	29	16	10
$\overline{r}_{\rm CP} - a$ (nm)	64	57	53
$\delta r_{\rm CP}$ (nm)	17	11	7

resonance condition is satisfied at long distances, the Casimir–Polder interaction is responsible for the excitation of atoms in a cylindrical shell with mean radial position, $\overline{r}_{\rm CP}$, given by

$$\overline{r}_{\rm CP} \simeq a + \frac{\lambda}{2\pi}\sqrt[4]{\frac{3\gamma_0}{8\pi\left(\omega_0^0 - \omega\right)}}. \tag{12}$$

The spatial width, δr, of the cylindrical shell containing excited atoms is defined by a position-dependent frequency width, $2\gamma(r)$, of an optical resonance. Assuming that, at the edges of the shell the probability of atomic excitation is half of that at the centre of the shell, one can evaluate the radii of the shell edges, r_1 and r_2, as roots of the equations

$$\omega_0\left(r_{1,2}\right) \simeq \omega_0\left(\overline{r}\right) \mp \gamma(r_{1,2}). \tag{13}$$

Hence, the spatial width of the cylindrical shell containing excited atoms is given by $\delta r = r_2 - r_1$. It can be easily shown that, when the average frequency shift, $\omega_0^0 - \omega_0(\overline{r})$, exceeds the natural linewidth, $\gamma(\overline{r})$, the spatial width of the shell is small compared to the shell radii, i.e. $\delta r \ll r_{1,2}$, and can be evaluated neglecting small variations in the spontaneous emission rate inside the shell, i.e. making the approximation $\gamma(r_{1,2}) \simeq \gamma(\overline{r}) \simeq \gamma_0$. For the van der Waals interaction this simplification results in an estimate of the spatial width of the shell that is given by

$$\delta r_{\rm vdW} \simeq \frac{2(\overline{r}_{\rm vdW} - a)^4\gamma_0}{3C_3}. \tag{14}$$

For the case of the Casimir–Polder interaction the above simplification yields a characteristic width

$$\delta r_{\rm CP} \simeq \frac{2\lambda}{3}\left(\frac{2\pi(\overline{r}_{\rm CP} - a)}{\lambda}\right)^5. \tag{15}$$

The total power of the fluorescent light exciting the guided fibre mode is proportional to the volume, V, of the cylindrical shell with inner radius, r_1, and outer radius, r_2, i.e. the volume $V = \pi\left(r_2^2 - r_1^2\right)l \simeq 2\pi\overline{r}\delta r l$, where l is the spatial extension of the atomic ensemble along the fibre. Hence, the power of the fluorescent light coupled into the guided mode can be evaluated from

$$P = 2\pi\hbar\omega\gamma^{(\rm g)}\left(\overline{r}\right)\frac{\Omega^2}{\gamma^2(\overline{r})}n(\overline{r})\overline{r}\delta r l. \tag{16}$$

For the van der Waals and Casimir–Polder interactions the mean radius and width of the shell containing excited atoms can be estimated from equations (11), (12), (14) and (15).

Numerical values of the mean radii and widths of the shells for the van der Waals and Casimir–Polder interactions for typical optical dipole transition parameters are given in table 1. The data have been calculated for a value of the van der Waals constant, $C_3 = 2\pi \cdot 2$ kHz $(\mu{\rm m})^3$, a wavelength, $\lambda = 800$ nm, and for three values of the laser field frequency, $\omega = \omega_0^0 - n\gamma_0$, with $n = 2, 3, 4$ and $2\gamma_0 = 2\pi \cdot 5$ MHz chosen as a typical value of the natural linewidth for the optical dipole transition. As can be seen from table 1, the above evaluations give very similar average distances for both the van der Waals and Casimir–Polder interactions. This implies that the Casimir–Polder contribution to the spectral lineshape is expected to be small when compared to that from the van der Waals interaction. In other words, the Casimir–Polder potential should yield a contribution comparable to that of the van der Waals potential only at such small distances where, physically, the van der Waals potential exists.

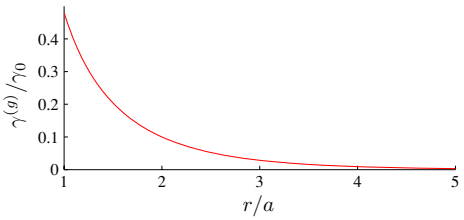

Figure 4. Normalized spontaneous decay rate of a two-level atom into the fundamental guided mode, $\rm HE_{11}$, as a function of distance between the atom and the axis of the optical nanofibre for a radius $a = 200$ nm.

3. Numerical evaluations

In our basic equation (10) there are two unknown quantities: the spontaneous emission rate into the guided mode and the spontaneous emission rate into the radiation modes. Of these two quantities, the most important for our analysis is the rate of spontaneous emission into the guided mode. This quantity varies sharply near the surface of the fibre and, therefore, strongly influences the rate of coupling of spontaneously emitted light into the fibre. The rate of spontaneous emission into the radiation modes changes weakly near the fibre, keeping its value approximately equal to the rate of spontaneous emission into free space. In the following analysis, we will neglect the weak spatial dependence of the spontaneous emission rate into the radiation modes and consider only the position dependence of the spontaneous emission rate into the guided mode.

A complete evaluation of the spontaneous emission rate into the fundamental guided mode of an optical fibre is presented in appendices A and B. The spatial distribution of the evanescent light field of a fundamental guided mode is given in appendix A, while the spontaneous emission rate into the fundamental mode is given in appendix B. Figure 4 shows the dependence of the spontaneous decay rate for a two-level atom as a function of the distance between the atom and the optical nanofibre surface calculated according to equation (B.10).

We can now estimate the fluorescence emission line spectrum for ^{85}Rb and ^{133}Cs atoms. We assume the atoms emit fluorescence light into an optical fibre made of fused

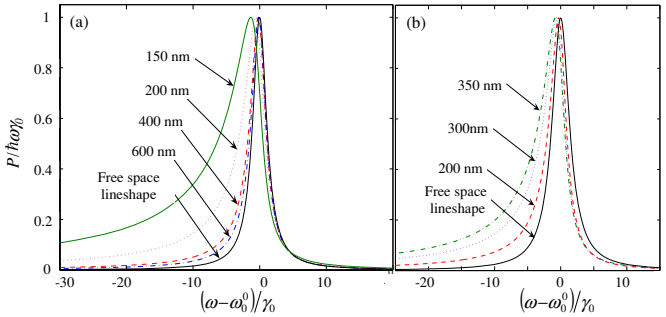

Figure 5. Frequency dependence of the fluorescence power from an atom cloud coupled into the optical nanofibre in the van der Waals approximation. (a) Rb atoms with fixed fibre radius $a = 200$ nm and an atomic cloud radius $R = 600$ nm, 400 nm, 200 nm and 150 nm. (b) Cs atoms with fixed cloud radius $R = 300$ nm and a nanofibre radius of 200 nm, 300 nm and 350 nm. The solid black line shows the free space lineshape and all lines are normalized to a maximum value of 1 for ease of comparison.

silica, with permittivity, $\varepsilon = 2.1$. The Rb atoms are assumed to be excited at the 5S–5P optical dipole transition, with a wavelength of 780 nm and a spontaneous decay rate of $2\gamma_0 = 2\pi \cdot 6$ MHz [26, 27] from the upper 5P state into free space. For the Rb optical transition under consideration the van der Waals constant is evaluated as $C_3 = 2\pi \cdot 3$ kHz $(\mu\text{m})^3$ [19, 28, 29]. Cs atoms are assumed to be excited at the 6S–6P optical transition with a wavelength of 852 nm and a spontaneous decay rate of $2\gamma_0 = 2\pi \cdot 5.2$ MHz [26] from the upper 6P state into free space. The van der Waals constant for the Cs atom optical transition is $C_3 = 2\pi \cdot 1.56$ kHz $(\mu\text{m})^3$ [19, 28, 29]. For both optical transitions, with relatively close wavelengths, the refractive index of the fibre is chosen to be $n_1 = 1.45$ and the refractive index of the outside medium is $n_2 = 1$.

We assume that the cold atoms are distributed in a spherically shaped cloud of radius R that is centred on the axis of the optical fibre of radius a and surrounds the fibre. The cloud has no atoms inside the cylindrical region occupied by the fibre. In the region outside the fibre the cloud has a Gaussian density distribution described in cylindrical coordinates z, r, ϕ as

$$n(z, r) = \frac{N}{\pi\sqrt{\pi}R^3} \exp\left[\frac{a^2 - r^2 - z^2}{R^2}\right], \tag{17}$$

where N is the total number of atoms and is given by

$$N = 2\pi \int n(r) r \mathrm{d}r \mathrm{d}z. \tag{18}$$

It is worth noting here that, for the shape of atom cloud that we consider, i.e. a cloud with an empty internal volume, one can expect an increase in the strength of the surface effects due to the increased ratio of the surface area to the cloud volume.

In figure 5 we show the estimated coupled fluorescence spectrum for rubidium and caesium atoms, calculated under the assumption that equation (9) has the same form as equation (6), i.e. in the approximation of the van der Waals shape for the total potential. Figure 5(a) shows the frequency dependence for rubidium atoms as the atom cloud size varies and the fibre radius is fixed. As one can see, the asymmetry of the fluorescence lineshape increases as the radius of the atomic

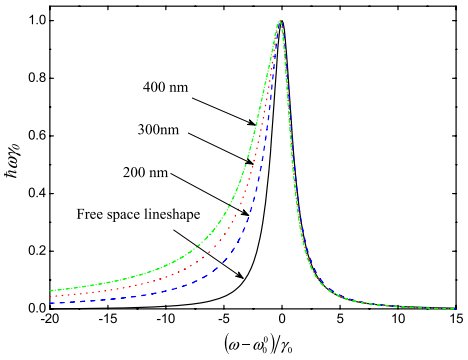

Figure 6. Frequency dependence of the fluorescence power from a Cs cloud coupled into the optical nanofibre for redshift contributions from both the van der Waals and Casimir–Polder effects. The cloud radius is $R = 400$ nm and the nanofibre radius is varied. The solid black line shows the free space lineshape and all lines are normalized to a maximum value of 1 for ease of comparison.

cloud decreases. In other words, the tighter the cloud around the fibre the more pronounced the asymmetry becomes. As the radius of the cloud increases, the atoms located further from the nanofibre are less influenced by the change in the van der Waals frequency shift and, hence, the shape of the fluorescence spectrum approaches that of the symmetrical, free space distribution.

In figure 5(b), we present the reverse situation for caesium atoms, i.e. the atom cloud size is kept constant while varying the size of the nanofibre. As can be seen, a very similar result is obtained. As we increase the fibre radius, more of the fluorescing atoms are very close to the surface of the fibre and, as a result, the van de Waals potential affects a greater proportion of the total atoms in the cloud, leading to more pronounced asymmetry in the lineshape.

If we now consider a total surface potential (cf equation (9)), which describes the van der Waals potential at short distances and the Casimir–Polder potential at long distances, we see that a similar phenomenon is observed

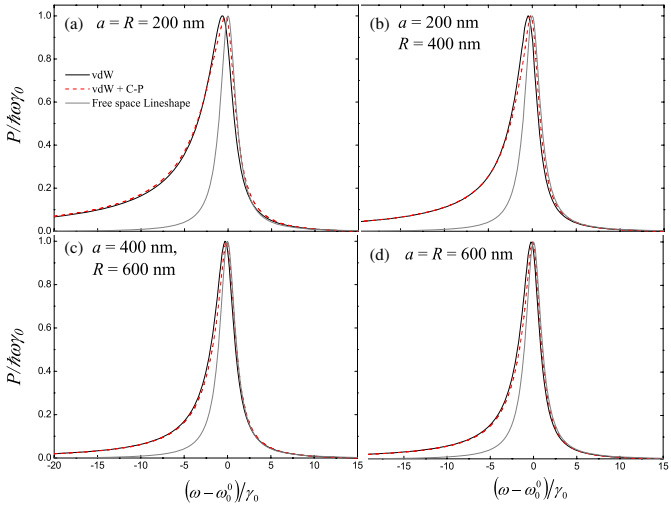

Figure 7. Frequency dependence of the fluorescence power from a Cs cloud coupled into the optical nanofibre for different lineshape contributions: van der Waals effect only (solid line), Casimir–Polder + van der Waals (dashed line), for different cloud radii and fibre radii. All lines are normalized to a maximum value of 1 and the free space lineshape (dotted line) is provided for ease of comparison between the curves.

(cf figure 6 for caesium atoms). It is clear that the most pronounced effect is obtained when the fibre radius approaches that of the effective cloud radius. This arises since there is a greater population of atoms fluorescing near the fibre surface under such conditions. In the case where the fibre radius and cloud radius are equal, we obtain the most evident asymmetry, as illustrated in figure 6 for $a = 400$ nm. Note that the inclusion of the Casimir–Polder potential at long distances has resulted in a slight reduction of the redshift of the peak position of the lineshape compared to that obtained for the van der Waals interaction alone (cf figure 5(b)). However, the overall asymmetry of the lineshape is still very clear at negative detunings. The reduction of the redshift can naturally be explained by an increased number of atoms with a reduced redshift value. In other words, the approximation $C_4 = 0$ slightly overestimates the value of the spectral line redshift.

The slight reduction in the observable redshift due to the inclusion of the Casimir–Polder effect is evident from the plots in figure 7. Hence, while the van der Waals interaction is clearly the dominant influence on the lineshape, the overall lineshape should include the contributions from the Casimir–Polder effect in order to obtain a precise prediction of the fluorescence coupled into a nanofibre. A comparative investigation of this behaviour for different values of a and R is given, in order to determine under what conditions this change to the lineshape, arising from the Casimir–Polder effect, can be neglected. Clearly, irrespective of the values chosen for a and R, no appreciable difference arises when one includes the Casimir–Polder effect. In fact, we see that the overall redshift decreases with increasing values of a and R. For $a = R = 200$ nm there is a small, but identifiable, difference between the two spectra as shown in figure 7(a).

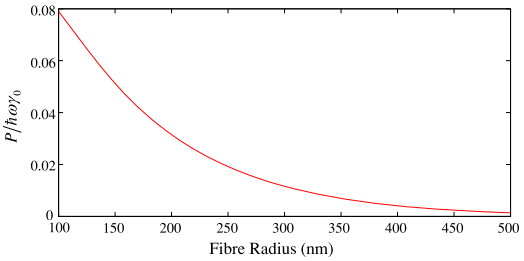

Figure 8. Power coupled into a nanofibre as a function of fibre radius. The power shown is the maximum power for each value of fibre radius. The data were plotted for a Rb cloud with $R = 500$ nm.

For larger values of R with respect to a (figures 7(b) and (c)), the difference between the lineshapes reduces as the spectra approach the free space lineshape. Even in the case of $a = R = 600$ nm (figure 7(d)), any difference between the two regimes is essentially unresolvable. One explanation behind this result is that, when $a = R$, very few atoms experience the Casimir–Polder interaction as the cloud density has decreased by a factor of $\exp\left(\frac{a+\lambda/10}{R}\right)^2$ in the region where Casimir–Polder dominance begins. When $R > a$ the density of atoms has also reduced significantly at the crossover region, thereby yielding a very small contribution to the lineshape from the distant atoms.

Note that, for ease of comparison, we have normalized all powers coupled into the nanofibre to a maximum value of 1 in figures 5–7. In reality, there are large differences in the total power coupled into nanofibres of different radii. In figure 8, we plot the total power coupled into a nanofibre as

a function of nanofibre radius and, as expected, the power reduces significantly with increasing fibre radius for a fixed atom cloud size.

4. Conclusion

We have examined the efficiency of coupling the fluorescence emitted from an ensemble of cold, two-level atoms into an optical nanofibre and we have calculated the frequency dependence of fluorescence power coupled into the fundamental guided mode of the nanofibre. We evaluated the coupled fluorescence spectrum by considering the total surface potential that describes the van der Waals potential at short distances and the Casimir–Polder potential at long distances. Our evaluations show that the van der Waals redshifts may be responsible for a pronounced asymmetry of the coupled fluorescence spectrum, whereas the Casimir–Polder redshifts may produce a slight asymmetry of the fluorescence line. The asymmetry is found to be more evident for atomic ensembles that are tightly confined around the optical nanofibre. We also found that the asymmetry of the fluorescence line increases as the fibre radius is increased and there is clear evidence of a long red tail. We conclude that for a correct and accurate comparison of the experimentally obtained profile of the lineshape with the theoretical lineshape one should generally consider the total surface potential taking into account both the van der Waals and Casimir–Polder redshifts. This is particularly important if one considers atom clouds that are very tightly confined around the nanofibre [12].

In this work we considered the fibre to be a flat surface, as seen by the atoms, due to the relatively short distances being considered. A more realistic approach would be to consider the cylindrical nature of the surface. Earlier work [18] has shown that the flat surface approach is a reasonable first approximation. Note also that, if the power coupled into the fibre were monitored at both ends, quantum correlations between the modes emitted in opposite or equal directions could be studied. Nayak *et al* [30] have recently conducted beautiful experiments based on this idea with laser-cooled Cs atoms. Using a Hanbury Brown–Twiss setup, the photon correlation was seen to change from antibunching to bunching as a function of increasing atom number, when photons were propagating in the same direction along the fibre. In contrast, when the photons were detected at opposite ends of the nanofibre, antibunching was always observed. However, for this type of experiment, the van der Waals and Casimir–Polder effects are negligible, since photon count rates, rather than emission spectra, are the quantities of interest [31].

Acknowledgments

This work was supported in part by Science Foundation Ireland under grant nos. 06/W.1/I866 and 07/RFP/PHYF518, and by the Russian Foundation for Basic Research (project no. 07-02-00748). LR acknowledges support from IRCSET under the Embark Initiative.

Appendix A. Spatial distribution of the electric field for the fundamental guided mode, HE_{11}, of an optical nanofibre

We represent the operator of a quantized vacuum electric field of the guided modes of a nanofibre in a standard form

$$\mathbf{E} = \sum \boldsymbol{\mathcal{E}}_\lambda a_\lambda + \text{h.c.}, \tag{A.1}$$

where $\boldsymbol{\mathcal{E}}_\lambda$ is the electric field of a single vacuum guided mode, a_λ is the photon annihilation operator, and index λ describes the direction of propagation and polarization of a single vacuum guided mode. The electric field of a single guided mode can be represented as [32]

$$\boldsymbol{\mathcal{E}}_\lambda = \mathrm{i}\sqrt{\frac{\hbar\omega_\lambda}{2\varepsilon_0 L}}\,\widetilde{\mathbf{e}}_\lambda \mathrm{e}^{\mathrm{i}\beta_\lambda z + \mathrm{i}m\varphi}, \tag{A.2}$$

where ω_λ is a mode frequency, β_λ is a propagation constant, $\widetilde{\mathbf{e}}_\lambda = \widetilde{\mathbf{e}}_\lambda(r,\phi)$ is a normalized amplitude of the electric field, m is a quantum number of the mode angular momentum and L is the length of a one-dimensional 'box' which is defined by a spatial periodicity of the field. The electric field amplitude of a single guided mode is normalized as

$$\int_0^{2\pi}\int_0^{\infty} n^2(r)\,|\widetilde{\mathbf{e}}_\lambda|^2\,\mathrm{d}\varphi r\mathrm{d}r = 1, \tag{A.3}$$

where $n(r)$ is the value of the refractive index equal to n_1 inside the fibre and $n_2 = 1$ outside the fibre. The above representation of the vacuum field corresponds to a standard form of the vacuum field Hamiltonian

$$\begin{aligned} H_{\text{vac}} &= 2\varepsilon_0\varepsilon \sum \int \mathrm{d}V\,|\boldsymbol{\mathcal{E}}_\lambda|^2 \left(a_\lambda^\dagger a_\lambda + \frac{1}{2}\right) \\ &= \sum \hbar\omega_\lambda \left(a_\lambda^\dagger a_\lambda + \frac{1}{2}\right). \end{aligned} \tag{A.4}$$

For the fundamental guided mode, HE_{11}, the propagation constant β is defined by the eigenvalue equation as

$$\begin{aligned} \frac{J_0(ha)}{ha\,J_1(ha)} = &-\left(\frac{n_1^2+n_2^2}{2n_1^2}\right)\frac{K_1'(qa)}{qa\,K_1(qa)} + \frac{1}{h^2a^2} \\ &- \left[\left(\frac{n_1^2-n_2^2}{2n_1^2}\right)^2\left(\frac{K_1'(qa)}{qa\,K_1(qa)}\right)^2 \right. \\ &\left. + \left(\frac{\beta}{n_1 k}\right)^2\left(\frac{1}{h^2a^2}+\frac{1}{q^2a^2}\right)^2\right]^{1/2}, \end{aligned}$$

where J_m are Bessel functions of the first kind, K_m are modified Bessel functions of the second kind, $k = \omega/c$ and

$$h = \sqrt{n_1^2k^2 - \beta^2}, \qquad q = \sqrt{\beta^2 - n_2^2k^2}.$$

We note that there are four different field distributions for the fundamental mode HE_{11}: two with opposite directions of propagation and two with opposite circular polarizations. In what follows, we write the field distribution for a guided mode with positive propagation constant and positive circular polarization using decomposition over cylindrical unit vectors

$$\widetilde{\mathbf{e}} = \mathbf{e}_r\widetilde{e}_r + \mathbf{e}_\varphi\widetilde{e}_\varphi + \mathbf{e}_z\widetilde{e}_z.$$

The cylindrical components of a normalized electric field amplitude for the HE_{11} mode in the core region are given by [33]

$$\widetilde{e}_r = \mathrm{i}A\frac{q}{h}\frac{K_1(qa)}{J_1(ha)}[(1-s)J_0(hr) - (1+s)J_2(hr)],$$
$$\widetilde{e}_\varphi = -A\frac{q}{h}\frac{K_1(qa)}{J_1(ha)}[(1-s)J_0(hr) + (1+s)J_2(hr)],$$
$$\widetilde{e}_z = 2A\frac{q}{\beta}\frac{K_1(qa)}{J_1(ha)}J_1(hr),$$

and outside of the core region are given by

$$\widetilde{e}_r = \mathrm{i}A[(1-s)K_0(qr) + (1+s)K_2(qr)],$$
$$\widetilde{e}_\varphi = -A[(1-s)K_0(qr) - (1+s)K_2(qr)],$$
$$\widetilde{e}_z = 2A\,(q/\beta)\,K_1(qr).$$

In the above equations, s is a dimensionless parameter such that

$$s = \frac{1/h^2a^2 + 1/q^2a^2}{S},$$

where the denominator is as

$$S = J_1'(ha)/haJ_1(ha) + K_1'(qa)/qaK_1(qa).$$

The normalization constant defined from equation (A.3) is

$$A = \frac{\beta}{2q}\frac{J_1(ha)/K_1(qa)}{\sqrt{2\pi a^2\left(n_1^2N_1 + n_2^2N_2\right)}},$$

where

$$N_1 = \frac{\beta^2}{4h^2}\Big\{(1-s)^2\big[J_0^2(ha) + J_1^2(ha)\big] + (1+s)^2\big[J_2^2(ha) - J_1(ha)J_3(ha)\big]\Big\} + \frac{1}{2}\big[J_1^2(ha) - J_0(ha)J_2(ha)\big]$$

and

$$N_2 = \frac{J_1^2(ha)}{2K_1^2(qa)}\left\{\frac{\beta^2}{2q^2}\big[(1-s)^2\big[K_1^2(qa) - K_0^2(qa)\big] - (1+s)^2\big[K_2^2(qa) - K_1(qa)K_3(qa)\big]\big] - K_1^2(qa) + K_0(qa)K_2(qa)\right\}.$$

The intensity distribution of the electric field inside the core is defined by a quantity

$$|\widetilde{\mathbf{e}}(r)|^2 = 2A^2\frac{K_1^2(qa)}{J_1^2(ha)}\left\{\frac{q^2}{h^2}\big[(1-s)^2J_0^2(hr) + (1+s)^2J_2^2(hr)\big] + \frac{2q^2}{\beta^2}J_1^2(hr)\right\} \tag{A.5}$$

and outside the core it is defined by the quantity

$$|\widetilde{\mathbf{e}}(r)|^2 = 2A^2\left[(1-s)^2K_0^2(qr) + (1+s)^2K_2^2(qr) + \frac{2q^2}{\beta^2}K_1^2(qr)\right]. \tag{A.6}$$

Appendix B. Evaluation of the spontaneous decay rate into the fundamental guided mode

The following derivation of the spontaneous emission rate follows a standard approach based on the Hamiltonian for a system 'two-level atom + vacuum field' given by

$$H = \hbar\omega_0 b^+b + \sum_\lambda \hbar\omega_\lambda\left(a_\lambda^+a_\lambda + 1/2\right) - \mathbf{d}\cdot\sum_\lambda\left(\boldsymbol{\mathcal{E}}_\lambda b^+a_\lambda + \boldsymbol{\mathcal{E}}_\lambda^* b a_\lambda^+\right), \tag{B.1}$$

where b^+ and b are the atomic excitation and de-excitation operators, a^+ and a are the creation and annihilation operators, and $\mathbf{d}$ is a matrix element of the atomic dipole moment. For the Hamiltonian (B.1) the equations for probability amplitudes for the simplest case of a vacuum field initially in the vacuum state are

$$\dot{c}_{\mathrm{e},0} = \frac{\mathrm{i}}{\hbar}\sum_\lambda \mathbf{d}\cdot\boldsymbol{\mathcal{E}}_\lambda \mathrm{e}^{-\mathrm{i}\Delta_\lambda t}c_{\mathrm{g},1_\lambda}, \tag{B.2}$$

$$\dot{c}_{\mathrm{g},1_\lambda} = \frac{\mathrm{i}}{\hbar}\mathbf{d}\cdot\boldsymbol{\mathcal{E}}_\lambda^*\mathrm{e}^{\mathrm{i}\Delta_\lambda t}c_{\mathrm{e},0}, \tag{B.2}$$

where $c_{\mathrm{g},1_\lambda}$ are the probability amplitudes of the states which include the ground atomic state and the state of the vacuum field with one photon in mode λ and $c_{\mathrm{e},0}$ is a probability amplitude of the state which includes the excited atomic state and the state of the vacuum field with zero photon numbers in all the modes.

Taking a formal solution of the second equation in the above set

$$c_{\mathrm{g},1_\lambda} = \frac{\mathrm{i}}{\hbar}\mathbf{d}\cdot\boldsymbol{\mathcal{E}}_\lambda^*\int_{t_0}^t \mathrm{e}^{\mathrm{i}\Delta_\lambda t'}c_{\mathrm{e},0}(t')\,\mathrm{d}t', \tag{B.3}$$

and substituting it into the first equation one can obtain an equation which describes the spontaneous decay of the upper atomic state

$$\dot{c}_{\mathrm{e},0} = -\frac{1}{\hbar^2}\sum_\lambda|\mathbf{d}\cdot\boldsymbol{\mathcal{E}}_\lambda|^2\int_{t_0}^t \mathrm{e}^{\mathrm{i}\Delta_\lambda(t'-t)}c_{\mathrm{e},0}(t')\,\mathrm{d}t'. \tag{B.4}$$

An application of the above equation to the vacuum modes of free space gives a well-known decay equation

$$\dot{c}_{\mathrm{e},0} = -\gamma_0 c_{\mathrm{e},0}, \tag{B.5}$$

where γ_0 is half the spontaneous decay rate into free space,

$$W_{\mathrm{sp}} = 2\gamma_0 = \frac{1}{4\pi\varepsilon_0}\frac{4d^2\omega_0^3}{3\hbar c^3}. \tag{B.6}$$

We now apply the basic equation (B.4) to the fundamental guided mode HE_{11} of the vacuum field. The vacuum field of a single guided mode can be considered as periodic with spatial period, L, and the periodicity condition can be written as $\beta_\alpha L = 2\pi n_\alpha$, where $n_\alpha = 1, 2, 3, \ldots$ defines different values of the propagation constant, β_α. By making use of the periodicity condition, the sum over discrete numbers, n_α, in equation (B.4) can be replaced by an integral such that

$$\sum \to \frac{L}{2\pi}\int \mathrm{d}\beta.$$

Taking into account a one-to-one correspondence between values of the propagation constant and frequencies of the

vacuum modes, $\beta = \beta(\omega)$, one can replace $\mathrm{d}\beta$ by $\mathrm{d}\beta = \widetilde{\beta}'\mathrm{d}\omega$, where $\widetilde{\beta}' = \mathrm{d}\beta/\mathrm{d}\omega$. This gives

$$\sum \to \frac{L}{2\pi}\int \widetilde{\beta}'\mathrm{d}\omega.$$

Next, integrating equation (B.4) over frequency and time and using an equation

$$\int \mathrm{e}^{\mathrm{i}(\omega-\omega_0)(t'-t)}\mathrm{d}\omega = 2\pi\delta(t-t'),$$

while taking into account that the fundamental mode HE_{11} has two directions of propagation and two polarizations, equation (B.4) can be rewritten as

$$\dot{c}_{\mathrm{e},0} = -\gamma^{(g)}c_{\mathrm{e},0}, \tag{B.7}$$

where $\gamma^{(\mathrm{g})}$ is half the spontaneous decay rate into the guided mode

$$W_{\mathrm{sp}}^{(\mathrm{g})} = 2\gamma^{(\mathrm{g})} = \frac{\omega_0\widetilde{\beta}'}{\varepsilon_0\hbar}\left|\mathbf{d}\cdot\widetilde{\mathbf{e}}\right|^2. \tag{B.8}$$

In the last equation, $\widetilde{\mathbf{e}}$ is an amplitude of the guided mode with a positive propagation constant and positive circular polarization. Note that equation (B.8) coincides with a corresponding equation from [6].

Assuming $d = d_+$ is a spherical component of the atomic dipole moment one can finally rewrite the spontaneous decay rate into the fundamental guided mode HE_{11} as

$$W_{\mathrm{sp}}^{(\mathrm{g})}(r) = 2\gamma^{(\mathrm{g})} = 2A^2\frac{\mathrm{d}^2\omega_0\widetilde{\beta}'}{\varepsilon_0\hbar}\Bigg[(1-s)^2K_0^2(qr) + (1+s)^2K_2^2(qr) + \frac{2q^2}{\beta^2}K_1^2(qr)\Bigg], \tag{B.9}$$

where the constant A is defined by equation (A.5). Equation (B.9) can be rewritten in a convenient form by introducing a dimensionless derivative, $\beta' = \mathrm{d}\beta/\mathrm{d}k = c\widetilde{\beta}'$, and making use of equation (B.6) for the spontaneous decay rate into free space,

$$W_{\mathrm{sp}}^{(\mathrm{g})}(r) = 2\gamma^{(\mathrm{g})} = \gamma_0\frac{3A^2\lambda^2\beta'}{\pi}\Bigg[(1-s)^2K_0^2(qr) + (1+s)^2K_2^2(qr) + \frac{2q^2}{\beta^2}K_1^2(qr)\Bigg]. \tag{B.10}$$

References

[1] Cai M, Painter O and Vahala K J 2000 *Phys. Rev. Lett.* **85** 74
[2] Ward J, O'Shea D, Shortt B, Morrissey M, Deasy K and Nic Chormaic S 2006 *Rev. Sci. Instrum.* **77** 083105
[3] Nha H and Jhe W 1997 *Phys. Rev.* A **56** 2213
[4] Søndergaard T and Tromborg B 2001 *Phys. Rev.* A **64** 033812
[5] Klimov V V and Ducloy M 2004 *Phys. Rev.* A **69** 013812
[6] Le Kien F, Dutta Gupta S, Balykin V I and Hakuta K 2005 *Phys. Rev.* A **72** 032509
[7] Sagué G, Vetsch E, Alt W, Meschede D and Rauschenbeutel A 2007 *Phys. Rev. Lett.* **99** 163602
[8] Nayak K P, Melentiev P N, Morinaga M, Le Kien F, Balykin V I and Hakuta K 2007 *Opt. Express* **15** 5431
[9] Morrissey M J, Deasy K, Wu Y, Chakrabarti S and Nic Chormaic S 2009 *Rev. Sci. Instrum.* **80** 053102
[10] Casimir H B G and Polder D 1948 *Phys. Rev.* **73** 360
[11] Dowling J P and Gea-Banacloche J 1996 *Adv. At. Mol. Opt. Phys.* **36** 1
[12] Balykin V I, Hakuta K, Le Kien F, Liang J Q and Morinaga M 2004 *Phys. Rev.* A **70** 011401
[13] Sagué G, Baade A and Rauschenbeutel A 2008 *New. J. Phys.* **10** 113008
[14] Le Kien F, Dutta Gupta S, Nayak K P and Hakuta K 2005 *Phys. Rev.* A **72** 063815
[15] Mancini S and Bose S 2004 *Phys. Rev.* A **70** 022307
[16] Nayak K P and Hakuta K 2008 *New J. Phys.* **10** 053003
[17] Le Kien F and Hakuta K 2007 *Phys. Rev.* A **75** 013423
[18] Le Kien F, Dutta Gupta S and Hakuta K 2007 *Phys. Rev.* A **75** 032508
[19] Oria M, Chevrollier M, Bloch D, Fichet M and Ducloy M 1999 *Europhys. Lett.* **14** 527
[20] Minogin V G and Nic Chormaic S 2009 *Laser Phys.* **19** at press, doi: 10.1134/S1054660X09170137
[21] Dzyaloshinskii I E, Lifshitz E M and Pitaevskii L P 1961 *Adv. Phys.* **10** 165
[22] Dzyaloshinskii I E, Lifshitz E M and Pitaevskii L P 1961 *Usp. Fiz. Nauk* **73** 381
[23] Barash Y S and Ginzburg V L 1984 *Usp. Phys. Nauk* **143** 360
[24] Tikochinsky Y and Spruch L 1993 *Phys. Rev.* A **48** 4223
[25] Fichet M, Schuller F, Bloch D and Ducloy M 1995 *Phys. Rev.* A **51** 1553
[26] Metcalf H J and van der Straten P 1999 *Laser Cooling and Trapping* (Berlin: Springer)
[27] Krishna A, Pandy K, Wasan A and Natarajan V 2005 *Europhys. Lett.* **72** 221
[28] Chevrollier M, Bloch D, Rahmat G and Ducloy M 1991 *Opt. Lett.* **16** 1879
[29] Johnson W R, Dzuba V A, Safronova U I and Safronova M S 2004 *Phys. Rev.* A **69** 022508
[30] Nayak K P, Le Kien F, Morinaga M and Hakuta K 2009 *Phys. Rev.* A **79** 021801
[31] Le Kien F and Hakuta K 2008 *Phys. Rev.* A **77** 033826
[32] Loudon R 1973 *The Quantum Theory of Light* (Clarendon: Oxford)
[33] Snyder A W and Love J D 1983 *Optical Waveguide Theory* (New York: Chapman and Hall)

IOP Publishing Measurement Science and Technology
Meas. Sci. Technol. **23** (2012) 015201 (8pp) doi:10.1088/0957-0233/23/1/015201

Sub-Doppler temperature measurements of laser-cooled atoms using optical nanofibres

Laura Russell[1,2,3,7,8], **Kieran Deasy**[2,4,8,9], **Mark J Daly**[1,2], **Michael J Morrissey**[5] **and Síle Nic Chormaic**[1,2,3,6]

[1] Physics Department, University College Cork, Cork, Ireland
[2] Photonics Centre, Tyndall National Institute, University College Cork, Prospect Row, Cork, Ireland
[3] Light-Matter Interactions Unit, Okinawa Institute of Science and Technology, Okinawa 904-0412, Japan
[4] Department of Applied Physics and Instrumentation, Cork Institute of Technology, Bishopstown, Cork, Ireland
[5] Institute of Electronic Structure and Laser, Foundation for Research and Technology-Hellas, PO Box 1527, GR-71110 Heraklion, Greece
[6] School of Physics, University of Kwa-Zulu Natal, Durban 4001, South Africa

E-mail: laura.russell@tyndall.ie

Received 22 June 2011, in final form 24 October 2011
Published 5 December 2011
Online at stacks.iop.org/MST/23/015201

Abstract
We present a method for measuring the average temperature of a cloud of cold ^{85}Rb atoms in a magneto-optical trap using an optical nanofibre. A periodic spatial variation is applied to the magnetic fields generated by the trapping coils and this causes the trap centre to oscillate, which, in turn, causes the cloud of cold atoms to oscillate. The optical nanofibre is used to collect the fluorescence emitted by the cold atoms, and the frequency response between the motion of the centre of the oscillating trap and the cloud of atoms is determined. This allows us to make measurements of cloud temperature both above and below the Doppler limit, thereby paving the way for nanofibres to be integrated with ultracold atoms for hybrid quantum devices.

Keywords: rubidium, laser cooling, temperature, nanofibre, forced oscillation

(Some figures in this article are in colour only in the electronic version)

1. Introduction

In recent studies, it has been shown that optical nanofibres exhibit excellent fluorescence detection sensitivity when implemented in a cold atom system [1–4]. These devices are fabricated by heating and stretching a segment of single-mode optical fibre until a subwavelength waist diameter is achieved [5–7]. When performed adiabatically [8], this process allows minimal optical transmission loss through the nanofibre. Recent work involving the use of optical nanofibres in laser cooling experiments has demonstrated their functionality both as sensors [1–4, 9, 10] and as a platform for atom trapping [1, 11, 12]. In both applications, the nanofibre acts as a non-destructive interface which can be used to confine, manipulate or probe cold atoms in a controlled manner, and typical atom cloud characteristics, such as loading time, spatial profile and lifetime, can be determined [3, 4]. As has been previously demonstrated [3], optical nanofibres can be used to detect small numbers of fluorescing atoms in their vicinity. By overlapping an atom cloud and a nanofibre, a significant proportion of fluorescent photons from the atom cloud are coupled into the guided modes of the fibre as illustrated in figure 1. These photons can be detected with

[7] Author to whom any correspondence should be addressed.
[8] Both authors have contributed equally to this publication.
[9] Current address: Department of Physics and Astronomy, University of Sheffield, Hounsfield Road, Sheffield S3 7RH, UK.

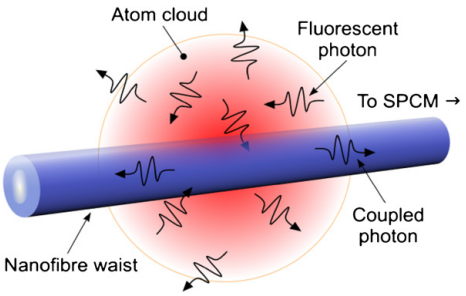

Figure 1. Schematic of the atom cloud overlapping the nanofibre, illustrating the coupling of fluorescence photons to the guided mode of the fibre.

a single photon counting module (SPCM) placed at either end of the fibre.

There have been a number of theoretical [13–16] and experimental [9, 10] studies on the coupling of the resonance fluorescence from laser-cooled atoms into the guided modes of optical nanofibres. Results have shown that the lineshape of the fluorescence is broadened and red-shifted by up to 5 MHz due to the van der Waals and Casimir–Polder [15] interactions which exist between the dielectric surface of the nanofibre and the laser-cooled atoms. In particular, the spontaneous emission rate of the atoms is enhanced when they are near the nanofibre surface [9, 17].

Here, we report on a new method for measuring the temperature of a cloud of cold atoms by coupling the resonant fluorescent photons from the laser-cooled atoms into the guided modes of the optical nanofibre. On imparting a one-dimensional oscillatory motion to the magnetic trap, the phase difference between the oscillations of the trap and the oscillations of the atom cloud can be determined by measuring the photon count rate at one end of the nanofibre. Thence, it is possible to estimate the temperature of the atoms via a determination of the spring constant of the trap [18]. This magnetic-field-based forced oscillation technique was originally implemented for a conventional fluorescence imaging setup [19, 20]. With an optical nanofibre, this measurement technique is highly sensitive to just a few atoms and has distinct advantages over alternative temperature measurement techniques since the nanofibre method is non-destructive. For example, time-of-flight measurements are appropriate for low-velocity atoms [21, 22] but require fast switching of the magnetic field coils and, while precise, it is a destructive technique. An extension of the time-of-flight method is that of release-recapture [23], whereby the atom cloud is allowed to expand ballistically for a pre-determined length of time. Both the cloud shape and capture region must be known in order to fully analyse the characteristic release-recapture motion. In general, the trapped atoms under study—either via their fluorescence signal or by using a resonant probe beam—are those that are coldest and, thus, are located closest to the centre of the magneto-optical trap (MOT) where the nanofibre is positioned. External observation using a photodiode gives a view of the whole cloud and no access to the inner distribution. However, the nanofibre is ideal for probing small numbers of atoms located near the nanofibre and in the central region of the trap.

The first demonstration of the forced harmonic MOT method by Steane and Foot [19] used the radiation force of an additional laser beam to push the trapped atoms away from the trap centre. However, they required three-dimensional sub-Doppler theory to calculate the pushing force. The motion of our atom cloud is restricted to one dimension, allowing straightforward analysis using the well-established forced harmonic oscillator model.

2. Theory of forced oscillation temperature measurement

To measure the temperature of a cold atom cloud, the system is viewed as isolated from the surrounding environment. This allows us to define the temperature, T, in terms of the average kinetic energy, $\langle E_k \rangle$, of the atomic sample [24]:

$$\tfrac{1}{2} k_B T = \langle E_k \rangle \,, \tag{1}$$

where k_B is Boltzmann's constant. An atom trapped in the oscillating MOT behaves as a damped harmonic oscillator [20], the motion of which is described by

$$m\ddot{x} = -\kappa x - \lambda \dot{x}, \tag{2}$$

where m is the atomic mass, x is the atom's position, κ is the spring constant and λ is the damping coefficient. We have neglected stochastic heating of the cloud due to the low atomic density.

In thermal equilibrium, the atom cloud has a thermal energy given by [19, 20]

$$k_B T = \kappa \langle r_x^2 \rangle = m \langle v^2 \rangle, \tag{3}$$

where $\langle r_x^2 \rangle$ is the $1/e^2$ radius of the atom cloud along the direction of forced oscillation and $\langle v^2 \rangle$ is the mean square atomic velocity. To measure κ, the cloud is forced to oscillate in the x-plane. The periodic motion of the trap centre is given by $\Delta x(t) = \xi_0 \cos(\omega t)$, where ξ_0 is the maximum displacement of the trap centre and ω is the applied oscillation frequency. By ensuring that the maximum displacement of the cloud is small, it remains within the linear regime of the trap and the motion of an atom within the trap is described by $x(t) = A(\omega) \cos(\omega t - \phi(\omega))$, where

$$A(\omega) = \frac{\omega_n^2 \xi_0}{\sqrt{\left(\omega_n^2 - \omega^2\right)^2 + \gamma^2 \omega^2}}, \tag{4}$$

and

$$\phi(\omega) = \frac{\pi}{2} - \tan^{-1} \frac{\omega_n^2 - \omega^2}{2\gamma\omega}. \tag{5}$$

Here, ω_n is the natural frequency of the trap and is related to the spring constant by $\kappa = m\omega_n^2$, and $\gamma = \lambda/2m$ is the damping constant. Therefore, by measuring the phase, $\phi(\omega)$, we can obtain κ, allowing the temperature to be determined from equation (3). It can be seen from equation (5) that the natural frequency and oscillation frequency are equal when $\phi(\omega) = \pi/2$.

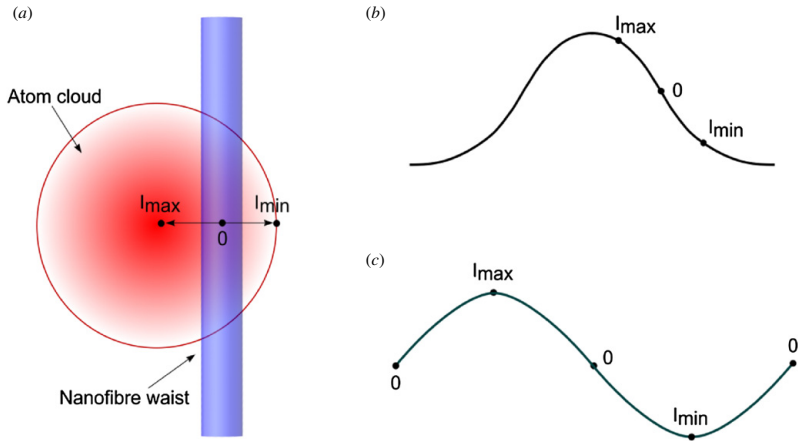

Figure 2. (*a*) Nanofibre positioned off-centre within the atom cloud, (*b*) Gaussian density profile of the atom cloud, (*c*) qualitative sketch of the nanofibre output for a sinusoidal oscillation of the atom cloud across the fibre.

3. Realization of temperature measurement

3.1. Principle

To carry out forced oscillation temperature measurements, typical methods of forcing the MOT to oscillate are using either a pushing laser beam [19] or superimposing a small oscillating magnetic field [20] on the main trapping field of the MOT. In the latter technique, the current supplied to a pair of translation Helmholtz coils is modulated, causing the atom cloud to oscillate and the motion is that of a forced, damped harmonic oscillator. Fluorescent photons from the atom cloud are focused onto a photodiode producing a sinusoidal output signal, which can be frequency analysed using a spectrum analyser. A plot of phase, $\phi(\omega)$, versus applied oscillation frequency, ω, is generated and the natural frequency is equal to the applied frequency when $\phi(\omega) = \pi/2$, as seen from equation (5). Once the natural frequency is known, the spring constant can be determined since $\kappa = m\omega_n^2$. The $1/e^2$ radius of the cloud is found by imaging it with a CCD camera.

In our setup, the current to just one of the anti-Helmholtz magnetic coils is modulated so that the minimum of the magnetic field oscillates over a small, one-dimensional spatial range, which is less than the radius of the atom cloud. The decision to modulate the current to an anti-Helmholtz coil rather than the smaller compensation coils was a technical one, based on the quality of the power supplies in use. Unlike conventional fluorescence detection schemes [20], an optical nanofibre is utilized instead of a photodiode (PD). The optical nanofibre passes vertically through the central region of the stationary trap and is connected to an SPCM. For comparison, we also make a single temperature measurement using the PD detection system similar to that described in [19].

We assume that the atom cloud has a Gaussian density profile and the number of photons coupled into the nanofibre is proportional to the atom density at any point in the cloud, as previously shown in [1]. The atom cloud and nanofibre are overlapped, with the nanofibre slightly off-centre within the cloud, as shown in figure 2(*a*). During the forced oscillation of the atom cloud, the nanofibre remains stationary. As the current in the coils reaches its maximum and minimum values, $I_{\max}$ and $I_{\min}$, the displacement of the atom cloud is largest after a specific length of time which depends on the frequency of the current modulation. These points of maximum displacement are illustrated in figure 2(*a*), with the corresponding points detailed on the density profile of the atom cloud shown in figure 2(*b*). If we assume that the oscillations of the cloud are small, the change in the density profile of the cloud can be assumed to be linear over this variation in position and a similar variation will occur in the number of photons coupled into the nanofibre. Hence, sinusoidal oscillations of the atom cloud across the nanofibre will lead to a sinusoidal variation in photon counts as detected with the SPCM. This is illustrated in figure 2(*c*).

3.2. Experimental method and results

The cold atom cloud is formed in a standard MOT configuration for ^{85}Rb [3, 25], where three orthogonal counter-propagating cooling beams intersect at the centre of an inhomogeneous magnetic field. The cooling laser is locked to the crossover peak, $^5S_{1/2}F_g = 3 \rightarrow {}^5P_{3/2}F_e = (2,4)_{co}$ and then red-shifted by 12.4 MHz from the cooling transition using an acousto-optical modulator. Each beam has a diameter of $\sim$20 mm and an intensity of $\sim$2 mW cm^{-2}. A similar setup is used for the re-pumping laser which is locked to the crossover peak, $^5S_{1/2}F_g = 2 \rightarrow {}^5P_{3/2}F_e = (1,3)_{co}$, and then shifted towards the re-pumping transition. The magnetic field is created by a pair of anti-Helmholtz coils and the field gradient is $\sim$15 G cm^{-1}. Typically, between 10^4 and 10^6 atoms were trapped in the MOT during the course of this work.

To fabricate the nanofibres, a heat-and-pull-technique is used [5–7]. A commercially available 780HP optical fibre is heated using an oxygen-butane flame and drawn out using a

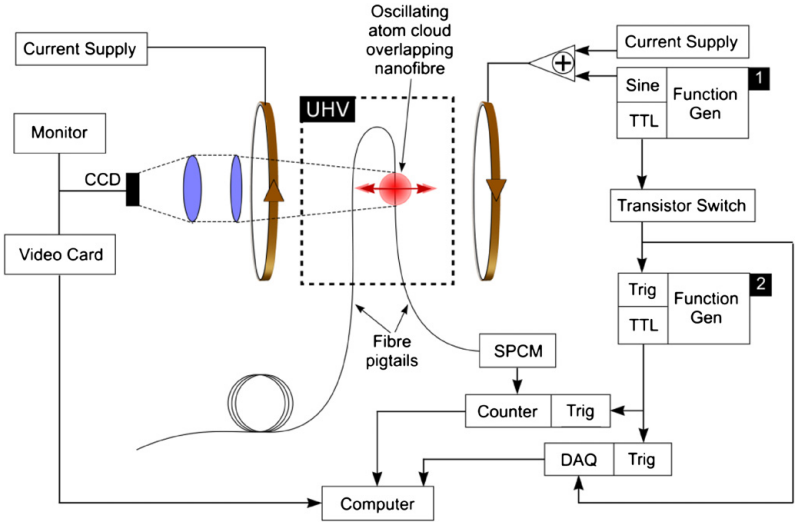

Figure 3. Schematic diagram of the experimental setup for carrying out temperature measurements using the forced oscillation technique. Only the nanofibre detection scheme is shown. SPCM: single photon counting module; DAQ: data acquisition card; UHV: ultra high vacuum; CCD: charge coupled device camera.

pair of stepper motors. This leads to tapering of the optical fibre to a minimum waist diameter. For these experiments, the transmission of the nanofibre was ∼60% compared to the transmission through the non-tapered fibre and the waist diameter was ∼700 nm, i.e. sub-wavelength. After fabrication, the nanofibre is mounted on an aluminium U-shaped mount so that it is vertical, reducing any gravitational bend or sag in the waist region. Initially, the nanofibre is aligned centrally in the MOT. The fibre pigtails are coupled into and out of the UHV chamber using a Teflon feed-through [26, 27].

A schematic diagram of the setup used for the forced oscillation temperature measurement is shown in figure 3. To determine the radius of the atom cloud, it is magnified and imaged on a CCD camera, which was calibrated using objects of known dimensions. The output of the CCD camera is sent to a TV monitor for real-time viewing and a video card for recording and imaging.

To take a single phase measurement, function generator 1 is set to a fixed oscillation frequency, ω, causing the atom cloud to oscillate. At the same time, the function generator outputs a TTL signal that is in phase with the oscillating output, as shown in figure 4. The TTL signal is split between a transistor switch and a data acquisition (DAQ) card. Initially, the transistor switch is closed and does not allow the TTL signal to pass. When the switch is opened, the TTL signal triggers function generator 2, which outputs a burst of 1000 TTL pulses of variable width depending on ω. This TTL signal is then used to trigger the counter of the SPCM and the DAQ card so that both measurements are synchronized. The DAQ card measures the applied modulation signal (reference), and the SPCM counter measures the modulated photon count rate (signal) through the nanofibre. This timing sequence is

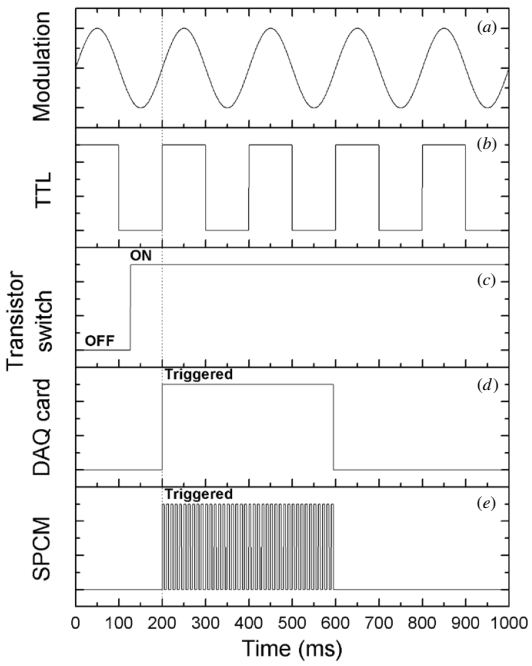

Figure 4. Timing diagram for the experiment.

illustrated in figure 4. The phase between the reference and the signal yields the natural frequency from equation (5).

Initially, a reference result was taken for the temperature of the cold atom cloud using the PD setup as mentioned.

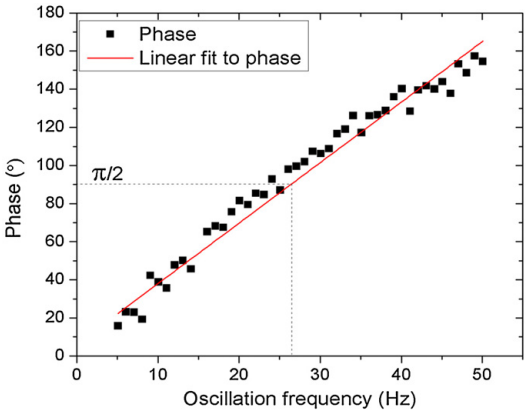

Figure 5. Plot of phase against oscillation frequency using a PD and spectrum analyser. This provides a reference value for the cold atom temperature as measured with a nanofibre.

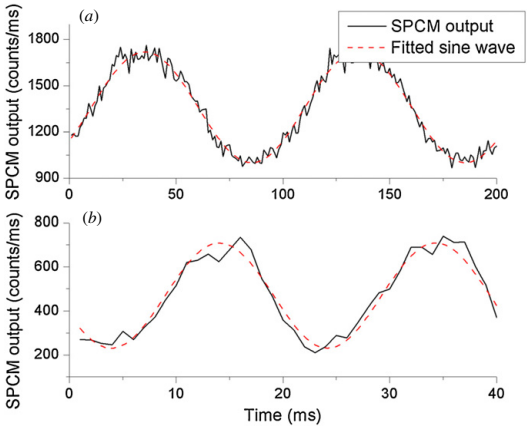

Figure 6. Plot of SPCM counts and fitted sine wave against time, for an oscillation frequency of (*a*) 10 Hz and (*b*) 50 Hz.

Figure 5 is a plot of phase versus applied oscillation frequency as measured directly using a spectrum analyser. When the phase is 90°, the natural frequency is equal to the applied frequency (see equation (5)) of 25.2 Hz. The $1/e^2$ radius was measured to be 1.01 mm and, using equation (3), an ensemble temperature of 260 μK was determined. The largest source of error in the temperature, T, for both the PD and nanofibre techniques, originates from measuring the radius of the atom cloud. Using a Gaussian fit to the cloud profile, the maximum error on the radius, Δr_x, is 0.5 pixels, equivalent to 0.023 mm in real space. Therefore, to determine the error for each temperature value, the following empirical formula was used:

$$\text{Error} = \left(2\frac{\Delta\omega_n}{\omega_n} + 2\frac{\Delta\langle r_x\rangle}{\langle r_x\rangle}\right)T. \qquad (6)$$

A sinusoidal fit was applied to each set of data in order to find the natural frequency. Figures 6(*a*) and (*b*) show two examples of the photon count rates obtained at one end of the fibre for two different applied modulation frequencies of 10 and 50 Hz, respectively. These data were then compared to the actual modulation data as measured using the DAQ card in order to determine the phase between the two signals.

For increasing oscillation frequency, an increase in the phase is observed as shown in figures 7 and 8. In figure 7, the normalized raw data from the SPCM are plotted against the phase angle for two complete oscillations of the cold atom cloud. For each increment in the oscillation frequency, the phase increases further away from the input modulation. In figure 8, the phase shift is plotted against the modulation frequency. Each point on this plot represents an averaged value of phase, calculated from a number of readings for each oscillation frequency. The experiment was repeated for frequencies ranging from 5 to 50 Hz and varying cloud radius—these results are presented in table 1.

The natural frequency was determined by averaging over a large number of readings for each oscillation frequency, and error approximation based on the standard deviation yields an

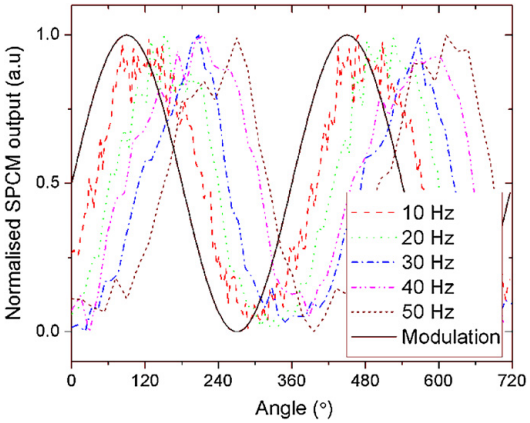

Figure 7. Plot of normalized SPCM output against rotation angle for various oscillation frequencies, showing the changing phase shift due to the modulation as the frequency increases.

Table 1. Estimated temperature values obtained for an atom cloud of varying radius and modulation frequency for a fixed laser detuning of −12 MHz.

Detection method	Frequency (Hz)	Spring constant (10^{-21} kg s^{-2})	Radius (mm)	Temperature (μK)
PD (reference)	25.2	3.56	1.01	260 ± 33
Nanofibre	25.2	3.56	1.15	338 ± 40
Nanofibre	26.8	4.02	1.29	482 ± 53
Nanofibre	28.2	4.45	0.64	130 ± 19

uncertainty of 2.5% for ω_n. This corresponds to a maximum uncertainty of 1° on the phase, $\phi(\omega)$.

By increasing the red-detuning of the cooling laser from the cooling transition, further cooling of the trapped atoms in the MOT can be achieved [24]. To investigate if the forced

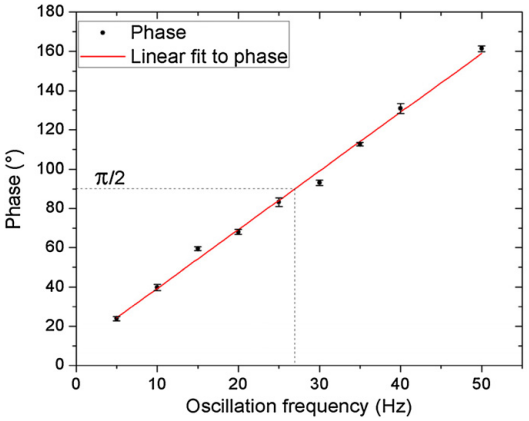

Figure 8. Plot of phase against oscillation frequency as determined from data taken using the nanofibre.

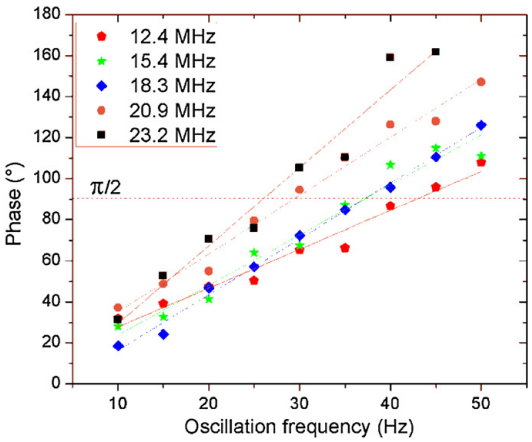

Figure 9. Plot of phase against oscillation frequency for various red-detunings from the cooling transition of ^{85}Rb.

oscillation setup using the nanofibre can detect such changes in the temperature of the atom cloud, temperature measurements were made for various red-detuning values of the cooling laser. Figure 9 is a plot of phase versus oscillation frequency for different red-detunings. The natural frequency can be obtained and, along with the radius of the atom cloud, the temperature can be determined. These results are presented in table 2 and figure 10.

As there exists some ambiguity in the literature concerning the definition of radius for an atom cloud with a Gaussian density distribution[10], we have analysed our system using, additionally, the $1/e$ radius and Gaussian full width at half maximum. Figure 10 plots the temperature of the atom cloud as a function of detuning for the three standard radius definitions used.

[10] See for example [1] ($1/e^2$), [9] ($1/\sqrt{e}$), [34] (σ_{rms}).

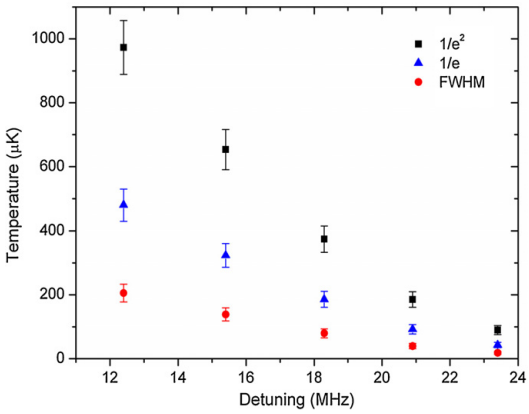

Figure 10. Plot of atom cloud temperature against detuning for three different definitions of cloud radius.

Table 2. Values of decreasing temperature for increasing red-detuning of the cooling laser based on the $1/e^2$ cloud radius.

Detuning (MHz)	Frequency (Hz)	Spring constant (10^{-21} kg s^{-2})	Radius (mm)	Temperature (μK)
12.4	43.1	10.4	1.14	973 ± 85
15.4	37.2	7.75	1.08	653 ± 63
18.3	37.2	7.75	0.82	374 ± 41
20.9	29.5	4.87	0.73	185 ± 24
23.4	26.0	3.79	0.57	89 ± 14

The results presented in table 2 and figure 10 are in agreement with the expected trend, showing a decrease in the atom cloud temperature with increased red-detuning from the cooling transition, regardless of which cloud radius definition is used. This consideration of cloud radius is particularly relevant when discussing the effect which the hot surface of the nanofibre has on the surrounding cold atoms. Importantly, we have observed a sub-Doppler temperature at large enough detuning, regardless of radius definition, thereby indicating that such low temperatures can be reached even with the hot fibre being present in the cloud. For the lower red-detuning values in table 2 and figure 10, radiation pressure forces may inflate the temperatures achieved as higher atom numbers would have been present under these conditions. The system is optically thin (< 0.3). It has been shown that one may see significant effects of radiation trapping when the resonant optical depth is of the order of 1 [28] or even a factor 10 lower [29]. Therefore, further analysis incorporating radiation trapping and heating effects will be the focus of future discussion.

4. Conclusion

We have demonstrated a non-destructive technique for measuring the temperature of a cloud of cold ^{85}Rb atoms held in a MOT. The technique used is that of forced oscillations, which takes advantage of the mechanical properties of the

MOT. The fluorescence photons from the trapped atoms were detected using an optical nanofibre, which was placed within the atomic sample. Good agreement was found between temperature measurements made using the optical nanofibre and the conventional fluorescence imaging method with a photodiode and, in each case, the forced oscillation technique was used. As expected, a decrease in atom temperature was observed for increased red-detuning of the cooling laser beams regardless of the definition of cloud radius used. The nanofibre-based temperature measurements yield marginally higher results than the corresponding fluorescence imaging method, and this may be attributed to the effect which the relatively hot surface of the nanofibre has on nearby laser-cooled atoms. Future work will concentrate on the effect that passing a probe beam through the fibre will have on the temperature, since probe beams are crucial for generating evanescent wave trapping sites around the fibre [12, 30, 31]. Currently, a long switch-off time for our magnetic field prevents us from making useful time-of-flight temperature measurements on our cloud. This technique will be implemented in future work.

Prior to this, two other significant non-destructive temperature measurement techniques have been reported [32, 33], both of which are performed *in situ*. In [33], atom numbers ranged from 10^5 to 10^7 and, for lower numbers, intensity correlation signals become quite small. In the course of the work reported here, it was found that, for lower atom numbers, it was more difficult, albeit not impossible, to achieve fluorescence coupling. Further studies will investigate the lower limit on the atom number within the system that still attains efficient fluorescence coupling into the nanofibre.

It is worth reiterating that sub-Doppler temperatures were observed for large red-detunings from the rubidium cooling transition. On this basis, it would be worthwhile investigating the influence of the optical nanofibre on the formation of even colder atomic systems, e.g. Bose–Einstein condensates, and such a study is crucial for determining the functionality of optical nanofibres in hybrid quantum systems for quantum communication schemes [12].

Acknowledgments

The authors wish to acknowledge the referees for their helpful comments. This work is partially supported by Science Foundation Ireland under grant nos 07/RFP/PHYF518 and 08/ERA/I1761 through the NanoSci-E+ Project NOIs, and the Higher Education Authority via the INSPIRE programme. LR acknowledges support from IRCSET under the Embark Initiative.

References

[1] Nayak K P, Melentiev P N, Morinaga M, Kien F L, Balykin V I and Hakuta K 2007 Optical nanofiber as an efficient tool for manipulating and probing atomic fluorescence *Opt. Express* **15** 5431–38

[2] Nayak K P and Hakuta K 2008 Single atoms on an optical nanofibre *New J. Phys.* **10** 053003

[3] Morrissey M J, Deasy K, Wu Y, Chakrabarti S and Nic Chormaic S 2009 Tapered optical fibers as tools for probing magneto-optical trap characteristics *Rev. Sci. Instrum.* **80** 053102

[4] Deasy K, Watkins A, Morrissey M, Schmidt R and Nic Chormaic S 2010 Few atom detection and manipulation using optical nanofibres *QuantumComm2009 (Lecture Notes of the Institute for Computer Sciences* vol 6*)* (New York: Springer) pp 200–9

[5] Kenny R P, Birks T A and Oakley K P 1991 Control of optical fibre taper shape *Electron. Lett.* **27** 1654–56

[6] Brambilla G, Finazzi V and Richardson D 2004 Ultra-low-loss optical fiber nanotapers *Opt. Express* **12** 2258–63

[7] Ward J M, O'Shea D G, Shortt B J, Morrissey M J, Deasy K and Nic Chormaic S G 2006 Heat-and-pull rig for fiber taper fabrication *Rev. Sci. Instrum.* **77** 083105

[8] Love J D, Henry W M, Stewart W J, Black R J, Lacroix S and Gonthier F 1991 Tapered single-mode fibres and devices: I. Adiabaticity criteria *IEE Proc.* J **138** 343–54

[9] Sagué G, Vetsch E, Alt W, Meschede D and Rauschenbeutel A 2007 Cold-atom physics using ultrathin optical fibers: light-induced dipole forces and surface interactions *Phys. Rev. Lett.* **99** 163602

[10] Das M, Shirasaki A, Nayak K P, Morinaga M, Le Kien F and Hakuta K 2010 Measurement of fluorescence emission spectrum of few strongly driven atoms using an optical nanofiber *Opt. Express* **18** 17154–64

[11] Sagué G, Baade A and Rauschenbeutel A 2008 Blue-detuned evanescent field surface traps for neutral atoms based on mode interference in ultrathin optical fibres *New J. Phys.* **10** 113008

[12] Vetsch E, Reitz D, Sagué G, Schmidt R, Dawkins S T and Rauschenbeutel A 2010 Optical interface created by laser-cooled atoms trapped in the evanescent field surrounding an optical nanofiber *Phys. Rev. Lett.* **104** 203603

[13] Le Kien F, Dutta Gupta S, Balykin V I and Hakuta K 2005 Spontaneous emission of a cesium atom near a nanofiber: efficient coupling of light to guided modes *Phys. Rev.* A **72** 032509

[14] Le Kien F, Dutta Gupta S and Hakuta K 2007 Optical excitation spectrum of an atom in a surface-induced potential *Phys. Rev.* A **75** 032508

[15] Russell L, Gleeson D A, Minogin V G and Nic Chormaic S 2009 Spectral distribution of atomic fluorescence coupled into an optical nanofibre *J. Phys. B: At. Mol. Opt. Phys.* **42** 185006

[16] Minogin V G and Nic Chormaic S 2009 Manifestation of the van der Waals surface interaction in the spontaneous emission of atoms into an optical nanofiber *Laser Phys.* **20** 32–7

[17] Le Kien F, Balykin V I and Hakuta K 2006 Scattering of an evanescent light field by a single cesium atom near a nanofiber *Phys. Rev.* A **73** 013819

[18] Wallace C D, Dinneen T P, Tan K Y N, Kumarakrishnan A, Gould P L and Javanainen J 1994 Measurements of temperature and spring constant in a magneto-optical trap *J. Opt. Soc. Am.* B **11** 703–11

[19] Steane A M and Foot C J 1991 Laser cooling below the Doppler limit in a magneto-optical trap *Europhys. Lett.* **14** 231–6

[20] Kohns P, Buch P, Süptitz W, Csambal C and Ertmer W 1993 On-line measurement of sub-Doppler temperatures in a Rb magneto-optical trap-by-trap centre oscillations *Europhys. Lett.* **22** 517–22

[21] Lett P D, Watts R N, Westbrook C I, Phillips W D, Gould P L and Metcalf H J 1988 Observation of atoms laser cooled below the Doppler limit *Phys. Rev. Lett.* **61** 169

[22] Salomon C, Dalibard J, Phillips W D, Clairon A and Guellati S 1990 Laser cooling of cesium atoms below 3 μK *Europhys. Lett.* **12** 683–8
[23] Chu S, Hollberg L, Bjorkholm J E, Cable A and Ashkin A 1985 Three-dimensional viscous confinement and cooling of atoms by resonance radiation pressure *Phys. Rev. Lett.* **55** 48–51
[24] Metcalf H J and van der Straten P 1999 *Laser Cooling and Trapping* (New York: Springer)
[25] Nic Chormaic S, Yarovitskiy A, Shortt B, Deasy K and Morrissey M 2005 Precision control of magneto-optically cooled rubidium atoms (Invited Paper) *Proc. SPIE* **5826** 83–93
[26] Abraham E R I and Cornell E A 1998 Teflon feedthrough for coupling optical fibers into ultrahigh vacuum systems *Appl. Opt.* **37** 1762–63
[27] Cowpe J and Pilkington R 2008 Swagelok ultra-torr based feed-through design for coupling optical fibre bundles into vacuum systems *Vacuum* **82** 1341–43
[28] Walker T, Sesko D and Wieman C 1990 Collective behavior of optically trapped neutral atoms *Phys. Rev. Lett.* **64** 408–11
[29] Stites R, Beeler M, Feeney L, Kim S and Bali S 2004 Sensitive measurement of radiation trapping in cold-atom clouds by intensity correlation detection *Opt. Lett.* **29** 2713–5
[30] Le Kien F, Balykin V I and Hakuta K 2004 Atom trap and waveguide using a two-color evanescent light field around a subwavelength-diameter optical fiber *Phys. Rev.* A **70** 063403
[31] Balykin V I, Hakuta K, Le Kien F, Liang J Q and Morinaga M 2004 Atom trapping and guiding with a subwavelength -diameter optical fiber *Phys. Rev.* A **70** 011401
[32] Meacher D R, Boiron D, Metcalf H, Salomon C and Grynberg G 1994 Method for velocimetry of cold atoms *Phys. Rev.* A **50** R1992
[33] Bali S, Hoffmann D, Simán J and Walker T 1996 Measurements of intensity correlations of scattered light from laser-cooled atoms *Phys. Rev.* A **53** 3469
[34] Pradhan S and Jagatap B N 2008 Measurement of temperature of laser cooled atoms by one-dimensional expansion in a magneto-optical trap *Rev. Sci. Instrum.* **79** 013101

1- and 2-Photon Absorption by Laser-Cooled ^{85}Rb Using an Optical Nanofiber

L. Russell[a,b,c], M. Daly[a,b,c] and S. Nic Chormaic[a,b,c,d]

[a]*Photonics Centre, Tyndall National Institute, University College Cork, Prospect Row, Cork, Ireland*
[b]*Department of Physics, University College Cork, Cork, Ireland*
[c]*Light-Matter Interactions Unit, Okinawa Institute of Science and Technology, Okinawa 904-0412, Japan*
[d]*School of Physics, University of Kwa-Zulu Natal, Durban 4001, South Africa*

Abstract. The characteristics of a cold cloud of ^{85}Rb can be non-destructively examined using an *optical nanofiber*. The nanofiber is a submicron-diameter cylindrical waveguide fabricated from commercially-available optical fiber using a heat-and-pull rig. The nanofiber can be used as a 'dark' or 'bright' probe depending on whether laser light is coupled into the nanofiber. We demonstrate the use of an optical nanofiber as an absorption spectroscopy tool for cold atoms. A frequency-scanned probe beam is launched through the nanofiber and the resonant light is absorbed at the waist of the nanofiber by nearby cold ^{85}Rb atoms. We present recent single-photon absorption results and comment on the role of surface interactions. Future work on 2-photon absorption using excited state electronic transitions in ^{85}Rb is discussed.

Keywords: nanofiber, rubidium, spectroscopy, laser cooling
PACS: 42.81.Pa, 42.81.Qb, 33.70.Jg, 34.35.+a

1. INTRODUCTION

The advances made in quantum information technology in recent years necessitate the use of nanoscale structures and devices as platforms for controlling and manipulating few and single particles. In the context of cold atoms, the optical nanofiber has established itself as an important tool not only for passive probing of thermal gases and cold atomic samples [1–3], but now also as an essential tool in spectroscopy and optical trapping (4–6).

Optical nanofibers are narrow glass waveguides fabricated from commercially-available optical fiber. Generally, to achieve waist diameters on the order of 500 nm, heat-and-pull methods are utilized [4–6]. This allows high transmission, sub-micron waist nanofibers to be fabricated from a length of optical fiber no more than a few centimeters long. Simple mounting and coupling systems are used to secure the nanofiber, e.g. for insertion in ultra-high vacuum (UHV) [7], [8].

As a 'dark probe', the nanofiber collects the fluorescent photons from surrounding laser-cooled atoms. Recent work has shown how the nanofiber can be employed to measure cloud temperature in conjunction with a forced oscillation method more usually performed with a photodiode detection scheme [9–11]. We have measured temperatures above and below the Doppler Limit of 143 μK for ^{85}Rb using the nanofiber. This implies that the nanofiber may be used in even colder systems,

Quantum Africa 2010: Theoretical and Experimental Foundations of Recent Quantum Technology
AIP Conf. Proc. 1469, 82-90 (2012); doi: 10.1063/1.4746064

although a study of thermal effects for sub-recoil limit atoms surrounding the dielectric surface is necessary.

Resonance fluorescence of atoms has been the subject of interest in quantum optical measurements for many years. There have been a number of theoretical [12–14] and experimental [15], [16] studies on the coupling of the resonance fluorescence from laser-cooled atoms into the guided modes of optical nanofibers. The resonance fluorescence has contributions from elastic scattering and inelastic scattering components. The elastic contribution comes from the well-known Rayleigh scattering and the inelastic component consists of fluorescence scattering. If the driving field is weak, the elastic scattering part dominates and if the driving field is strong, the inelastic part dominates.

For typical radii of optical nanofibers in the range from 200-600 nm, and atomic clouds that are tightly confined around the nanofiber, the fluorescence spectrum exhibits a well-pronounced asymmetry caused by the van der Waals redshift and a slight reduction in the asymmetry arising from the Casimir-Polder redshift [17]. The primary broadening mechanism at small distances from the nanofiber surface is the van der Waals interaction. These considerations are significant for developing techniques for trapping cold atoms around optical nanofibers.

The optical nanofiber is used not only as a tool for measurements of MOT characteristics but also to perform spectroscopy on the cold atomic sample. In this work, we summarize recent single-photon absorption results and discuss the role and relevance of surface interactions in the experimental cold cloud of atoms. An illustration of our system is presented in figure 1. The cold ^{85}Rb cloud is aligned centrally around the nanofiber to maximize the coupling between the resonant fluorescence photons and the HE_{11} mode of the nanofiber. The probe beam is derived from one of the cooling beams and is coupled to the nanofiber. A suitable low-light detector is connected at the opposite end of the nanofiber for data acquisition. Further experimental details are provided in the Experimental Setup which is followed by Results from the 1-photon absorption experiments. An outlook for 2-photon experiments is then provided.

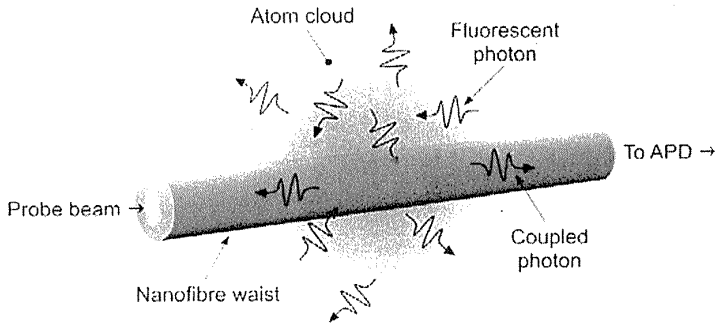

FIGURE 1. Illustration of a cloud of atoms surrounding an optical nanofiber. Spontaneously emitted photons produced by the laser cooling process can couple to the guided mode of the nanofiber and be collected by a suitable detector. With the addition of a frequency-scanned probe beam, the nanofiber is used as a 'bright' probe.

2. EXPERIMENTAL SETUP

The cold atom cloud is formed in a standard magneto-optical trap (MOT) configuration for ^{85}Rb [1], where three orthogonal counter-propagating cooling beams intersect at the centre of an inhomogeneous magnetic field. The cooling laser is locked to the crossover peak, $^5S_{1/2}F_g = 3 \rightarrow {}^5P_{3/2}F_e = (2,4)_{co}$ and then frequency-shifted using an acousto-optical modulator (AOM) to a point which is 12.4 MHz red-detuned from the cooling transition of ^{85}Rb. Each beam has a diameter of 20 mm and an intensity of 3 mW/cm^2. A similar setup is used for the re-pumping laser which is locked to the crossover peak, $^5S_{1/2}F_g = 2 \rightarrow {}^5P_{3/2}F_e = (1,3)_{co}$ and then frequency-shifted towards the re-pumping transition. The magnetic field is created by a pair of anti-Helmholtz coils and the field gradient is approximately 15 G/cm. The base pressure in the ultra-high vacuum (UHV) system is 10^{-9} mbar and rubidium is introduced to the chamber using a resistively-heated getter source.

To fabricate the nanofiber, a heat-and-pull-technique is used [6]. Commercially-available 780HP optical fiber is heated using an oxygen-butane flame and drawn out using a pair of stepper motors. This leads to tapering of the optical fiber to a minimum waist diameter. For the 1-photon experiments the transmission of the nanofiber was 80% and its diameter was ~600 nm. After fabrication, the nanofiber is glued to an aluminium U-shaped mount so that it is oriented vertically, reducing any gravitational bend or sag in the waist region. The MOT is aligned so that the rubidium cloud surrounds the nanofiber. The fiber pigtails are coupled into and out of the UHV chamber using a Teflon feed-through [7], [8].

The nanofiber probe beam is prepared by coupling a small percentage of the zero order cooling beam into a double-pass AOM setup [18]. The resulting probe beam can then be scanned across the cooling transition of ^{85}Rb from -30 MHz to +60 MHz. This is achieved by applying a sawtooth voltage signal to the AOM VCO to ramp the beam detuning across the transition frequency.

Figure 2 shows the setup used for triggering the data acquisition for single-photon absorption. An optical chopper was used to switch on and off the probe beam before it entered a double-pass AOM system – see figure 3. To ensure that the spectroscopy is performed while the cooling laser and repump laser are deactivated, a square wave generator is used to supply a wave with magnitude +1 V to the AOM drivers. After adjusting the time delay, the cooling beam and repump beam were shut off while the nanofiber probe beam was ramped across the ^{85}Rb cooling transition as illustrated in figure 2.

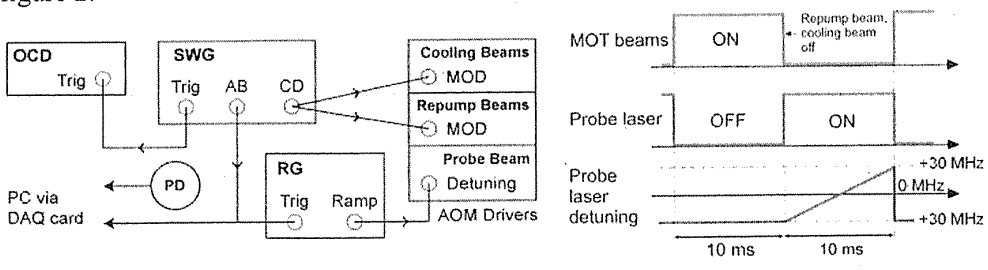

FIGURE 2. (Left) Schematic illustration of the experimental setup for single-photon absorption. OCD

= optical chopper driver, SWG = square wave generator, RG = ramp generator, AOM = acousto-optic modulator, DAQ = data acquisition card, PD = photodiode. (Right) Timing scheme for single-photon absorption.

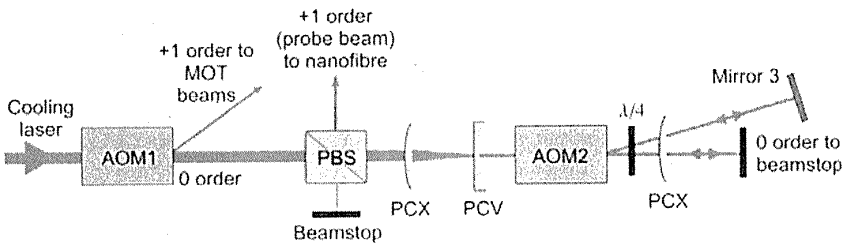

FIGURE 3. Double-pass AOM setup. PBS = polarizing beam splitter, PCX = plano-convex lens, PCV = plano-concave lens.

To perform a single photon absorption experiment as a function of probe beam detuning, the magnetic field for the MOT was switched on and a number of data sets were accumulated successively and averaged – during which, the probe beam was ramped from negative to positive detuning. The magnetic field and rubidium source was then switched off to record a set of reference signals. By comparing the probe signal while the MOT was activated and while it was deactivated, the transmission profile could be obtained.

3. RESULTS

1-Photon Absorption by Cold ^{85}Rb

A comprehensive example of our experimental data is shown in figure 4. We observe an asymmetric absorbance profile (the negative logarithm of the transmission, $-\ln T$) centered on the cooling transition of ^{85}Rb – this is shown by the blue solid line plot in figure 4. To calibrate the x-axis of this plot in terms of probe beam detuning, the AOM calibration curve was used to map the AOM VCO (voltage controlled oscillator) to values of frequency in MHz. This non-linear calibration curve is shown in figure 5 below.

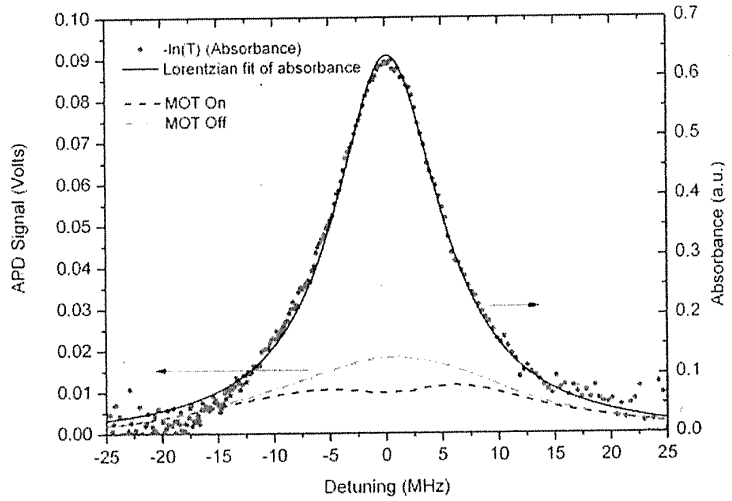

FIGURE 4. Transmission data from a single photon absorption experiment. The lower two lines (dot-dash red and dashed black) show the absorption of the probe beam by the cold atoms surrounding the nanofiber. The blue scatter plot is the absorbance, i.e. the negative logarithm of the transmission, T (i.e. MOT on / MOT off). The x-axis is calibrated in terms of positive and negative detuning centered on the peak of the absorbance plot. The black solid plot is a Lorentzian fit to the absorbance.

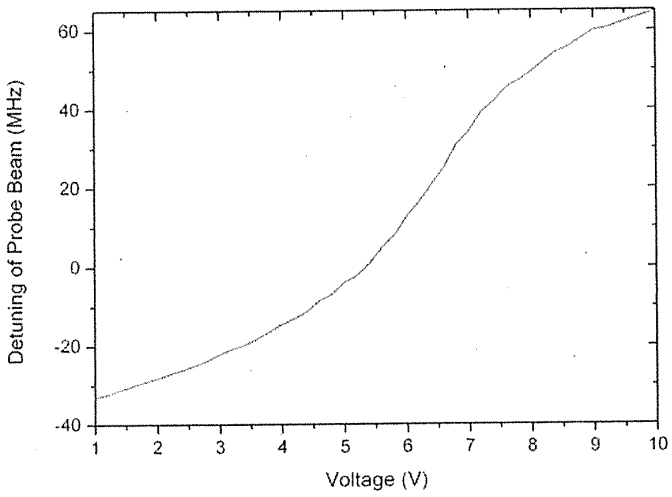

FIGURE 5. AOM calibration curve for probe beam detuning.

The Lorentzian fit for the spectrum in figure 4 yields an estimation of (11 ± 1) MHz for the linewidth, γ. This is significantly larger than the natural linewidth of 6 MHz for the $^5S_{1/2}F_g = 3 \rightarrow {}^5P_{3/2}F_e = 4$ transition in ^{85}Rb. In this case, the input probe beam power was approximately 125 pW. By varying the input power, a variation in linewidth is

evident as demonstrated in figure 6 below. Even with low probe beam powers, large circulation intensities of this light will exist at the nanofibre waist allowing the electronic transition to be easily saturated. With larger saturation parameters, S_0, the linewidth will be broadened according to $\gamma\sqrt{(1+S_0)}$. Thus, with lower probe powers and suitable detectors, it is possible to retrieve lineshapes which are almost free from power broadening.

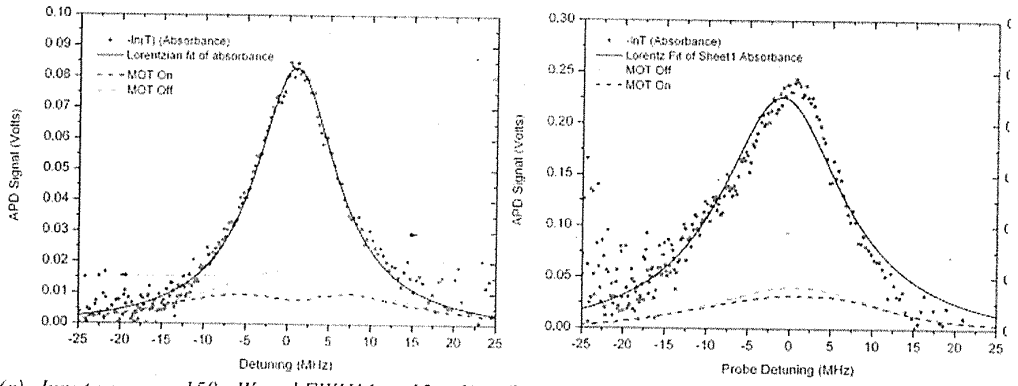

(a) Input power = 150 pW and FWHM = (12 ± 1) MHz

(b) Input power = 330 pW and FWHM = (18 ± 1) MHz

FIGURE 6. Lineshapes for two different probe beam power levels.

One would expect to observe inhomogeneous broadening on the red side of the absorbance spectrum [14], [17], [19]. In our system, the evanescent coupling region extends from the nanofibre surface radially outwards to a *1/e* distance of about 400 nm. On the other hand, the van der Waals interaction is dominant for a fraction of this distance – up to $\lambda/10$ from the nanofibre surface. All atoms which are within the evanescent region have some finite probability of coupling to the nanofibre, even if they are far from the surface. Only a small fraction of those atoms are within the region of significant surface interactions and contribute to an asymmetric lineshape. Thus, we observe symmetric profiles for our "large" clouds.

Due to the van der Waals and Casimir-Polder surface interactions, the center of the profile is expected to shift by a value on the order of -0.5 MHz [17]. This is beyond what we can currently detect and will be the subject of further study.

Outlook: 2-Photon Absorption by Cold ^{85}Rb

In future work we will perform a 2-photon experiment. At low power levels, 2-photon absorption may be useful for optical switching or for quantum logic gates based on the Zeno effect in the context of trapped atoms along a nanofiber [20–22].

Two-photon absorption using an optical nanofiber in a rubidium vapor has been demonstrated recently [23]. In this work, 2-photon absorption was observed with probe beam power levels of less than 150 nW which corresponds to less than 20 photons on average in the waist region of the nanofiber at any time. We propose to carry out a similar experiment with laser-cooled ^{85}Rb using the scheme illustrated in

figure 7 below. A photon at frequency ω_1 is detuned from the resonant frequency of the first atomic transition by an amount δ, which produces a virtual population of the second atomic state. A second photon at frequency ω_2 gives a detuning of the sum of the photon energies from the energy of the upper atomic state. We hold ω_1 = 780 nm constant while scanning the frequency ω_2 of the second photon over the 776 nm transition. 2-photon absorption will be observed as a decrease in the transmission of the light at frequency ω_2, as well as monitoring the color of the fluorescent emission by the atoms using a spectrometer.

Our setup is shown in figure 8. We monitor the probe beam wavelength with a wavemeter during the experiment. Triggering is performed using the trigger input on the piezo control module.

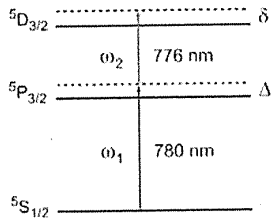

FIGURE 7 - 2-photon absorption in a three-level atom. A virtual population of the intermediate state will be generated by the cooling laser, while we scan over the final state, $^5D_{3/2}$, by a detuning Δ using a second laser tuned to 776 nm.

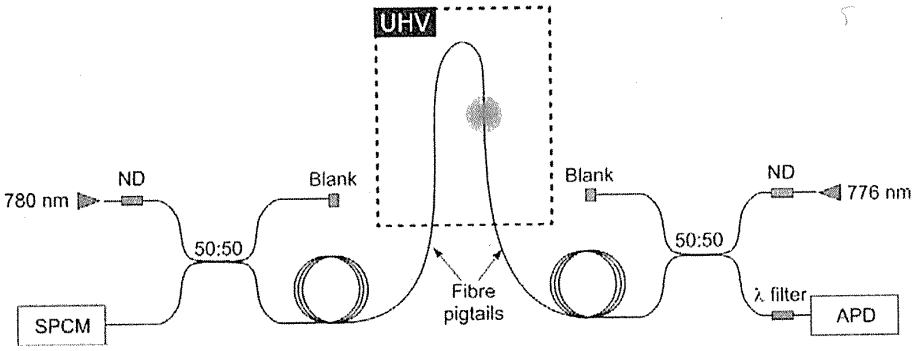

FIGURE 8 - The setup proposed to observe Doppler-free, 2-photon absorption in an optical nanofiber.

For small diameter nanofibers (~400 nm), a significant fraction of the probe beam propagates in the evanescent field surrounding the cylindrical dielectric. For a thermal atom, transit-time broadening due to the atom's limited interaction time with the evanescent field will be pronounced. We expect this contribution to be reduced in the case of atoms in an MOT.

4. CONCLUSION

We have demonstrated the use of optical nanofiber as a bright probe for spectroscopy in cold atomic samples. The nanofiber can be placed within the sample of cold atoms and suitable low-light detectors can be used to detect the fluorescent photons coupled to the guided mode of the nanofiber. To investigate fluorescence lineshape broadening due to the van der Waals and Casimir-Polder interactions, a frequency-scanned probe beam was launched through the nanofiber with center detuning on-resonance with cooling transition of ^{85}Rb. By plotting the transmission of the probe as a function of its detuning we observe broadened, Lorentzian spectra. For typical cloud sizes (500 μm and above), inhomogeneous broadening is not readily seen. Future work will investigate 2-photon absorption in the atomic system. This study may be relevant for quantum logic gates from 2-photon schemes via trapping sites along a nanofiber.

5. ACKNOWLEDGMENTS

This work is supported by Science Foundation Ireland under Grant No. 08/ERA/I1761 through the NanoSci-E+ project NOIs. L.R. acknowledges support form IRCSET under the Embark Initiative.

6. REFERENCES

1. M. J. Morrissey, K. Deasy, Y. Wu, S. Chakrabarti, and S. Nic Chormaic, 'Tapered optical fibers as tools for probing magneto-optical trap characteristics', *Rev. Sci. Instrum.*, vol. 80, no. 5, p. 053102, 2009.
2. K. Deasy, A. Watkins, M. Morrissey, R. Schmidt, and S. N. Chormaic, 'Few Atom Detection and Manipulation Using Optical Nanofibres', in *Quantum Communication and Quantum Networking*, vol. 36, A. Sergienko, S. Pascazio, and P. Villoresi, Eds. Berlin, Heidelberg: Springer Berlin Heidelberg, 2010, pp. 200–209.
3. S. M. Hendrickson, T. B. Pittman, and J. D. Franson, 'Nonlinear transmission through a tapered fiber in rubidium vapor', *J. Opt. Soc. Am. B*, vol. 26, no. 2, pp. 267–271, Feb. 2009.
4. R. P. Kenny, T. A. Birks, and K. P. Oakley, 'Control of optical fibre taper shape', *Electronics Letters*, vol. 27, no. 18, pp. 1654–1656, Aug. 1991.
5. G. Brambilla, V. Finazzi, and D. Richardson, 'Ultra-low-loss optical fiber nanotapers', *Opt. Express*, vol. 12, no. 10, pp. 2258–2263, May 2004.
6. J. M. Ward, D. G. O'Shea, B. J. Shortt, M. J. Morrissey, K. Deasy, and S. G. Nic Chormaic, 'Heat-and-pull rig for fiber taper fabrication', *Rev. Sci. Instrum.*, vol. 77, no. 8, p. 083105, 2006.
7. E. R. I. Abraham and E. A. Cornell, 'Teflon Feedthrough for Coupling Optical Fibers Into Ultrahigh Vacuum Systems', *Appl. Opt.*, vol. 37, no. 10, pp. 1762–1763, Apr. 1998.
8. J. Cowpe and R. Pilkington, 'Swagelok Ultra-Torr based feed-through design for coupling optical fibre bundles into vacuum systems', *Vacuum*, vol. 82, no. 11, pp. 1341–1343, Jun. 2008.
9. L. Russell, K. Deasy, M. J. Daly, M. J. Morrissey, and S. N. Chormaic, 'Sub-Doppler temperature measurements of laser-cooled atoms using optical nanofibres', *Measurement Science and Technology*, vol. 23, no. 1, p. 015201, Jan. 2012.
10. A. M. Steane and C. J. Foot, 'Laser Cooling below the Doppler Limit in a Magneto-Optical Trap', *Europhys. Lett.*, vol. 14, no. 3, pp. 231–236, Feb. 1991.

11. P. Kohns, P. Buch, W. Süptitz, C. Csambal, and W. Ertmer, 'On-Line Measurement of Sub-Doppler Temperatures in a Rb Magneto-optical Trap-by-Trap Centre Oscillations', *Europhys. Lett.*, vol. 22, no. 7, pp. 517–522, Jun. 1993.
12. F. Le Kien, S. Dutta Gupta, V. I. Balykin, and K. Hakuta, 'Spontaneous emission of a cesium atom near a nanofiber: Efficient coupling of light to guided modes', *Phys. Rev. A*, vol. 72, no. 3, p. 032509, 2005.
13. F. L. Kien, S. D. Gupta, and K. Hakuta, 'Optical excitation spectrum of an atom in a surface-induced potential', *Phys. Rev. A*, vol. 75, no. 3, p. 032508, Mar. 2007.
14. V. G. Minogin and S. N. Chormaic, 'Manifestation of the van der Waals surface interaction in the spontaneous emission of atoms into an optical nanofiber', *Laser Phys.*, vol. 20, no. 1, pp. 32–37, Jul. 2009.
15. G. Sagué, E. Vetsch, W. Alt, D. Meschede, and A. Rauschenbeutel, 'Cold-Atom Physics Using Ultrathin Optical Fibers: Light-Induced Dipole Forces and Surface Interactions', *Phys. Rev. Lett.*, vol. 99, no. 16, p. 163602, Oct. 2007.
16. M. Das, A. Shirasaki, K. P. Nayak, M. Morinaga, F. Le Kien, and K. Hakuta, 'Measurement of fluorescence emission spectrum of few strongly driven atoms using an optical nanofiber', *Opt. Express*, vol. 18, no. 16, pp. 17154–17164, 2010.
17. L. Russell, D. A. Gleeson, V. G. Minogin, and S. N. Chormaic, 'Spectral distribution of atomic fluorescence coupled into an optical nanofibre', *J. Phys. B: At. Mol. Opt. Phys.*, vol. 42, no. 18, p. 185006, Sep. 2009.
18. E. A. Donley, T. P. Heavner, F. Levi, M. O. Tataw, and S. R. Jefferts, 'Double-pass acousto-optic modulator system', *Review of Scientific Instruments*, vol. 76, no. 6, p. 063112–063112–6, Jun. 2005.
19. K. P. Nayak, P. N. Melentiev, M. Morinaga, F. L. Kien, V. I. Balykin, and K. Hakuta, 'Optical nanofiber as an efficient tool for manipulating and probing atomic Fluorescence', *Opt. Express*, vol. 15, no. 9, pp. 5431–5438, Apr. 2007.
20. M. Bajcsy, S. Hofferberth, V. Balic, T. Peyronel, M. Hafezi, A. S. Zibrov, V. Vuletic, and M. D. Lukin, 'Efficient All-Optical Switching Using Slow Light within a Hollow Fiber', *Phys. Rev. Lett.*, vol. 102, no. 20, p. 203902, May 2009.
21. H. You, S. M. Hendrickson, and J. D. Franson, 'Enhanced two-photon absorption using entangled states and small mode volumes', *Phys. Rev. A*, vol. 80, no. 4, p. 043823, Oct. 2009.
22. B. C. Jacobs and J. D. Franson, 'All-optical switching using the quantum Zeno effect and two-photon absorption', *Phys. Rev. A*, vol. 79, no. 6, p. 063830, Jun. 2009.
23. S. M. Hendrickson, M. M. Lai, T. B. Pittman, and J. D. Franson, 'Observation of Two-Photon Absorption at Low Power Levels Using Tapered Optical Fibers in Rubidium Vapor', *Phys. Rev. Lett.*, vol. 105, no. 17, p. 173602, Oct. 2010.

Optics Communications 309 (2013) 313–317

Contents lists available at ScienceDirect

Optics Communications

journal homepage: www.elsevier.com/locate/optcom

Measurements on release–recapture of cold ^{85}Rb atoms using an optical nanofibre in a magneto-optical trap

L. Russell [a,b,c,*], R. Kumar [a,b,c], V. B. Tiwari [a,b,d], S. Nic Chormaic [a,c,e]

[a] Physics Department, University College Cork, Cork, Ireland
[b] Tyndall National Institute, Lee Maltings, Propsect Row, Cork, Ireland
[c] Light-Matter Interactions Unit, OIST Graduate University, 1919-1 Tancha, Onna-son, Okinawa 904-0495, Japan
[d] Laser Physics Applications Section, Raja Ramanna Centre for Advanced Technology, Indore 452013, India
[e] School of Chemistry and Physics, University of Kwa-Zulu Natal, Durban 4001, South Africa

ARTICLE INFO

Article history:
Received 29 March 2013
Received in revised form
14 July 2013
Accepted 27 July 2013
Available online 9 August 2013

Keywords:
Laser cooling
Optical nanofiber
Rubidium
Release–recapture
Temperature

ABSTRACT

We have performed release–recapture temperature measurements of laser-cooled ^{85}Rb atoms using an optical nanofibre (ONF) in a magneto-optical trap (MOT). The effects of changing the cooling laser light-shift parameter on the temperature of the cold atoms and spring constant of the trap are studied. By varying the cold atom number density near the ONF, the onset of the multiple scattering regime is observed without the need for an estimation of the atom cloud size. Moreover, this sensitive ONF assisted release–recapture technique is easily able to detect any optical misalignment of the cooling laser beams in the MOT.

1. Introduction

Temperature is undeniably one of the most important characteristics of a laser-cooled sample of atoms that one can measure. By experimentally determining the ensemble temperature, T, quantities such as spring constant and diffusion coefficient can be estimated [1,2], temperature and density regimes can be mapped out [3], and a wealth of information regarding the efficiency of the trapping, cooling and compression scheme can be revealed [4,5]. Although there now exist many temperature measurement techniques, for example [6,7], the most commonly implemented methods use the thermal expansion of the cloud – time-of-flight (TOF) measurements – to estimate T [8,9]. In this paper, we focus on the release–recapture (RR) which is sensitive to the velocity distribution of the cloud. For temperatures at the Doppler limit (144 μk for ^{85}Rb) and above, as is the case in this work, the RR method is well-suited. At temperatures significantly below the Doppler limit, gravity begins to play a role in the thermal expansion of a cold cloud of atoms because the initial velocity of the atoms becomes small compared to the velocity acquired due to gravity during the expansion phase.

An optical nanofibre (ONF) [10,11] is generally made from standard optical fibre which is heated and simultaneously pulled to produce a subwavelength diameter fibre. ONFs can be used to couple light into optical resonators [12–15] and for characterising and guiding particles [16,17]. Spontaneous emission into the guided modes of an optical nanofiber is enhanced [18], making it an ideal high-sensitivity tool for channeling atomic fluorescence to a detector. Thus, in recent years, ONFs have also been shown to act as a measurement tool and delivery platform for cold atoms [19–26] and atomic vapours [27,28].

Here, the RR method is performed by positioning a cold cloud of ^{85}Rb atoms centrally around an ONF. Previous works show that, despite the presence of the hot ONF surface in the cloud of cold atoms, sub-Doppler temperatures can still be obtained with large red-detunings of the cooling laser beams [25].

2. Background

If a spherical cloud of atoms, with a Gaussian velocity distribution, is allowed to expand homogeneously from an initial finite diameter, the fraction of atoms, f_r, remaining after the release time, Δt_2, is given by

$$f_r = \frac{1}{\pi^{3/2}} \int_0^{v_c/v_T} e^{-u^2} u^2 \, du \cdot 4\pi, \tag{1}$$

* Corresponding author at: Physics Department, University College Cork, Cork, Ireland.
E-mail address: laura.russell@oist.jp (L. Russell).

0030-4018/$ - see front matter © 2013 Published by Elsevier B.V.
http://dx.doi.org/10.1016/j.optcom.2013.07.080

where $u^2du\cdot 4\pi$ is the spherical polar coordinate for velocity. The thermal velocity of the atoms in the MOT at a temperature T is $v_T=\sqrt{2k_BT/m}$ and $v_c=R_c/\Delta t_2$ is the velocity at which the atoms just reach a position R_c in the time interval Δt_2. The capture region is characterised by the radius of the MOT beams, R_c. Integrating Eq. (1) yields

$$f_r=-\frac{2e^{-v_c^2/v_T^2}v_c}{\sqrt{\pi}v_T}+\mathrm{Erf}\left[\frac{v_c}{v_T}\right]. \tag{2}$$

Eq. (2) describes f_r as a function of Δt_2. This equation is fitted to the experimental data by taking R_c as known and v_T is the fitting parameter.

3. Experiment

The cold ^{85}Rb atom cloud is formed with a standard MOT configuration of three orthogonal, counter-propagating cooling beams intersecting at the centre of an inhomogeneous magnetic field. The cooling laser is locked to the crossover peak, $^2S_{1/2}F_g=3\rightarrow{}^2P_{3/2}F_e=(2,4)_{co}$ and then red-detuned from the cooling transition using an acousto-optical modulator (AOM). This detuning is controlled by the frequency input (0–10 V) to the AOM driver. Each beam has a maximum diameter of 24 mm (controlled via an aperture). The repumping laser is locked to the crossover peak, $^2S_{1/2}F_g=2\rightarrow{}^2P_{3/2}F_e=(1,3)_{co}$. The magnetic field is created by a pair of coils, each carrying currents of $\sim$4 A in opposite directions, to generate an axial field gradient in the region of 15 G/cm at the centre of the MOT. Between 10^4 and 10^8 atoms are trapped in the MOT depending on experimental parameters.

To fabricate the ONF, the usual heat-and-pull-technique [29] is used with Fibercore SM750 fibre. For these experiments, the transmission of the ONF was $\sim$60% and the waist diameter was $\sim$1 μm (as determined with a scanning electron microscope). Further details about the experimental characteristics of an ONF can be found in [22]. The fibre pigtails are coupled into and out of the UHV chamber using a Teflon feed-through [30] and one end is connected to a single photon counting module (SPCM[1]). The cloud is aligned centrally around the ONF using imaging techniques and optimisation of the fluorescence coupling into the fibre guided modes is detected by the SPCM. Final adjustments to cloud position are made with magnetic coil currents.

3.1. Procedure

The cooling laser beams were switched on and off with an AOM in order to achieve the desired loading, release and recapture sequence (see Figs. 1 and 2). A recapture time, Δt_3, of 50 ms was used to ensure that no background vapour atoms are recaptured by the MOT. The loading time of the MOT is typically $\sim$1 s. The magnetic field stays on at all times.

To perform a temperature measurement, the cloud of atoms was loaded for 10 s (Δt_1) to ensure that a steady-state number of atoms was reached. Then, the cooling laser was switched off using the AOM for a time Δt_2 to allow the cloud to expand freely. Δt_2 is varied each time the sequence is repeated: $\Delta t_2=5$ ms, 10 ms, 20 ms, … 150 ms. After the release time has passed, the cooling laser is switched on for $\Delta t_3=50$ ms to recapture the cloud. The cooling beams are switched off again with the AOM for 50 ms to provide a suitable contrast between the signal from the recaptured atoms and the background level. The sequence is recommenced for the next value of Δt_2. An image of the cloud is recorded using a CMOS camera and image analysis is performed to estimate the cloud radius.

Following this release and recapture process, fast atoms escape the MOT after a short release time and slower atoms are lost only after longer release times. To estimate the temperature of the atoms, the fraction of remaining atoms is calculated as a function of Δt_2. This is proportional to the fluorescence coupled into the nanofibre. This method is sensitive to the velocity distribution of the cloud.

4. Results and discussion

Temperatures approaching the Doppler limit have been observed at moderate detunings when the alignment of MOT beams has been particularly good. For example, for a detuning of -2.6Γ (where $\Gamma=2\pi\times 5.9$ MHz is the natural linewidth of the $5^2S_{1/2}\rightarrow 5^2P_{3/2}$ transition in ^{85}Rb) with a cooling laser intensity per beam, I_{beam}, of $2.9I_s$ (where $I_s=1.6$ mW/cm^2 for $\sigma^{\pm}$-polarised light on the ^{85}Rb cooling transition), T is estimated to be 167 μK (Fig. 3). Poor MOT beam alignment would mean that atoms may leave the capture region in a non-isotropic way, the signature of which is an immediate and sharp decrease in recaptured atoms. The importance of precise optical alignment and power equalisation in the MOT beams is well known [31,32]. For example, [31] reports a temperature and associated variation of (147 ± 25) μK depending on the alignment of the laser beams. By using the ONF as the detection tool, the effect of beam misalignment and power mismatching is detectable with a greater sensitivity than for fluorescence imaging techniques.

The temperature of the cold atoms as a function of I_{beam} was investigated (Fig. 4) and measurements show that a span of a few hundred μK can be observed when varying I_{beam} from 2.5 mW/cm^2 to 6.7 mW/cm^2 at a constant cooling laser red-detuning of $\sim 2\Gamma$. As expected, the temperature reduces as laser intensity is reduced [33].

Traditionally, R_c is the quantity with the greatest uncertainty. A small change in R_c ($\sim$2.5 mm) when fitting Eq. (2) to the data results in a temperature shift of the order of the error bars seen in Figs. 4–6.

In order to compare the RR temperature measurements with another technique, we have taken data directly from previous work which used the method of forced oscillations to estimate cloud temperature (see [25] for full details). Table 1 presents a comparison of results for temperature as a function of cooling laser red-detuning. The results found using each technique correlate quite well. In particular, for higher detunings, the T values which have been estimated with each method agree more strongly. Lower values of red-detuning were not easily examined with the ONF used for RR as the sacrifice in N_A was sufficient to lower the fluorescence coupling signal significantly.

From Fig. 5, it is clear that temperatures obtained with the RR technique increase linearly with the light-shift parameter, $\Omega^2/|\delta|\Gamma$, as expected [2]. The spring constant, κ, can be inferred from these temperature values. κ describes the restoring force in the MOT and is a particularly relevant quantity in relation to compressing atoms to high density. To determine κ it is assumed that, in thermal equilibrium, the atom cloud has a thermal energy given by $k_BT=\kappa\langle r^2\rangle=m\langle v^2\rangle$, where T is the experimentally determined cold atom cloud temperature, k_B is Boltzmann's constant, r is the radius of the atom cloud, and $\langle v^2\rangle$ is the mean square atomic velocity [1,4]. For each value of red-detuning, the cloud radius is estimated using image analysis. Fig. 6 shows that the spring constant increases with intensity at low intensity or detuning values and then levels off at some critical value of the light-shift parameter. Wallace et al. [2] report that the spring constant is not independent of I_{beam} until a moderately high value of the light-shift parameter is reached.

[1] Perkin and Elmer single photon counting module; model: SPCM-AQR-14; dark count=100 counts s^{-1}; quantum efficiency=60% at 780 nm.

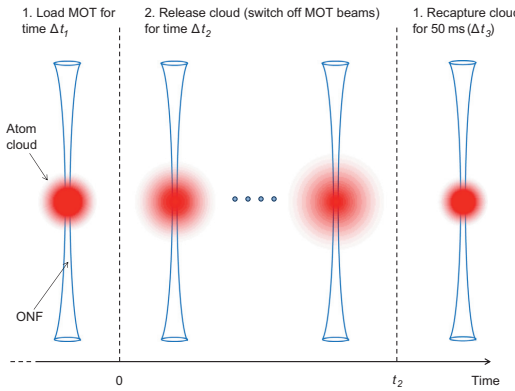

Fig. 1. Illustration of the release and recapture sequence as a function of time. The cloud is positioned centrally around the ONF. The cloud is loaded for a time Δt_1 and then released from the trap for a time Δt_2. Δt_2 is varied from sequence to sequence to build up a profile of the velocity of the atoms in the MOT. The recapture time, Δt_3, is set to 50 ms. The cloud is then released once more for 50 ms, before repeating the entire sequence.

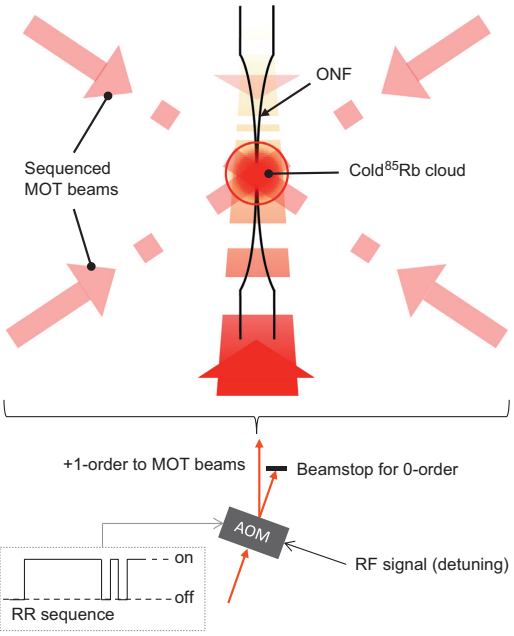

Fig. 2. Illustration of the experimental setup. The 1st-order beam from an AOM is expanded and split into three equal-intensity cooling beams for the MOT. The ^{85}Rb cloud is positioned centrally around the ONF. The cooling beams are switched on and off according to the sequence shown here with an AOM. Beam detuning is controlled via the tunable RF input on the AOM.

It is interesting to observe that, as evident in Fig. 6, κ levels off above light-shift parameter values of ≈ 1. As the most dense part of the cloud is being studied with the ONF, this may be an

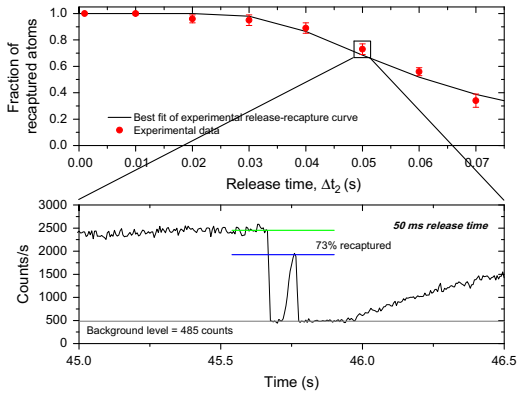

Fig. 3. Fraction of recaptured atoms estimated from the fluorescence data obtained from an optical nanofibre placed near the cold cloud of atoms. For a release time, Δt_2, of 50 ms, 73% of the expanded cloud was recaptured with $\delta = -2.6\Gamma$ and cooling laser intensity of $2.9I_s$ (4.6 mW/cm^2) per beam.

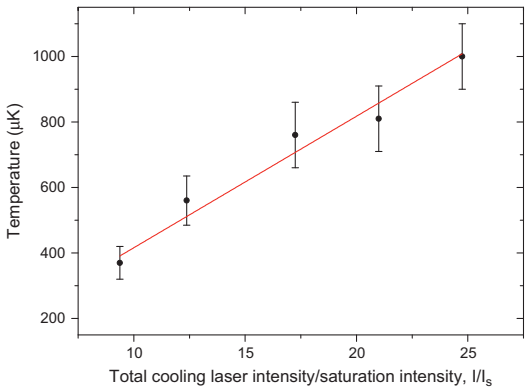

Fig. 4. Temperature as a function of cooling laser intensity normalised to the saturation intensity, I_s ($\delta = -2\Gamma$). The solid red line is a linear fit to the experimental data. (For interpretation of the references to color in this figure caption, the reader is referred to the web version of this article.)

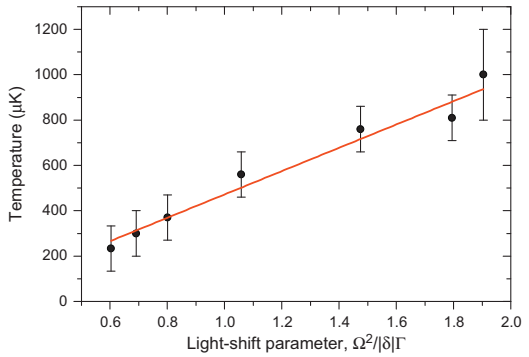

Fig. 5. Temperature of the cloud as measured with RR plotted against the dimensionless light-shift parameter $\Omega^2/|\delta|\Gamma$ (black circles) and a linear fit (red solid line) to the data. (For interpretation of the references to color in this figure caption, the reader is referred to the web version of this article.)

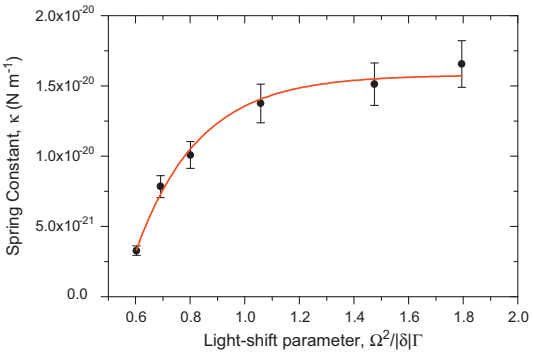

Fig. 6. Spring constant against dimensionless light-shift parameter $\Omega^2/|\delta|\Gamma$ (black circles) with a fit for a guide to the eye (red, solid line). (For interpretation of the references to color in this figure caption, the reader is referred to the web version of this article.)

Table 1
Variation of temperature with cooling laser red detuning in units of the natural linewidth using two different measurement techniques. I_{beam} was approximately $2.2I_s$ for release–recapture and $1.3I_s$ for forced oscillation. Forced oscillation data is taken directly from [25].

Method	Red detuning (Γ)	Temperature (mK)
Release recapture	1.1	1.80 ± 0.20
	2.0	0.56 ± 0.13
	3.5	0.23 ± 0.03
Forced oscillation	2.1	0.97 ± 0.08
	2.6	0.65 ± 0.06
	3.1	0.37 ± 0.04
	3.5	0.18 ± 0.02

interesting observation when compared to measurements done with photodiodes.

As atom number is increased in the MOT, the regime of operation transitions from temperature-limited (TL) to multiple-scattering (MS) [34–36]. In the TL regime, the cold atoms are essentially non-interacting because N_A is small (typically less than 10^4) and the density is low. The cloud acts as an ideal gas in this regime, and, as more atoms are loaded into the trap, the size of the cloud remains the same while the density increases linearly and its distribution remains Gaussian [37]. For larger N_A ($\geq 10^5$) the cloud begins operating in the MS regime and the density becomes largely independent of N_A [38]. Two effects are seen in this regime. Firstly, repulsive forces caused by the re-absorption of scattered photons lead to an increase in the cloud size while the density remains constant. This radiation trapping effect determines the density and temperature of cold atoms [3,39]. For example, at $N_A \sim 10^7$ the cloud density is maintained and the optical thickness is such that, on an average, each photon absorbed from the cooling laser beams will, after re-emission, scatter no more than once on its way out of the cloud. This determines the spatial growth of the cloud as N_A increases beyond 10^7 [40]. The second effect is due to an attenuation force which arises from the intensity gradients in the MOT beams and the absorption of such by the atoms [38,41]. This results in spatial compression of the cloud and a small reduction in spring constant of the trap [42]. When the MOT transitions from the TL to the MS regime, the atom distribution may or may not change from Gaussian to flat-topped. Thus, at higher cloud densities, cloud images may not be a direct indicator of density. Measurements using an ONF negate the use of imaging analysis to estimate cloud volume (for example, [39]) making it simpler to observe regime-change in the MOT via fluorescence coupling.

By considering an observation volume surrounding the ONF, cloud density can be studied as the light-shift parameter is varied. It is assumed that atoms within a hollow observation cylinder with an outer radius equal to the ONF radius + 300 nm are most likely to emit fluorescence into the guided mode of the ONF [19,22]. This number of effective atoms, n_{eff}, can be estimated at one end of the ONF using $n_{eff} = 2C_P/R_{sc}\eta_{ONF}Q\eta_{QD}$ where R_{sc} is the atomic scattering rate, η_{ONF} is the average coupling efficiency of photons into the guided ONF mode in one direction (estimated at 2% using previous work based on ^{133}Cs [43]), Q is the ONF transmission from the middle of the ONF waist to the detector (the transmission through the entire length of fibre is 60% so Q=77% for half the fibre length), and η_{QD} is the quantum efficiency of the SPCM (60%). The quantity C_P is the fluorescent count rate obtained by the SPCM and is obtained from the RR raw data. The scattering rate, R_{sc}, is described by [35]

$$R_{sc} = \frac{\Gamma}{2}\frac{C_1^2\Omega_{tot}^2/2}{\delta^2+\Gamma^2/4+C_2^2\Omega_{tot}^2/2}. \quad (3)$$

Here, Ω_{tot} is the Rabi frequency for all MOT beams and is taken to be six times that of any one of the trapping beams. C_1 and C_2 are average Clebsch–Gordan co-efficients. The values of C_1^2 and C_2^2 are assumed to be equal due to optical pumping among the Zeeman sublevels in the presence of strong coupling between atoms and the radiation field [35].

If N_{eff} is plotted as a function of light-shift parameter, saturation of the atom number commences from $\Omega^2/|\delta|\Gamma \sim 1.2$ onwards (Fig. 7). As the observation volume is fixed by the ONF radius, this saturation effect is due to the spatial expansion of the cloud while it maintains constant density and may also indicate the onset of the MS regime in the MOT.

5. Outlook and conclusion

The temperature of a cold ensemble of ^{85}Rb atoms has been measured using the RR method with an ONF. The RR sequence was applied to an AOM allowing the MOT beams to be switched off rapidly. The results presented here agree with those found by the forced oscillation method [25] and again reinforce the viability of placing the ONF in yet colder atomic samples. This work has highlighted the sensitivity of the cloud temperature to small changes in beam misalignment, detunings, and intensities, and

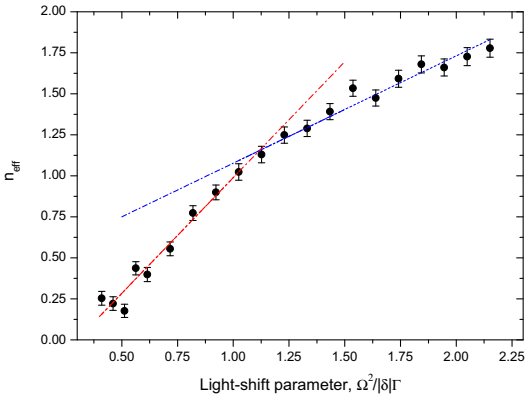

Fig. 7. Estimation of effective atom-number, n_{eff}, with increasing dimensionless light-shift parameter $\Omega^2/|\delta|\Gamma$ (black circles) with two linear fits to indicate the change in slope around a light-shift parameter 1.2.

demonstrates the ability to detect these temperature changes with the ONF. As the detector can be positioned anywhere in the cloud of atoms, a systematic temperature measurement, while exploring the entire parameter space, can be performed.

Free-space RR measurements show that, with the same variation in laser cooling intensity as we have used, a few hundred μK span can be observed. The results here display this trend and, additionally, provide detailed information about the velocity distribution of the atom cloud. In particular, with the ONF-based RR method, the system is sensitive to atoms near the fibre surface and, using data analysis, it is possible to generate a decay curve that shows how those near-surface atoms with a high velocity leave the capture region quickly and do not continue to contribute to the signal detected via the ONF.

Values for the springs constant of the MOT, inferred from temperature results, increase with cooling laser intensity until some critical value of the light-shift parameter is reached (≈ 1) and then begin to level out. Further, by examining coupling signal strengths while varying the light-shift parameter, the density regime in which the MOT is operating can be identified.

Acknowledgments

The authors wish to thank W. Cotter for help in creating the AOM sequencing programme. This work is partially supported by Science Foundation Ireland under Grant nos. 07/RFP/PHYF518 and 08/ERA/I1761 through the NanoSci-E+ Project NOIs, OIST Graduate University and the Higher Education Authority via the INSPIRE programme. LR acknowledges support from IRCSET under the Embark Initiative.

References

[1] P. Kohns, P. Buch, W. Suptitz, C. Csambal, W. Ertmer, Europhysics Letters (EPL) 22 (1993) 517.
[2] C.D. Wallace, T.P. Dinneen, K.Y.N. Tan, A. Kumarakrishnan, P.L. Gould, J. Javanainen, Journal of the Optical Society of America B 11 (1994) 703.
[3] A. Vorozcovs, M. Weel, S. Beattie, S. Cauchi, A. Kumarakrishnan, Journal of the Optical Society of America B 22 (2005) 943.
[4] A.M. Steane, C.J. Foot, Europhysics Letters (EPL) 14 (1991) 231.
[5] S. Tung, Y. Chen, C. Lin, L. Hsu, I. Yu, Chinese Journal of Physics 38 (2000) 395.
[6] D.R. Meacher, D. Boiron, H. Metcalf, C. Salomon, G. Grynberg, Physical Review A 50 (1994) R1992.
[7] R. Silva, K. Magalhaes, E. Henn, L. Marcassa, V. Bagnato, Optics Communications 265 (2006) 526.
[8] S. Chu, L. Hollberg, J.E. Bjorkholm, A. Cable, A. Ashkin, Physical Review Letters 55 (1985) 48.
[9] P.D. Lett, R.N. Watts, C.I. Westbrook, W.D. Phillips, P.L. Gould, H.J. Metcalf, Physical Review Letters 61 (1988) 169.
[10] J.D. Love, W.M. Henry, W.J. Stewart, R.J. Black, S. Lacroix, F. Gonthier, IEE Proceedings J, Optoelectronics (1991) 138 343.
[11] G. Brambilla, Journal of Optics 12 (2010) 043001.
[12] J.C. Knight, G. Cheung, F. Jacques, T.A. Birks, Optics Letters 22 (1997) 1129.
[13] M.L. Gorodetsky, V.S. Ilchenko, Journal of the Optical Society of America B 16 (1999) 147.
[14] J.M. Ward, S. Nic Chormaic, Applied Physics B 100 (2010) 847.
[15] A. Watkins, J. Ward, S. Nic Chormaic, Japanese Journal of Applied Physics 51 (2012) 052501.
[16] G. Brambilla, G.S. Murugan, J.S. Wilkinson, D.J. Richardson, Optics Letters 32 (2007) 3041.
[17] M.C. Frawley, A. Petcu-Colan, V.G. Truong, S. Nic Chormaic, Optics Communications 285 (2012) 4648.
[18] F. Le Kien, S. Dutta Gupta, V.I. Balykin, K. Hakuta, Physical Review A 72 (2005) 1.
[19] K.P. Nayak, P.N. Melentiev, M. Morinaga, F.L. Kien, V.I. Balykin, K. Hakuta, Optics Express 15 (2007) 5431.
[20] L. Russell, D.A. Gleeson, V.G. Minogin, S. Nic Chormaic, Journal of Physics B: Atomic, Molecular and Optical Physics 42 (2009) 185006.
[21] V.G. Minogin, S. Nic Chormaic, Laser Physics 20 (2009) 32.
[22] M.J. Morrissey, K. Deasy, Y. Wu, S. Chakrabarti, S. Nic Chormaic, The Review of Scientific Instruments 80 (2009) 053102.
[23] E. Vetsch, D. Reitz, G. Sagué, R. Schmidt, S.T. Dawkins, A. Rauschenbeutel, Physical Review Letters 104 (2010) 203603.
[24] L. Russell, M. Daly, S. Nic Chormaic, 1- and 2-photon absorption by laser-cooled Rb-85 using an optical nanofiber, in: Quantum Africa 2010: Theoretical and experimental foundations of recent quantum technology, vol. 1469, American Institute of Physics, 2010, pp. 82–90.
[25] L. Russell, K. Deasy, M.J. Daly, M.J. Morrissey, S. Nic Chormaic, Measurement Science and Technology 23 (2012) 015201.
[26] A. Goban, K.S. Choi, D.J. Alton, D. Ding, C. Lacroûte, M. Pototschnig, T. Thiele, N.P. Stern, H.J. Kimble, Physical Review Letters 109 (2012) 033603.
[27] S.M. Hendrickson, M.M. Lai, T.B. Pittman, J.D. Franson, Physical Review Letters 105 (2010) 173602.
[28] S.M. Spillane, G.S. Pati, K. Salit, M. Hall, P. Kumar, R.G. Beausoleil, M.S. Shahriar, Physical Review Letters 100 (2008) 231.
[29] J.M. Ward, D.G. O'Shea, B.J. Shortt, M.J. Morrissey, K. Deasy, S.G. Nic Chormaic, Review of Scientific Instruments 77 (2006) 083105.
[30] E.R. Abraham, E.A. Cornell, Applied Optics 37 (1998) 1762.
[31] P.V.D. Straten, H. Metcalf, The quest for BEC, in: Interactions in Ultracold Gases: From Atoms to Molecules, September, Wiley-VCH Verlag GmbH and Co., 2002, pp. 1–70.
[32] C.G. Townsend, N.H. Edwards, K.P. Zetie, C.J. Cooper, J. Rink, C.J. Foot, Physical Review A 53 (1996) 1702.
[33] P.D. Lett, W.D. Phillips, S.L. Rolston, C.E. Tanner, R.N. Watts, C.I. Westbrook, Journal of the Optical Society of America B 6 (1989) 2084.
[34] T. Walker, D. Sesko, C. Wieman, Physical Review Letters 64 (1990) 408.
[35] C.G. Townsend, N.H. Edwards, C.J. Cooper, K.P. Zetie, C.J. Foot, A.M. Steane, P. Szriftgiser, H. Perrin, J. Dalibard, Physical Review A 52 (1995) 1423.
[36] V.B. Tiwari, S. Singh, H.S. Rawat, M.P. Singh, Journal of Physics B: Atomic, Molecular and Optical Physics 41 (2008) 205301.
[37] I. Guedes, M.T.D. Araujo, D.M.B.P. Milori, G.I. Surdutovich, V.S. Bagnato, S.C. Zilio, Journal of the Optical Society of America B 11 (1994) 1935.
[38] D.W. Sesko, T.G. Walker, C.E. Wieman, Journal of the Optical Society of America B 8 (1991) 946.
[39] K.R. Overstreet, P. Zabawa, J. Tallant, A. Schwettmann, Optics Express 13 (2005) 9672.
[40] K. Lindquist, M. Stephens, C. Wieman, Physics Review A 46 (1992) 4082.
[41] J. Dalibard, Optics Communications 68 (1988) 203.
[42] J.A. Greenberg, M. Ori, A.M.C. Dawes, D.J. Gauthier, Optics Express 15 (2007) 17699.
[43] F. Le Kien, V.I. Balykin, K. Hakuta, Physical Review A 73 (2006) 013819.

Experimental studies on a dark magneto-optical trap for ^{85}Rb

L. Russell[a,b], R. Kumar[a,b], V. B. Tiwari[a, d], S. Nic Chormaic[a,b,d]
[a]Department of Physics, University College Cork, Cork, Ireland; [b]Light-Matter Interactions Unit, OIST Graduate University, 1919-1 Tancha, Onna-son, Okinawa 904-0495, Japan; [c]Laser Physics Applications Section, Raja Ramanna Centre for Advanced Technology, Indore 452013, India; [d]School of Chemistry and Physics, University of Kwa-Zulu Natal, Durban 4001, South Africa

ABSTRACT

This work is concerned with density enhancements in a laser-cooled sample of ^{85}Rb using a dark magneto-optical trap (MOT). The density of atoms in a standard MOT is limited to approximately ~10^{11} atoms/cm^3 due to radiation pressure and collisions. The dark MOT (DMOT) circumvents problems associated with radiation pressure in the atom cloud. To create a DMOT, a donut-shaped repump beam is projected on to the cloud of ^{85}Rb. The dark region in the center of the donut is attenuated by ~10^{-4} compared to the bright outer ring. Atoms which encounter this dark region in the repump beam are scattered to the lower hyperfine ground level, $F = 2$, otherwise known as the dark hyperfine level. Additionally, a depump beam is used to force more atoms into $F = 2$. Results using free-space spectroscopy are presented to demonstrate the effect of the donut-shaped repump beam and the depump beam on the population distribution of the atoms in the hyperfine ground states. A tapered optical fiber is used to measure the quality of the DMOT via a parameter, p, and a strong population transfer from the bright, $F = 3$, to the dark, $F = 2$, hyperfine ground level is demonstrated. The tapered fiber, with a waist of ~ 1 μm, is made from commercially-available optical fiber and is used to detect fluorescence from the cold ^{85}Rb coupled into the fiber guided modes. This work lays the foundation for optical nanofiber absorption spectroscopy with a small number of atoms in an optically-dense system.

Keywords: laser-cooling, dark MOT, rubidium, tapered optical fiber, optical nanofiber, atom cloud density

1. INTRODUCTION

The tapered optical fiber (TOF), otherwise known as the optical micro/nanofiber depending on the waist diameter, is an ultrathin light guide usually fabricated from commercially available fiber using a heat-and-pull technique[1]. The enhancement of the spontaneous emission from atoms surrounding a TOF into its guided modes[2] is well known, making it an ideal high-sensitivity tool for channeling atomic fluorescence to a detector. In recent years, TOFs have been used as active or passive probes for cold atoms[3-11] and hot atomic vapors[12-14]. In the work reported here, atom cloud density enhancement techniques for a sample of laser-cooled ^{85}Rb atoms are studied in order to increase the fluorescence and/or absorption signals obtainable with TOFs. The density of atoms in a standard magneto-optical trap (MOT) is limited to ~10^{11} atoms/cm^3 for two reasons. First, a transfer of kinetic energy occurs when a ground state atom collides with an excited state atom leading to a trap loss rate that is proportional to the number of atoms trapped. The second limitation is due to laser-cooled atoms in the MOT reabsorbing scattered photons, a phenomenon known as *radiation pressure*. The outward radiation pressure of the fluorescent light balances the confining forces of the trapping laser beams at a particular density and, at this point, if the number of atoms is increased, the atom cloud simply grows in size rather than in density. For the TOF, this is a major consideration; if one wishes to do absorption experiments using optical nanofibers, as many atoms as possible are required to fill the evanescent region around the fiber in order to optimize the signal quality.

In 1993 Ketterle *et al.*[15] demonstrated a new design of MOT, known as the *dark* MOT (DMOT), which confined sodium atoms in the lower (or dark) hyperfine ground level, where they are unperturbed by the cooling beams and, thus, the DMOT is free from the density limitations of a standard *bright* MOT (BMOT). By reducing the intensity of the repump beams used in the standard BMOT configuration almost all the atoms are transferred from the bright hyperfine ground level to the dark hyperfine ground level. Although a small excitation rate is optimal for confining large numbers of atoms at a high density, the maximum possible excitation rate is required to efficiently capture atoms from a vapor and load them into a MOT. By using bright and dark regions in the repump beam simultaneously, both of these requirements can be fulfilled; a donut-shaped (or hollow) repump beam can be used for this as it consists of a bright outer ring of light,

containing a dark inner circle. An atom which encounters the central dark region (i.e. the region with negligible repump intensity) will only spend a very short time in the cooling cycle before being shelved into the dark hyperfine level.

One way of working with a BMOT and DMOT is by generating them sequentially in time using triggered, mechanical shutters and AOMs. However, an alternative approach is to generate the BMOT and DMOT in different spatial regions of the trap, as achieved using the aforementioned donut-shaped repump beam. The spatially generated DMOT has experimental advantages since atoms can be continuously loaded into the dark region from the outer bright MOT where the usual processes occur. In fact, although the inner, dark region is not really a magneto-optical trap, the outer bright region still captures background atoms and feeds the dark section. In other words, experimental parameters for the atoms at the trap center can be monitored and adjusted, while simultaneously maintaining the high loading rate achievable with the bright MOT. This is possible because the trapped atom cloud is localized near the minimum of the magnetic field, whereas the capture of atoms occurs throughout the whole intersection volume of the cooling laser beams. Note that only the spatial DMOT is considered in the work that follows. This arrangement is very appealing for optical-fiber-based work. For example, the possibility of continuous absorption measurements via a TOF probe becomes available. Permyakova *et al.*[16] report that, even with moderate beam powers of the order of 6 mW, the dark MOT can capture a large number of atoms and achieve optical densities as high as 9. Thus, by using low cooling laser intensities (for confining large numbers of atoms at a high density) in a DMOT scheme, high signal-to-noise ratios for the fluorescence coupling can be achieved for minimal beam powers. This leads to the potential demonstration of non-linear optics effects in the atom cloud without requiring high laser powers.

In the mid-1990s, Townsend *et al.*[17] demonstrated atom densities of nearly 10^{12} cm^{-3} in a DMOT for cesium. Prior to this, no report of similar density enhancements for elements other than sodium had been reported. The larger hyperfine splittings found in heavier alkali-metal atoms means that the dark MOT technique is not as straightforward as it is for sodium. For example, a ^{85}Rb atom will undergo many cooling cycles (from $F = 3 \rightarrow F' = 4$, see Fig. 1) before falling to the $F = 2$ dark, hyperfine ground level due to spontaneous Raman processes. This cycling time can be shortened by using an additional *depump* beam, tuned to the $F = 3 \rightarrow F' = 3$ transition (see Fig. 1). The experimental setup described in Townsend *et al.*[17] employed two hollow repump beams in addition to the depump beam to force cesium atoms into the dark, hyperfine ground level.

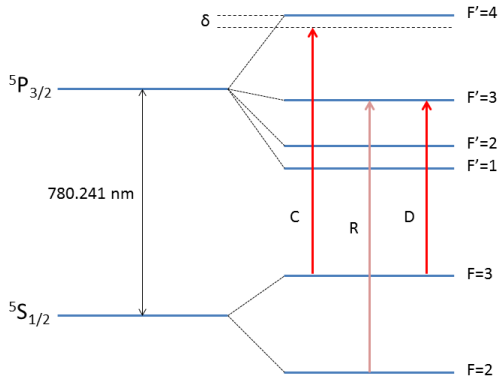

Fig. 1. Energy levels used in the dark MOT for ^{85}Rb. 'C' represents the cooling laser, 'R' represents the repump beam, and 'D' represents the depump beam.

2. EXPERIMENTAL SETUP

2.1. Laser configuration

A retro-reflected three beam MOT configuration is used for laser-cooling and trapping ^{85}Rb atoms. The donut-shaped repump beam is generated in the following manner. First, the laser beam is expanded in a telescope setup to a diameter of 25 mm (see Fig. 2). A separate, unity magnification telescope is used to place a shadow in the beam and project it on to the atom cloud. A glass slide with an opaque circle as the shadow is placed near the focal point of the telescope and

aligned to create the hollow, donut-shaped, repump beam at the MOT. The opaque circle has a transmission of 10^{-4} as determined experimentally. If the circle were placed in the beam without being incorporated in a telescope system, Fresnel diffraction effects would occur at the trap center. This would diminish the efficiency of the dark MOT in shelving atoms into the $F = 2$ dark, hyperfine ground level. To facilitate rapid swapping from a DMOT to a BMOT, the slide with the shadow in the optical path of the repump beam can be easily unclipped from its holder and removed, turing the donut beam into a standard Gaussian repump beam.

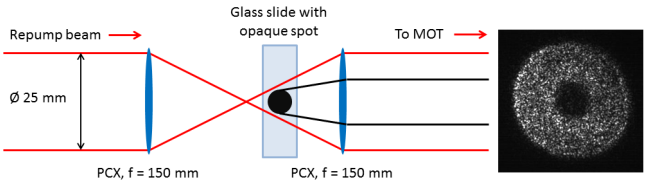

Fig. 2. Left: Experimental setup used to create the hollow repump beam using a unity magnifier with an opaque circle positioned near the center of two lenses. This imaging setup reduces Fresnel diffraction in the beam at the position of the MOT. Right: Repump beam profile obtained.

For rubidium, simply having a hollow repump beam is not enough to generate a large dark state fraction[17]. This is in contrast to sodium, where the splitting between the ground hyperfine levels is small enough to ensure that off-resonant scattering from the excited, F', level to the lowest hyperfine level occurs with reasonably high frequency over the many cooling cycles. In ^{85}Rb, the splitting between the hyperfine ground levels, $F = 2$ and $F = 3$, is approximately 3 GHz and, therefore, the central, dark region of the repump beam is simply not sufficient to generate a good DMOT. An additional depump beam is used, tuned near $F = 3 \rightarrow F' = 3$, to force more atoms into the lower (dark) level, as indicated in Fig. 1. In fact, the depump beam can be used with a normal, Gaussian profile repump beam to reach a moderate fraction of dark atoms. This is termed a forced, dark MOT (FDMOT). However, the combination of the depump beam and the hollow repump beam allows one to reach very dark MOTs and is the preferred technique to use.

Rather than directing the hollow repump beam along a path which copropagates with a cooling beam a separate path is used. The reason for this is due to the retro-reflecting mirrors in the cooling beam path for the MOT design. If the hollow repump beam were aligned such that it passed centrally through the cloud, but reflected back off a retro-reflecting mirror, in general, the back-reflected dark spot would not align with the forward propagating one and could destroy the DMOT.

2.2. Quantifying the DMOT quality

To quantify the 'darkness' of the trap Ketterle *et al.*[15] introduced a quality parameter, p, that denotes the fraction of atoms in the bright, ground hyperfine level compared to the total number of atoms in the ground state, where

$$p = \frac{N_b}{N_b + N_d}. \tag{1}$$

N_b is the number of atoms in the bright hyperfine level ($F = 3$) and N_d is the number of atoms in the dark hyperfine level ($F = 2$). The quality of the DMOT is determined from p, where $p = 1$ represents a 100% bright MOT and $p = 0$ is a 100% dark MOT. For the measurements of p reported here a TOF with diameter ~1 μm is passed through the center of the atom cloud. Resonance fluorescence emitted from the laser-cooled atoms couples into the guided modes of the TOF and is subsequently measured at one fiber pigtail end using a single photon counting module (SPCM). The recorded count rate is proportional to the number of atoms in whichever hyperfine ground level is probed, thereby enabling a measurement of p to be performed. Alternatively, p can be estimated from the magnitude of observed absorption dips if free-space spectroscopy is performed.

3. EXPERIMENTAL STUDIES

3.1. Free-space spectroscopy of the DMOT

The experimental setup is shown in Fig. 3. Initially, a free-space probe beam is passed through the atom cloud for absorption spectroscopy measurements, as illustrated in Fig. 3(a). The free-space probe beam is aligned with the center of the cloud so that it will pass through the dark region of the DMOT. The probe beam is obtained from a 780 nm ECDL

operating in scanning mode and frequency tuned via saturated absorption spectroscopy. The beam, after passing through the cloud, is directed to an avalanche photodiode (APD) (Hamamatsu model: C5460-01). The output signal of the APD is sent to a computer where it is analyzed via LabVIEW.

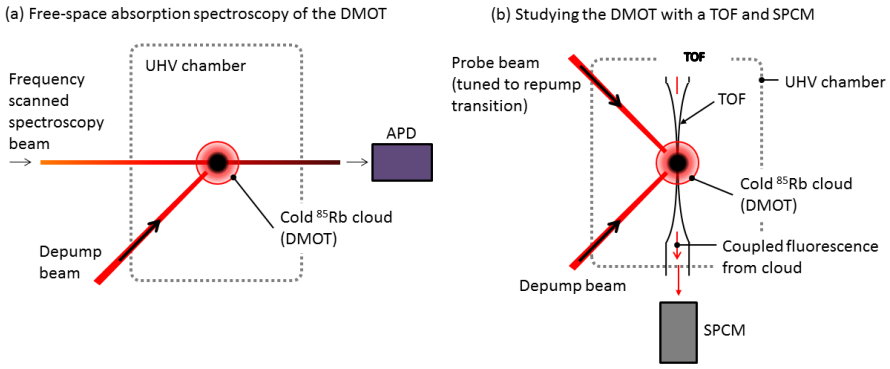

Fig. 1. Experimental setup. (a): free-space spectroscopy on the DMOT incorporating a frequency-scanned probe beam, APD: avalanche photodiode. (b): probing the DMOT with an optical fiber, TOF: tapered optical fiber.

Figure 4 (upper plot) shows the absorption spectra obtained using the free-space method to obtain a bright MOT. The lower plot in Fig. 4 shows the spectra for a well-optimized dark MOT (with hollow repump beam and depump light). It is evident that the magnitude of the $F = 2 \rightarrow F' = 1,2,3$ dips has doubled for the DMOT compared to the BMOT, while the magnitude of the $F = 3 \rightarrow F' = 2,3,4$ dips has approximately halved, indicating a clear enhancement of the atom population in the $F = 2$ hyperfine level for the DMOT compared to the BMOT.

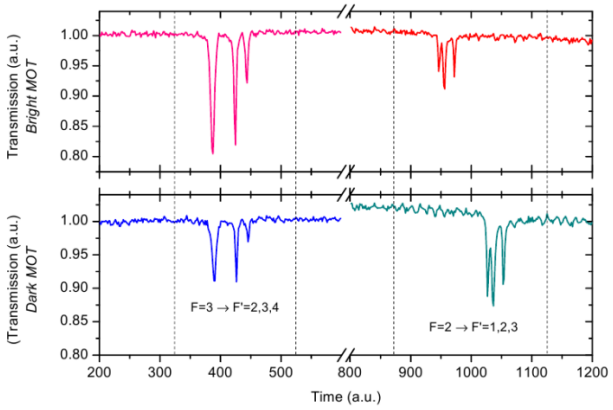

Fig. 2. Upper trace: Free-space absorption spectroscopy on a BMOT. Lower trace: Free-space absorption spectroscopy on an optimized DMOT. The DMOT here is created using a hollow repump MOT beam and a depump beam. There is clearly more population in the $F = 2$ lower hyperfine level for the DMOT compared to the BMOT.

An alternative way to create a dark MOT is to create a forced dark MOT (FDMOT). This can be obtained by applying the depump beam to the BMOT without placing a shadow in the repump MOT beam (i.e. without the donut-shaped beam, but rather a standard Gaussian). Figure 5 shows the spectra obtained for both the FDMOT and the DMOT. The DMOT actually allows more $F = 3$ atoms in the trapping region than the FDMOT since the depump beam, when aligned correctly, only affects those atoms in the dark region of the donut-shaped repump beam. The DMOT is advantageous in

this case as the outer, bright region continues to feed the inner, dark region, thereby continuously feeding the DMOT. In other words, having a large population of bright $F = 3$ atoms around the dark $F = 2$ atoms is better for the overall atom number throughout the cloud.

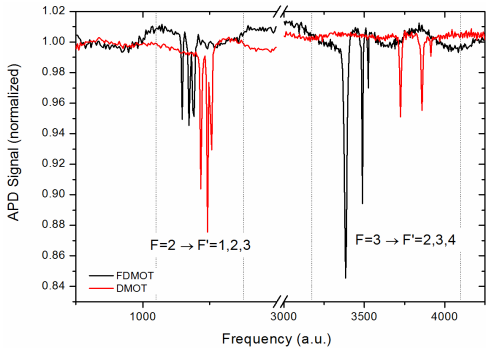

Fig. 3. Comparison between FDMOT (black plot) and DMOT (red plot). Although the FDMOT allows a large number of atoms to remain in $F = 3$, the DMOT is advantageous as much lower p values can be achieved, indicating a darker atom cloud.

3.2. Characterizing the DMOT with a TOF

By using beam stops to block and unblock the depump beam and/or the probe beam, different populations of atoms can be studied using an ~ 1 μm diameter tapered optical fiber (Fibercore SM750) passing through the atom cloud. An SPCM is connected to one end of the TOF so that atomic fluorescence from the atom cloud can be recorded. The setup is shown in Fig. 3(b). In the previous section, a probe beam generated by an ECDL was used. Here, the probe beam is derived from the repump beam of the MOT and aligned, in free-space, with the center of the atom cloud. The frequency of this probe beam is fixed with an AOM and tuned to the repump transition of ^{85}Rb. Figure 6 shows two loading curves: the upper (black) plot is for a BMOT and the lower (red) plot is for a DMOT. The DMOT in this instance has no depump shining on it and, thus, it is not extremely dark (i.e. p is not very low). This explains why the resulting coupling is relatively large (~750 counts/5 ms) compared to the coupling from the BMOT (~2000 counts/5 ms). The steady state count rate for both curves is proportional to the number of atoms in $F = 3$ although the distribution of atoms between both hyperfine ground states, $F = 2$ and $F = 3$, is different in each case. However, these two sets of data are not sufficient to determine the population of each ground state or how dark the DMOT is. To determine the value of p with the SPCM and ONF two sets of data must be recorded and analyzed. This is explained in the following section.

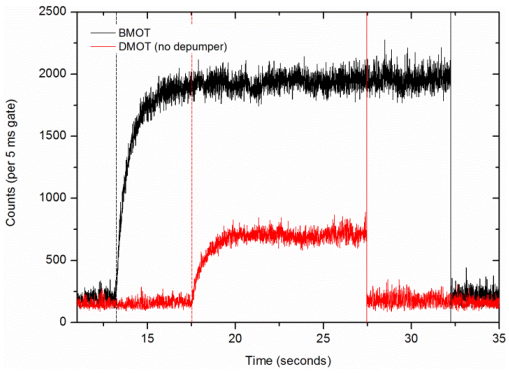

Fig. 4. Loading curves for a BMOT (black, upper) and a DMOT (red, lower). This plot shows the residual fluorescence coupling that can be obtained using a DMOT of modest p value. In this case, the DMOT has been created with the hollow repump beam only (no depump light has been used).

Figure 7(a) shows the fluorescence count rate through the fiber for a DMOT created with a hollow repump beam (no depumping beam). At ~7.5 s, the magnetic field is switched on and the DMOT loads. The fluorescence level increases from 125 counts/2 ms (indicated by the red line that shows the background light coupling into the fiber) to ~ 275 counts/2 ms due to the residual bright atoms in the DMOT. In other words, the $F = 3$ atoms contribute ~150 counts/2 ms to the signal. This is the numerator of p as given in Eq. 1 and has been determined by forming a DMOT with just a hollow repump beam. In Fig. 7(b), the fluorescence signal is recorded for a DMOT created with a hollow repump beam and the depumper. This yields the baseline count rate of 175 counts/2 ms (blue line) and, thus, the numerator of p in this case is 50 counts/2 ms. Furthermore, in this plot, the probe beam is added to the optical configuration. This probe beam is tuned to the repumping transition of ^{85}Rb and aligned with the dark region of the cloud. Thus, it "fills in" the dark central region of the donut-shaped repump beam, thereby recreating a standard BMOT configuration. The probe switches on for 100 ms at 1 Hz repetition rate, while the depump switches off at the same time and rate. The observed spikes in the fluorescence count rate (~1150 counts/2 ms) coupled into the tapered optical fiber are from atoms in both the ground state hyperfine levels, $F = 2$ and 3. This is the denominator of p. By taking the ratio of the baseline (125 counts/2 ms) in Fig. 7(a) to the peak counts in Fig. 7(b), and correcting for the background level, the value for p is determined as ~ 0.10 in a dark MOT without the depumper. However, with the inclusion of the depumper the dark MOT is improved and a value of $p \sim 50/1150 \approx 0.04$ is obtained.

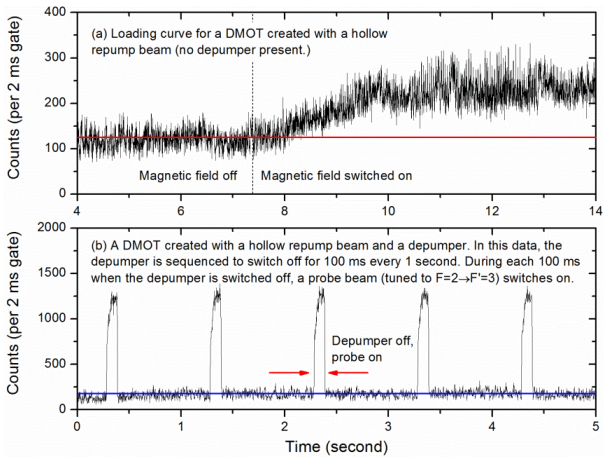

Fig. 5. Florescence count rate coupled into the tapered optical fiber for: (a) A DMOT created with a hollow repump beam and no depump light. At 7.5 s, the magnetic field is switched on to allow the DMOT to load. The fluorescence level increases from 125 counts/2 ms to 275 counts/2 ms. This is due to remaining bright atoms in $F = 3$ in the DMOT. (b) A DMOT created with a hollow repump beam and a depumper. The depumper is switched **off** for 100 ms at 1 Hz repetition rate. Additionally, there is also a probe beam that switches on when the depump is off. This probe beam is aligned with the center of the DMOT and tuned to the repump transition of ^{85}Rb ($F = 2 \rightarrow F' = 3$). The height of the peaks in this plot (~1150 counts/2 ms) are proportional to the number of atoms in both hyperfine ground levels. In both plots the donut-shaped repump beam is on at all times. By taking the ratio of the baseline counts in (a) to the peaks in (b) the value for p is determined to be ~0.10. However, by including the depumper, p is determined using the baseline of (b) (blue line): 50/1150 ≈ 0.04.

3.3. DMOT loading times

Loading curves can be analyzed for the DMOT and BMOT via the ONF. Figure 8 shows a loading curve for a BMOT (upper panel) and a loading curve for a DMOT (lower panel). Both curves have been background-corrected. The BMOT curve yields a loading rate, R_B, of 15.4×10^4 counts/s by fitting it with $N(t)=R_B/\Gamma(1-e^{-\Gamma t})$ where Γ is the collisional loss rate in the MOT. The plot in the lower panel is the loading curve for a DMOT which has been created with a hollow repump beam and a depumper. The spikes in fluorescence occurring at 1 Hz (for 100 ms duration) are due to the simultaneous switching off of the depumper and switching on the probe beam for detection purposes. As discussed previously, these conditions (depumper off and probe on) recreate the conditions for a BMOT and provide a measurement of the denominator of p. These peaks in the DMOT curve reach values of $\sim1\times10^5$ counts/s, matching the steady state count rate

of the upper (BMOT) loading curve. The baseline curve of the DMOT plot represents the loading curve of the fraction of $F = 3$ atoms present in the DMOT. The DMOT does not help the loading process so the loading rate cannot be larger in the DMOT than in the BMOT. In Fig. 8 one can see that the loading rate of the DMOT, R_D, is ~ $0.2R_B$. For this DMOT, $p = 0.22$. The change in R_D can be also be examined as a function of p. In Fig. 8(b), p is varied (using different depumper intensities) over the range 0.08 to 0.50. The loading rate of the DMOT decreases for lower p values as expected[18].

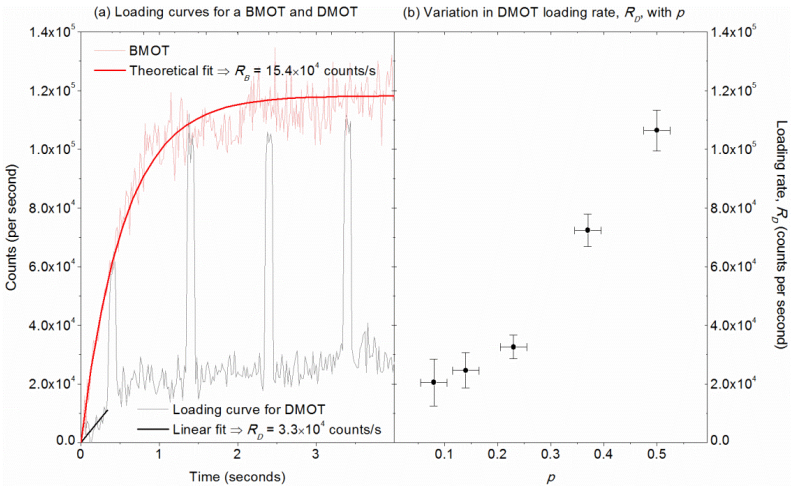

Fig. 6. Background-corrected loading curves for the BMOT and DMOT are shown in (a) with theoretical fits to determine the loading rates: $R_B = 15.4\times10^4$ counts/s, $R_D = 3.3\times10^4$ counts/s. In this case, $p = 0.22$ for the DMOT. (b) Changing R_D for varying p.

4. CONCLUSION

In conclusion, this work examined the implementation of a DMOT in order to circumvent the density-limitations of a BMOT. The density of atoms in a BMOT is a property that is limited by (a) reabsorption of emitted photons within the cloud and (b) collisions between ground state and excited state atoms leading to kinetic losses. For the TOF, this is a major consideration. If one wishes to do absorption style experiments using a TOF, for example, signal quality will be improved dramatically by forcing as many atoms as possible to fill the evanescent region around the fiber. Although there will still be collisional losses in a DMOT (unless $p = 0$), the reabsorption of scattered photons is no longer a dominant problem. By packing more atoms closer to the fiber surface, the evanescent field of a resonant beam passing through the fiber would be easily absorbed by nearby atoms. A density improvement is therefore critical to achieve high optical densities, thereby allowing demonstrations of nonlinear effects such as electromagnetically induced transparency (EIT) and slow light.[19,20] The DMOT reported here was created with a donut-shaped repump beam and a depump beam. The DMOT was characterized in two different ways. Firstly, free-space absorption spectroscopy was performed to obtain absorption spectra for the BMOT and DMOT. Secondly, with a probe beam (tuned to the repump transition), a tapered optical fiber was used to collect the resonant fluorescence from the atoms. The variation in DMOT loading rate, R_D, for changing p was measured via the TOF, with the lowest values of R_D obtained for the darkest DMOTs.

ACKNOWLEDGEMENTS

This work was supported by Science Foundation Ireland under Grant No. 08/ERA/I1761 through the NanoSci- E+ Transnational Programme, NOIs, and OIST Graduate University. LR acknowledges support from IRCSET through the Embark Initiative.

REFERENCES

[1] Ward, J. M., O'Shea, D. G., Shortt B. J., Morrissey, M. J., Deasy, K.D. and Nic Chormaic, S., "Heat-and-pull rig for fiber taper fabrication," Rev. Sci. Instrum. 77, 083105 (2006).

[2] Le Kien, F., Dutta Gupta, S., Balykin, V. I. and Hakuta, K., "Spontaneous emission of a cesium atom near a nanofiber: Efficient coupling of light to guided modes," Phys. Rev. A 72, 1–7 (2005).

[3] Nayak, K. P., Melentiev, P. N., Morinaga, M., Le Kien, F., Balykin, V. I. and Hakuta, K., "Optical nanofiber as an efficient tool for manipulating and probing atomic fluorescence," Opt. Exp. 15, 5431–8 (2007).

[4] Russell, L., Gleeson, D. A., Minogin, V. G. and Nic Chormaic, S., "Spectral distribution of atomic fluorescence coupled into an optical nanofiber," Journal of Physics B: Atomic, Molecular and Optical Physics 42, 185006 (2009).

[5] Minogin, V. G. and Nic Chormaic, S., "Manifestation of the van der Waals surface interaction in the spontaneous emission of atoms into an optical nanofiber," Las. Phys. 20, 32–37 (2009).

[6] Morrissey, M. J., Deasy, K., Wu, Y., Chakrabarti, S. and Nic Chormaic, S., "Tapered optical fibers as tools for probing magneto-optical trap characteristics," Rev. Sci. Instr. 80, 053102 (2009).

[7] Vetsch, E. Reitz, D., Sagué, G., Schmidt, R., Dawkins, S. T. and Rauschenbeutel, A., "Optical Interface Created by Laser-Cooled Atoms Trapped in the Evanescent Field Surrounding an Optical Nanofiber," Phys. Rev. Lett. 104, 203603 (2010).

[8] Russell, L., Daly, M. and Nic Chormaic, S., "1- and 2-photon absorption by laser-cooled Rb-85 using an optical nanofiber," Quantum Africa 2010: Theoretical and experimental foundations of recent quantum technology 82–90 (2010).

[9] Russell, L., Deasy, K., Daly, M. J., Morrissey, M. J. and Nic Chormaic, S., "Sub-Doppler temperature measurements of laser-cooled atoms using optical nanofibers," Meas. Sci. Technol. 23, 015201 (2012).

[10] Goban, A., Choi, K. S., Alton, D. J., Ding, D., Lacroûte, C., Pototschnig, M., Thiele, T., Stern, N. P. and Kimble, H. J., "Demonstration of a State-Insensitive, Compensated Nanofiber Trap," Phys. Rev. Lett. 109, 033603 (2012).

[11] Russell, L., Kumar, R., Tiwari, V. B. and Nic Chormaic, S., "Measurements on release-recapture of cold ^{85}Rb atoms using an optical nanofiber in a magneto-optical trap," arXiv:1303.7344v2 (2013).

[12] Spillane, S. M., Pati, G. S., Salit, K.., Hall, M., Kumar, P., Beausoleil, R. G. and Shahriar, M. S., "Observation of Nonlinear Optical Interactions of Ultralow Levels of Light in a Tapered Optical Nanofiber Embedded in a Hot Rubidium Vapor," Phys. Rev. Lett. 100, 1–4 (2008).

[13] Hendrickson, S. M., Lai, M. M., Pittman, T. B. and Franson, J. D., "Observation of Two-Photon Absorption at Low Power Levels Using Tapered Optical Fibers in Rubidium Vapor," Phys. Rev. Lett. 105, 173602 (2010).

[14] Watkins, A., Tiwari, V. B., Ward, J. M. and Nic Chormaic, S., "Observation of Zeeman shift in the rubidium D2 line using an optical nanofiber in vapor, " arXiv:1208.4708v3 (2013).

[15] Ketterle, W., Davis, K. B., Joffe, M. A., Martin, A. and Pritchard, D. E., "High densities of cold atoms in a dark spontaneous-force optical trap," Phys. Rev. Lett. 70, 2253–2256 (1993).

[16] Permyakova, O. I., Yakovlev, A. V. and Chapovskii, P. L., "Measurement of the lifetime of rubidium atoms in a dark magneto-optical trap," Quant. Elect. 38, 884–888 (2008).

[17] Townsend, C. G., Edwards, N. H., Zetie, K. P., Cooper, C. J., Rink, J. and Foot, C. J., "High-density trapping of cesium atoms in a dark magneto-optical trap," Phys. Rev. A 53, 1702–1714 (1996).

[18] Kim, J. Y. and Cho, D., "Dark-Spot Magneto-Optical Trap of Cesium Atoms," J. Kor. Phys. Soc. 39, 864–868 (2001).

[19] Braje, D., Balić, V., Yin, G. and Harris, S., "Low-light-level nonlinear optics with slow light," Phys. Rev. A 68, 1–4 (2003).

[20] Hakuta, K., "Single atoms on an optical nanofiber: a novel work system for slow light," Proc. SPIE 6904, 690406-1-5 (2008).

Bibliography

[1] J. Schmiedmayer, "A wire trap for neutral atoms," *Applied Physics B*, vol. 60, pp. 169–179, 1995.

[2] J. Reichel, W. Hänsel, and T. Hänsch, "Atomic micromanipulation with magnetic surface traps," *Physical Review Letters*, vol. 83, pp. 3398–3401, Oct. 1999.

[3] J. Fortagh, A. Grossmann, C. Zimmermann, and T. Hänsch, "Miniaturized wire trap for neutral atoms," *Physical Review Letters*, vol. 81, pp. 5310–5313, Dec. 1998.

[4] R. Folman, P. Krüger, D. Cassettari, B. Hessmo, T. Maier, and J. Schmiedmayer, "Controlling cold atoms using nanofabricated surfaces: atom chips," *Physical Review Letters*, vol. 84, pp. 4749–4752, May 2000.

[5] A. Ashkin, "Trapping of atoms by resonance radiation pressure," *Physical Review Letters*, vol. 40, no. 12, pp. 729–732, 1978.

[6] S. Chu, J. E. Bjorkholm, A. Ashkin, and A. Cable, "Experimental observation of optically trapped atoms," *Physical Review Letters*, vol. 57, no. 3, pp. 314–317, 1986.

[7] J. D. Miller, R. A. Cline, and D. J. Heinzen, "Far-off-resonance optical trapping of atoms," *Physical Review A*, vol. 47, no. 6, pp. 4567–4570, 1993.

[8] M. J. Renn, D. Montgomery, O. Vdovin, D. Z. Anderson, C. E. Wieman, and E. A. Cornell, "Laser-guided atoms in hollow-core optical fibers," *Physical Review Letters*, vol. 75, no. 18, pp. 3253–3256, 1995.

[9] D. Müller, E. Cornell, D. Anderson, and E. Abraham, "Guiding laser-cooled atoms in hollow-core fibers," *Physical Review A*, vol. 61, p. 033411, Feb. 2000.

[10] V. I. Balykin, K. Hakuta, F. Le Kien, J. Q. Liang, and M. Morinaga, "Atom trapping and guiding with a subwavelength-diameter optical fiber," *Physical Review A*, vol. 70, p. 011401, July 2004.

[11] F. Le Kien, V. I. Balykin, and K. Hakuta, "Atom trap and waveguide using a two-color evanescent light field around a subwavelength-diameter optical fiber," *Physical Review A*, vol. 70, pp. 1–9, Dec. 2004.

[12] G. Sagué, A. Baade, and A. Rauschenbeutel, "Blue-detuned evanescent field surface traps for neutral atoms based on mode interference in ultrathin optical fibres," *New Journal of Physics*, vol. 10, p. 113008, Nov. 2008.

[13] E. Vetsch, D. Reitz, G. Sagué, R. Schmidt, S. T. Dawkins, and A. Rauschenbeutel, "Optical interface created by laser-cooled atoms trapped in the evanescent field surrounding an optical nanofiber," *Physical Review Letters*, vol. 104, p. 203603, May 2010.

[14] A. Goban, K. S. Choi, D. J. Alton, D. Ding, C. Lacroûte, M. Pototschnig, T. Thiele, N. P. Stern, and H. J. Kimble, "Demonstration of a state-insensitive, compensated nanofiber trap," *Physical Review Letters*, vol. 109, p. 033603, July 2012.

[15] M. J. Morrissey, K. Deasy, Y. Wu, S. Chakrabarti, and S. Nic Chormaic, "Tapered optical fibers as tools for probing magneto-optical trap characteristics," *The Review of Scientific Instruments*, vol. 80, p. 053102, May 2009.

[16] K. S. Choi, H. Deng, J. Laurat, and H. J. Kimble, "Mapping photonic entanglement into and out of a quantum memory," *Nature*, vol. 452, pp. 67–71, Mar. 2008.

[17] K. Hammerer, A. S. Soerensen, and E. S. Polzik, "Quantum interface between light and atomic ensembles," *Reviews of Modern Physics*, vol. 82, pp. 1041–1093, Apr. 2010.

[18] N. Sangouard, C. Simon, H. de Riedmatten, and N. Gisin, "Quantum repeaters based on atomic ensembles and linear optics," *Reviews of Modern Physics*, vol. 83, pp. 33–80, Mar. 2011.

[19] J. Lee, D. H. Park, S. Mittal, M. Dagenais, and S. L. Rolston, "Integrated optical dipole trap for cold neutral atoms with an optical waveguide coupler," *New Journal of Physics*, vol. 15, p. 043010, Apr. 2013.

[20] J. Piilo and K.-A. Suominen, "Optical shielding of cold collisions in blue-detuned near-resonant optical lattices," *Physical Review A*, vol. 66, p. 013401, July 2002.

[21] J. Piilo, "Collision rates in near-resonant optical lattices," *Journal of the Optical Society of America B*, vol. 20, no. 5, pp. 1135–1140, 2003.

[22] S. Chu, L. Hollberg, J. E. Bjorkholm, A. Cable, and A. Ashkin, "Three-dimensional viscous confinement and cooling of atoms by resonance radiation pressure," *Physical Review Letters*, vol. 55, pp. 48–51, July 1985.

[23] J. Dalibard, S. Reynaud, and C. Cohen-Tannoudji, "Proposals of stable optical traps for neutral atoms," *Optics Communications*, vol. 47, no. 6, pp. 395–399, 1983.

[24] W. Phillips and H. Metcalf, "Laser deceleration of an atomic beam," *Physical Review Letters*, vol. 48, pp. 596–599, Mar. 1982.

[25] E. L. Raab, M. Prentiss, A. Cable, S. Chu, and D. E. Pritchard, "Trapping of neutral sodium atoms with radiation pressure," *Physical Review Letters*, vol. 59, pp. 2631–2634, Dec. 1987.

[26] P. D. Lett, R. N. Watts, C. I. Westbrook, W. D. Phillips, P. L. Gould, and H. J. Metcalf, "Observation of atoms laser cooled below the Doppler limit," *Physical Review Letters*, vol. 61, pp. 169–173, July 1988.

[27] A. W. Snyder, "Surface mode coupling along a tapered dielectric rod," *IEEE Transactions on Antennas and Propagation*, vol. 13, no. 5, pp. 821–822, 1965.

[28] A. W. Snyder, "Surface mode propagation along an array of dielectric rods with all elements excited identically," *IEEE Transactions on Antennas and Propagation*, vol. 14, no. 4, pp. 510–511, 1966.

[29] G. T. D. Francia, "Retina cones as dielectric antennas," *Journal of the Optical Society of America*, vol. 39, p. 324, Apr. 1949.

[30] J. M. Enoch, "Optical properties of the retinal receptors," *Journal of the Optical Society of America*, vol. 53, p. 71, Jan. 1963.

[31] C. V. Boys, "On the production, properties, and some suggested uses of the finest threads," *Proceedings of the Physical Society of London*, vol. 9, no. 1, 1887.

[32] R. Threfall, *On Laboratory Arts*. London: Macmillan, 1898.

[33] N. S. Kapany, "High-resolution fibre optics using sub-micron multiple fibres," *Nature*, vol. 184, pp. 881–883, 1959.

[34] T. H. Maiman, "Stimulated optical radiation in ruby," *Nature*, vol. 187, pp. 493–494, 1960.

[35] K. C. Kao and G. A. Hockham, "Dielectric-fibre surface waveguides for optical frequencies," *Proc. IEEE*, vol. 113, no. 7, pp. 1151–1158, 1966.

[36] X.-H. Zheng, "Understanding radiation from dielectric tapers," *Journal of the Optical Society of America A*, vol. 6, p. 190, Feb. 1989.

[37] M. Cada, F. Xiang, and L. B. Felsen, "A substantially improved treatment of intrinsic modes in tapered optical waveguides," *IEEE Journal of Quantum Electronics*, vol. 25, no. 5, pp. 933–938, 1989.

[38] T. Tamir, "Guided-wave methods for optical configurations," *Applied Physics*, vol. 25, no. 3, pp. 201–210, 1981.

[39] S. Weis, "Visualization of modal irradiance patterns in an optical fiber," *Education, IEEE Transactions on*, vol. 35, pp. 109–111, May 1992.

[40] F. Bilodeau, K. O. Hill, D. C. Johnson, and S. Faucher, "Compact, low-loss, fused biconical taper couplers: overcoupled operation and antisymmetric supermode cutoff," *Optics Letters*, vol. 12, pp. 634–6, Aug. 1987.

[41] T. Birks, "Twist-induced tuning in tapered fiber couplers," *Applied Optics*, vol. 28, pp. 4226–33, Oct. 1989.

[42] J. C. Knight, G. Cheung, F. Jacques, and T. A. Birks, "Phase-matched excitation of whispering-gallery-mode resonances by a fiber taper," *Optics Letters*, vol. 22, pp. 1129–31, Aug. 1997.

[43] T. E. Dimmick, G. Kakarantzas, T. a. Birks, and P. S. Russell, "Carbon dioxide laser fabrication of fused-fiber couplers and tapers.," *Applied Optics*, vol. 38, pp. 6845–8, Nov. 1999.

[44] S. Lacroix, F. Gonthier, and J. Bures, "All-fiber wavelength filter from successive biconical tapers," *Optics Letters*, vol. 11, pp. 671–3, Oct. 1986.

[45] D. T. Cassidy, D. C. Johnson, and K. O. Hill, "Wavelength-dependent transmission of monomode optical fiber tapers: errata.," *Applied Optics*, vol. 25, p. 328, Feb. 1986.

[46] J. Lou, L. Tong, and Z. Ye, "Modeling of silica nanowires for optical sensing," *Optics Express*, vol. 13, pp. 2135–40, Mar. 2005.

[47] N. Periasamy and F. P. Schiller, "Laser amplification in an optical fiber by evanescent field coupling," *Applied Physics*, vol. 24, pp. 201–203, 1981.

[48] H. Injeyan and N. G. Alexopoulos, "Light amplification by evanescent wave coupling in a multimode fiber," *Applied Optics*, vol. 21, no. 11, pp. 1928–1932, 1982.

[49] H. MacKenzie and F. Payne, "Evanescent field amplification in a tapered single-mode optical fibre," *Electronics Letters*, vol. 26, no. 2, p. 130, 1990.

[50] T. Birks, W. J. Wadsworth, and P. S. Russell, "Supercontinuum generation in tapered fibers," *Optics Letters*, vol. 25, pp. 1415–7, Oct. 2000.

[51] S. Leon-Saval, T. Birks, W. Wadsworth, P. St J Russell, and M. Mason, "Supercontinuum generation in submicron fibre waveguides," *Optics Express*, vol. 12, pp. 2864–9, June 2004.

[52] J. Bures and R. Ghosh, "Power density of the evanescent field in the vicinity of a tapered fiber," *Journal of the Optical Society of America A*, vol. 16, pp. 1992–1996, Aug. 1999.

[53] A. Anderson, S. Haroche, E. A. Hinds, W. Jhe, D. Meschede, and L. Moi, "Reflection of thermal Cs atoms grazing a polished glass surface," *Physical Review A*, vol. 34, no. 4, pp. 4–7, 1986.

[54] V. I. Balykin, V. S. Letokhov, Y. B. Ovchinnikov, and A. I. Sidorov, "Mirror reflection of atoms by laser light," *Physical Review Letters*, vol. 60, no. May, pp. 2137–2140, 1988.

[55] V. I. Balykin, V. S. Letokhov, Y. B. Ovchinnikov, and A. I. Sidorov, "Reflection of an atomic beam from a gradient of an optical field," *JETP Letters*, vol. 45, no. 6, pp. 282–284, 1987.

[56] J. Fu, X. Yin, and L. Tong, "Two-colour atom guide and 1D optical lattice using evanescent fields of high-order transverse modes," *Journal of Physics B: Atomic, Molecular and Optical Physics*, vol. 40, pp. 4195–4210, Nov. 2007.

[57] P. Schneeweiss, S. T. Dawkins, R. Mitsch, D. Reitz, E. Vetsch, and A. Rauschenbeutel, "A nanofiber-based optical conveyor belt for cold atoms," *Applied Physics B*, vol. 110, pp. 279–283, Dec. 2012.

[58] F. Le Kien, S. Dutta Gupta, V. I. Balykin, and K. Hakuta, "Spontaneous emission of a cesium atom near a nanofiber: efficient coupling of light to guided modes," *Physical Review A*, vol. 72, pp. 1–7, Sept. 2005.

[59] F. Le Kien, V. I. Balykin, and K. Hakuta, "Scattering of an evanescent light field by a single cesium atom near a nanofiber," *Physical Review A*, vol. 73, p. 013819, Jan. 2006.

[60] F. Le Kien and K. Hakuta, "Spontaneous radiative decay of translational levels of an atom near a dielectric surface," *Physical Review A*, vol. 75, p. 013423, Jan. 2007.

[61] F. Le Kien, S. Dutta Gupta, and K. Hakuta, "Optical excitation spectrum of an atom in a surface-induced potential," *Physical Review A*, vol. 75, p. 032508, Mar. 2007.

[62] F. Le Kien, S. Gupta, K. Nayak, and K. Hakuta, "Nanofiber-mediated radiative transfer between two distant atoms," *Physical Review A*, vol. 72, p. 063815, Dec. 2005.

[63] K. P. Nayak, P. N. Melentiev, M. Morinaga, F. L. Kien, V. I. Balykin, and K. Hakuta, "Optical nanofiber as an efficient tool for manipulating and probing atomic fluorescence," *Optics Express*, vol. 15, pp. 5431–8, Apr. 2007.

[64] G. Sagué, E. Vetsch, W. Alt, D. Meschede, and A. Rauschenbeutel, "Cold-atom physics using ultrathin optical fibers: light-induced dipole forces and surface interactions," *Physical Review Letters*, vol. 99, Oct. 2007.

[65] L. Russell, D. A. Gleeson, V. G. Minogin, and S. Nic Chormaic, "Spectral distribution of atomic fluorescence coupled into an optical nanofibre," *Journal of Physics B: Atomic, Molecular and Optical Physics*, vol. 42, p. 185006, Sept. 2009.

[66] L. Russell, M. Daly, and S. Nic Chormaic, "1- and 2-photon absorption by laser-cooled Rb-85 using an optical nanofiber," in *Quantum Africa 2010: Theoretical and experimental foundations of recent quantum technology*, vol. 1469, pp. 82–90, American Institute of Physics, Sept. 2010.

[67] K. Deasy, A. Watkins, M. Morrissey, R. Schmidt, and S. Nic Chormaic, "Few atom detection and manipulation using optical nanofibres," in *Quantum Communication and Quantum Networking* (A. Sergienko, S. Pascazio,

and P. Villoresi, eds.), vol. 36, pp. 200–209, Berlin, Heidelberg: Springer Berlin Heidelberg, 2010.

[68] L. Russell, K. Deasy, M. J. Daly, M. J. Morrissey, and S. Nic Chormaic, "Sub-Doppler temperature measurements of laser-cooled atoms using optical nanofibres," *Measurement Science and Technology*, vol. 23, p. 015201, Jan. 2012.

[69] L. Russell, R. Kumar, V. B. Tiwari, and S. Nic Chormaic, "Measurements on release-recapture of cold ^{85}Rb atoms using an optical nanofibre in a magneto-optical trap," *Optics Communications*, vol. 309, pp. 313–317, 2013.

[70] W. Alt, "An objective lens for efficient fluorescence detection of single atoms," *Optik - International Journal for Light and Electron Optics*, vol. 113, pp. 142–144, Jan. 2002.

[71] H. J. Metcalf and P. van der Straten, *Laser Cooling and Trapping*. Springer, 1999.

[72] W. D. Phillips, "Laser cooling and trapping of neutral atoms," *Reviews of Modern Physics*, vol. 70, no. 3, pp. 721–741, 1998.

[73] C. J. Hawthorn, K. P. Weber, and R. E. Scholten, "Littrow configuration tunable external cavity diode laser with fixed direction output beam," *Review of Scientific Instruments*, vol. 72, no. 12, p. 4477, 2001.

[74] C. E. Wieman and L. Hollberg, "Using diode lasers for atomic physics," *Review of Scientific Instruments*, vol. 62, no. 1, pp. 1–20, 1991.

[75] L. Ricci, M. Weidemüller, T. Esslinger, A. Hemmerich, C. Zimmermann, V. Vuletic, W. Koenig, and T. W. Hänsch, "A compact grating-stabilized diode laser system for atomic physics," *Optics Communications*, vol. 117, pp. 541–549, 1995.

[76] H. Youk, "Numerical study of quadrupole magnetic traps for neutral atoms: anti-Helmholtz coils and a U-chip," *Canadian Undergraduate Physics Journal*, vol. 3, no. 2, pp. 13–18, 2005.

[77] M. V. R. K. Murty, "The use of a single plane parallel plate as a lateral shearing interferometer with a visible gas laser source," *Applied Optics*, vol. 3, pp. 531–534, Apr. 1964.

[78] S. Pricking and H. Giessen, "Tapering fibers with complex shape," *Optics Express*, vol. 18, pp. 3426–37, Feb. 2010.

[79] A. Yariv, *Optical Electronics*. Oxford University Press, 4th ed., 1990.

[80] A. Petcu-Colan, *Higher order modes in few-mode nanofibres*. Masters disseration, University College Cork, 2012.

[81] M. C. Frawley, A. Petcu-Colan, V. G. Truong, and S. Nic Chormaic, "Higher order mode propagation in an optical nanofiber," *Optics Communications*, vol. 285, pp. 4648–4654, Oct. 2012.

[82] A. W. Snyder and W. R. Young, "Modes of optical waveguides," *Journal of the Optical Society of America*, vol. 68, p. 297, Mar. 1978.

[83] D. Gloge, "Weakly guiding fibers," *Applied Optics*, vol. 10, pp. 2252–8, Oct. 1971.

[84] J. M. Ward, D. G. O'Shea, B. J. Shortt, M. J. Morrissey, K. Deasy, and S. G. Nic Chormaic, "Heat-and-pull rig for fiber taper fabrication," *Review of Scientific Instruments*, vol. 77, no. 8, p. 083105, 2006.

[85] M. Sumetsky, Y. Dulashko, and A. Hale, "Fabrication and study of bent and coiled free silica nanowires: Self-coupling microloop optical interferometer," *Optics Express*, vol. 12, pp. 3521–31, July 2004.

[86] L. Shi, X. Chen, H. Liu, Y. Chen, Z. Ye, W. Liao, and Y. Xia, "Fabrication of submicron-diameter silica fibers using electric strip heater," *Optics Express*, vol. 14, pp. 5055–60, June 2006.

[87] G. Brambilla, V. Finazzi, and D. Richardson, "Ultra-low-loss optical fiber nanotapers," *Optics Express*, vol. 12, pp. 2258–2263, May 2004.

[88] M. Fujiwara, K. Toubaru, and S. Takeuchi, "Optical transmittance degradation in tapered fibers," *Optics Express*, vol. 19, pp. 8596–8601, Apr. 2011.

[89] R. P. Kenny, T. A. Birks, and K. P. Oakley, "Control of optical fibre taper shape," *Electronics Letters*, vol. 27, pp. 1654–1656, Aug. 1991.

[90] J. D. Love, W. M. Henry, W. J. Stewart, R. J. Black, S. Lacroix, and F. Gonthier, "Tapered single-mode fibres and devices. I. Adiabaticity criteria," in *Optoelectronics, IEE Proceedings J*, vol. 138, pp. 343–354, Oct. 1991.

[91] W. V. Sorin, "Control of optical fibre taper shape," *Electronics Letters*, vol. 27, pp. 144–54, Feb. 1991.

[92] T. Birks and Y. Li, "The shape of fiber tapers," *Journal of Lightwave Technology*, vol. 10, no. 4, pp. 432–438, 1992.

[93] D. J. Alton, N. P. Stern, T. Aoki, H. Lee, E. Ostby, K. J. Vahala, and H. J. Kimble, "Strong interactions of single atoms and photons near a dielectric boundary," *Nature Physics*, vol. 7, pp. 159–165, Nov. 2010.

[94] M. Schlosser, S. Tichelmann, J. Kruse, and G. Birkl, "Scalable architecture for quantum information processing with atoms in optical microstructures," *Quantum Information Processing*, vol. 10, pp. 907–924, Sept. 2011.

[95] H. B. G. Casimir and D. Polder, "The influence of retardation on the London-van der Waals forces," *Physical Review*, vol. 73, no. 4, pp. 360–372, 1948.

[96] J. P. Dowling and J. Gea-Banacloche, "Evanescent light-wave atom mirrors, resonators, waveguides, and traps," *Advances in Atomic, Molecular, and Optical Physics*, vol. 37, pp. 1–94, 1996.

[97] P. E. Barclay, K. Srinivasan, O. Painter, B. Lev, and H. Mabuchi, "Integration of fiber-coupled high-Q SiN[sub x] microdisks with atom chips," *Applied Physics Letters*, vol. 89, no. 13, p. 131108, 2006.

[98] D. A. Smith, S. Aigner, S. Hofferberth, M. Gring, M. Andersson, S. Wildermuth, P. Krüger, S. Schneider, T. Schumm, and J. Schmiedmayer, "Absorption imaging of ultracold atoms on atom chips," *Optics Express*, vol. 19, pp. 8471–85, Apr. 2011.

[99] V. G. Minogin and S. Nic Chormaic, "Manifestation of the van der Waals surface interaction in the spontaneous emission of atoms into an optical nanofiber," *Laser Physics*, vol. 20, pp. 32–37, July 2009.

[100] H. Nha and W. Jhe, "Cavity quantum electrodynamics for a cylinder: inside a hollow dielectric and near a solid dielectric cylinder," *Physical Review A*, vol. 56, no. 3, pp. 2213–2220, 1997.

[101] T. Soendergaard, "General theory for spontaneous emission in active dielectric microstructures: example of a fiber amplifier," *Physical Review A*, vol. 64, p. 033812, Aug. 2001.

[102] V. Klimov and M. Ducloy, "Spontaneous emission rate of an excited atom placed near a nanofiber," *Physical Review A*, vol. 69, p. 013812, Jan. 2004.

[103] D. W. Vernooy and H. J. Kimble, "Quantum structure and dynamics for atom galleries," *Physical Review A*, vol. 55, no. 2, pp. 1239–1261, 1997.

[104] L. D. S. Menezes, S. Goetzinger, A. Mazzei, V. Sandoghdar, and O. Benson, "Nanoparticles and microspheres: tools to study the interaction of quantum emitters via shared optical modes," in *Laser Resonators and Beam Control VII* (A. V. Kudryashov, ed.), vol. 5333, pp. 174–182, June 2004.

[105] M. Rosenblit, Y. Japha, P. Horak, and R. Folman, "Simultaneous optical trapping and detection of atoms by microdisk resonators," *Physical Review A*, vol. 73, p. 063805, June 2006.

[106] M. Cai, O. Painter, and K. Vahala, "Observation of critical coupling in a fiber taper to a silica-microsphere whispering-gallery mode system," *Physical Review Letters*, vol. 85, pp. 74–7, July 2000.

[107] K. P. Nayak and K. Hakuta, "Single atoms on an optical nanofibre," *New Journal of Physics*, vol. 10, p. 053003, May 2008.

[108] M. Oria, M. Chevrollier, D. Bloch, M. Fichet, and M. Ducloy, "Spectral observation of surface-induced van der Waals attraction on atomic vapour," *Europhysics Letters (EPL)*, vol. 14, no. 6, p. 527, 1991.

[109] I. E. Dzyaloshinskii, E. M. Lifshitz, and L. P. Pitaevskii, "The general theory of van der Waals forces," *Advances in Physics*, vol. 10, no. 38, pp. 37–41, 1961.

[110] Y. S. Barash and V. L. Ginzburg, "Some problems in the theory of van der Waals forces," *Soviet Physics Uspekhi*, vol. 27, no. 7, p. 7, 1984.

[111] Y. Tikochinsky and L. Spruch, "Retarded Casimir interaction in the asymptotic domain of an electron and a dielectric wall," *Physical Review A*, vol. 48, no. 6, pp. 4223–4235, 1993.

[112] M. Fichet, F. Schuller, D. Bloch, and M. Ducloy, "Van der Waals interactions between excited-state atoms and dispersive dielectric surfaces," *Physical Review A*, vol. 51, no. 2, pp. 1553–1564, 1995.

[113] A. Krishna, K. Pandey, A. Wasan, and V. Natarajan, "High-resolution hyperfine spectroscopy of excited states using electromagnetically induced transparency," *Europhysics Letters (EPL)*, vol. 72, pp. 221–227, Oct. 2005.

[114] M. Chevrollier, D. Bloch, G. Rahmat, and M. Ducloy, "Van der Waals-induced spectral distortions in selective-reflection spectroscopy of Cs vapor: the strong atom-surface interaction regime," *Optics Letters*, vol. 16, pp. 1879–81, Dec. 1991.

[115] W. Johnson, V. Dzuba, U. Safronova, and M. Safronova, "Finite-field evaluation of the Lennard-Jones atom-wall interaction constant C_3 for alkali-metal atoms," *Physical Review A*, vol. 69, p. 022508, Feb. 2004.

[116] M. C. Frawley, S. Nic Chormaic, and V. G. Minogin, "The van der Waals interaction of an atom with the convex surface of a nanocylinder," *Physica Scripta*, vol. 85, p. 058103, May 2012.

[117] K. P. Nayak, F. Le Kien, M. Morinaga, and K. Hakuta, "Antibunching and bunching of photons in resonance fluorescence from a few atoms into guided modes of an optical nanofiber," *Physical Review A*, vol. 79, p. 021801, Feb. 2009.

[118] F. Le Kien and K. Hakuta, "Correlations between photons emitted by multiatom fluorescence into a nanofiber," *Physical Review A*, vol. 77, p. 033826, Mar. 2008.

[119] A. M. Steane, M. Chowdhury, and C. J. Foot, "Radiation force in the magneto-optical trap," *Journal of the Optical Society of America B*, vol. 9, no. 12, pp. 2142–2158, 1992.

[120] A. K. Mohapatra, *Study of atom-surface interaction using laser cooled atoms*. PhD dissertation, Tata Institute of Fundamental Research, 2005.

[121] M. H. Anderson, W. Petrich, J. R. Ensher, and E. A. Cornell, "Reduction of light-assisted collisional loss rate from a low-pressure vapor-cell trap," *Physical Review A*, vol. 50, pp. R3597–R3600, Nov. 1994.

[122] P. Kohns, P. Buch, W. Suptitz, C. Csambal, and W. Ertmer, "On-line measurement of sub-Doppler temperatures in a Rb magneto-optical trap-by-trap centre oscillations," *Europhysics Letters (EPL)*, vol. 22, pp. 517–522, June 1993.

[123] C. D. Wallace, T. P. Dinneen, K. Y. N. Tan, A. Kumarakrishnan, P. L. Gould, and J. Javanainen, "Measurements of temperature and spring constant in a magneto-optical trap," *Journal of the Optical Society of America B*, vol. 11, p. 703, May 1994.

[124] A. Vorozcovs, M. Weel, S. Beattie, S. Cauchi, and A. Kumarakrishnan, "Measurements of temperature scaling laws in an optically dense magneto-optical trap," *Journal of the Optical Society of America B*, vol. 22, no. 5, p. 943, 2005.

[125] A. M. Steane and C. J. Foot, "Laser cooling below the Doppler limit in a magneto-optical trap," *Europhysics Letters (EPL)*, vol. 14, pp. 231–236, Feb. 1991.

[126] S. Tung, Y. Chen, C. Lin, L. Hsu, and I. Yu, "Cooling atoms below 100 μK," *Chinese Journal of Physics*, vol. 38, no. 2, pp. 395–399, 2000.

[127] D. R. Meacher, D. Boiron, H. Metcalf, C. Salomon, and G. Grynberg, "Method for velocimetry of cold atoms," *Physical Review A*, vol. 50, no. 3, p. R1992, 1994.

[128] R. Silva, K. Magalhaes, E. Henn, L. Marcassa, and V. Bagnato, "Temperature determination for magneto optical trapped atoms using a single parameter transient absorption," *Optics Communications*, vol. 265, no. 2, pp. 526–531, 2006.

[129] P. D. Lett, W. D. Phillips, S. L. Rolston, C. E. Tanner, R. N. Watts, and C. I. Westbrook, "Optical molasses," *Journal of the Optical Society of America B*, vol. 6, pp. 2084–2107, Nov. 1989.

[130] S. Pradhan and B. N. Jagatap, "Measurement of temperature of laser cooled atoms by one-dimensional expansion in a magneto-optical trap," *The Review of Scientific Instruments*, vol. 79, p. 013101, Jan. 2008.

[131] T. Walker, D. Sesko, and C. Wieman, "Collective behavior of optically trapped neutral atoms," *Physical Review Letters*, vol. 64, pp. 408–411, Jan. 1990.

[132] R. Stites, M. Beeler, L. Feeney, S. Kim, and S. Bali, "Sensitive measurement of radiation trapping in cold-atom clouds byintensity correlation detection," *Optics Letters*, vol. 29, pp. 2713–2715, Dec. 2004.

[133] P. van der Straten and H. Metcalf, "The quest for BEC," in *Interactions in Ultracold Gases: From Atoms to Molecules*, no. September, ch. 1, pp. 1–70, Wiley-VCH Verlag GmbH and Co., 2002.

[134] C. G. Townsend, N. H. Edwards, K. P. Zetie, C. J. Cooper, J. Rink, and C. J. Foot, "High-density trapping of cesium atoms in a dark magneto-optical trap," *Physical Review A*, vol. 53, pp. 1702–1714, Mar. 1996.

[135] C. G. Townsend, N. H. Edwards, C. J. Cooper, K. P. Zetie, C. J. Foot, A. M. Steane, P. Szriftgiser, H. Perrin, and J. Dalibard, "Phase-space density in the magneto-optical trap," *Physical Review A*, vol. 52, no. 2, pp. 1423–1440, 1995.

[136] V. B. Tiwari, S. Singh, H. S. Rawat, and M. P. Singh, "Measurements on impulsive force-induced dynamics of a cold ^{85}Rb atom cloud in a magneto-optical trap," *Journal of Physics B: Atomic, Molecular and Optical Physics*, vol. 41, no. 205301, p. 205301, 2008.

[137] I. Guedes, M. T. D. Araujo, D. M. B. P. Milori, G. I. Surdutovich, V. S. Bagnato, and S. C. Zilio, "Forces acting on magneto-optically trapped atoms," *Journal of the Optical Society of America B*, vol. 11, no. 10, pp. 1935–1940, 1994.

[138] D. W. Sesko, T. G. Walker, and C. E. Wieman, "Behavior of neutral atoms in a spontaneous force trap," *Journal of the Optical Society of America B*, vol. 8, pp. 946–958, May 1991.

[139] K. R. Overstreet, P. Zabawa, J. Tallant, and A. Schwettmann, "Multiple scattering and the density distribution of a Cs MOT," *Optics Express*, vol. 13, no. 24, pp. 9672–9682, 2005.

[140] K. Lindquist, M. Stephens, and C. Wieman, "Experimental and theoretical study of the vapor-cell Zeeman optical trap," *Physics Review A*, vol. 46, no. 7, pp. 4082–4091, 1992.

[141] J. Dalibard, "Laser cooling of an optically thick gas: the simplest radiation pressure trap?," *Optics Communications*, vol. 68, no. 3, pp. 203–208, 1988.

[142] J. A. Greenberg, M. Ori, A. M. C. Dawes, and D. J. Gauthier, "Absorption-induced trapping in an anisotropic magneto-optical trap," *Optics Express*, vol. 15, no. 26, pp. 17699–17708, 2007.

[143] S. Bali, D. Hoffmann, J. Simán, and T. Walker, "Measurements of intensity correlations of scattered light from laser-cooled atoms," *Physical Review A*, vol. 53, p. 3469, May 1996.

[144] W. Ketterle, K. B. Davis, M. A. Joffe, A. Martin, and D. E. Pritchard, "High densities of cold atoms in a dark spontaneous-force optical trap," *Physical Review Letters*, vol. 70, pp. 2253–2256, Apr. 1993.

[145] O. I. Permyakova, A. V. Yakovlev, and P. L. Chapovskii, "Measurement of the lifetime of rubidium atoms in a dark magneto-optical trap," *Quantum Electronics*, vol. 38, pp. 884–888, Sept. 2008.

[146] J. Y. Kim and D. Cho, "Dark-Spot Magneto-Optical Trap of Cesium Atoms," *Journal of the Korean Physical Society*, vol. 39, no. 5, pp. 864–868, 2001.

[147] D. Braje, V. Balić, G. Yin, and S. Harris, "Low-light-level nonlinear optics with slow light," *Physical Review A*, vol. 68, pp. 1–4, Oct. 2003.

[148] G. Labeyrie, E. Vaujour, C. A. Müller, D. Delande, C. Miniatura, D. Wilkowski, and R. Kaiser, "Slow diffusion of light in a cold atomic cloud," *Physical Review Letters*, vol. 91, no. 22, p. 223904, 2003.

[149] K. Hakuta, "Optical nanofibers for manipulating atoms and photons," in *Slow and Fast Light*, p. SWA5, Optical Society of America, July 2007.

[150] M. Bajcsy, S. Hofferberth, V. Balic, T. Peyronel, M. Hafezi, A. S. Zibrov, V. Vuletic, and M. D. Lukin, "Efficient all-optical switching using slow light within a hollow fiber," *Physical Review Letters*, vol. 102, p. 3902, May 2009.

[151] R. Garcia-Fernandez, W. Alt, F. Bruse, C. Dan, K. Karapetyan, O. Rehband, a. Stiebeiner, U. Wiedemann, D. Meschede, and a. Rauschenbeutel, "Optical nanofibers and spectroscopy," *Applied Physics B*, vol. 105, pp. 3–15, Sept. 2011.

[152] Y.-W. Lin, H.-C. Chou, P. P. Dwivedi, Y.-C. Chen, and I. A. Yu, "Using a pair of rectangular coils in the MOT for the production of cold atom clouds with large optical density," *Optics Express*, vol. 16, pp. 3753–61, Mar. 2008.

[153] H. Yan-Xu, L. Yong-Hong, Z. Chun-Hong, L. Shu-Jing, and W. Hai, "Realization of high optical density Rb magneto-optical trap," *Chinese Physics Letters*, vol. 26, p. 023201, Feb. 2009.

[154] N. Phillips, A. Gorshkov, and I. Novikova, "Light storage in an optically thick atomic ensemble under conditions of electromagnetically induced transparency and four-wave mixing," *Physical Review A*, vol. 83, p. 063823, June 2011.

[155] E. A. Donley, T. P. Heavner, F. Levi, M. O. Tataw, and S. R. Jefferts, "Double-pass acousto-optic modulator system," *Review of Scientific Instruments*, vol. 76, p. 063112, June 2005.

[156] K. Hakuta, "Single atoms on an optical nanofiber: a novel work system for slow light," *Proceedings of SPIE*, vol. 6904, pp. 06–1–5, 2008.

[157] K. Nayak, M. Das, F. Le Kien, and K. Hakuta, "Spectroscopy of near-surface atoms using an optical nanofiber," *Optics Communications*, vol. 285, no. 23, pp. 4698–4704, 2012.

[158] S. M. Hendrickson, M. M. Lai, T. B. Pittman, and J. D. Franson, "Observation of two-photon absorption at low power levels using tapered optical fibers in rubidium vapor," *Physical Review Letters*, vol. 105, p. 173602, Oct. 2010.

[159] J. Franson, B. Jacobs, and T. Pittman, "Quantum computing using single photons and the Zeno effect," *Physical Review A*, vol. 70, p. 062302, Dec. 2004.

[160] B. C. Jacobs and J. D. Franson, "All-optical switching using the quantum Zeno effect and two-photon absorption," *Physical Review A*, vol. 79, p. 063830, June 2009.

[161] G. S. Cassany, *Cold atom physics using ultra-thin optical fibres*. PhD dissertation, Rheinischen Friedrich-Wilhelms-Universität Bonn, 2008.

[162] Y. Chen, Y. Liao, L. Hsu, and I. A. Yu, "Simple technique for directly and accurately measuring the number of atoms in a magneto-optical trap," *Physical Review A*, vol. 64, no. 031401, p. 031401, 2001.

[163] K. E. Gibble, S. Kasapi, and S. Chu, "Improved magneto-optic trapping in a vapor cell," *Optics Letters*, vol. 17, no. 7, pp. 526–528, 1992.

[164] F. L. Kien, V. I. Balykin, and K. Hakuta, "State-insensitive trapping and guiding of cesium atoms using a two-color evanescent field around a subwavelength-diameter fiber," *Journal of the Physics Society Japan*, vol. 74, pp. 910–917, Mar. 2005.

[165] G. Brambilla, G. S. Murugan, J. S. Wilkinson, and D. J. Richardson, "Optical manipulation of microspheres along a subwavelength optical wire," *Optics Letters*, vol. 32, pp. 3041–3, Oct. 2007.

[166] G. Senthil Murugan, G. Brambilla, J. S. Wilkinson, and D. J. Richardson, "Optical propulsion of individual and clustered microspheres along sub-micron optical wires," *Japanese Journal of Applied Physics*, vol. 47, pp. 6716–6718, Aug. 2008.

[167] A. V. Masalov and V. G. Minogin, "Pumping of higher-order modes of an optical nanofiber by laser excited atoms," *Laser Physics Letters*, vol. 10, p. 075203, July 2013.

[168] R. Loudon, *The Quantum Theory of Light*. Oxford: Clarendon, 1973.

[169] E. R. Abraham and E. A. Cornell, "Teflon feedthrough for coupling optical fibers into ultrahigh vacuum systems," *Applied Optics*, vol. 37, pp. 1762–3, Apr. 1998.

[170] M. Akulin, "Quantum lens for atomic waves," *Physical Review Letters*, vol. 72, no. 4, pp. 437–442, 1994.

[171] H. Ban, M. Jacka, J. Hanssen, J. Reader, and J. McClelland, "Laser cooling transitions in atomic erbium," *Optics Express*, vol. 13, pp. 3185–95, Apr. 2005.

[172] G. Brambilla, "Optical fibre nanowires and microwires: a review," *Journal of Optics*, vol. 12, p. 043001, Apr. 2010.

[173] K.-A. Brickman, M.-S. Chang, M. Acton, A. Chew, D. Matsukevich, P. Haljan, V. Bagnato, and C. Monroe, "Magneto-optical trapping of cadmium," *Physical Review A*, vol. 76, p. 043411, Oct. 2007.

[174] T. M. Brzozowski, M. Maczynska, M. Zawada, J. Zachorowski, and W. Gawlik, "Time-of-flight measurement of the temperature of cold atoms for short trap-probe beam distances," *Journal of Optics B: Quantum and Semiclassical Optics*, vol. 4, pp. 62–66, Feb. 2002.

[175] O. Carnal, "Young's double-slit experiment with atoms: a simple atom interferometer," *Physical Review Letters*, vol. 66, no. 21, pp. 2689–2692, 1991.

[176] H. B. G. Casimir and D. Polder, "Influence of retardation on the London–van der Waals forces," *Nature*, vol. 158, pp. 787–788, Nov. 1946.

[177] Y. Castin, J. Dalibard, and C. Cohen-Tannoudji, "Laser cooling and trapping of neutral atoms," in *Proceedings of the Trento Workshop on Bose-*

Einstein Condensation (A. Griffin, D. W. Snoke, and S. Stringari, eds.), p. 173, 1993.

[178] J. Dalibard, C. Salomon, A. Aspect, E. Arimondo, R. Kaiser, N. Vansteenkiste, and C. Cohen-Tannoudji, "New schemes in laser cooling," *Atomic Physics XI*, p. 199, 1989.

[179] K. Deasy, *Quantum engineering of laser-cooled atoms: experiments and theory*. PhD thesis, CIT, 2011.

[180] J. Denschlag, D. Cassettari, and J. Schmiedmayer, "Guiding neutral atoms with a wire," *Physical Review Letters*, vol. 82, pp. 2014–2017, Mar. 1999.

[181] M. L. Gorodetsky and V. S. Ilchenko, "Optical microsphere resonators: optimal coupling to high-Q whispering-gallery modes," *Journal of the Optical Society of America B*, vol. 16, p. 147, Jan. 1999.

[182] J. Guest, N. Scielzo, I. Ahmad, K. Bailey, J. Greene, R. Holt, Z.-T. Lu, T. O'Connor, and D. Potterveld, "Laser trapping of ^{225}Ra and ^{226}Ra with repumping by room-temperature blackbody radiation," *Physical Review Letters*, vol. 98, p. 093001, Feb. 2007.

[183] H. Hachisu, K. Miyagishi, S. Porsev, A. Derevianko, V. Ovsiannikov, V. Pal'chikov, M. Takamoto, and H. Katori, "Trapping of neutral mercury atoms and prospects for optical lattice clocks," *Physical Review Letters*, vol. 100, p. 053001, Feb. 2008.

[184] J. He, B. Yang, Y. Cheng, T. Zhang, and J. Wang, "Extending the trapping lifetime of single atom in a microscopic far-off-resonance optical dipole trap," *Frontiers of Physics*, vol. 6, pp. 262–270, Apr. 2011.

[185] J. He, B. Yang, T. Zhang, and J. Wang, "Extending a release-and-recapture scheme to single atom optical tweezer for effective temperature evaluation," *Chinese Physics B*, vol. 20, p. 073701, July 2011.

[186] D. W. Keith, "Free-standing gratings and lenses for atom optics," *Journal of Vacuum Scienceand Technology B*, vol. 9, p. 2846, Nov. 1991.

[187] P. Kulatunga, H. Busch, L. Andrews, and C. Sukenik, "Two-color polarization spectroscopy of rubidium," *Optics Communications*, vol. 285, pp. 2851–2853, June 2012.

[188] M. Lu, S. H. Youn, and B. L. Lev, "Trapping ultracold dysprosium: a highly magnetic gas for dipolar physics," *Physical Review Letters*, vol. 104, p. 063001, Feb. 2010.

[189] I. Manai, R. Horchani, H. Lignier, P. Pillet, D. Comparat, A. Fioretti, and M. Allegrini, "Rovibrational cooling of molecules by optical pumping," *Physical Review Letters*, vol. 109, p. 183001, Oct. 2012.

[190] S. Mancini and S. Bose, "Engineering an interaction and entanglement between distant atoms," *Physical Review A*, vol. 70, p. 022307, Aug. 2004.

[191] J. McClelland and J. Hanssen, "Laser cooling without repumping: a magneto-optical trap for erbium atoms," *Physical Review Letters*, vol. 96, p. 143005, Apr. 2006.

[192] K. Nakayama, Y. Yoshikawa, H. Matsumoto, Y. Torii, and T. Kuga, "Precise intensity correlation measurement for atomic resonance fluorescence from optical molasses," *Optics Express*, vol. 18, no. 7, pp. 33–36, 2010.

[193] M. Ol'Shanii, Y. Ovchinnikov, and V. Letokhov, "Laser guiding of atoms in a hollow optical fiber," *Optics Communications*, vol. 98, no. 1-3, pp. 77–79, 1993.

[194] H. Perrin, P. Lemonde, F. Pereira dos Santos, V. Josse, B. Laburthe Tolra, F. Chevy, and D. Comparat, "Application of lasers to ultra-cold atoms and molecules," *Comptes Rendus Physique*, vol. 12, pp. 417–432, May 2011.

[195] G. Reinaudi, C. B. Osborn, M. McDonald, S. Kotochigova, and T. Zelevinsky, "Optical production of stable ultracold $^{88}Sr_2$ molecules," *Physical Review Letters*, vol. 109, p. 115303, Sept. 2012.

[196] T. M. Roach, H. Abele, M. G. Boshier, H. L. Grossman, K. P. Zetie, and E. A. Hinds, "Realization of a magnetic mirror for cold atoms," *Physical Review Letters*, vol. 75, no. 4, pp. 629–632, 1995.

[197] E. S. Shuman, J. F. Barry, and D. Demille, "Laser cooling of a diatomic molecule," *Nature*, vol. 467, pp. 820–3, Oct. 2010.

[198] S. M. Spillane, G. S. Pati, K. Salit, M. Hall, P. Kumar, R. G. Beausoleil, and M. S. Shahriar, "Observation of nonlinear optical interactions of ultralow levels of light in a tapered optical nanofiber embedded in a hot rubidium vapor," *Physical Review Letters*, vol. 100, pp. 23 1–4, June 2008.

[199] D. Sukachev, K. Chebakov, a. Sokolov, a. Akimov, N. Kolachevsky, and V. Sorokin, "Laser cooling of thulium atoms," *Optics and Spectroscopy*, vol. 111, pp. 633–638, Oct. 2011.

[200] L. Tong, J. Lou, and E. Mazur, "Single-mode guiding properties of subwavelength-diameter silica and silicon wire waveguides," *Optics Express*, vol. 12, pp. 1025–35, Mar. 2004.

[201] V. Vuletic, T. W. Hänsch, and C. Zimmermann, "Steep magnetic trap for ultra cold atoms," *Europhysics Letters (EPL)*, vol. 36, pp. 349–354, Nov. 1996.

[202] L. Wang, Z. Ji, J. Yuan, Y. Yang, Y. Zhao, J. Ma, L. Xiao, and S. Jia, "Investigation of ultracold atoms and molecules in a dark magneto-optical trap," *Chinese Physics B*, vol. 21, p. 113402, Nov. 2012.

[203] J. Ward, *Erbium doped fluoride and phosphate whispering gallery resonators*. PhD thesis, Cork Institute of Technology, 2007.

[204] A. Watkins, *Evanescent field sensing: optical nanofibres , whispering-gallery-mode microspherical and microbubble resonators*. PhD thesis, University College Cork, 2012.

[205] A. Watkins, J. Ward, and S. Nic Chormaic, "Thermo-optical tuning of whispering gallery modes in erbium: ytterbium doped glass microspheres to arbitrary probe wavelengths," *Japanese Journal of Applied Physics*, vol. 51, p. 052501, Apr. 2012.

[206] A. Watkins, J. Ward, Y. Wu, and S. Nic Chormaic, "Single-input spherical microbubble resonator," *Optics Letters*, vol. 36, no. 11, pp. 2113–2115, 2011.